

Manifestations of strong correlations and disorder in selected problems of condensed matter physics

Krsnik, Juraj

Doctoral thesis / Disertacija

2022

Degree Grantor / Ustanova koja je dodijelila akademski / stručni stupanj: **University of Zagreb, Faculty of Science / Sveučilište u Zagrebu, Prirodoslovno-matematički fakultet**

Permanent link / Trajna poveznica: <https://um.nsk.hr/um:nbn:hr:217:390421>

Rights / Prava: [In copyright](#) / [Zaštićeno autorskim pravom.](#)

Download date / Datum preuzimanja: **2024-10-19**



Repository / Repozitorij:

[Repository of the Faculty of Science - University of Zagreb](#)





University of Zagreb

FACULTY OF SCIENCE
DEPARTMENT OF PHYSICS

Juraj Krsnik

**Manifestations of strong correlations
and disorder in selected problems of
condensed matter physics**

DOCTORAL DISSERTATION

Zagreb, 2022.



University of Zagreb

FACULTY OF SCIENCE
DEPARTMENT OF PHYSICS

Juraj Krsnik

**Manifestations of strong correlations
and disorder in selected problems of
condensed matter physics**

DOCTORAL DISSERTATION

Supervisor:

dr. sc. Osor Slaven Barišić

Zagreb, 2022.



Sveučilište u Zagrebu

PRIRODOSLOVNO–MATEMATIČKI FAKULTET
FIZIČKI ODSJEK

Juraj Krsnik

**Manifestacija jakih korelacija i nereda u
odabranim problemima fizike
kondenzirane tvari**

DOKTORSKI RAD

Mentor:

dr. sc. Osor Slaven Barišić

Zagreb, 2022.

Information on supervisor

Osor Slaven Barišić is a senior researcher at the Institute of Physics in Zagreb, currently serving as director. His interests focus on theoretical condensed matter and statistical physics, with subjects involving strongly correlated systems, electron-phonon correlations, the role of impurities and disorder, phase transitions, and transport properties in solid state systems. In the course of his research, he has co-authored 35 research papers with over 1100 citations according to the Web of Science Core Collection. He is a member of the project “QuantiXLie - Scientific Center of Excellence for Quantum and Complex Systems, and Representations of Lie Algebras” funded by the European Structural and Investment Funds, and was recently the principal investigator of the project “The physics of many body systems – exploiting the world of complexity” funded by the Croatian Science Foundation. He is teaching the postgraduate course “Theoretical Condensed Matter Physics” at the Faculty of Science, University of Zagreb.

Acknowledgements

I thank all the people who gave me support during my doctoral studies and writing of this thesis, including my family, friends, colleagues, and acquaintances. However, there are a few people I would especially like to thank.

First and foremost, I would like to sincerely thank my supervisor Dr. Osor Slaven Barišić for his guidance, knowledge, support, understanding, and patience.

Drugo, želio bih se poimence zahvaliti djevojci Lei, baki Barbari, djedu Milanu i sestri Antoniji, koji su svaki na svoj način oplemenili moj život i pomogli izradi ovoga rada.

No, najdublje zahvale ipak zaslužuju moji roditelji, otac Kristijan i majka Jasminka, bez kojih ne bih bio tu i to što jesam.

The support from Croatian Science Foundation Project No. IP-2016-06-7258 and the QuantiXLie Center of Excellence, a project cofinanced by the Croatian government and European Union through the European Regional Development Fund - the Competitiveness and Cohesion Operational Program (Grant No. KK.01.1.1.01.0004) is acknowledged.

*Za vsaku dobro reč,
Kaj reči si mi znala,
Za vsaki pogled tvoj,
Za vsaki smeh tvoj, fala!*

*Tak malo dobroga
V življenju tu se najde,
I če je sunce čas,
Za oblak taki zajde.*

*A ti si v srce mi
Tak puno sunca dala.
Kaj morem ti neg reč:
Od vsega srca Fala!*

Dragutin Domjanić

Abstract

This thesis deals with several problems in condensed matter theory involving strong correlations and/or a disorder. It is divided into four parts, with the effects of electron-phonon interaction appearing as the key subject of the first three parts. The focus of the last part is on the role of strong disorder in strongly correlated systems.

In the first part, we provide the exact solution to the polaronic impurity problem and exploit it to study some aspects of local and transport properties in systems with dilute concentrations of polaronic impurities. We find a non-universal power-law decay of the electron mobility with temperature in bulk systems, which may be relevant for rationalizing the unconventional power-law exponents observed in organic semiconductors.

In the next step, the translational invariance of the electron-phonon system is restored. In the second part, we perturbatively address the polaron problem. We show that the leading order momentum-dependent electron self-energy becomes suppressed in the antiadiabatic limit. We argue that the polarization may be treated within the two-vertices renormalization scheme, with vertex corrections involving electron processes only.

Several experimental findings are analyzed by simulating angle-resolved photoemission spectroscopy (ARPES), electron energy loss spectroscopy, and phonon spectra for cases of strongly doped polar semiconductors in the third part. We show that ARPES spectra can provide a robust estimate of the electron-phonon interaction range. Emphasis is placed on the importance of the coupling strength in shaping both raw and integrated spectra of phonon-plasmon coupled systems.

In the last part of the thesis, we consider the very interesting phenomenon of many-body localization (MBL). We argue that the change from the thermal to the MBL phase may be thought of as a percolation transition in the Fock space, with the anomalous transport behaviors characterizing the large portion of the thermal phase.

Keywords: polaronic impurity, polaron, vertex corrections, phonon sidebands, phonon-plasmon coupling, many-body localization

Prošireni sažetak

U ovom radu teorijski je izučavano nekoliko odabranih problema u fizici kondenzirane tvari koji uključuju jako međudjelovanje *i*/ili nered. Rad je podijeljen u četiri dijela, gdje je okosnica prvih triju tema elektron-fonon međudjelovanje, dok se u zadnjem dijelu rada proučava međuigra elektronskog međudjelovanja i jakog nereda. Prvo poglavlje služi kao općeniti uvod u sve četiri teme, a uključuje kratak osvrt na modernu fiziku kondenzirane tvari i osnovne koncepte vezane uz dijagramatski perturbativni razvoj s posebnim naglaskom na važnost analize Feynmanovih dijagrama u vremenskoj domeni.

U žarištu interesa prvog dijela rada je model polaronske nečistoće koji uključuje vezanje elektrona s lokalnim fononskim stupnjem slobode na čvoru rešetke koji slama translacijsku invarijantnost modela. U poglavlju 2 izvedeno je egzaktno rješenje modela u formalizmu Greenovih funkcija. Uveden je operator $\hat{\Gamma}$ preko kojega je izražena egzaktna Greenova funkcija relevantna za problem polaronske nečistoće, a koja uključuje i sve neelastične procese vezane uz emisiju i apsorpciju realnih fonona. Budući da je elektron-fonon međudjelovanje unutar modela ograničeno na jedan čvor rešetke sa nečistoćom, moguće je izraziti matrične elemente operatora $\hat{\Gamma}$ preko proširenih razlomaka koji uključuju samo lokalne Greenove funkcije slobodnog elektrona. Za danu rešetku, pripadna lokalna Greenova funkcija slobodnog elektrona može biti izračunata analitički ili numerički, čime je egzaktno riješen problem polaronske nečistoće za sustav s proizvoljnom dimenzijom i geometrijom rešetke.

To egzaktno rješenje se dalje koristi u poglavljima 3 i 4 za analizu odabranih lokalnih i transportnih svojstava sustava s malim koncentracijama polaronskih nečistoća. U poglavlju 3 dobiven je tako zatvoreni izraz za koeficijent transmisije za proces tuneliranja elektrona kroz polaronsku nečistoću u sustavima reducirane dimenzije, relevantan za analizu spektara dobivenih neelastičnom elektronskom tunelirajućom spektroskopijom. Uočeno je da u punom dinamičkom problemu transmisija kao funkcija energije elektrona doživljava maksimume i minimume diktirane fononskom energetskom skalom za jako elektron-fonon vezanje.

U poglavlju 4 razmatraju se trodimenzionalni sustavi. Računanjem lokalne gustoće stanja pokazano je da za dovoljno snažno elektron-fonon vezanje može doći do stvaranja velikog broja vezanih elektronskih stanja čija je konkretna struktura vrlo osjetljiva na parametre modela. Potpis jakog elektron-fonon vezanja također je uočen i u delokaliziranom dijelu elektronskog spektra karakteriziranim jasnom rezonantnom strukturom koja ukazuje na rezonantno raspršenje elektrona na polaronskoj nečistoći. Računanjem svih elastičnih i neelastičnih parcijalnih udarnih presjeka za raspršenje elektrona na polaronskoj nečistoći dobiveno je relaksacijsko vrijeme elektrona te mobilnost elektrona kao funkcija temperature. Uočen je pad mobilnosti s potencijom

temperature vrlo osjetljivom na parametre modela. Ovakvo neuniverzalno ponašanje mobilnosti potencijalno može objasniti nekonvencionalne eksponente u padu mobilnosti s temperaturom zabilježenim u nekim organskim poluvodičima.

U drugom i trećem dijelu rada uvodi se elektron-fonon međudjelovanje na svaki čvor rešetke čime se vraća translacijska invarijantnost elektron-fonon sistema. Poglavlje 5 uvodno je poglavlje u drugi dio rada i posvećeno je polaronskom problemu koji je analiziran metodama dijagramatske perturbativne teorije s naglaskom stavljenim na vršne popravke. Prvo su proučavana elektronska svojstva polarona računanjem vlastite energije elektrona te karakterističnih svojstava koherentne polaronske vrpce u vodećem i prvom sljedećem redu razvoja po elektron-fonon međudjelovanju. Jedan od glavnih rezultata poglavlja 6 jest da je nelokalni dio vodeće vršne popravke vlastitoj energiji elektrona potisnut kvadratom adijabatskog parametra u antiadijabatskoj granici.

U poglavlju 7 polaronski problem dodatno je izučavan kroz prizmu fononskog stupnja slobode. Izvedeno je egzaktno rješenje za $\mathbf{q} = 0$ dio fononskog propagatora te je argumentirano da polarizacija može biti tretirana u shemi s dva renormalizirana elektron-fonon vrha, gdje vršna funkcija uključuje samo elektronske procese. Pomoću te činjenice izvedena je egzaktna renormalizacija elektron-fonon vrha u "ladder" aproksimaciji. Također je argumentirano da je renormalizacija fononske frekvencije u polaronskoj granici zanemariva uz činjenicu da se određeni dio njezine spektralne težine prelijeva u polaronsku vrpcu. Uz navedeni transfer fononske spektralne težine dodatno je uočeno i stvaranje viška fononske spektralne težine u polaronskoj vrpici. Ovaj višak spektralne težine, nazvan fononska produkcija, odgovara oblaku fonona vezan uz elektron u osnovnom stanju polarona.

Elektronska i fononska svojstva translacijski invarijantnih elektron-fonon sistema analizirana su metodama dijagramatske perturbativne teorije i u trećem dijelu rada, ali sada u slučajevima sa znatnim dopiranjem, odnosno kada degeneracija elektronskog plina bitno dolazi do izražaja. Rezultati u poglavlju 8 izravno su vezani na eksperimentalne spektre mjerene kutno-razlučivom fotoelektronskom spektroskopijom (ARPES - angle-resolved photoemission spectroscopy) polarnih materijala. Ti ARPES spektri sadržavaju karakteristične fononske pojaseve koji su simulirani računanjem vlastite energije šupljine u vodećem i prvom sljedećem redu razvoja po elektron-fonon međudjelovanju. Stavljajući fokus na imaginarni dio vodeće vlastite energije šupljine koja ulazi u simulirani ARPES spektar u energetsom prozoru pridruženom prvom fononskom pojasu, pokazano je da se distribucija njenog intenziteta u k prostoru značajno mijenja varirajući doseg elektron-fonon međudjelovanja. Na temelju te distribucije intenziteta imaginarnog dijela vlastite energije šupljine uvedeno je nekoliko parametara za karakterizaciju distribucije koji pružaju robusnu procjenu efektivnog dosega elektron-fonon međudjelovanja u stvarnim materijalima.

U poglavlju 9 fonon-plazmon vezanje u trodimenzionalnim i dvodimenzionalnim sustavima je sistematizirano analizirano kroz prizmu komplementarnih EELS (electron energy loss spectroscopy) spektara i fononskih spektralnih funkcija računatih unutar aproksimacije nasumičnih

faza. Pokriven je cijeli eksperimentalno relevantni parametarski prostor problema, određen adijabatskim parametrom, odnosno elektronskom gustoćom i jačinom elektron-fonon međudjelovanja. Uočeno je da jakost međudjelovanja igra značajnu ulogu u preraspodjeli spektralne težine među vezanim pobuđenjima u EELS spektru, što otvara mogućnost procjene jakosti međudjelovanja iz eksperimentalnih integriranih EELS spektara. Projekcijom vezanih pobuđenja na fononski stupanj slobode ponovno su uočeni značajni doprinosi fononskoj produkciji za jako vezanje, ali čija se fizikalna priroda razlikuje od one u polaronskoj granici i znatno ovisi o adijabatskom parametru. Konkretno, u adijabatskoj granici ona je posljedica mekšanja fononske frekvencije, dok je u antiadijabatskoj granici fononska produkcija povezana s oblakom virtualnih fonona koji je vezan na kolektivnu elektronsku oscilaciju plazme. Također su komentirana fononska svojstva fonon-plazmon problema dobivena u aproksimaciji statičkog zasjenjenja i granici statičke polarizacije od kojih se prva redovno koristi u proučavanju neadijabatskih efekata na fononska svojstva u *ab initio* modeliranju. Pokazano je da aproksimacija statičkog zasjenjenja ne može reproducirati fononski spektar dobiven u aproksimaciji nasumičnih faza niti u jednom dijelu parametarskog prostora, dok se aproksimacija statičke polarizacije pokazuje prihvatljivom za opis fononske spektralne funkcije jedino u adijabatskoj granici trodimenzionalnih sustava. Treći dio rada završava poglavljem 10 u kojem je pokazano da vršne korekcije u “ladder” aproksimaciji mekšaju $2k_F$ singularnost Lindhardove funkcije.

U zadnjem, četvrtom dijelu rada napušta se elektron-fonon međudjelovanje i proučava se međuigra elektronskog međudjelovanja i nereda u kontekstu fenomena mnogočestične lokalizacije (MBL - many-body localization). Kao model za istraživanje ovog fenomena promatra se jednodimenzionalni lanac s neredom i koreliranim fermionima bez spina čijem se rješavanju pristupa metodama numeričke egzaktne dijagonalizacije. Uvod u ovo vrlo dinamično područje istraživanja dan je u poglavlju 11, gdje je posebno naglašeno da je MBL faza izoliranog sustava, koja se pojavljuje za dovoljno jaki nered, karakterizirana odsustvom transporta i neergodičnim ponašanjem. S druge strane, za slabi nered isti model pokazuje tendencije ergodičnog ponašanja koji vodi do termalizacije sistema pa za neku kritičnu vrijednost jačine nereda dolazi do termalnog-MBL prijelaza.

U poglavlju 12 pokazano je da prilikom tog prijelaza dolazi do fundamentalne promjene u klasterizaciji mnogočestičnih stanja u Fockovom prostoru. Dok za jake nered u MBL fazi stanja u Fockovom prostoru imaju tendenciju grupirati se u mnogo klastera s malim brojem stanja, za male nered dolazi do formacije jednog makroskopskog klastera što upućuje na perkolacijsku prirodu termalnog-MBL prijelaza u Fockovom prostoru stanja.

Egzistencija MBL faze ima snažne implikacije i na transportna svojstva, odnosno na relaksaciju gustoće fermiona u realnom prostoru. U zadnjem poglavlju 13 relaksacija gustoće početnog stanja sustava prema ravnoteži u termalnoj fazi proučavana je klasičnim jednadžbama ne uzimajući u obzir učinke kvantnih interferencija mnogočestičnih stanja, gdje su dodatno uzeti u obzir samo rezonantni prijelazi između mnogočestičnih stanja. Za vrlo slabe nered dobiveno

je difuzno ponašanje, dok su približavanjem kritičnoj vrijednosti nereda uočena anomalna transportna svojstva sa sporijom relaksacijom prema ravnotežnom stanju nego što je očekivano kod difuznog ponašanja. Rezultati dobiveni preko klasičnih jednadžbi za relaksaciju početnog stanja dobro se slažu s rezultatima dobivenima punim kvantnim računima te ukazuju na eksponencijalno trnjenje efektivnog parametra difuzije s jakošću nereda.

Ključne riječi: polaronska nečistoća, polaron, vršne popravke, fononski pojasevi, fonon-plazmon vezanje, mnogočestična lokalizacija

Contents

Information on supervisor	i
Acknowledgements	iv
Abstract	iv
Prošireni sažetak	v
1 General introduction	1
1.1 Condensed matter physics: a brief retrospective	1
1.2 Feynman diagrams: frequency vs time domain	4
1.3 Outline and contributions of the thesis	7
Part I Polaronic impurity model	11
2 Exact solution	12
2.1 Model Hamiltonian	12
2.2 Experimental motivation	13
2.3 Green's function approach	14
2.3.1 Local operator $\hat{\Gamma}$	15
2.3.2 Static case	17
2.3.3 Dynamic case	17
2.3.4 Combining static and dynamic contributions	20
2.3.5 Green's function $G_{ll}^{1,0}(\omega)$	21
2.4 Conclusions	23
3 Tunneling through a polaronic impurity	24
3.1 Transmission coefficient	24
3.2 Conclusions	27

4	Scattering on polaronic impurities	28
4.1	Scattering cross section	28
4.1.1	Scattered wave	28
4.1.2	Probability current	30
4.1.3	Partial scattering cross sections	31
4.1.4	Total scattering cross section	32
4.2	Intermezzo: localized electron states	33
4.2.1	Scattering cross section dependence on impurity parameters	33
4.2.2	Local density of states	35
4.3	Electron mobility	37
4.3.1	Static case	38
4.3.2	Dynamic case	40
4.4	Conclusions	42
Part II	Perturbative approach to the polaron problem	44
5	The polaron concept	45
5.1	Relevance of polaronic physics	45
5.2	Model Hamiltonian	46
5.3	Categorization of polarons	47
5.4	Theoretical approaches to the polaron problem	48
5.4.1	DMFT of polarons - bridging the gap between the polaronic impurity and the polaron problem	48
6	Electronic properties of polarons	51
6.1	Leading order weak coupling perturbation theory	52
6.1.1	Electron spectral properties	53
6.1.2	Renormalization effects	55
6.2	Next-to-leading order weak coupling perturbation theory	58
6.2.1	Non-crossing diagram	59
6.2.2	Crossing diagram	60

6.2.3	Total next-to-leading order contributions to the renormalized electron properties	62
6.3	Strong coupling perturbation theory	64
6.3.1	Atomic limit	64
6.3.2	Small t expansion	65
6.4	Conclusions	65
7	Phononic properties of polarons	67
7.1	Ward identity	68
7.1.1	The $\mathbf{q} = 0$ mode	70
7.2	Diagrammatic expansion of polarization	70
7.2.1	Leading order and leading self-energy corrections	71
7.2.2	Leading vertex contribution	72
7.2.3	Ladder approximation	76
7.3	Phonon spectral properties	78
7.3.1	Phonon transfer and phonon production	79
7.3.2	Renormalized electron propagator	81
7.3.3	Small polaron	82
7.4	Conclusions	82
 Part III Spectral properties of moderately to heavily doped polar systems		 84
8	Electron spectral properties	85
8.1	Leading order weak coupling perturbation theory	85
8.1.1	First phonon sideband	86
8.1.2	Comment on the leading order diagram in the time domain	87
8.2	Next-to-leading order weak coupling perturbation theory	89
8.2.1	Exchange processes	91
8.3	Determination of electron-phonon interaction range from ARPES spectra	94
8.3.1	Modeling prerequisites	95
8.3.2	Short-range interaction	97

8.3.3	Long-range interaction	98
8.3.4	Anomalous phonon sideband structures	100
8.3.5	Confinement estimators	101
8.3.6	Application to real experimental ARPES data	103
8.4	Conclusions	105
9	Phonon-plasmon coupling	106
9.1	Introduction	106
9.2	Random phase approximation	108
9.2.1	EELS spectrum	109
9.2.2	Phonon spectral function	112
9.2.3	Adiabaticity parameter and limiting behaviors	115
9.3	3D case	118
9.3.1	Weak coupling	118
9.3.2	Strong coupling	122
9.4	2D case	125
9.4.1	Weak coupling	125
9.4.2	Strong coupling	126
9.5	Static screening and static polarization approximation	129
9.6	Conclusions	132
10	Vertex corrections and the $2k_F$ singularity	134
10.1	Anatomy of the leading order vertex function	134
10.2	$2k_F$ singularity	135
10.2.1	Leading order polarization	135
10.2.2	Leading vertex contribution to polarization	136
10.2.3	Ladder approximation	138
10.3	Conclusions	141

Part IV Competition between interactions and disorder: many-body

localization	143
11 From Anderson to many-body localization	144
11.1 Anderson localization	144
11.2 Many-body localization	146
11.2.1 Properties of many-body localized systems	147
11.2.2 Local integrals of motion	149
11.2.3 Thermal-MBL transition	150
11.2.4 Experimental observations of the MBL phenomenon	151
12 MBL as a percolation phenomenon	152
12.1 MBL model in the Anderson many-body basis	152
12.2 Many-body clustering	154
12.3 Percolation in the Fock space	156
12.3.1 Statistics of cluster sizes	156
12.4 Conclusions	157
13 Anomalous transport properties	159
13.1 Density relaxations	160
13.1.1 Rate equations	160
13.1.2 Full diagonalization of rate equations	162
13.1.3 Direct time integration of rate equations	165
13.1.4 Characteristics of anomalous transport	167
13.2 Conclusions	169
Summary	170
A Derivations related to fermion self-energy	A-1
A.1 Leading order fermion self-energy	A-1
A.1.1 Finite electron densities	A-1
A.2 Next-to-leading order fermion self-energy	A-6
A.2.1 Non-crossing diagram	A-6
A.2.2 Crossing diagram	A-8

A.2.3	Bubble diagram	A-12
A.2.4	Polaron limit	A-15
B	Derivations related to phonon polarization	B-1
B.1	The homogeneous $ \mathbf{q} = 0$ mode	B-1
B.2	Next-to-leading order phonon polarization	B-2
B.2.1	Self-energy contributions	B-2
B.2.2	Vertex contribution	B-4
B.2.3	Ward identity	B-6
B.2.4	Polaron limit	B-7
B.3	$2k_F$ singularity	B-12
C	Comment on the expansion of the Green's function	C-1
D	Phonon production for squeezed states	D-1
	References	172
	Curriculum Vitae with the List of Publications	193

General introduction

1.1 Condensed matter physics: a brief retrospective

It is human nature to try to understand the world that surrounds us. From elementary particles to the condensed matter we meet on a daily basis, to astronomical objects, nature is pervaded with enchanting physical phenomena puzzling the human mind for over a few thousand years. But the human mind is inexorable and just as miraculous, and the unified picture of building blocks of nature describing elementary particles and fundamental interactions emerged by the name of Standard model [1]. One is tempted to say that with the discovery of those fundamental physical laws and principles, more often than not expressed by means of pleasant mathematical equations, the job of physicists is done, but this cannot be further from the truth. As it happens, nature is more complex, and this complexity is hidden under the notion of “many”. Indeed, large and correlated aggregates of elementary particles, to cite the words from P. W. Anderson’s renowned *More is different* [2], constituting condensed matter is what underlies a plethora of fascinating phenomena observed in our everyday lives.

One may argue that the theory of matter is as old as ancient civilizations. Both ancient Greeks, Indians, and Tibetans claimed that all complexity of matter may be explained in terms of a few classical elements: water, fire, earth, air, and aether [3]. The idea of an atom was born in ancient Greece as well, albeit centuries past since the theory of classical elements was abandoned and the atomic theory, preceded by the ideas of Josip Ruđer Bošković, was widely accepted as the true theory of matter. The theory defines the atom as the basic particle that composes chemical elements, which are in turn rigorously classified in the periodic table [4]. All matter is correspondingly made up of a huge and (not necessarily) a different number of those elements. Similarly as different groups of chemical elements in the periodic table have different physical properties, it was recognized that the physical properties of matter composed of distinct chemical elements may vary significantly as well. However, it was not until the advent of statistical physics, quantum mechanics, and quantum field theory that the theory and the understanding of matter flourished.

The main actors of the modern condensed matter theory are atomic cores, formed by an atom’s nucleus and core electrons tightly bound to it, and valence electrons set in the framework of non-relativistic quantum field theories. The irony is that although all degrees of freedom and their interactions are formally known, that is to say, the microscopic equations of motion describing dynamics of matter can be formally written, to find their exact solutions is impossible

in practice. The main reason for that lies in particle interactions, which drastically complicate equations of motion when many (of the order 10^{23}) correlated particles constituting the matter are taken under consideration.

An elegant way to overcome peculiarities of particle interactions is to treat them within various mean-field schemes, where the effect of interactions is confined within effective single-particle potentials, usually determined self-consistently. Those schemes proved to be very fruitful in understanding materials' properties, especially in the early stages of condensed matter theory. In that regard, one of the earliest successes of condensed matter theory was the development of the band theory [4], when it was realized that electrons moving in a periodic potential of fixed atomic cores, that is in a crystal lattice, occupy continuous energy ranges called bands, well separated by energetically forbidden zones called gaps. This naturally explained why are some materials with partially filled bands metals, while other semiconductors or insulators, depending on the size of a band gap between the highest occupied (valence) band and the lowest unoccupied (conduction) band.

Essences of the theory of metals were furthermore understood in the framework of Landau's phenomenological Fermi-liquid theory [5] and later elaborated within the random phase approximation (RPA) scheme on a microscopic level [6–8], explaining why a dense system of fermions with generic two-particle interactions behaves similarly as a free fermion system. At about the same time as the RPA was applied to describe a normal state of the metal, the BCS theory of superconductivity [9] emerged, unraveling the mystery of a dissipation-free electrical current conduction reported experimentally for the first time almost 50 years earlier by Heike Kamerlingh Onnes [10]. A crucial ingredient of the BCS theory is the lattice-mediated attractive electron-electron interaction, which is shown to destabilize the Fermi sea in the favor of a Cooper-pair condensate, resulting in a metal-superconductor transition. The phenomenon of superconductivity, therefore, highlighted a decisive role of atomic cores' dynamics in understanding the fundamental properties of materials.

The physical properties of many materials were shown to be well described by means of the above-mentioned and several other similar theories. Since their behavior is well understood from today's point of view, we call those materials conventional. However, there exist several classes of non-conventional materials like cuprates [11], various oxides [12, 13], and organics [14], which, among other, strange spectral and transport properties puzzle physicists to date. Although it is not completely clear whether those peculiar properties stem from electron-electron, electron-lattice, or some combination of both interactions, it is widely accepted that strong correlations play a dominant role in shaping their rich phase diagrams. Interestingly, those phase diagrams are oftentimes heavily dependent on chemical doping which opens the question about the role of disorder just as well, further supported by the fact that every synthesized sample is inherently prone to structural inhomogeneities.

Roughly speaking, at the present time, there are two alternative approaches commonly

invoked to theoretically study the properties of both conventional and non-conventional matter, both with their shortcomings and advantages. The first relies on the computational modeling of matter going under the name of density functional theory (DFT), also called *ab initio* modeling. It is based on two Hohenberg-Kohn theorems [15], which state that the ground state properties of a many electron system are uniquely determined by an electron density that depends on only three spatial coordinates. This electron density in turn defines an energy functional for the system and the theorems prove that the ground state electron density minimizes this energy functional. The main game of DFT is therefore to guess and minimize the energy functional that best suits the lattice structure and chemical elements composing material of interest to obtain its ground state electron density and ground state properties. One of the main advantages of such an approach is that it can for a relatively cheap computational price predict realistic electron and lattice spectra, providing a direct quantitative comparison of theory with real-life experiments. On the other hand, it is not the most powerful tool when the qualitative understanding of phenomena is of interest. Furthermore, it struggles to model materials with strong correlations. Despite that, DFT is among the most popular methods used by the condensed matter community.

Where the DFT lags, the second approach excels. It does not bear any particular name and does not rely on a single theory, but rather encompasses a bunch of various analytical and numerical schemes to tackle minimal model (toy) Hamiltonians. The *modus operandi* is to, based on a theoretical intuition or experimental results, single out the most relevant degrees of freedom that capture the essential physical behavior one seeks to understand and write down a toy Hamiltonian describing them and their interactions. The procedure is further continued either by the numerical study of the toy Hamiltonian, for example by the exact numerical diagonalization, by invoking analytical approaches like the diagrammatic perturbation theory, or by some combination of both. The advantage of the exact numerical diagonalization is that it provides a full solution for the problem, albeit it is oftentimes restricted to small system sizes, which makes it difficult to interpret the results in the thermodynamic limit. On the other hand, the diagrammatic perturbation theory is convenient since it provides a picturesque way of representing physical processes in terms of Feynman diagrams, rendering the diagrammatic perturbation theory a suitable choice when the qualitative description of phenomena is of interest. The downside is, however, that the number of contributions in a given perturbation order grows exponentially as the perturbation order increases, making it difficult to tame when no small perturbation parameter exists. Anyhow, in this thesis we follow this second approach to study the effects of interactions and disorder in various condensed matter systems. In particular, we mainly use the diagrammatic perturbation theory and the Feynman representation of physical processes to study systems with primarily significant electron-lattice interactions. When the interplay of strong electronic correlations and disorder without any particular small parameter is of interest, numerical methods are rather invoked.

1.2 Feynman diagrams: frequency vs time domain

When it comes to the perturbation expansion in a many-body quantum field theory, one of the most useful tools to study system's properties is a Green's function, or a two-point correlator, defined in the case of fermions by

$$G(i, t; i', t') = -i \langle \Omega | \hat{T} [c_i^\dagger(t) c_{i'}(t')] | \Omega \rangle . \quad (1.1)$$

The expectation value is taken in the ground state $|\Omega\rangle$ of the full Hamiltonian \hat{H} , implicitly entailing zero temperature calculations suitable for a discussion of ground state properties and low energy excitations. The operator $c_i^\dagger(t)$ ($c_i(t)$) denotes the creation (annihilation) of a fermion with the quantum number i at the time t , and the operator \hat{T} is a time order product with the property

$$\hat{T} [A(t)B(t')] = \begin{cases} A(t)B(t') , & t > t' , \\ B(t')A(t) , & t < t' . \end{cases} \quad (1.2)$$

The time evolution of the annihilation (and similarly the creation) operator is given by

$$c_i(t) = e^{i\hat{H}t} c_i e^{-i\hat{H}t} , \quad (1.3)$$

providing an interpretation of the Green's function as amplitude for the process in which a particle with the quantum number i at the time t is added (removed) to (from) the system, after which the system with an additional (missing) particle evolves under its Hamiltonian dynamics, and ending with a particle labeled by the quantum number i' being removed (added) at the time t' . As the depicted process principally describes the propagation of a single particle, Green's function is also called the propagator.

Generally, as in any perturbation theory, we divide the full Hamiltonian into two parts

$$\hat{H} = \hat{H}_0 + \hat{V} , \quad (1.4)$$

where \hat{H}_0 part of the Hamiltonian can be solved and \hat{V} represents all other contributions to the full Hamiltonian whose effects are treated perturbatively. Since \hat{H}_0 is fully solvable, its ground state $|\Omega\rangle_0$ and all excited states are formally known. Within the scope of this thesis, \hat{H}_0 is usually contributed by the Fermi sea of electrons populating a single band, $|\Omega\rangle_0 \equiv |FS\rangle$, with each electron sitting in a Bloch state with the energy $\varepsilon_{\mathbf{k}}$ labeled by the (crystal) momentum \mathbf{k} . By neglecting for the moment the perturbation \hat{V} , the Green's function then takes a simple form

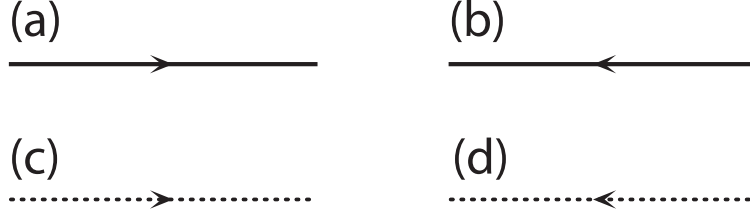


Figure 1.1: Pictorial representation of the fermion propagator. Propagators in (a) and (b) are conceptually equal, corresponding both to the Green's function in the frequency domain, Eq. (1.7). The direction of arrows only denotes the flow of momentum. On the other hand, the arrows in (c) and (d) explicitly represent the direction of time. Correspondingly, the dotted propagator (c) corresponds to the propagation of an electron, while the dotted propagator (d) to the propagation of a hole, that is, to the first and the second term in Eqs. (1.5) and (1.7), respectively.

$$\begin{aligned}
G_0(\mathbf{k}, t; \mathbf{k}, t') &= -i \langle FS | \hat{T} \left[c_{\mathbf{k}}^\dagger(t) c_{\mathbf{k}}(t') \right] | FS \rangle \\
&= -i \left[\Theta(t - t') n_{FD}(\xi_{\mathbf{k}}) - \Theta(t' - t) n_{FD}(-\xi_{\mathbf{k}}) \right] e^{-i\xi_{\mathbf{k}}(t-t')} \delta_{\mathbf{k}, \mathbf{k}'},
\end{aligned} \tag{1.5}$$

where the energy $\xi_{\mathbf{k}} = \varepsilon_{\mathbf{k}} - \mu$ is the electron energy measured from the Fermi level μ . In the Fermi sea, all states below (above) the Fermi level are occupied (empty). This is well captured by the Fermi-Dirac distribution

$$n_{FD}(\xi_{\mathbf{k}}) \equiv n_{\mathbf{k}} = \frac{1}{e^{\frac{\xi_{\mathbf{k}}}{k_B T}} + 1}, \tag{1.6}$$

which takes the form of the step function $\Theta(\xi_{\mathbf{k}})$ as $T \rightarrow 0$.

For translationally invariant Hamiltonians \hat{H}_0 in time, such as the ones usually considered in this thesis, the time-dependent Green's function in Eq. (1.5) depends only on the time difference $t - t'$. It is then suitable to perform the Fourier transform of Eq. (1.5), resulting in a frequency-dependent Green's function

$$G_0(\mathbf{k}, E) = \frac{1 - n_{\mathbf{k}}}{E - \xi_{\mathbf{k}} + i\eta} + \frac{n_{\mathbf{k}}}{E - \xi_{\mathbf{k}} - i\eta}, \tag{1.7}$$

where $\eta \rightarrow 0^+$. While the first term in Eqs. (1.5) and (1.7) can be attributed to the propagation of an electron with the energy $\xi_{\mathbf{k}} = \varepsilon_{\mathbf{k}} - \mu > 0$ added above the Fermi sea, the second term is slightly more delicate to interpret. Evidently, it corresponds to the propagation of a system with an electron missing from the Fermi sea. However, the same process can be rather viewed as the propagation of a hole added to the Fermi sea with the negative energy $\xi_{\mathbf{k}} = \varepsilon_{\mathbf{k}} - \mu < 0$, propagating backward in time, according to the second term in Eq. (1.5). In any case, valuable information encoded in the frequency-dependent Green's function is immediately apparent - its poles correspond to the excitation energies of the system.

With the perturbation \hat{V} included, the full Green's function cannot be generally put in such a simple form. Nevertheless, Wick's theorem [16] ensures that it can be represented by means of Green's functions corresponding solely to the unperturbed Hamiltonian \hat{H}_0 . This was further elaborated by Richard Feynman, who noted that each contribution in the perturbation series for the full Green's function can be represented by a drawing, called after him a Feynman diagram. Thus, by representing the Green's function in Eq. (1.7) by a suitable symbol, a Feynman diagram can be sketched for each order of the perturbation theory contributing to the full Green's function. The advantage of this approach is twofold. First of all, since each symbol attributed to the Green's function in Eq. (1.7) represents the propagation of an electron or a hole, Feynman diagrams provide a pictorial way of representing physical processes appearing in each order of perturbation theory. Secondly, there exists a one-to-one mapping between Feynman diagrams and corresponding mathematical expressions appearing in the perturbation theory, meaning that the whole complicated mathematical apparatus behind the perturbation theory can be put aside and one can immediately start by considering physical processes of interest.

The most common way is to work with frequency-dependent Green's functions and to draw Feynman diagrams in the frequency domain. The standardized way of representing the frequency-dependent fermion propagator in Eq. (1.7) is to use a solid line, Figs. 1.1(a) and 1.1(b). Here, the direction of the arrow does not have any deeper physical meaning other than to denote the direction of the momentum flow. Correspondingly, the lines in Figs. 1.1(a) and 1.1(b) are conceptually indistinguishable.

An alternative, seldom used approach is to work with Feynman diagrams in the time domain. The purpose of it is to strictly distinguish the propagation of an electron and the propagation of a hole, represented by the dotted lines in Figs. 1.1(c) and 1.1(d), respectively, highlighting the difference between the frequency and the time representation of Feynman diagrams. In contrast to the frequency representation, arrows now explicitly show the direction of time, pointing forward for the electron propagating forward, and backward for the hole propagating backward in time. Since this approach explicitly reveals the role of electrons and holes in physical processes, Feynman diagrams in the time domain may prove to be helpful when a deeper understanding of microscopic mechanisms behind physical phenomena will be of interest.

In this thesis, the majority of the focus is put on electron-lattice interactions, so this brief introduction would not be complete without commenting on the lattice degrees of freedom. Similarly as for fermions, the lattice Green's function is defined as a two-point correlator of the atomic core displacement (from the equilibrium position) operator $x_{\mathbf{q}}$

$$D(\mathbf{q}; t, t') = -i \frac{2M\omega}{\hbar} \langle \Omega | \hat{T} [x_{\mathbf{q}}(t)x_{-\mathbf{q}}(t')] | \Omega \rangle , \quad (1.8)$$

where ω is the frequency of lattice oscillations and M is the characteristic atomic core mass. However, it is much more common to reexpress the lattice Green's function in terms of the

quanta of lattice vibrations called phonons. In particular, with $a_{\mathbf{q}}^{\dagger}(t)$ ($a_{\mathbf{q}}(t)$) being the creation (annihilation) operator of a phonon with the (quasi) momentum \mathbf{q} , the Green's function in Eq. (1.8) takes the form

$$D(\mathbf{q}; t, t') = -i \langle \Omega | \hat{T} [A_{\mathbf{q}}(t) A_{-\mathbf{q}}(t')] | \Omega \rangle , \quad (1.9)$$

where $A_{\mathbf{q}} = a_{\mathbf{q}} + a_{-\mathbf{q}}^{\dagger}$. Accordingly, hereafter the term lattice vibrations will be replaced by the notion of phonons, and the Green's function in Eq. (1.9) named the phonon Green's function or the phonon propagator, since the phonon can be thought of as a particle carrying momentum and energy propagating through the system.

As we have argued, all physical processes can be sketched with the use of Feynman diagrams and processes involving the electron-phonon interaction are no exception. Thus, to represent the phonon propagator in Feynman diagrams we will use wavy lines. Because of the symmetry

$$D(\mathbf{q}; t - t') = D(-\mathbf{q}; t' - t) , \quad (1.10)$$

phonons can be viewed as going in either direction in time, making no differences between the phonon propagators in the frequency and the time domain. Consequently, the arrows on phonon propagators may be omitted. Nevertheless, it should be emphasized that the momentum is preserved by interactions, denoted by vertices in Feynman diagrams. Vertices representing the bare electron-phonon coupling are denoted with full circles.

Lastly, in systems with finite electron densities, the electron-electron interaction cannot be overlooked. When drawing Feynman diagrams, it will be represented by a dashed line. Since the interaction is instantaneous, it does not make sense to associate the direction of time with the line.

1.3 Outline and contributions of the thesis

The content of this thesis can be divided into four main parts, with each part covering several chapters. Effects of electron-phonon interaction are appearing as the key subject of the first three parts, discussing impurity problems, polaronic correlations, and the interplay between direct electron repulsion in the presence of correlations mediated by a crystal lattice. The focus of the last part is on the role of the strong disorder in strongly correlated systems in the context of the fundamental problem of many-body localization. It is the purpose of this section to provide a summary and the main contributions of each chapter.

Part I: Polaronic impurity problem

In Part I, we deal with the polaronic impurity problem, which involves coupling between an electron and a local phonon degree of freedom at an impurity site, together with the change in the atomic orbital energy. We seek the solution to the problem within Green's function formalism in Chapter 2. We introduce an operator $\hat{\Gamma}$ in terms of which the full Green's function relevant for the problem can be expressed, which apart from elastic processes, includes all inelastic processes involving emission and absorption of real phonons as well. Because the electron-phonon coupling is being restricted to the single impurity site, we are able to calculate all matrix elements of $\hat{\Gamma}$ in terms of the continued fractions involving only unperturbed local electron Green's functions. For a given lattice dimension and geometry, the corresponding unperturbed local electron Green's function can be calculated either analytically or numerically, since it involves the simple problem of finding solutions to a non-interacting tight-binding problem. This provides us in the next step with the exact solution to the polaronic impurity problem.

The exact solution to the polaronic impurity problem is used in Chapter 3 to study electron transmission through the polaronic impurity in systems with the reduced dimensionality relevant for inelastic electron tunneling spectroscopy measurements. We find the closed expression for the transmission coefficient and show that it exhibits multiple maxima and minima as a function of the incident electron energy governed by the phonon energy scale for strong couplings.

Local and transport properties of bulk three-dimensional (3D) systems in the presence of dilute concentrations of polaronic impurities are analyzed in Chapter 4. By studying the local density of states, we show that strong electron-phonon couplings may lead to many localized electron states, whose exact structure is very sensitive to impurity parameters. We observe signatures of the strong coupling also in the delocalized part of electron spectra, manifested through the resonant structure of the local density of states and pointing to the resonant electron scattering on polaronic impurities. By calculating all elastic and inelastic scattering cross sections for the electron scattering on a polaronic impurity, to the best of our knowledge not considered in previous works, we obtain the electron relaxation time and the electron mobility as a function of temperature. We observe power-law decay of the mobility with temperature, with the exponent very sensitive to impurity parameters. The latter can explain unconventional power-law exponents observed experimentally in organic semiconductors.

Part II: Perturbative approach to the polaron problem

In Parts II and III, the translationally invariant electron-phonon problem is restored by introducing the electron-phonon coupling on each lattice site. Chapter 5 is devoted to the introduction to the polaron limit of the problem, studied in Part II with the methods of the diagrammatic perturbation theory, with the special emphasis put on vertex corrections. In particular, in Chapter 6 we study the electronic properties of polarons by considering the electron self-energy and the characteristic

behaviors of the polaron band in the leading and the next-to-leading order of the perturbation theory in electron-phonon coupling. We show that the leading order momentum-dependent electron self-energy becomes suppressed with the square of the adiabaticity parameter in the antiadiabatic limit.

Several analytical results regarding phononic properties of polarons are obtained in Chapter 7. We provide the exact solution for the $\mathbf{q} = 0$ part of the phonon propagator and argue that the phonon polarization may be treated within the two-vertices renormalization scheme, with the vertex function involving electron processes only. This fact is exploited to obtain analytically the vertex renormalization in the ladder approximation. We also argue that the renormalization of the phonon frequency is negligible, with the important fact that some of its spectral weight is being transferred to the polaron band. Apart from the effects associated with the transfer of the phonon spectral weight, we also observe an additional phonon spectral weight in the polaron band. We call this additional phonon spectral weight a phonon production, which may be attributed to the cloud of virtual phonons accompanying the electron in the polaron ground state.

Part III: Spectral properties of moderately to heavily doped polar systems

We continue with the analysis of electron and phonon properties in translationally invariant electron-phonon problems in Part III, but now for strongly doped polar systems. The results presented in Chapter 8 are directly related to the experimental angle-resolved photoemission spectroscopy (ARPES) spectra of polar materials. These ARPES spectra contain characteristic phonon sidebands, which we simulate by calculating the leading and the next-to-leading order hole self-energy in electron-phonon coupling. By focusing on the imaginary part of the leading order hole self-energy entering the simulated ARPES spectra in the energy range of the first phonon sideband, we show that the confinement of its intensity in the momentum space changes drastically by varying the range of the electron-phonon interaction. Based on that confinement, we introduce several confinement estimators, which may provide a robust estimate of the electron-phonon interaction range in real materials.

In Chapter 9, we analyze the phonon-plasmon coupling in 3D and two-dimensional (2D) systems through the prism of complementary electron energy loss spectroscopy (EELS) spectra and phonon spectral functions calculated within the RPA. We cover the whole experimentally relevant parametric space spanned by the electron-phonon interaction strength and the adiabaticity parameter, that is, the electron density. We find that the electron-phonon interaction strength plays a determining role in distributing spectral weights among coupled excitations, which opens the possibility of estimating it directly from measured EELS spectra. The projection of the excitations onto the phonon degree of freedom reveals for strong couplings large phonon production contributions, which are of very different origins depending on the adiabaticity parameter. In

particular, in the adiabatic regime, it is the consequence of phonon softening effects, while in the antiadiabatic regime the phonon production can be related to the cloud of phonons following plasma oscillations. We also comment on phonon properties of phonon-plasmon coupled systems within the static screening and the static polarization approximation, where the former is being frequently used in studying the impact of nonadiabatic effects on phonon spectra in *ab initio* modeling. We find that the static screening approximation generally fails to reproduce full RPA phonon spectra in the whole parametric space in both 3D and 2D cases, while the static polarization approximation works well only in the 3D adiabatic regime. Part III ends with Chapter 10, where we show that vertex corrections in the ladder approximation tend to soften the $2k_F$ singularity of the Lindhard function.

Part IV: Competition between interactions and disorder: many-body localization

In the last Part IV of the thesis, we abandon the lattice degrees of freedom and consider the interplay of electronic correlations and disorder in the context of the many-body localization (MBL) phenomenon. An introduction to this very dynamic field of research is given in Chapter 11. As for the model exhibiting the MBL phenomenon, we consider the disordered chain of spinless interacting fermions which we approach by using the numerical exact diagonalization. The many-body localized phase, observed within the considered model for sufficiently strong disorders, is characterized by the absence of transport and non-ergodic behaviors. On the other hand, when the disorder is weak the same model exhibits ergodic behaviors, leaving us with the conclusion that the thermal-MBL transition takes place for some critical value of disorder strength.

In Chapter 12, we show that the thermal-MBL transition is accompanied by the drastic change in clustering of many-body states in the Fock space. For strong disorders when the many-body localized phase is expected, we show that states in the Fock space tend to group into many clusters containing no more than a few states, while for weak disorders one macroscopically large cluster emerges, indicating the percolative nature of the thermal-MBL transition, albeit in the Fock space.

The existence of the MBL drastically influences transport properties in real space as well. In the last Chapter 13, we study the relaxation of the charge density distribution of some initial states in the thermal phase toward the equilibrium via the simplified rate equations, omitting the quantum interferences effects between many-body states. In addition, we consider only resonant transitions between many-body states, neglecting thus perturbatively small contributions. For weak disorders, we notice the diffusive behavior, while for stronger disorders anomalous transport properties are observed, including very slow relaxation processes toward the equilibrium. The results obtained via the rate equations agree well with the full quantum calculations and suggest the exponential decrease of the effective diffusion parameter as the disorder strength increases.

Part I

Polaronic impurity model

Exact solution

Parts of Chapter 2 have been published in [17].

The number of exactly solvable (interacting) quantum models can be counted on the fingers of one hand. One of them is the polaronic impurity model. To our surprise, to the best of our knowledge, the scattering part of the polaronic impurity problem was not discussed in a closed form, albeit the exact results for tunneling through a polaronic impurity on one-dimensional (1D) lattices were obtained numerically [18–20]. In Part I of the thesis, we provide the exact analytical solution of the problem, and discuss its relevance in the context of local and transport properties of 1D and 3D systems, with the majority of focus being put on the 3D case.

2.1 Model Hamiltonian

In its essence, the polaronic impurity model describes an electron that locally interacts with an impurity characterized by the phonon degree of freedom. There are several variations of the model, albeit the concrete model Hamiltonian considered in this thesis reads

$$\hat{H} = \sum_{\mathbf{k}} \varepsilon_{\mathbf{k}} c_{\mathbf{k}}^{\dagger} c_{\mathbf{k}} + \omega_0 a_1^{\dagger} a_1 + \left[\varepsilon_0 + g(a_1^{\dagger} + a_1) \right] c_1^{\dagger} c_1, \quad (2.1)$$

The scheme of the model for a 3D simple cubic lattice is shown in Fig. 2.1. Here, the operators $c_{\mathbf{k}}^{\dagger}(c_{\mathbf{k}})$ and $a_1^{\dagger}(a_1)$ create (annihilate) the electron with the wave vector \mathbf{k} in a band with the dispersion $\varepsilon_{\mathbf{k}}$ and the phonon with the frequency ω_0 (we set $\hbar = 1$ throughout the thesis and recover its full value when needed) at the site 1 of a lattice, respectively. In particular, the site 1 denotes the impurity site that hosts the electron-phonon interaction g and breaks the translational symmetry of the lattice. Let us just briefly mention that other variations of the model may for example include multiple phonon modes [18], or extend the electron-phonon interaction over several lattice sites [19].

For our upcoming analysis, it is convenient to divide the full Hamiltonian \hat{H} in Eq. (2.1) into two parts, \hat{H}_0 and \hat{V} . We take that \hat{H}_0 includes the non-interacting electron, $\hat{H}_{el} = \sum_{\mathbf{k}} \varepsilon_{\mathbf{k}} c_{\mathbf{k}}^{\dagger} c_{\mathbf{k}}$, and phonon, $\hat{H}_{ph} = \omega_0 a_1^{\dagger} a_1$, part of the Hamiltonian. The rest of the Hamiltonian involving the electron-phonon interaction g and the impurity orbital energy ε_0 is put into \hat{V} . The orbital energy at all other lattice sites is taken as zero energy.

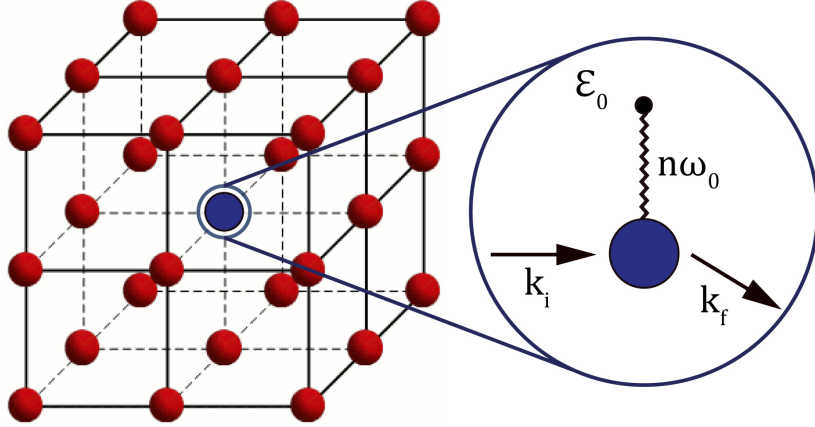


Figure 2.1: Scheme of the polaronic impurity model in Eq. (2.1) for a 3D simple cubic lattice. The impurity site I is denoted with the blue color, hosting the electron-phonon coupling g .

2.2 Experimental motivation

The initial interest in studying the polaronic impurity problem stemmed from the inelastic electron tunneling spectroscopy measurements [21]. The experimental setup we should have in mind is a metal-insulator (molecule/oxide/quantum dot)-metal junction for which an I-V characteristic is measured. For low bias voltages, the linear dependence of the I-V characteristic is expected in accordance with Ohm's law. However, for higher voltages nonlinearities and nonmonotonocities of the I-V characteristic are generally anticipated. Indeed, it was found that d^2I/dV^2 characteristics of molecular junctions show clear signatures related to vibrational excitations of molecular impurities in the insulator [22–28]. In particular, the characteristics showed resonant peaks and minima appearing at characteristic vibrational frequency scales of the system. This electron tunneling through a molecular junction can be in the most simple approximation modeled via an electron moving on a 1D lattice and running into a barrier containing a phonon degree of freedom. Indeed, this scenario is well captured by the polaronic impurity Hamiltonian in Eq. (2.1) in the 1D case.

Whether there exists such relevance of the polaronic impurity model for the description of transport properties of bulk materials is yet unknown. Perhaps, this is so because peculiarities of the polaronic impurity model are rarely if at all, examined for 3D (and 2D) lattices. However, it was just recently realized that polaronic impurities may serve as strong phonon scatterers, drastically reducing the thermal conductivity in anatase TiO_2 single crystals [29]. Moreover, we find that electron scattering on polaronic impurities may provide some insights into the anomalous transport properties observed in some organic semiconductors [30–32]. In particular, unconventional power-law behaviors of mobility with temperature were reported for those materials and there is still an ongoing debate about what physical mechanism lies behind such behaviors. It is not uncommon that the electron-phonon interaction plays a very important role in organics. A great number of theoretical works try to explain those unconventional power law behaviors by

means of various electron-phonon theories [33–39], but we are not aware of any work invoking the polaronic impurity model. However, we cannot stress enough that here we provide a full solution to the polaronic impurity model and examine general behaviors of the electron mobility within the model, prior to any application of the obtained results to some specific experimental finding. Whether polaronic impurities play a significant role in shaping the transport properties of transition-metal oxides and organic semiconductors is indeed an interesting question, which serves as a motivation for the possible continuation of the results obtained in this thesis.

2.3 Green’s function approach

In order to examine electron transport properties, we adopt the usual relaxation time approximation [40] and consider the electron scattering on polaronic impurities. We use Green’s function formalism and generalize the standard textbook approach to the scattering problem [41] by introducing the unperturbed Green’s function of the electron-phonon system

$$\hat{G}^{(0)}(\omega) = 1/(\omega - \hat{H}_0 + i\eta), \quad (2.2)$$

with $\hat{H}_0 = \hat{H}_{el} + \hat{H}_{ph}$, and the full Green’s function

$$\hat{G}(\omega) = 1/(\omega - \hat{H} + i\eta), \quad (2.3)$$

with $\hat{H} = \hat{H}_0 + \hat{V}$. Note the factor $i\eta$, pointing to the fact that only an electron (and not a hole) may propagate in the system. This is so because we are interested in the case when only one electron is injected into an otherwise empty band. Correspondingly, the time-ordered fermion Green’s function is used and the renormalization of phonons is absent since it necessarily involves the creation of an electron-hole pair.

It should also be stressed that two of Green’s functions in Eqs. (2.2) and (2.3) are neither pure fermion nor pure boson propagators, but rather simultaneously describe the propagation of both the electron and the phonon. This is evident from our definition of \hat{H}_0 containing both the unperturbed electron and the phonon, and is particularly clear in the real space representation of $\hat{G}^{(0)}(\omega)$ and $\hat{G}(\omega)$ [42]

$$G_{\mathbf{n},\mathbf{m}}^{(0)\gamma,\alpha}(\omega) = \langle 0 | \frac{(a_1)^\gamma}{\sqrt{\gamma!}} c_{\mathbf{n}} \frac{1}{\omega - \hat{H}_0} c_{\mathbf{m}}^\dagger \frac{(a_1^\dagger)^\alpha}{\sqrt{\alpha!}} | 0 \rangle, \quad (2.4)$$

and

$$G_{\mathbf{n},\mathbf{m}}^{\gamma,\alpha}(\omega) = \langle 0 | \frac{(a_1)^\gamma}{\sqrt{\gamma!}} c_{\mathbf{n}} \frac{1}{\omega - \hat{H}} c_{\mathbf{m}}^\dagger \frac{(a_1^\dagger)^\alpha}{\sqrt{\alpha!}} | 0 \rangle. \quad (2.5)$$

Here, the Greek letters α and γ denote the number of phonons in the initial and in the final (after the scattering) state, respectively. The Latin letters denote lattice sites at which the electron is created/annihilated. As an example, $G_{\mathbf{n},\mathbf{m}}^{\gamma,\alpha}(\omega)$ describes a process in which an electron is injected at the site \mathbf{m} of the crystal containing α phonons, after which the electron may interact with the phonon, and as a result γ phonons are left at the time when the electron leaves the system at the site \mathbf{n} .

This mixed character of the Green's functions should not particularly trouble us. In fact, it is easy to show that all final results regarding the electron subsystem may be expressed by means of the pure electron propagator. The crucial step to note is that the non-interacting Green's function is diagonal in the phonon number and that it is given by the pure electron propagator whose argument is shifted by the energy of phonons present in the system

$$G_{\mathbf{n},\mathbf{m}}^{(0)\gamma,\alpha}(\omega) = \delta_{\gamma,\alpha} G_{\mathbf{n},\mathbf{m}}^{(0)\alpha,\alpha}(\omega) = \delta_{\gamma,\alpha} G_{\mathbf{n},\mathbf{m}}^{(0)0,0}(\omega - \alpha\omega_0) = \delta_{\gamma,\alpha} G_{\mathbf{n},\mathbf{m}}^{(0)}(\omega - \alpha\omega_0) . \quad (2.6)$$

Here, we recognize $G_{\mathbf{n},\mathbf{m}}^{(0)0,0}(\omega - \alpha\omega_0)$ as the purely electronic propagator. Thus, we may omit zeros in the superscript. Its matrix elements may usually be calculated analytically or numerically, depending on a system dimension and geometry of the lattice [41].

2.3.1 Local operator $\hat{\Gamma}$

Our goal is to completely solve the polaronic impurity problem by finding the exact expression for the full propagator $\hat{G}(\omega)$. Since the unperturbed propagator $\hat{G}^{(0)}(\omega)$ is known, we can exploit the interaction \hat{V} to relate it with $\hat{G}(\omega)$

$$\hat{G}(\omega) = \hat{G}^{(0)}(\omega) + \hat{G}^{(0)}(\omega) \hat{V} \hat{G}(\omega) . \quad (2.7)$$

However, this relation is not so convenient since on the right-hand side of Eq. (2.7) the unknown $\hat{G}(\omega)$ appears. This can be overcome by introducing the T -matrix, $\hat{\mathcal{T}}(\omega) = \hat{V} \hat{G}(\omega) (\omega - \hat{H}_0)$, which transforms Eq. (2.7) into

$$\hat{G}(\omega) = \hat{G}^{(0)}(\omega) + \hat{G}^{(0)}(\omega) \hat{\mathcal{T}}(\omega) \hat{G}^{(0)}(\omega) . \quad (2.8)$$

Evidently, it is sufficient to calculate all matrix elements of the T -matrix to completely determine Green's function $\hat{G}(\omega)$. Let us add that the T -matrix may also be used to construct eigenstates $|\psi\rangle$ of \hat{H}

$$|\psi\rangle = |\phi\rangle + \hat{G}^{(0)}(\omega) \hat{\mathcal{T}}(\omega) |\phi\rangle , \quad (2.9)$$

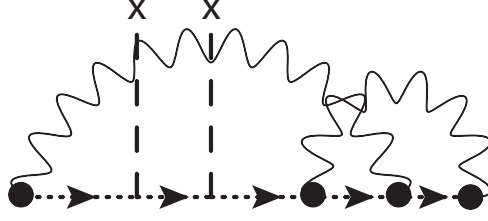


Figure 2.2: Typical diagram contributing to $\Gamma^{0,0}$ involving the static ε_0 scattering (vertical dashed lines) and the dynamic scattering on phonons (wavy lines).

where $|\phi\rangle$ is an eigenstate of \hat{H}_0 , which will prove especially handy later.

In the polaronic impurity model given by Eq. (2.1), the interaction \hat{V} is restricted to a single site \mathbf{l} , being local in real space

$$V_{\mathbf{n},\mathbf{m}}^{\gamma,\alpha} = \delta_{\mathbf{n},\mathbf{l}}\delta_{\mathbf{m},\mathbf{l}} \left[\delta_{\gamma,\alpha}\varepsilon_0 + g(\sqrt{\gamma}\delta_{\gamma,\alpha+1} + \sqrt{\alpha}\delta_{\gamma,\alpha-1}) \right]. \quad (2.10)$$

Correspondingly, so is the T -matrix, $\mathcal{T}_{\mathbf{n},\mathbf{m}}^{\gamma,\alpha}(\omega) = \delta_{\mathbf{n},\mathbf{l}}\delta_{\mathbf{m},\mathbf{l}}\mathcal{T}_{\mathbf{l},\mathbf{l}}^{\gamma,\alpha}(\omega) \equiv \mathcal{T}^{\gamma,\alpha}(\omega)$, and consequently the matrix representation of Eqs. (2.7) and (2.8) reads

$$G_{\mathbf{n},\mathbf{m}}^{\gamma,\alpha}(\omega) = \delta_{\gamma,\alpha}G_{\mathbf{n},\mathbf{m}}^{(0)\alpha,\alpha}(\omega) + G_{\mathbf{n},\mathbf{l}}^{(0)\gamma,\gamma}(\omega) \sum_{\zeta} V_{\mathbf{l},\mathbf{l}}^{\gamma,\zeta} G_{\mathbf{l},\mathbf{m}}^{\zeta,\alpha}(\omega), \quad (2.11)$$

and

$$G_{\mathbf{n},\mathbf{m}}^{\gamma,\alpha}(\omega) = \delta_{\gamma,\alpha}G_{\mathbf{n},\mathbf{m}}^{(0)\alpha,\alpha}(\omega) + G_{\mathbf{n},\mathbf{l}}^{(0)\gamma,\gamma}(\omega)\mathcal{T}^{\gamma,\alpha}(\omega)G_{\mathbf{l},\mathbf{m}}^{(0)\alpha,\alpha}(\omega). \quad (2.12)$$

We find particularly convenient to introduce and the third matrix equation

$$G_{\mathbf{n},\mathbf{m}}^{\gamma,\alpha}(\omega) \equiv \delta_{\gamma,\alpha}G_{\mathbf{n},\mathbf{m}}^{(0)\alpha,\alpha}(\omega) + G_{\mathbf{n},\mathbf{l}}^{(0)\gamma,\gamma}(\omega)\hat{\Gamma}^{\gamma,\alpha}(\omega)G_{\mathbf{l},\mathbf{m}}^{\alpha,\alpha}(\omega), \quad (2.13)$$

where we have introduced a local operator $\hat{\Gamma}(\omega)$, whose matrix elements are defined via Eq. (2.13), $\Gamma_{\mathbf{n},\mathbf{m}}^{\gamma,\alpha}(\omega) = \delta_{\mathbf{n},\mathbf{l}}\delta_{\mathbf{m},\mathbf{l}}\Gamma_{\mathbf{l},\mathbf{l}}^{\gamma,\alpha}(\omega) \equiv \Gamma^{\gamma,\alpha}(\omega)$.

In particular, $\Gamma^{0,0}$ corresponds to the electron self-energy with a typical diagram shown in Fig. 2.2. The electron propagator $G_{\mathbf{l},\mathbf{l}}^{(0)}$ is represented by the horizontal dotted lines, the vertical dashed lines correspond to the static $\varepsilon_0 \neq 0$ scattering, whereas the wavy lines correspond to the phonon propagators. Generally, the diagrammatic representation of the T -matrix involves both the reducible and the irreducible diagrams, while the operator $\hat{\Gamma}$ involves only irreducible ones.

To justify the introduction of the local operator $\hat{\Gamma}$, we consider Eq. (2.13) in the elastic case $\gamma = \alpha$ and for $\mathbf{n} = \mathbf{l}$

$$G_{\mathbf{l},\mathbf{m}}^{\alpha,\alpha}(\omega) = \frac{G_{\mathbf{l},\mathbf{m}}^{(0)\alpha,\alpha}(\omega)}{1 - G_{\mathbf{l},\mathbf{l}}^{(0)\alpha,\alpha}(\omega)\Gamma^{\alpha,\alpha}(\omega)}. \quad (2.14)$$

By putting this result back into Eq. (2.13) and by comparing it with Eq. (2.12), the relation between matrix elements of the local operator $\hat{\Gamma}(\omega)$ and matrix elements of the T -matrix can simply be read out

$$\mathcal{T}^{\gamma,\alpha}(\omega) = \frac{\Gamma^{\gamma,\alpha}(\omega)}{1 - G_{11}^{(0)\alpha,\alpha}(\omega)\Gamma^{\alpha,\alpha}(\omega)}. \quad (2.15)$$

Therefore, in order to find the full solution to the problem, it is enough to find all matrix elements of the local operator $\hat{\Gamma}(\omega)$. As we shall show, this can be achieved in the whole parametric space of the Hamiltonian in Eq. (2.1).

2.3.2 Static case

To demonstrate the elegance of the present formalism, we first consider the simpler static $g = 0$ case, when only the electron orbital energy at the impurity site is changed. In that case, the interaction matrix elements simplify to $V_{\mathbf{n},\mathbf{m}}^{\gamma,\alpha} = \delta_{\mathbf{n},\mathbf{l}}\delta_{\mathbf{m},\mathbf{l}}\delta_{\gamma,\alpha}\varepsilon_0 \neq 0$. We note that $\gamma = \alpha$ since there are no processes in which the initial number of phonons is changed. Consequently, both Eqs. (2.11) and (2.13) read

$$G_{\mathbf{n},\mathbf{m}}^{\alpha,\alpha}(\omega) = G_{\mathbf{n},\mathbf{m}}^{(0)\alpha,\alpha}(\omega) + G_{\mathbf{n},\mathbf{l}}^{(0)\alpha,\alpha}(\omega) \varepsilon_0 G_{\mathbf{l},\mathbf{m}}^{\alpha,\alpha}(\omega), \quad (2.16)$$

yielding the simple expressions for the matrix elements of the local operator $\hat{\Gamma}$, $\Gamma^{\gamma,\alpha}(\omega) = \delta_{\gamma,\alpha}\varepsilon_0$, and the T -matrix, $\mathcal{T}^{\gamma,\alpha}(\omega) = \delta_{\gamma,\alpha}(\varepsilon_0^{-1} - G_{11}^{(0)\alpha,\alpha}(\omega))^{-1}$. We note also that Eq. (2.16) takes the Dyson form for the Green's function at the impurity site, $\mathbf{n} = \mathbf{m} = \mathbf{l}$

$$G_{11}^{\alpha,\alpha}(\omega) = \frac{1}{\left[G_{11}^{(0)\alpha,\alpha}(\omega)\right]^{-1} - \varepsilon_0}. \quad (2.17)$$

Before moving to the case of dynamical impurity, it is particularly interesting to comment on the $|\varepsilon_0| \rightarrow \infty$ limit, corresponding to the vacancy or the infinite barrier problem. In this limit, the T -matrix is independent of impurity parameters, $\mathcal{T}(\omega) = -1/G^{(0)}(\omega)$, yielding

$$G_{\mathbf{n},\mathbf{m}}(\omega) = G_{\mathbf{n},\mathbf{m}}^{(0)}(\omega) - \frac{G_{\mathbf{n},\mathbf{l}}^{(0)}(\omega)G_{\mathbf{l},\mathbf{m}}^{(0)}(\omega)}{G_{11}^{(0)}(\omega)}. \quad (2.18)$$

2.3.3 Dynamic case

We now switch on the electron-phonon interaction. We assume that all static scattering effects have been embedded into $G_{\mathbf{n},\mathbf{m}}^{\gamma,\alpha}(\omega)|_{g=0} \equiv \delta_{\gamma,\alpha}G_{I_{\mathbf{n},\mathbf{m}}}^{\alpha,\alpha}(\omega)$, with $G_{I_{\mathbf{l},\mathbf{l}}}^{\alpha,\alpha}(\omega) \equiv G_I^{\alpha,\alpha}(\omega) = G_I(\omega - \alpha\omega_0)$, as described in previous Subsection 2.3.2. Eqs. (2.10) and (2.11) now give

$$G_{\mathbf{n},\mathbf{m}}^{\gamma,\alpha}(\omega) = \delta_{\gamma,\alpha} G_{I_{\mathbf{n},\mathbf{m}}}^{\gamma,\alpha}(\omega) + G_{I_{\mathbf{n},\mathbf{l}}}^{\gamma,\gamma}(\omega) g \left(\sqrt{\gamma+1} G_{I_{\mathbf{l},\mathbf{m}}}^{\gamma+1,\alpha}(\omega) + \sqrt{\gamma} G_{I_{\mathbf{l},\mathbf{m}}}^{\gamma-1,\alpha}(\omega) \right). \quad (2.19)$$

In order to proceed, we take advantage of the ansatz [42]

$$G_{I_{\mathbf{l},\mathbf{m}}}^{\gamma-1,\alpha}(\omega) = \sqrt{\gamma} A_{\gamma}(\omega) G_{I_{\mathbf{l},\mathbf{m}}}^{\gamma,\alpha}(\omega), \quad \sqrt{\gamma+1} G_{I_{\mathbf{l},\mathbf{m}}}^{\gamma+1,\alpha}(\omega) = B_{\gamma}(\omega) G_{I_{\mathbf{l},\mathbf{m}}}^{\gamma,\alpha}(\omega). \quad (2.20)$$

As shown in [42], $A_{\gamma}(\omega)$ may be represented by the finite continued fraction

$$A_{\gamma}(\omega) = \frac{g}{G_I^{-1}(\omega - (\gamma-1)\omega_0) - \frac{(\gamma-1)g^2}{G_I^{-1}(\omega - (\gamma-2)\omega_0) - \frac{(\gamma-2)g^2}{G_I^{-1}(\omega - (\gamma-3)\omega_0) - \dots}}}, \quad (2.21)$$

while $B_{\gamma}(\omega)$ by the infinite continued fraction

$$B_{\gamma}(\omega) = \frac{(\gamma+1)g}{G_I^{-1}(\omega - (\gamma+1)\omega_0) - \frac{(\gamma+2)g^2}{G_I^{-1}(\omega - (\gamma+2)\omega_0) - \frac{(\gamma+3)g^2}{G_I^{-1}(\omega - (\gamma+3)\omega_0) - \dots}}}. \quad (2.22)$$

Correspondingly, by successive applications of Eq. (2.20), the right-hand side of Eq. (2.19) may be expressed in terms of only diagonal (hereafter we really mean diagonal in the phonon number) matrix elements of the full Green's function.

In fact, the diagonal matrix elements of the full Green's function are straightforwardly obtained by applying Eq. (2.20) once in Eq. (2.19)

$$G_{\mathbf{n},\mathbf{m}}^{\alpha,\alpha}(\omega) = G_{I_{\mathbf{n},\mathbf{m}}}^{\alpha,\alpha}(\omega) + G_{I_{\mathbf{n},\mathbf{l}}}^{\alpha,\alpha}(\omega) [g\alpha A_{\alpha}(\omega) + gB_{\alpha}(\omega)] G_{I_{\mathbf{l},\mathbf{m}}}^{\alpha,\alpha}(\omega). \quad (2.23)$$

On the other hand, the evaluation of the non-diagonal, $\gamma \neq \alpha$, matrix elements $G_{\mathbf{n},\mathbf{m}}^{\gamma,\alpha}(\omega)$ demands a little bit more work. In that case, Eq. (2.19) gives

$$G_{\mathbf{n},\mathbf{m}}^{\gamma,\alpha}(\omega) = G_{I_{\mathbf{n},\mathbf{l}}}^{\gamma,\gamma}(\omega) g \left(\sqrt{\gamma+1} G_{I_{\mathbf{l},\mathbf{m}}}^{\gamma+1,\alpha}(\omega) + \sqrt{\gamma} G_{I_{\mathbf{l},\mathbf{m}}}^{\gamma-1,\alpha}(\omega) \right), \quad (2.24)$$

and it is necessary to consider cases for $\gamma > \alpha$ and $\gamma < \alpha$ separately.

Here we consider the situation $\gamma > \alpha$, while the case with $\gamma < \alpha$ is treated analogously. In order to obtain diagonal matrix elements on the right-hand side of Eq. (2.24), successive applications of Eqs. (2.20) may be utilized to get from $G_{I_{\mathbf{l},\mathbf{m}}}^{\gamma+1,\alpha}(\omega)$ and $G_{I_{\mathbf{l},\mathbf{m}}}^{\gamma-1,\alpha}(\omega)$ to $G_{I_{\mathbf{l},\mathbf{m}}}^{\alpha,\alpha}(\omega)$. In particular, we have

$$\begin{aligned}
G_{1,\mathbf{m}}^{\gamma+1,\alpha}(\omega) &= \frac{B_\gamma(\omega)G_{1,\mathbf{m}}^{\gamma,\alpha}(\omega)}{\sqrt{\gamma+1}} = \frac{B_\gamma(\omega)B_{\gamma-1}(\omega)G_{1,\mathbf{m}}^{\gamma-1,\alpha}(\omega)}{\sqrt{(\gamma+1)\gamma}} \\
&= \frac{B_\gamma(\omega)B_{\gamma-1}(\omega)\dots B_\alpha(\omega)G_{1,\mathbf{m}}^{\alpha,\alpha}(\omega)}{\sqrt{(\gamma+1)\gamma\cdots(\alpha+1)}},
\end{aligned} \tag{2.25}$$

and

$$\begin{aligned}
G_{1,\mathbf{m}}^{\gamma-1,\alpha}(\omega) &= \frac{B_{\gamma-2}(\omega)G_{1,\mathbf{m}}^{\gamma-2,\alpha}(\omega)}{\sqrt{(\gamma-1)}} = \frac{B_{\gamma-2}(\omega)B_{\gamma-3}(\omega)G_{1,\mathbf{m}}^{\gamma-3,\alpha}(\omega)}{\sqrt{(\gamma-1)(\gamma-2)}} \\
&= \frac{B_{\gamma-2}(\omega)B_{\gamma-3}(\omega)\dots B_\alpha(\omega)G_{1,\mathbf{m}}^{\alpha,\alpha}(\omega)}{\sqrt{(\gamma-1)(\gamma-2)\cdots(\alpha+1)}},
\end{aligned} \tag{2.26}$$

which yields the expression for $G_{\mathbf{n},\mathbf{m}}^{\gamma,\alpha}(\omega)$ in terms of the diagonal matrix elements $G_{\mathbf{n},\mathbf{m}}^{\alpha,\alpha}(\omega)$

$$G_{\mathbf{n},\mathbf{m}}^{\gamma,\alpha}(\omega) = \begin{cases} G_{I_{\mathbf{n},1}}^{\gamma,\gamma}(\omega)g\sqrt{\frac{\alpha!}{\gamma!}}(\gamma+B_\gamma(\omega)B_{\gamma-1}(\omega))\prod_{i=\alpha}^{\gamma-2}B_i(\omega)G_{1,\mathbf{m}}^{\alpha,\alpha}(\omega), & \gamma > \alpha+1, \\ G_{I_{\mathbf{n},1}}^{\gamma,\gamma}(\omega)g\sqrt{\frac{\alpha!}{\gamma!}}(\gamma+B_\gamma(\omega)B_\alpha(\omega))G_{1,\mathbf{m}}^{\alpha,\alpha}(\omega), & \gamma = \alpha+1. \end{cases} \tag{2.27}$$

Following the similar procedure, we obtain for $\gamma < \alpha$

$$G_{\mathbf{n},\mathbf{m}}^{\gamma,\alpha}(\omega) = \begin{cases} G_{I_{\mathbf{n},1}}^{\gamma,\gamma}(\omega)g\sqrt{\frac{\alpha!}{\gamma!}}(1+\gamma A_\gamma(\omega)A_\alpha(\omega))G_{1,\mathbf{m}}^{\alpha,\alpha}(\omega), & \gamma = \alpha-1, \\ G_{I_{\mathbf{n},1}}^{\gamma,\gamma}(\omega)g\sqrt{\frac{\alpha!}{\gamma!}}(1+\gamma A_\gamma(\omega)A_{\gamma+1}(\omega))\prod_{i=\gamma+2}^{\alpha}A_i(\omega)G_{1,\mathbf{m}}^{\alpha,\alpha}(\omega), & \gamma < \alpha-1. \end{cases} \tag{2.28}$$

What is left to do is to compare expressions in Eqs. (2.23), (2.27), and (2.28) with Eq. (2.13), and to simply read out the matrix elements $\tilde{\Gamma}^{\gamma,\alpha}(\omega)$. For $\gamma = \alpha$, by comparing Eqs. (2.13) and (2.23) we have

$$\tilde{\Gamma}^{\alpha,\alpha}(\omega) = g\alpha A_\alpha(\omega) + gB_\alpha(\omega), \tag{2.29}$$

while by comparing Eq. (2.13) with Eqs. (2.27) and (2.28) for non-diagonal, $\gamma \neq \alpha$, matrix elements we get

$$\tilde{\Gamma}^{\gamma,\alpha}(\omega) = \begin{cases} g \sqrt{\frac{\alpha!}{\gamma!}} (\gamma + B_\gamma(\omega) B_{\gamma-1}(\omega)) \prod_{i=\alpha}^{\gamma-2} B_i(\omega), & \gamma > \alpha + 1, \\ g \sqrt{\frac{\alpha!}{\gamma!}} (\gamma + B_\gamma(\omega) B_\alpha(\omega)), & \gamma = \alpha + 1, \\ g \sqrt{\frac{\alpha!}{\gamma!}} (1 + \gamma A_\gamma(\omega) A_\alpha(\omega)), & \gamma = \alpha - 1, \\ g \sqrt{\frac{\alpha!}{\gamma!}} (1 + \gamma A_\gamma(\omega) A_{\gamma+1}(\omega)) \prod_{i=\gamma+2}^{\alpha} A_i(\omega), & \gamma < \alpha - 1 \end{cases} \quad (2.30)$$

Since now all matrix elements of the local operator $\hat{\Gamma}$ are known, the polaronic impurity model in Eq. (2.1) is fully solved.

2.3.4 Combining static and dynamic contributions

We note that the matrix elements of the local operator $\hat{\Gamma}$ in Eqs. (2.29) and (2.30) are denoted with a tilde. The reason is that this operator $\hat{\tilde{\Gamma}}(\omega)$ is defined by assuming that the unperturbed Green's function already contains all static scattering processes. In other words, it is defined via Eq. (2.13) in terms of the Green's function $\hat{G}_I(\omega)$.

However, we actually need to attain the matrix elements of $\hat{\Gamma}$ with respect to the Green's function for which the translational symmetry is preserved, that is $\hat{G}^{(0)}(\omega)$, since this Green's function is the starting point of all our calculations. In order to do that, we substitute Eq. (2.16) in Eq. (2.23)

$$\begin{aligned} G_{\mathbf{n},\mathbf{m}}^{\alpha,\alpha}(\omega) &= G_{\mathbf{n},\mathbf{m}}^{(0)\alpha,\alpha}(\omega) + G_{\mathbf{n},\mathbf{l}}^{(0)\alpha,\alpha}(\omega) \varepsilon_0 G_{\mathbf{l},\mathbf{m}}^{\alpha,\alpha}(\omega) + \\ &+ \left[G_{\mathbf{n},\mathbf{l}}^{(0)\alpha,\alpha}(\omega) + G_{\mathbf{n},\mathbf{l}}^{(0)\alpha,\alpha}(\omega) \varepsilon_0 G_{\mathbf{l},\mathbf{l}}^{\alpha,\alpha}(\omega) \right] [g\alpha A_\alpha(\omega) + gB_\alpha(\omega)] G_{\mathbf{l},\mathbf{m}}^{\alpha,\alpha}(\omega) \\ &= G_{\mathbf{n},\mathbf{m}}^{(0)\alpha,\alpha}(\omega) + G_{\mathbf{n},\mathbf{l}}^{(0)\alpha,\alpha}(\omega) [g\alpha A_\alpha(\omega) + gB_\alpha(\omega)] G_{\mathbf{l},\mathbf{m}}^{\alpha,\alpha}(\omega) + \\ &+ G_{\mathbf{n},\mathbf{l}}^{(0)\alpha,\alpha}(\omega) \varepsilon_0 \left\{ G_{\mathbf{l},\mathbf{m}}^{\alpha,\alpha}(\omega) + G_{\mathbf{l},\mathbf{l}}^{\alpha,\alpha}(\omega) [g\alpha A_\alpha(\omega) + gB_\alpha(\omega)] G_{\mathbf{l},\mathbf{m}}^{\alpha,\alpha}(\omega) \right\} \\ &= G_{\mathbf{n},\mathbf{m}}^{(0)\alpha,\alpha}(\omega) + G_{\mathbf{n},\mathbf{l}}^{(0)\alpha,\alpha}(\omega) [\varepsilon_0 + g\alpha A_\alpha(\omega) + gB_\alpha(\omega)] G_{\mathbf{l},\mathbf{m}}^{\alpha,\alpha}(\omega), \end{aligned} \quad (2.31)$$

where in obtaining the last equality Eq. (2.23) for $\mathbf{n} = \mathbf{l}$ was used. By comparing now this expression with the definition of the diagonal matrix elements $\Gamma^{\alpha,\alpha}$ in Eq. (2.13), we have

$$\Gamma^{\alpha,\alpha}(\omega) = \varepsilon_0 + \tilde{\Gamma}^{\alpha,\alpha}(\omega) = \varepsilon_0 + g\alpha A_\alpha(\omega) + gB_\alpha(\omega). \quad (2.32)$$

Note that the full Green's function at the impurity site, $\mathbf{n} = \mathbf{m} = \mathbf{l}$, in Eq. (2.31) takes the Dyson form.

Moreover, non-diagonal, $\gamma \neq \alpha$, matrix elements $\Gamma^{\gamma,\alpha}(\omega)$ are given by

$$G_{\mathbf{n},\mathbf{m}}^{\gamma,\alpha}(\omega) = G_{\mathbf{n},\mathbf{l}}^{(0)\gamma,\gamma}(\omega) \Gamma^{\gamma,\alpha}(\omega) G_{\mathbf{l},\mathbf{m}}^{\alpha,\alpha}(\omega), \quad (2.33)$$

which combined with

$$G_{\mathbf{n},\mathbf{m}}^{\gamma,\alpha}(\omega) = G_{I_{\mathbf{n},1}}^{\gamma,\gamma}(\omega) \tilde{\Gamma}^{\gamma,\alpha}(\omega) G_{\mathbf{l},\mathbf{m}}^{\alpha,\alpha}(\omega) = G_{\mathbf{n},1}^{(0)\gamma,\gamma}(\omega) \frac{G_{I_{\mathbf{n},1}}^{\gamma,\gamma}(\omega)}{G_{\mathbf{n},1}^{(0)\gamma,\gamma}(\omega)} \tilde{\Gamma}^{\gamma,\alpha}(\omega) G_{\mathbf{l},\mathbf{m}}^{\alpha,\alpha}(\omega), \quad (2.34)$$

and Eqs. (2.16) and (2.17) finally gives

$$\Gamma^{\gamma,\alpha}(\omega) = \frac{G_{I_{\mathbf{n},1}}^{\gamma,\gamma}(\omega)}{G_{\mathbf{n},1}^{(0)\gamma,\gamma}(\omega)} \tilde{\Gamma}^{\gamma,\alpha}(\omega) = \left(1 + \varepsilon_0 G_{I_{\mathbf{n},1}}^{\gamma,\gamma}(\omega)\right) \tilde{\Gamma}^{\gamma,\alpha}(\omega) = \frac{\tilde{\Gamma}^{\gamma,\alpha}(\omega)}{1 - \varepsilon_0 G_{\mathbf{l},1}^{(0)\gamma,\gamma}(\omega)}. \quad (2.35)$$

We stress one more time that expressions in Eqs. (2.32) and (2.35) hold irrespectively of a lattice dimension and geometry, allowing us to employ them to study both the electron tunneling and scattering in the 1D and 3D case, respectively.

2.3.5 Green's function $G_{\mathbf{l},1}^{1,0}(\omega)$

To provide a pictorial example of how our developed formalism accounts for the exact solution, we consider the case of Green's function $G_{\mathbf{l},1}^{1,0}(\omega)$. This Green's function describes a process in which an electron enters the system and emits a real phonon, with no phonons previously present in the system. For this purpose, we assume that all the static scattering processes have already been accounted for and we are interested only in the effects due to the electron-phonon interaction.

By referencing to Eq. (2.27), we have for the full Green's function $G_{\mathbf{l},1}^{1,0}(\omega)$

$$G_{\mathbf{l},1}^{1,0}(\omega) = G_{h_{\mathbf{l},1}}^{1,1}(\omega) g (1 + B_1(\omega) B_0(\omega)) G_{\mathbf{l},1}^{0,0}(\omega). \quad (2.36)$$

From here, we can use Eq. (2.23) to express $G_{\mathbf{l},1}^{0,0}(\omega)$ in the Dyson form, yielding

$$G_{\mathbf{l},1}^{1,0}(\omega) = G_{h_{\mathbf{l},1}}^{1,1}(\omega) g (1 + B_1(\omega) B_0(\omega)) G_{h_{\mathbf{l},1}}^{0,0}(\omega) \left[1 - g B_0(\omega) G_{h_{\mathbf{l},1}}^{0,0}(\omega)\right]^{-1}. \quad (2.37)$$

We focus on a few lowest order processes, so we expand the denominator with respect to g

$$G_{\mathbf{l},1}^{1,0}(\omega) = G_{h_{\mathbf{l},1}}^{1,1}(\omega) g (1 + B_1(\omega) B_0(\omega)) G_{h_{\mathbf{l},1}}^{0,0}(\omega) \left(1 + g B_0(\omega) G_{h_{\mathbf{l},1}}^{0,0}(\omega)\right). \quad (2.38)$$

Analogously, the lowest order expansions of the continued fractions $B_\alpha(\omega)$ read $B_0(\omega) \approx$

$gG_{l,l}^{1,1}(\omega)$ and $B_1(\omega) \approx 2gG_{l,l}^{2,2}(\omega)$. By keeping only contributions to the third order in g , we finally get

$$G_{l,l}^{1,0}(\omega) \approx G_{l,l}^{1,1}(\omega)gG_{l,l}^{0,0}(\omega) + G_{l,l}^{1,1}(\omega)gG_{l,l}^{0,0}(\omega)gG_{l,l}^{1,1}(\omega)gG_{l,l}^{0,0}(\omega) + 2G_{l,l}^{1,1}(\omega)gG_{l,l}^{2,2}(\omega)gG_{l,l}^{1,1}(\omega)gG_{l,l}^{0,0}(\omega) . \quad (2.39)$$

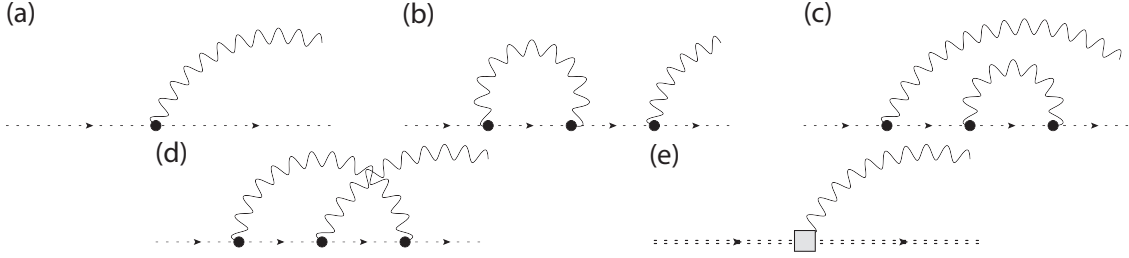


Figure 2.3: (a) Leading and (b)-(d) next-to-leading order contributions to $G_{l,l}^{1,0}(\omega)$. (e) The exact $G_{l,l}^{1,0}(\omega)$. Single dotted lines represent the electron propagator with the static scattering included; double dotted lines represent the exact one. The full circle represents the electron-phonon vertex g , while the square in (e) is the exact electron-phonon vertex function.

The three (actually four) contributions in Eq. (2.39) are diagrammatically sketched in Figs. 2.3(a)-(d). It is worth emphasizing that the appearance of Green's functions and vertices in three contributions of Eq. (2.39), from right to left, exactly follows the time order of events depicted in Figs. 2.3(a)-(d). In particular, the first contribution in Eq. (2.39), corresponding to Fig. 2.3(a), describes a process in which an electron propagates ($G_{l,l}^{0,0}(\omega)$) and emits (g) a phonon, after which the electron and the phonon continue to propagate through the system ($G_{l,l}^{1,1}(\omega)$). Evidently, there are no virtual phonons involved, nor the renormalization of the vertex g , so this is the lowest order process which contributes to $G_{l,l}^{1,0}(\omega)$.

This changes with the next-to-leading order process corresponding to the second contribution in Eq. (2.39) and Fig. 2.3(b). Namely, it takes into account the renormalization of the incoming electron propagator ($G_{l,l}^{0,0}(\omega)$) due to the emission of a virtual phonon. By inspecting Eq. (2.36), this term comes from the expansion of the full Green's function $G_{l,l}^{0,0}(\omega)$.

Finally, the term with continued fractions in Eq. (2.36) yields the remaining two next-to-leading contributions, which are depicted by two diagrams in Figs. 2.3(c) and (d), and which equally contribute to $G_{l,l}^{1,0}(\omega)$ - note the factor 2 in Eq. (2.39). In particular, the diagram in Fig. 2.3(c) describes the renormalization of the outgoing propagator ($G_{l,l}^{1,1}(\omega)$). On the other hand, the diagram in Fig. 2.3(d) corresponds to the leading vertex correction, involving the crossing of the phonon propagators. It is particularly interesting that those two diagrams give the same contribution, which is a direct consequence of the locality of the electron-phonon

interaction in real space. Namely, all electron-phonon interaction vertices are limited to a single (impurity) site.

Based on this low order expansion, we anticipate that all processes involving the renormalization of the ingoing and outgoing propagators, as well as the renormalization of the electron-phonon vertex, will be covered when all higher order contributions would be considered. This would finally result in the exact propagator $G_{11}^{1,0}(\omega)$ depicted in Fig. 2.3(e), where the exact propagators $G_{11}^{0,0}(\omega)$, $G_{11}^{1,1}(\omega)$, and the exact vertex function, denoted with the square, appear.

2.4 Conclusions

Within Green's function formalism, we provide the exact analytical solution to the polaronic impurity problem involving the electron interaction with the local phonon degree of freedom and the change of the atomic orbital energy at the impurity site for an arbitrary lattice model. Apart from the diagonal Green's functions in the phonon number, we obtain all the non-diagonal Green's functions describing processes with emission and absorption of real phonons, where the latter are of utter importance in studying the inelastic electron transmission and the inelastic scattering on polaronic impurities. The key to solving the problem lies in the locality of the electron-phonon interaction in real space, which ensures that the full Green's function can be expressed by means of continued fractions containing only the local free electron Green's function. A vertex contribution to the full Green's function in a given order turned out to be exactly equal to a non-vertex contribution, whose diagrammatic representations involve the same number of phonon lines when cut with vertical lines at any instance of time.

Tunneling through a polaronic impurity

Parts of Chapter 3 have been published as the supplemental material to [17].

In this short Chapter 3, we exploit the exact solution of Chapter 2 to study electron tunneling across molecular junctions.

3.1 Transmission coefficient

The presence of impurities profoundly affects transport properties in low-dimensional systems ($D \leq 2$). Those effects are particularly prominent in 1D systems since a propagating electron cannot avoid an impurity site. Thus, in the 1D case, the impurity for the propagating electron acts as an unavoidable barrier resulting in a tunneling problem, where one can study the electron transmission/reflection through the impurity site.

The problem of electron tunneling in the presence of polaronic impurities gained a lot of theoretical interest [18–20, 43–46] due to its relevance for the inelastic electron tunneling spectroscopy, as already emphasized at the beginning of Chapter 2. In particular, it was solved in the continuum limit [43], whereas the problem on a lattice was exactly solved only numerically [18–20]. Using our formalism, we are able to solve the problem for an arbitrary system of interest without the need for any approximations.

To set us in the framework of the tunneling problem, we consider the situation with α phonons present at the impurity and the electron moving on a 1D lattice (with the lattice constant $a = 1$), from left to right in the \hat{x} direction toward the impurity site $l = 0$. The electron has a momentum \mathbf{k} and an energy $\varepsilon_\alpha = -2t \cos(\mathbf{k} \cdot \hat{x})$, where t is the nearest neighbor hopping integral. By reaching the impurity site the electron has a certain probability to be transmitted/reflected. The probability of finding the electron with a momentum \mathbf{k}' and an energy $\varepsilon_\gamma = -2t \cos(\mathbf{k}' \cdot \hat{x})$ at the site $|\mathbf{r}| > |l|$, together with γ phonons present at the impurity site defines the transmission coefficient

$$T_{\gamma\alpha}(\varepsilon_\alpha) = N |\langle \mathbf{r}, \gamma | \psi \rangle|^2, \quad (3.1)$$

where $|\psi\rangle = |\mathbf{k}, \alpha\rangle + \hat{G}^{(0)}(\omega) \hat{\mathcal{T}}(\omega) |\mathbf{k}, \alpha\rangle$ is the state describing the scattered electron and γ phonons left in the system, in accordance with Eq. (2.9). The factor N accounts for the degeneracy of choosing the impurity site from N possible lattice sites.

In order to proceed, we note that the initial state is simply a product of the Bloch and the phonon state

$$|\mathbf{k}, \alpha\rangle = \frac{1}{\sqrt{N}} \sum_{\mathbf{j}} e^{i\mathbf{k}\cdot\mathbf{j}} |\mathbf{j}, \alpha\rangle . \quad (3.2)$$

Accordingly, we have for the scattered state

$$|\psi\rangle = \frac{1}{\sqrt{N}} \sum_{\mathbf{j}} e^{i\mathbf{k}\cdot\mathbf{j}} |\mathbf{j}, \alpha\rangle + \frac{1}{\sqrt{N}} \sum_{\mathbf{j}} e^{i\mathbf{k}\cdot\mathbf{j}} \hat{G}^{(0)}(\omega) \sum_{\zeta, \xi} |\mathbf{l}, \zeta\rangle \mathcal{T}^{\zeta, \xi}(\omega) \langle \mathbf{l}, \xi | \mathbf{j}, \alpha \rangle , \quad (3.3)$$

where we have exploited the T -matrix written in the $|\mathbf{j}, \alpha\rangle$ basis.

To compute now the scalar product in Eq. (3.1), we recall that the states $|\mathbf{j}, \alpha\rangle$ are orthonormal, $\langle \mathbf{i}, \alpha | \mathbf{j}, \beta \rangle = \delta_{\mathbf{i}, \mathbf{j}} \delta_{\alpha, \beta}$, while the matrix elements of the electron Green's function for the 1D lattice satisfy [41]

$$\langle \mathbf{r}, \gamma | G^{(0)}(\omega) | \mathbf{l}, \alpha \rangle = \delta_{\gamma, \alpha} G_{\mathbf{r}, \mathbf{l}}^{(0)\alpha, \alpha}(\omega) = \delta_{\gamma, \alpha} e^{i\mathbf{k}'\cdot(\mathbf{r}-\mathbf{l})} G_{\mathbf{l}, \mathbf{l}}^{(0)\alpha, \alpha}(\omega) . \quad (3.4)$$

By taking into account all the above expressions, we get for the transmission coefficient

$$\begin{aligned} T_{\gamma\alpha}(\varepsilon_\alpha) &= \left| \delta_{\gamma, \alpha} e^{i\mathbf{k}\mathbf{r}} + e^{i\mathbf{k}\mathbf{l}} e^{i\mathbf{k}'\cdot(\mathbf{r}-\mathbf{l})} G_{\mathbf{l}, \mathbf{l}}^{(0)\gamma, \gamma}(\omega) \mathcal{T}^{\gamma, \alpha}(\omega) \right|^2 \\ &= \left| \delta_{\gamma, \alpha} e^{i\mathbf{k}\mathbf{r}} + e^{i\mathbf{k}\mathbf{l}} e^{i\mathbf{k}'\cdot(\mathbf{r}-\mathbf{l})} \frac{G_{\mathbf{l}, \mathbf{l}}^{(0)\gamma, \gamma}(\omega) \Gamma^{\gamma, \alpha}(\omega)}{1 - G_{\mathbf{l}, \mathbf{l}}^{(0)\alpha, \alpha}(\omega) \Gamma^{\alpha, \alpha}(\omega)} \right|^2 . \end{aligned} \quad (3.5)$$

It is convenient to separately consider elastic, $\mathbf{k} = \mathbf{k}'$ and $\gamma = \alpha$, and inelastic, $\mathbf{k} \neq \mathbf{k}'$ and $\gamma \neq \alpha$, tunneling cases, yielding

$$T_{\gamma\alpha}(\varepsilon_\alpha) = \begin{cases} \frac{1}{\left| 1 - G_{\mathbf{l}, \mathbf{l}}^{(0)\alpha, \alpha}(\omega) \Gamma^{\alpha, \alpha}(\omega) \right|^2} , & \text{elastic} , \\ \frac{G_{\mathbf{l}, \mathbf{l}}^{(0)\gamma, \gamma}(\omega) \Gamma^{\gamma, \alpha}(\omega)}{\left| 1 - G_{\mathbf{l}, \mathbf{l}}^{(0)\alpha, \alpha}(\omega) \Gamma^{\alpha, \alpha}(\omega) \right|^2} , & \text{inelastic} . \end{cases} \quad (3.6)$$

Here, it cannot be overstated that ω is the total energy of the electron-phonon system, $\omega = \varepsilon_\alpha + \alpha\omega_0 = \varepsilon_\gamma + \gamma\omega_0$, while $T_{\gamma\alpha}(\varepsilon_\alpha)$ exclusively depends on the incoming electron energy ε_α .

Next, we have to take into account the conservation of electron current. The total current produced by the ingoing electron with the momentum $\mathbf{k} = k\hat{x}$ reads

$$j = \sum_{\mathbf{i}} \langle \mathbf{k} | \hat{j}_{\mathbf{i}} | \mathbf{k} \rangle , \quad (3.7)$$

where $\hat{j}_i = it (c_i^\dagger c_{i-1} - c_{i-1}^\dagger c_i)$ is the current density operator at the site i [47]. Since $|\mathbf{k}\rangle$ is a Bloch state, we calculate

$$\begin{aligned} \langle \mathbf{k} | c_i^\dagger c_{i-1} | \mathbf{k} \rangle &= \frac{1}{N} \sum_{\mathbf{n}, \mathbf{m}} e^{-i\mathbf{k} \cdot R_{\mathbf{m}}} e^{i\mathbf{k} \cdot R_{\mathbf{n}}} \langle R_{\mathbf{m}} | c_i^\dagger c_{i-1} | R_{\mathbf{n}} \rangle \\ &= \delta_{i-1, \mathbf{n}} \delta_{i, \mathbf{m}} \frac{1}{N} \sum_{\mathbf{n}, \mathbf{m}} e^{-i\mathbf{k} \cdot R_{\mathbf{m}}} e^{i\mathbf{k} \cdot R_{\mathbf{n}}} = \frac{1}{N} e^{-i\mathbf{k} \cdot \hat{x}}, \end{aligned} \quad (3.8)$$

where we have used $R_{i\pm 1} = R_i \pm \hat{x}$ ($a = 1$). Analogously, we have $\langle \mathbf{k} | c_{i-1}^\dagger c_i | \mathbf{k} \rangle = \frac{1}{N} e^{i\mathbf{k} \cdot \hat{x}}$, so by going back to Eq. (3.7) the total current of the ingoing electron reads

$$j = it \frac{1}{N} \sum_{\mathbf{i}} \left[e^{-i\mathbf{k} \cdot \hat{x}} - e^{i\mathbf{k} \cdot \hat{x}} \right] = (it) [-2i \sin(\mathbf{k} \cdot \hat{x})] \frac{1}{N} \sum_{\mathbf{i}} = 2t \sin(\mathbf{k} \cdot \hat{x}). \quad (3.9)$$

Similarly, we have for the current of the outgoing electron scattered on the impurity

$$j' = 2t \sin(\mathbf{k}' \cdot \hat{x}) [T_{\gamma\alpha}(\varepsilon_\alpha) + R_{\gamma\alpha}(\varepsilon_\alpha)]. \quad (3.10)$$

Here, we have immediately divided the total outgoing current in the γ, α channel on the transmitted $j'_T = 2t \sin(\mathbf{k}' \cdot \hat{x}) T_{\gamma\alpha}(\varepsilon_\alpha)$ and the reflected $j'_R = 2t \sin(\mathbf{k}' \cdot \hat{x}) R_{\gamma\alpha}(\varepsilon_\alpha)$ current, where $R_{\gamma\alpha}(\varepsilon_\alpha) = 1 - T_{\gamma\alpha}(\varepsilon_\alpha)$ is the reflection coefficient, and \mathbf{k}' can be obtained by means of the energy conservation law

$$\varepsilon_\alpha = -2t \cos(\mathbf{k} \cdot \hat{x}) = -2t \cos(\mathbf{k}' \cdot \hat{x}) + \omega_0 (\gamma - \alpha). \quad (3.11)$$

Lastly, by assuming that the system is in the thermal equilibrium, the probability of finding α phonons initially present in the system at a temperature T is given by the distribution $P(\alpha, T) = (1 - e^{-\omega_0/T}) e^{-\alpha\omega_0/T}$ ($k_B = 1$). During the process of tunneling the initial number of phonons α may change to arbitrary γ (however, restricted by the energy conservation law, Eq. (3.11)), so we have to take account of all possible tunneling channels γ, α . In particular, the total transmission at an arbitrary temperature T reads

$$T(\varepsilon_\alpha) = \left(1 - e^{-\omega_0/T}\right) \sum_{\alpha, \gamma} e^{-\alpha\omega_0/T} \frac{j'_T}{j} = \left(1 - e^{-\omega_0/T}\right) \sum_{\alpha, \gamma} e^{-\alpha\omega_0/T} \frac{\sin(\mathbf{k}' \cdot \hat{x}) T_{\gamma\alpha}(\varepsilon_\alpha)}{\sin(\mathbf{k} \cdot \hat{x})}. \quad (3.12)$$

As an example, we show in Fig. 3.1 the electron transmission in dependence on the incoming electron energy for the system parameters $t = 1$, $\omega_0 = 0.5$, $\varepsilon_0 = 0.1$, and $g = 0, 2$, at zero temperature. For the weak static impurity, when the electron-phonon coupling is absent, only

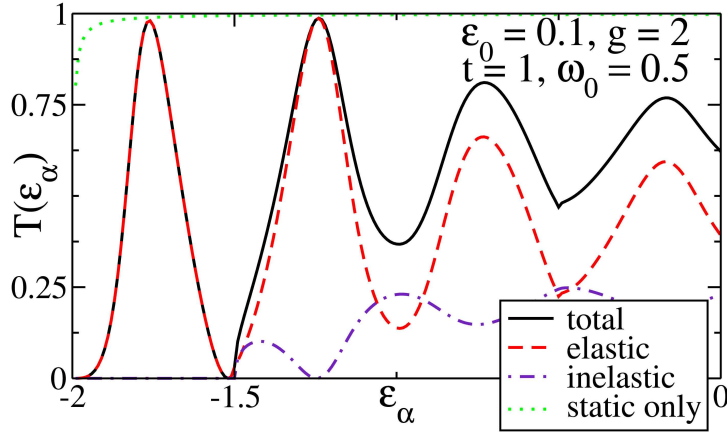


Figure 3.1: Electron transmission in dependence on the incoming electron energy for the system parameters $t = 1$, $\omega_0 = 0.5$, $\varepsilon_0 = 0.1$, and $g = 0, 2$, at zero temperature. The black solid curve represents the total transmission in the presence of the finite electron-phonon coupling, while the red dashed curve and the violet dot-dashed curve denote its elastic and inelastic contributions, respectively. The green dashed curve represents the transmission when only the static impurity is present, $g = 0$.

low energy electrons are reflected by the impurity, green dashed curve in Fig. 3.1. Contrary, for the strong electron-phonon coupling, the energy dependence of the transmission is governed by the phonon frequency scale, where energy regions with both minima and maxima of the electron transmission are observed. This is well in accordance with the experimental findings [22–28].

Since the results shown in Fig. 3.1 were obtained for the zero temperature case, there were no phonons that the electron could have absorbed upon reaching the impurity. Consequently, absorption channels were absent and the inelastic tunneling turned on as soon as the incident electron energy become high enough for the emission of a phonon. As seen from Fig. 3.1, this inelastic contribution to the total transmission is for most energies ε_α negligible compared to the elastic contribution, albeit both contributions get comparable when the electron energy $\varepsilon_\alpha = -2t + n\omega_0$ is the multiple of the phonon energy ω_0 , with the electron energy measured from the bottom of the band, $\varepsilon_B = -2t$.

3.2 Conclusions

We apply the exact analytical solution of the polaronic impurity model in Eq. (2.1) to calculate the electron transmission coefficient for the process involving tunneling of the electron through the polaronic impurity. We observe multiple minima and maxima of the electron transmission as a function of the incident electron energy for strong couplings. Our formalism and results may be relevant for the interpretation of inelastic electron tunneling spectroscopy measurements.

Scattering on polaronic impurities

Parts of Chapter 4 have been published in [17].

Given the great attention that the polaronic impurity problem acquired in the context of electron tunneling across molecular junctions, it comes as a surprise that the problem was seldom if at all, considered for bulk ($D > 1$) systems. Motivated by that, and the fact that our exact solution works for an arbitrary system dimension, we investigate some aspects of electronic transport properties in the presence of polaronic impurities in the 3D case. In particular, we put the majority of focus on the temperature dependence of electron mobility.

Additionally, we comment on the appearance of localized electron states outside the continuum of delocalized states. Such localized states exist for arbitrary weak (static) impurities in the 1D case, while in the 3D case the impurity should be strong enough for a localized state to appear [41]. In that regard, it is particularly interesting to study how the dynamic nature of impurity influences the structure of localized states. In contrast to the previous approaches [18–20], where this part of the Hilbert space is not so simple to include even in the 1D case, within our formalism it is straightforwardly addressed.

4.1 Scattering cross section

In order to address electronic transport properties, we first consider the electron scattering cross section due to the scattering on a single polaronic impurity. For that purpose, we refer to the general approach to stationary scattering problems in quantum mechanics [48]. Namely, we are interested in a solution that has the asymptotic form of a plane wave plus an outgoing scattered wave, which is well described by Eq. (2.9).

4.1.1 Scattered wave

To be specific, similarly as in the 1D case, let us take that the initial state (prior to the scattering event) involves α phonons and an incident electron with an energy ε_α and a momentum \mathbf{k} . The electron eventually scatters at the impurity site $\mathbf{l} = 0$, and, as a result, γ phonons and the electron with an energy ε_γ and a momentum \mathbf{k}' are left in the system. The state after the scattering is described by Eq. (3.3), with the wave function given by

$$\psi = \langle \mathbf{r}, \gamma | \psi \rangle = \sum_{\mathbf{j}} e^{i\mathbf{k}\mathbf{j}} \langle \mathbf{r}, \gamma | \mathbf{j}, \alpha \rangle + \sum_{\mathbf{j}} e^{i\mathbf{k}\mathbf{j}} \sum_{\kappa, \zeta} \langle \mathbf{r}, \gamma | \hat{G}^{(0)}(\omega) | \mathbf{l}, \kappa \rangle \mathcal{T}^{\kappa, \zeta}(\omega) \langle \mathbf{l}, \zeta | \mathbf{j}, \alpha \rangle, \quad (4.1)$$

which with the use of Eq. (2.6) and the orthonormality of states $|\mathbf{j}, \alpha\rangle$ simplifies to

$$\psi = \delta_{\gamma, \alpha} e^{i\mathbf{k}\mathbf{r}} + G_{\mathbf{r}, \mathbf{l}}^{(0)\gamma, \gamma}(\omega) \mathcal{T}^{\gamma, \alpha}(\omega). \quad (4.2)$$

Hereafter, we consider the simple cubic lattice with the lattice constant a and the electron dispersion $\varepsilon = -2t [\cos(\mathbf{k} \cdot a\hat{x}) + \cos(\mathbf{k} \cdot a\hat{y}) + \cos(\mathbf{k} \cdot a\hat{z})]$, characterized by the nearest neighbor hopping integral t . The local Green's function $G_{\mathbf{l}, \mathbf{l}}^{(0)}(\omega)$ for such a lattice may be obtained in a closed form in terms of the complete elliptic integrals of the first kind [49], and can be easily evaluated numerically [50].

While for high order contributions to $\mathcal{T}^{\gamma, \alpha}(\omega)$ the exact form of $G_{\mathbf{l}, \mathbf{l}}^{(0)}(\omega)$ has to kept, $G_{\mathbf{r}, \mathbf{l}}^{(0)\gamma, \gamma}(\omega)$ in Eq. (4.2) may be approximated by its asymptotic form at great distances from the impurity site $|\mathbf{r}| \gg |\mathbf{l}| = 0$ given by [51, 52]

$$\begin{aligned} G_{|\mathbf{r}| \rightarrow \infty}^{(0)} &\approx \frac{-a}{4\pi |t|} \sum_{\mathbf{k}'} \sqrt{\frac{\sin^2 k'_x + \sin^2 k'_y + \sin^2 k'_z}{\sin^2 k'_x \cos k'_y \cos k'_z + \sin^2 k'_y \cos k'_z \cos k'_x + \sin^2 k'_z \cos k'_x \cos k'_y}} \frac{e^{i\mathbf{k}' \cdot \mathbf{r}}}{r} \\ &\equiv \sum_{\mathbf{k}'} F(\mathbf{k}') \frac{e^{i\mathbf{k}' \cdot \mathbf{r}}}{r}. \end{aligned} \quad (4.3)$$

Here, the sum involves only those momenta \mathbf{k}' which satisfy two conditions

$$\varepsilon_{\gamma} = \varepsilon_{\gamma}(\mathbf{k}'), \quad \text{and} \quad \nabla_{\mathbf{k}} \varepsilon_{\gamma}(\mathbf{k}') \parallel \hat{r}, \quad (4.4)$$

with \hat{r} the direction of the position vector \mathbf{r} relative to $\mathbf{l} = 0$. In particular, the first condition is nothing but the energy conservation law which for the given energy ε_{γ} of the scattered electron determines an energy surface in the momentum space. The second condition is more stringent and says that the direction of the greatest rate of increase of the energy at point \mathbf{k}' has to be collinear with \hat{r} . That is, momenta \mathbf{k}' are uniquely determined by ε_{γ} and \hat{r} and the outgoing scattered wave in Eq. (4.2) is a sum of waves with various momenta \mathbf{k}'

$$\psi \approx \delta_{\gamma, \alpha} e^{i\mathbf{k}\mathbf{r}} + \sum_{\mathbf{k}'} F(\mathbf{k}') \frac{e^{i\mathbf{k}'\mathbf{r}}}{r} \mathcal{T}^{\gamma, \alpha}(\omega). \quad (4.5)$$

4.1.2 Probability current

As a next step in evaluating the electron scattering cross section, we need to determine the probability current

$$\mathbf{j} = \frac{\hbar}{m} \Re \{ -i\psi^* \nabla_{el} \psi \} , \quad (4.6)$$

where the operator $\nabla_{el} \equiv \nabla$ acts only on the electron degree of freedom. For that purpose, we use Eqs. (4.2) and (4.3) to calculate

$$\psi^* = e^{-i\mathbf{k}\mathbf{r}} + \mathcal{T}^{\gamma, \alpha*}(\omega) \sum_{\mathbf{k}'} F^*(\mathbf{k}') \frac{e^{-i\mathbf{k}'\mathbf{r}}}{r} , \quad (4.7)$$

and

$$\nabla \psi = i\mathbf{k}e^{i\mathbf{k}\mathbf{r}} + \mathcal{T}^{\gamma, \alpha*}(\omega) \sum_{\mathbf{k}'} \left[i\mathbf{k}' F(\mathbf{k}') \frac{e^{i\mathbf{k}'\mathbf{r}}}{r} - F(\mathbf{k}') \frac{e^{i\mathbf{k}'\mathbf{r}}}{r^2} \hat{\mathbf{r}} \right] , \quad (4.8)$$

giving in total

$$\begin{aligned} \psi^* \nabla \psi &= i\mathbf{k} + \mathcal{T}^{\gamma, \alpha}(\omega) \sum_{\mathbf{k}'} \left[i\mathbf{k}' F(\mathbf{k}') \frac{e^{i(\mathbf{k}'-\mathbf{k})\mathbf{r}}}{r} - F(\mathbf{k}') \frac{e^{i(\mathbf{k}'-\mathbf{k})\mathbf{r}}}{r^2} \hat{\mathbf{r}} \right] + \\ &+ i\mathbf{k} \mathcal{T}^{\gamma, \alpha}(\omega) \sum_{\mathbf{k}''} F^*(\mathbf{k}'') \frac{e^{i(\mathbf{k}-\mathbf{k}'')\mathbf{r}}}{r} + |\mathcal{T}^{\gamma, \alpha}(\omega)|^2 \sum_{\mathbf{k}'\mathbf{k}''} i\mathbf{k}' F(\mathbf{k}') F^*(\mathbf{k}'') \frac{e^{i(\mathbf{k}'-\mathbf{k}'')\mathbf{r}}}{r^2} + \\ &- |\mathcal{T}^{\gamma, \alpha}(\omega)|^2 \sum_{\mathbf{k}'\mathbf{k}''} F(\mathbf{k}') F^*(\mathbf{k}'') \frac{e^{i(\mathbf{k}'-\mathbf{k}'')\mathbf{r}}}{r^3} \hat{\mathbf{r}} . \end{aligned} \quad (4.9)$$

We can immediately ignore the last term in Eq. (4.9) because it goes like r^{-3} . Furthermore, in general, the sum $\sum_{\mathbf{k}'} e^{i(\mathbf{k}'-\mathbf{k})\mathbf{r}}$ oscillates rapidly due to the nonlinearity of \mathbf{r} and $\mathbf{k}'(\mathbf{k})$, and as a result such terms are strongly suppressed and can be neglected. Thus, we can in addition neglect the second, third, and fourth terms in Eq. (4.9). Only the fifth term survives under the condition $\mathbf{k}' = \mathbf{k}''$ giving

$$\psi^* \nabla \psi \approx i\mathbf{k} + |\mathcal{T}^{\gamma, \alpha}(\omega)|^2 \sum_{\mathbf{k}'} i\mathbf{k}' \frac{|F(\mathbf{k}')|^2}{r^2} , \quad (4.10)$$

and yielding finally for the probability current

$$\mathbf{j} \approx \frac{\hbar}{m} \mathbf{k} + \frac{\hbar}{m} |\mathcal{T}^{\gamma, \alpha}(\omega)|^2 \sum_{\mathbf{k}'} \mathbf{k}' \frac{|F(\mathbf{k}')|^2}{r^2} . \quad (4.11)$$

The first term in Eq. (4.11) corresponds to the incident current \mathbf{j}_{in} , while the second term to the scattered current \mathbf{j}_{sc} .

4.1.3 Partial scattering cross sections

We are now finally in a position to calculate the electron scattering cross section. The number of particles crossing the area that subtend a solid angle $d\Omega$ at the origin (the impurity) is given by $\mathbf{j}_{sc} \cdot \hat{r} dA$, while the incident flux is simply $\mathbf{j}_{in} \cdot \hat{k}$. Therefore, the partial differential cross section in the γ, α scattering channel is given by

$$\frac{d\sigma^{\gamma,\alpha}(\varepsilon_\alpha)}{d\Omega} = \frac{\mathbf{j}_{sc} \cdot \hat{r} dA}{\mathbf{j}_{in} \cdot \hat{k} d\Omega} = |\mathcal{T}^{\gamma,\alpha}(\omega)|^2 \sum_{\mathbf{k}'} |F(\mathbf{k}')|^2 \frac{\mathbf{k}' \cdot \hat{r}}{k}. \quad (4.12)$$

Since the T -matrix is momentum independent, the anisotropy of the scattering cross section arises only due to the anisotropy of the Green's function $G_{r,1}^{(0)\gamma,\gamma}(\omega)$. This is in Eq. (4.12) manifested as a sum over different wave vectors \mathbf{k}' . However, we are mostly interested in the scattering of low-frequency electrons close to the bottom of the band, when $G_{r,1}^{(0)\gamma,\gamma}(\omega)$ may be approximated by its isotropic low-frequency form corresponding to the outgoing s wave. In particular, close to the bottom of the band the electron dispersion effectively becomes quadratic, $\varepsilon \approx tk^2$. This implies that there is only one \mathbf{k}' for a given \hat{r} and the two vectors are mutually collinear $\mathbf{k}' \cdot \hat{r} = k'$ [52]. Furthermore, $F(\mathbf{k}') \approx -\frac{a}{4\pi|t|}$, so the scattered current reduces to

$$\mathbf{j}_{sc} \approx \frac{\hbar}{m} \mathbf{k}' \frac{a^2}{16\pi^2 t^2} \frac{|\mathcal{T}^{\gamma,\alpha}(\omega)|^2}{r^2}, \quad (4.13)$$

and correspondingly the partial differential cross section in the γ, α scattering channel reads

$$\frac{d\sigma^{\gamma,\alpha}(\varepsilon_\alpha)}{d\Omega} = \frac{a^2}{16\pi^2 t^2} \frac{k'}{k} |\mathcal{T}^{\gamma,\alpha}(\omega)|^2, \quad (4.14)$$

being isotropic in real space. Note that the exact form of $G_{1,1}^{(0)\gamma,\gamma}(\omega)$ has to be kept in the isotropic $\mathcal{T}^{\gamma,\alpha}(\omega)$ nonetheless.

The partial cross section in the γ, α channel is now easily obtained by the integration over all solid angles

$$\sigma^{\gamma,\alpha}(\varepsilon_\alpha) = \int \frac{d\sigma^{\gamma,\alpha}(\varepsilon_\alpha)}{d\Omega} d\Omega = \frac{a^2}{4\pi t^2} \sqrt{\frac{\varepsilon_\gamma}{\varepsilon_\alpha}} |\mathcal{T}^{\gamma,\alpha}(\varepsilon_\alpha + \alpha\omega_0)|^2, \quad (4.15)$$

where ε_α and ε_γ satisfy the energy conservation law $\varepsilon_\alpha + \alpha\omega_0 = \varepsilon_\gamma + \gamma\omega_0$. As an example, we show in Fig. 4.1(a) the partial cross sections for several elastic and inelastic scattering channels as a function of the incoming electron energy ε_α . We set $a^2 = 1$, which is the area associated with a unit cell. The phonon frequency scale has its strong reflection in Fig. 4.1(a), similarly to the

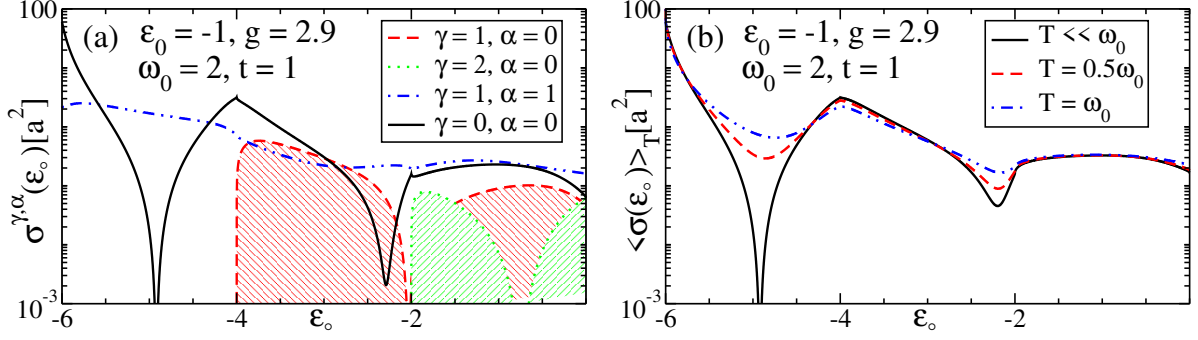


Figure 4.1: (a) Partial scattering cross sections for a few elastic and inelastic scattering channels and (b) the total scattering cross section as a function of the incoming electron energy ε_α for the system parameters $t = 1$, $\varepsilon_0 = -1$, $\omega_0 = 2$, and $g = 2.9$

energy dependence of the transmission coefficient in Fig. 3.1. In particular, ω_0 characterizes the energy thresholds for the inelastic scattering involving phonon emission ($\gamma > \alpha$) processes and governs to a great extent the energy-dependence of all $\sigma^{\gamma,\alpha}$. This is particularly prominent for low energies ε_α of the incoming electron, when $\sigma^{0,0}$ in Fig. 3.1 reaches very large values. Note that we have only shown the phonon emission channels in Fig. 3.1. This is so because phonon absorption channels are related to phonon emission channels by the time-reversal symmetry, $\mathcal{T}^{\gamma,\alpha}(\omega) = \mathcal{T}^{\alpha,\gamma}(\omega)$, that is, $\varepsilon_\gamma \sigma^{\gamma,\alpha}(\varepsilon_\alpha) = \varepsilon_\alpha \sigma^{\alpha,\gamma}(\varepsilon_\gamma)$.

4.1.4 Total scattering cross section

Similarly as in the tunneling problem, for the state of the system involving an incident electron with the energy ε_α and α phonons at the impurity site, the total cross section for the electron scattering is obtained by summing over all possible final states resulting from all the elastic and inelastic scattering processes, $\sum_\gamma \sigma^{\gamma,\alpha}(\varepsilon_\alpha)$. Moreover, for the system in the thermal equilibrium, the total cross section $\langle \sigma(\varepsilon_\alpha) \rangle_T$, as a function of the incident electron energy ε_α , is obtained by additionally averaging over the phonon thermal distribution $P(\alpha, T)$ for the initial number of phonons α , giving in total

$$\langle \sigma(\varepsilon_\alpha) \rangle_T = (1 - e^{-\omega_0/T}) \sum_{\alpha,\gamma} e^{-\alpha\omega_0/T} \sigma^{\gamma,\alpha}(\varepsilon_\alpha). \quad (4.16)$$

The total electron scattering cross section for the generic system parameters is shown in Fig. 4.1(b) for three different temperatures. As anticipated, for low temperatures the total scattering cross section for low energy electrons is determined solely by the $\sigma^{0,0}$ channel, prominently showing the resonant structure. However, as soon as electrons become more energetic, or as the temperature gets elevated, this resonant structure is smoothed, resulting in an almost constant cross section for all electrons.

4.2 Intermezzo: localized electron states

Although we have set up everything for the calculation of the electron relaxation time due to the scattering on polaronic impurities, in this Section 4.2 we slightly deviate from our main goal of calculating the electron mobility and exploit the developed formalism to consider the structure of localized electron states relevant for the energy-loss spectroscopy, atom-probe tomography, and scanning tunneling microscopy [53–56]. As is well known, in the presence of static impurities localized states may appear below or above the continuum of delocalized states [41]. The same is true with polaronic impurities, with an additional factor that the impurity is dynamic, so a much richer structure of localized states is generally anticipated in comparison to the simpler static case.

4.2.1 Scattering cross section dependence on impurity parameters

To gain an initial insight into the structure of localized electron states, it is sufficient to examine the scattering cross section of the lowest energy electron in dependence on impurity parameters describing the impurity strength. In the polaronic impurity model, those two parameters are ε_0 and g .

To be specific, we consider the zero temperature case, $T = 0$, when there are no thermally excited phonons present in the system ($\alpha = 0$) and assume that the electron occupies the lowest energy state of the band, $\varepsilon_\alpha = \varepsilon_B$. Consequently, the electron does not have enough energy to emit phonons, so the total scattering cross section for this electron is contributed only by the elastic 0, 0 channel

$$\sigma(\varepsilon_B) = \sigma^{0,0}(\varepsilon_B) = \frac{a^2}{4\pi t^2} |\mathcal{T}^{0,0}(\varepsilon_B)|^2 . \quad (4.17)$$

From Eq. (2.15), we have for the matrix element $\mathcal{T}^{0,0}(\varepsilon_B)$

$$\mathcal{T}^{0,0}(\varepsilon_B) = \frac{\Gamma^{0,0}(\varepsilon_B)}{1 - G_{1,1}^{(0)}(\varepsilon_B)\Gamma^{0,0}(\varepsilon_B)} , \quad (4.18)$$

where

$$\Gamma^{0,0}(\varepsilon_B) = \varepsilon_0 + gB_0(\varepsilon_B) . \quad (4.19)$$

Static case

It is instructive to consider first the static case with $g = 0$. Then $\Gamma^{0,0}(\varepsilon_B) = \varepsilon_0$ and

$$\mathcal{T}^{0,0}(\varepsilon_B) = \frac{\varepsilon_0}{1 - G_{1,1}^{(0)}(\varepsilon_B)\varepsilon_0}, \quad (4.20)$$

so the scattering cross section equals

$$\sigma(\varepsilon_B) = \frac{a^2}{4\pi t^2} \frac{\varepsilon_0^2}{\left|1 - G_{1,1}^{(0)}(\varepsilon_B)\varepsilon_0\right|^2} = \frac{a^2}{4\pi t^2} \frac{\varepsilon_0^2}{\left[1 - \operatorname{Re}G_{1,1}^{(0)}(\varepsilon_B)\varepsilon_0\right]^2 + \left[\operatorname{Im}G_{1,1}^{(0)}(\varepsilon_B)\varepsilon_0\right]^2}. \quad (4.21)$$

As the bottom of the band is approached, in the 3D case holds

$$\lim_{\omega \rightarrow \varepsilon_B} \operatorname{Im}G_{1,1}^{(0)}(\omega) = 0, \quad (4.22)$$

and the scattering cross section in Eq. (4.21) acquires the resonant behavior around the critical value ε_{cr} of the impurity parameter ε_0 defined by

$$1 - \operatorname{Re}G_{1,1}^{(0)}(\varepsilon_B)\varepsilon_{cr} = 0. \quad (4.23)$$

This pole of the scattering cross section indicates the appearance of a true localized state. The critical (minimal) value of the impurity strength for this localized state to appear is $\varepsilon_{cr} = \frac{1}{|\operatorname{Re}G_{1,1}^{(0)}(\varepsilon_B)|}$. In particular, for the 3D simple cubic lattice this criterion gives $\varepsilon_{cr} \approx 4|t|$, which almost perfectly matches the reported value in [57]. Contrary, in 1D and 2D cases $|\operatorname{Re}G_{1,1}^{(0)}(\varepsilon_B)| \rightarrow \infty$ and the localized state emerges for an arbitrary weak impurity. In any case, it is important to note that one and only one ε_{cr} may solve Eq. (4.23), so one static impurity may result in maximally one localized state.

Dynamic case

As we shall now argue, this situation changes with the inclusion of the finite electron-phonon coupling. In the weak coupling limit, we can expand the local operator $\hat{\Gamma}$ in the powers of g and keep only the lowest order terms. The first correction in g of $\Gamma^{0,0}(\varepsilon_B)$ reads

$$\Gamma^{0,0}(\varepsilon_B) \approx \varepsilon_0 + g^2 G_I(\varepsilon_B - \omega_0), \quad (4.24)$$

resulting in a somewhat more complicated form for the scattering cross section

$$\sigma(\varepsilon_B) = \frac{a^2}{4\pi t^2} \frac{|\varepsilon_0 + g^2 G_I(\varepsilon_B - \omega_0)|^2}{\left|1 - G_{1,1}^{(0)}(\varepsilon_B) [\varepsilon_0 + g^2 G_I(\varepsilon_B - \omega_0)]\right|^2}. \quad (4.25)$$

In principle, the scattering cross section acquires two new qualitative features due to the introduction of the electron-phonon interaction. First, because of the form of the denominator, Eq. (4.25) may exhibit more than one pole, which potentially results in the appearance of many localized states. Generally, as the electron-phonon coupling increases, the increasing number of contributions to $\Gamma^{0,0}(\varepsilon_B)$ has to be kept, leading to the increasing number of localized states. Secondly, for certain impurity parameters, concretely those corresponding to the zeros of $\Gamma^{0,0}(\varepsilon_B)$, the numerator of Eq. (4.25) may vanish as well. As we will later show, for those impurity parameters the electron mobility diverges and the polaronic impurity appears fully transparent for the propagating electron.

4.2.2 Local density of states

The above analysis based on poles of the scattering cross section showed us, without the need for any computational effort, that many localized electron states may appear in the presence of a polaronic impurity. In order to gain deeper insights into the precise structure of those localized electron states, we further investigate local electron properties.

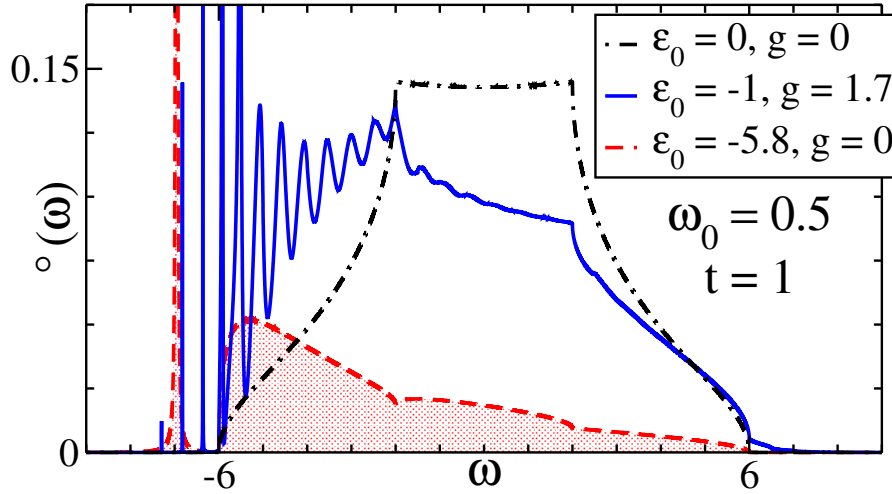


Figure 4.2: Exact LDoS at the impurity site for different polaronic impurity parameters.

The suitable quantity for studying in detail the local electron properties, in particular the localized electron states, is the local density of states (LDoS) defined by

$$\rho(\omega) = -\pi^{-1} \text{Im} G_{11}^{0,0}(\omega) . \quad (4.26)$$

$G_{11}^{0,0}(\omega)$ can be straightforwardly computed by means of the Dyson equation given by Eq. (2.14) for $\mathbf{m} = 1$ and $\alpha = 0$, and the easily attainable matrix element $\Gamma^{0,0}$. In order to discuss the properties of LDoS in the presence of the polaronic impurity, we show in Fig. 4.2 the exact $\rho(\omega)$ for three different impurity parameter sets. In particular, with the dot-dashed black curve, the LDoS for the unperturbed electron is shown. It exhibits the $\rho(\omega) \propto \sqrt{\omega}$ behavior near the band's

edges, $|\omega| \sim 6$, and the Van Hove singularities, as is expected for the 3D simple cubic lattice. By introducing the (attractive) static impurity, much of the LDoS, shown with the red dashed line, is shifted toward the bottom of the band. Since for the chosen parameters the impurity is strong enough, $\varepsilon_0 = -5.8 > \varepsilon_{cr}$, for a localized state to appear, we readily observe the localized state as a resonance below the continuum, $\omega < -6$.

The most interesting is, however, the case with the strong electron-phonon coupling $g = 1.7$, $\varepsilon_0 = -1$. It is evident that the corresponding LDoS, shown by the full blue curve in Fig. 4.2, exhibits multiple resonances below the continuum, corresponding to multiple localized states. Although this is not fully apparent from Fig. 4.2, the differences in energies of localized states closer to the continuum are weakly softened in comparison to the bare phonon energy ω_0 . This points to the anharmonicity effects, which are weaker for the deep localized states. These harmonic deep localized states involve large lattice deformations because of which the electron is heavily dressed. Consequently, the corresponding electron spectral weight is strongly suppressed in comparison to electron spectral weights of shallow states just below the continuum, suggesting the weakening of dressing effects for states closer to the continuum.

The phonon nature of the impurity also greatly affects the continuum of electron states, the energy region $-6 \leq \omega \leq 6$ in Fig. 4.2. In particular, similarly to the transmission coefficient in Fig. 3.1 and the scattering cross section in Fig. 4.1, we observe alternate occurrences of minima and maxima of the LDoS, with the alternation dictated by the phonon energy ω_0 . Although broadened due to being embedded in the continuum of delocalized states, these maxima are still well defined, giving rise to the resonant scattering of electrons on the impurity. In other words, although the corresponding electrons are delocalized, they spent a significantly large amount of time in the vicinity of the impurity site.

Number of localized states

It is by now quite obvious that the specific structure of localized states heavily depends on the impurity parameters. Consequently, it is a tedious task to analyze distinct properties of the LDoS in the whole parametric space. However, the thing which is both instructive and fairly easy to implement is the counting of the number of localized states in dependence on the impurity strength parameters, ε_0 and g . For that purpose, we have developed an algorithm that counts the maxima below the continuum in the LDoS, providing the number of resonances, that is, the number of localized states.

For our customary choice of parameters, $t = 1$ and $\omega_0 = 0.5$, the number of localized states in dependence on the impurity strength, ε_0 and g , is shown as a contour plot in Fig. 4.3. The region without localized states is denoted with black color, while regions get brighter as the number of localized states increases. As expected, in the static case, $g = 0$, no localized states exist for a weak impurity, $|\varepsilon_0| < |\varepsilon_{cr}| \approx 4$. However, the critical value ε_{cr} softens as soon as

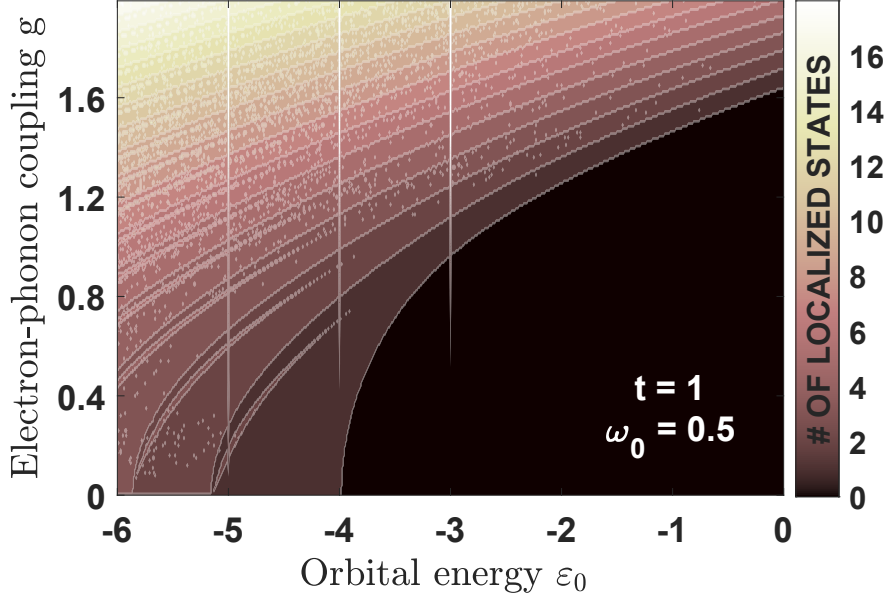


Figure 4.3: The number of localized states in dependence on the impurity strength parameters, ε_0 and g , for $t = 1$ and $\omega_0 = 0.5$.

the electron-phonon coupling is included, $|\varepsilon_{cr}(g \neq 0)| < |\varepsilon_{cr}(g = 0)|$, suggesting that phonons assist the static impurity to localize an electron. Eventually, for values of the electron-phonon coupling exceeding the critical value $g_{cr} \sim 1.6$, phonons alone ($\varepsilon_0 = 0$) are able to localize the electron.

As we have shown in Subsection 4.2.1, the presence of a single static impurity may result in maximally one localized state. This is no longer true even for very small, but finite electron-phonon couplings. In particular, for finite g , by increasing $|\varepsilon_0|$ additional localized states appear above some threshold values ε_{cr_i} , as can be clearly seen from Fig. 4.3.

Similarly, the appearance of localized states may be initiated by raising the electron-phonon coupling strength above threshold values g_{cr_i} for some fixed ε_0 . In that regard, it is interesting to note that the electron-phonon coupling is much more efficient in producing localized electron states than the impurity orbital energy. In other words, in order to increase the number of localized states by one, the relative change in the electron-phonon coupling strength may be smaller than the relative change in the impurity orbital energy, $|g_{cr_i} - g_{cr_{i+1}}| < |\varepsilon_{cr_i} - \varepsilon_{cr_{i+1}}|$, at least for the parameter space shown in Fig. 4.3.

4.3 Electron mobility

We head back to our main objective of calculating the electron mobility for non-degenerate electrons in the presence of polaronic impurities. Henceforth, we assume that the concentration of impurities n_i is dilute and that they are randomly distributed, so that correlation effects due

to the scattering by multiple different impurities may be neglected. In such cases, the total scattering cross section (due to all impurities) may be simply obtained as a product $n_i \langle \sigma(\varepsilon_\alpha) \rangle_T$, where $\langle \sigma(\varepsilon_\alpha) \rangle_T$ is the scattering cross section due to a single impurity given by Eq. (4.16).

With the total scattering cross section known, it is now trivial to obtain the electron mean free path, $l^{-1}(\varepsilon_\alpha, T) = n_i \langle \sigma(\varepsilon_\alpha) \rangle_T$, and the electron relaxation time

$$\tau^{-1}(\varepsilon_\alpha, T) = l^{-1}(\varepsilon_\alpha, T) v_\alpha = n_i \langle \sigma(\varepsilon_\alpha) \rangle_T v_\alpha , \quad (4.27)$$

where $v_\alpha = \frac{a}{\hbar} \sqrt{4t\varepsilon_\alpha}$ is the velocity of the incident electron situated near the bottom of the band, which in turn can be exploited to calculate the mobility for non-degenerate electrons [58], such as electrons in weakly doped semiconductors

$$\mu(T) = \frac{|e|}{m_{el}} \frac{2}{3k_B T} \int \varepsilon^{\frac{3}{2}} \tau(\varepsilon, T) e^{-\varepsilon/k_B T} d\varepsilon \Big| \int \varepsilon^{\frac{1}{2}} e^{-\varepsilon/k_B T} d\varepsilon . \quad (4.28)$$

Here, it should be stressed that we assume that polaronic impurities are the only source of electron scatterers. With additional types of relaxation processes included, we may use Matthiessen's rule [40] to account for the total relaxation time.

4.3.1 Static case

It is again instructive to consider the static case, $g = 0$, first. Then, as we have already discussed in Subsection 4.2.1, the temperature independent total scattering section is contributed only by the 0, 0 channel

$$\sigma(\varepsilon_\alpha) = \sigma^{0,0}(\varepsilon_\alpha) = \frac{a^2}{4\pi t^2} |\mathcal{T}^{0,0}(\varepsilon_\alpha)|^2 , \quad (4.29)$$

with

$$\mathcal{T}^{0,0}(\varepsilon_\alpha) = \frac{\varepsilon_0}{1 - G_{11}^{(0)}(\varepsilon_\alpha)\varepsilon_0} . \quad (4.30)$$

Weak impurity

Specifically, for a weak impurity, $|\varepsilon_0| \ll 1$, the T -matrix is particularly simple, $\mathcal{T}^{0,0} \approx \varepsilon_0$, leaving the total scattering cross section both temperature and energy independent

$$\sigma = \frac{a^2}{4\pi t^2} \varepsilon_0^2 = \text{const} . \quad (4.31)$$

In such circumstances, the temperature independent relaxation time has a trivial energy dependence, $\tau^{-1}(\varepsilon_\alpha) \propto \sqrt{\varepsilon_\alpha}$, coming from the electron velocity, and the expression for the mobility

in Eq. (4.28) reduces to

$$\mu(T) \propto \frac{1}{k_B T} \int \varepsilon_\alpha e^{-\varepsilon_\alpha/k_B T} d\varepsilon_\alpha \Big| \int \varepsilon_\alpha^{\frac{1}{2}} e^{-\varepsilon_\alpha/k_B T} d\varepsilon_\alpha . \quad (4.32)$$

While evaluating the integrals in Eq. (4.32), we can set the upper limits of integrations to $+\infty$ since we are only interested in the states near the bottom of the band. The two integrations then give [59]

$$\int_0^{+\infty} \varepsilon e^{-\varepsilon/k_B T} d\varepsilon = (k_B T)^2 , \quad (4.33)$$

and

$$\int_0^{+\infty} \varepsilon^{\frac{1}{2}} e^{-\varepsilon/k_B T} d\varepsilon = \frac{\sqrt{\pi}}{2} (k_B T)^{\frac{3}{2}} , \quad (4.34)$$

resulting in the simple power-law behavior of mobility with temperature

$$\mu(T) \propto T^{-\nu} , \quad \text{with } \nu = \frac{1}{2} . \quad (4.35)$$

Vacancy/infinite barrier case

It is also worth commenting on the opposite case of an infinitely strong impurity, $|\varepsilon_0| \rightarrow \infty$, when the impurity acts as a vacancy/infinite barrier. In that case, the T -matrix in Eq. (4.30) approximately equals

$$\mathcal{T}^{0,0}(\varepsilon_\alpha) \approx -\frac{1}{G_{1,1}^{(0)}(\varepsilon_\alpha)} \approx -\frac{1}{G_{1,1}^{(0)}(\varepsilon_\alpha \approx 0)} , \quad (4.36)$$

where we have exploited the fact that near the bottom of the band $[G_{1,1}^{(0)}(\varepsilon_\alpha)]^{-1}$ does not vary much. Consequently, the scattering cross section is again energy independent and the mobility follows the power-law behavior in Eq. (4.35), the same as in the weak impurity case.

Reference value for mobility

We find it particularly convenient to exploit the vacancy/infinite barrier problem to set the reference value for mobility. In particular, in that special case, with the use of Eqs. (4.27), (4.28), (4.29), and (4.36), we have

$$\mu_V(T) = \frac{|e|}{m_{el}} \frac{4\pi\hbar t^2 |G_{1,1}^{(0)}(\varepsilon_\alpha = 0)|^2}{n_i \alpha^3 \sqrt{4t}} \frac{2}{3k_B T} \int \varepsilon e^{-\varepsilon/k_B T} d\varepsilon \Big| \int \varepsilon^{\frac{1}{2}} e^{-\varepsilon/k_B T} d\varepsilon , \quad (4.37)$$

where we have recovered \hbar , a , and k_B . With the results in Eqs. (4.33) and (4.34), and the expression for the effective mass $m = \frac{\hbar^2}{2ia^2}$, Eq. (4.37) gives

$$\mu_V(T) = \frac{16\sqrt{\pi}}{3} \frac{|e|}{\hbar n_i a} t^{\frac{3}{2}} |G_{1,1}^{(0)}(\varepsilon_\alpha = 0)|^2 (k_B T)^{-\frac{1}{2}}. \quad (4.38)$$

Finally, to define the reference value μ_0 , we evaluate the mobility in Eq. (4.38) at the temperature corresponding to the phonon energy, $k_B T = \hbar \omega_0$. Specifically, for the choice of parameters $a = 1\text{\AA}$, $n_i = (10a)^{-3}$, and $t = 2\omega_0 = 1\text{eV}$, we have

$$\mu_0 \equiv \mu_V(k_B T = \hbar \omega_0) = 1093.570337 \times \frac{|e|a^2}{\hbar} \approx 166.14 \frac{\text{cm}^2}{\text{Vs}}. \quad (4.39)$$

4.3.2 Dynamic case

As soon as the electron-phonon coupling g is turned on, such closed-form expressions for the temperature dependence of the mobility generally become too inconvenient to be analyzed analytically. Therefore, for cases with the finite electron-phonon coupling, we evaluate numerically the mobility in Eq. (4.28), with scattering cross sections/relaxation times calculated exactly within the formalism developed in Chapters 2 and 4.

Temperature dependence

The polaronic impurity parameters may largely differ from one real material to another, affecting the mobility differently over a wide temperature range. Here, we are mostly interested in the temperature regime, $T \leq \omega_0$, for which thermally activated scattering processes on acoustical phonons, that frequently dominate at higher temperatures, may not be so prominent as the effects coming from polaronic impurities. In particular, we show in Fig. 4.4 the temperature dependence of the mobility in the log-log scale for three sets of parameters. The case with the weak electron-phonon coupling, $g/\omega_0 \ll 1$, is shown with the full green line. Evidently, the corresponding mobility shows the power-law behavior, $\mu(T) \propto T^{-\nu}$, in a wide range of temperatures, further supported by the fit, $\log \mu(T) = -\nu \log T + C$, yielding $\nu = \frac{1}{2}$, similarly as in the case with the weak static impurity. This behavior can be rationalized by noting that for weak couplings g the scattering cross section is mainly dominated by the $\sigma^{0,0}$ channel, which is in turn almost energy independent, similarly as it was in the purely static case.

More interesting cases are, however, cases with strong electron-phonon couplings. In order to probe the mobility in the strong coupling regime, we have fixed the ratio $g/\omega_0 = 1.45$ and considered two different phonon energies, $\omega_0 = 0.5$ and $\omega_0 = 2$. The temperature dependence of mobility for those two choices of ω_0 is shown in Fig. 4.4 with the dot-dashed blue line and the dashed red line, respectively. Although the corresponding mobility shows a more complex

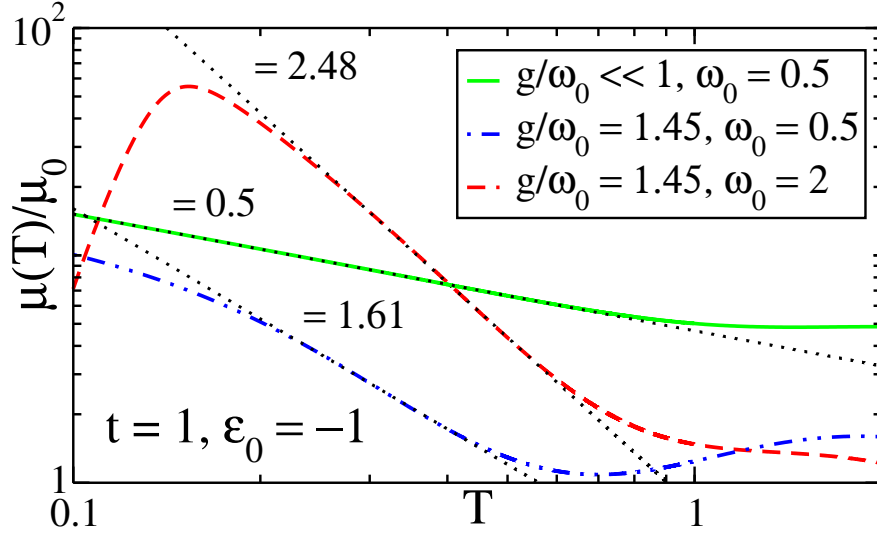


Figure 4.4: Mobility $\mu(T)$ as a function of temperature for different couplings g shown in the log-log scale. Fits $\log \mu(T) = -\nu \log T + C$ are shown with the dashed lines.

temperature dependence than in the weak coupling case, we note that in the relevant temperature range, $0.2 \leq T \leq 0.5$, they again exhibit the power-law behavior. However, the fits now give $\nu = 1.61$ and $\nu = 2.48$ for the case with $\omega_0 = 0.5$ and $\omega_0 = 2$, respectively. As it seems, those unconventional power-law behaviors are always present, albeit highly non-universal. In other words, the coefficient ν is highly sensitive to impurity parameters. The scattering on polaronic impurities thus may serve as a possible explanation for the broad range of power-law exponents observed experimentally in various organic crystals [30–32]. It is worth commenting that the two cases with $g/\omega_0 = 1.45$, for which the unconventional power-law behaviors are observed, fall into the highly non-perturbative regime for which the total scattering cross section is contributed by many different scattering channels γ, α . Namely, it implies contributions from processes described by many high-order diagrams, with many different scattering channels and partial cross sections becoming increasingly important upon increasing the temperature.

Lastly, regarding the temperature dependence of mobility, we note that the power-law behavior is generally followed by a weak upturn of mobility at elevated temperatures. It is important to realize that this is not the effect of the phonon nature of the impurity, but rather a consequence of the slight energy dependence of the scattering cross section. Namely, at elevated temperatures higher energy states also contribute to the scattering cross section, resulting in the observed upturn.

Sensitivity of mobility on impurity parameters

As our last remark to the polaronic impurity problem, we consider in Fig. 4.5 the sensitivity of mobility on impurity parameters ε_0 and g (inset) for three different temperatures. We immediately note that all singularities are sensitive to the electron incident energy and get

averaged out at elevated T . In particular, as T approaches ω_0 in Fig. 4.5, thermal averages in Eqs. (4.16) and (4.28) make μ a smooth function of impurity parameters.

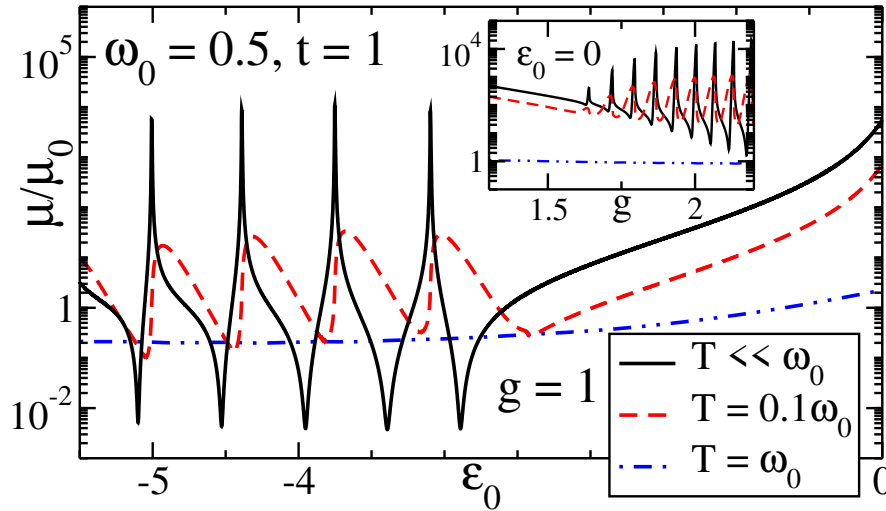


Figure 4.5: Mobility $\mu(T)$, shown in the lin-log scale, as a function of ε_0 and g (inset).

We therefore focus only on the low-temperature case, $T \ll \omega_0$, shown with the full black line in Fig. 4.5. The structure of the corresponding mobility is very rich, showing multiple minima and maxima as the impurity parameters are varied. In particular, when the model parameters satisfy resonant scattering conditions, μ drops sharply, corresponding to a large residual resistivity due to a strong relaxation of electron momenta. For the same model parameters, the scattering cross section diverges, indicating the appearance of localized states. By comparing values of ε_i for which the mobility takes minimum values in Fig. 4.5, we note that they roughly match the values ε_{cr_i} for which localized states appear in Fig. 4.3 for the fixed $g = 1$. The same holds for $\varepsilon_0 = 0$ and the critical values of g_{cr_i} , shown in the inset of Fig. 4.3. Between the two minima, the divergences of the mobility are fully apparent as well. This behavior stems from zeros of $\mathcal{T}^{0,0} \propto \Gamma^{0,0}$ and indicates a fully transparent behavior of polaronic impurities for some fine-tuned model parameters.

4.4 Conclusions

We exploit the exact solution of the polaronic impurity model in Eq. (2.1) to exactly solve the problem of electrons in 3D weakly doped semiconductors strongly scattered by polaronic impurities, which concentration is assumed to be low. Similarly like the electron transmission, the electron scattering cross section as a function of the incident electron energy shows multiple minima and maxima governed by the phonon energy scale. The rich resonant structure of the electron scattering cross section is also apparent when it is analyzed as a function of impurity parameters at low temperatures. These resonances point to the appearance of localized electron

states, which exact structure, studied by the local density of states, heavily depends on impurity parameters. Generally, for strong electron-phonon couplings, many localized electron states appear, which is in sharp contrast with the case of a static impurity when only one localized state may emerge. By calculating the total scattering cross section, including all elastic and inelastic scattering processes, the electron relaxation time and the electron mobility are obtained. The temperature dependence of the electron mobility shows the power-law dependence, with the exponent being highly sensitive to impurity parameters. The latter may explain unconventional power-law exponents observed experimentally in organic semiconductors. This is a highly non-perturbative effect for which a large number of scattering channels γ, α calculated in very high orders has to be taken into account. We also note that for some specific impurity parameters the low-temperature electron mobility diverges, indicating the possibility of a fully transparent behavior of polaronic impurities.

Part II

Perturbative approach to the polaron problem

The polaron concept

In the next two Parts II and III of the thesis, we restore the translational invariance of a lattice by considering the electron-phonon coupling at every lattice site. Our main goal is to address two aspects of the translationally invariant electron-phonon system. First, we go beyond the leading order of the perturbation theory in electron-phonon interaction to study both electron and phonon properties, putting a special emphasis on the role of vertex corrections. Second, we aim to understand peculiarities and find the correct perturbative treatment of the translationally invariant electron-phonon system for very different electron density cases. In particular, in Part II we consider the situation when the electron density is so low that each electron may be treated independently - the problem known as the polaron problem, while cases with finite electron densities are left to be discussed in Part III.

The notion of polaron was first introduced by Landau back in 1933 [60], attributed to an electron trapped by a polarizable lattice deformation. Since then, the concept of polaron was generalized to describe any single quantum degree of freedom interacting with a bath of bosons. For example, we can mention ripplons, identified with a self-trapped electron on a surface deformation of liquid ^4He (rippion) [61–63], angulons as quantum rotors dressed by a quantum bose field [64, 65], and Bose polarons describing a mobile impurity strongly interacting with a surrounding Bose-Einstein condensate [66, 67]. In particular, the latter gained a lot of attention in the past years due to the experimental realizations in ultracold atom systems [68, 69]. However, from the whole zoo of polaron quasiparticles that emerged during the past 90 years, in this thesis, we put focus on the polaron problem in the spirit of Landau’s seminal work. That is, we analyze the problem of a single electron interacting with a single phonon mode.

5.1 Relevance of polaronic physics

Before we introduce the polaron model Hamiltonian and start with the showcase of our contributions to polaron physics, we want to emphasize its invaluable importance stemming from the growing number of experimental evidence of polaronic effects in a great variety of materials. It is by now well established that in some conventional ionic and covalent materials, like KCl and GaAs, the electron-phonon interaction accounts for the renormalized inertial mass of electrons due to the surrounding cloud of phonons influencing their motion [70]. Colossal magnetoresistance in transition metal manganites is also believed to be a consequence of po-

laronic effects [71–74], supported by the thermally activated hopping reported in manganites films [75] originating from the small polaron physics. Peculiarities of transport properties of some quasi-1D systems [76–82] exhibiting the Peierls instability [83], particularly conductive polymers, are argued to be of polaronic (soliton) origins as well. Apart from transport, polaronic effects also greatly influence the spectral properties of materials. One of the greatest hallmarks of polaronic correlations is the occurrence of phonon sidebands in ARPES measurements of transition metal oxides [84–87]. Last but not least, the open question remains whether and to what extent polaronic effects shape the puzzling phase diagrams of unconventional superconductors like cuprates [88]. Indeed, there exist several indications that the electron-phonon interaction plays an important role in the physics of cuprates [89–94]. In addition, it is worth mentioning that Alexandrov and Mott proposed a theory of high-temperature superconductivity based solely on the electron-phonon interaction in terms of the Bose-Einstein condensate of small bipolaronic states [95]. However, despite the great theoretical and experimental effort invested in understanding the properties of cuprate materials, their anomalous behaviors and the role of electron-phonon interaction is far from understood.

5.2 Model Hamiltonian

The model Hamiltonian which captures the main essences of the polaron problem is given by

$$\hat{H} = \sum_{\mathbf{k}} \varepsilon_{\mathbf{k}} c_{\mathbf{k}}^{\dagger} c_{\mathbf{k}} + \sum_{\mathbf{k}} \omega_{\mathbf{k}} a_{\mathbf{k}}^{\dagger} a_{\mathbf{k}} + \sum_{\mathbf{k}, \mathbf{q}} \frac{g(\mathbf{k}, \mathbf{q})}{\sqrt{N}} c_{\mathbf{k}+\mathbf{q}}^{\dagger} c_{\mathbf{k}} \left(a_{-\mathbf{q}}^{\dagger} + a_{\mathbf{q}} \right). \quad (5.1)$$

Here, the operator $c_{\mathbf{k}}^{\dagger}$ ($c_{\mathbf{k}}$) creates (annihilates) an electron with a momentum \mathbf{k} and an energy $\varepsilon_{\mathbf{k}}$, while the operator $a_{\mathbf{k}}^{\dagger}$ ($a_{\mathbf{k}}$) creates (annihilates) a phonon with a momentum \mathbf{k} and a frequency $\omega_{\mathbf{k}}$. The electron-phonon coupling is described by the last term of the Hamiltonian, characterized by an electron-phonon matrix element $g(\mathbf{k}, \mathbf{q})/\sqrt{N}$, where N is the number of lattice sites. Throughout the thesis, we will mostly consider scenarios where electrons couple to an optical phonon, which frequency can be approximated by a constant, $\omega_{\mathbf{k}} = \omega_0$.

There are two frequently used electron-phonon matrix elements used in theoretical studies. The first one implies that the electron-phonon interaction is long-ranged

$$g(\mathbf{k}, \mathbf{q}) = g(\mathbf{q}) \propto \frac{1}{\sqrt{q^{D-1}}}, \quad (5.2)$$

which identifies the model in Eq. (5.1) with the Fröhlich model, where D is a dimension of a system. The second choice, known in the literature as the Holstein coupling, corresponds to the momentum-independent electron-phonon interaction

$$g(\mathbf{k}, \mathbf{q}) = g, \quad (5.3)$$

describing the short-range interaction in real space. It is worth noting that the Holstein model can be interpreted as a strongly screened Fröhlich model. Thus, we can argue that by considering the Holstein model, screening effects are *a priori* taken into account.

5.3 Categorization of polarons

Despite the apparent simplicity of the Hamiltonian in Eq. (5.1), its solution cannot be obtained in a closed form. Consequently, one can find various nomenclatures and classifications of polarons in the literature, among which we highlight [96] as the most systematic and detailed. For example, some of the classifications include large and small polarons, adiabatic and antiadiabatic regimes, delocalized and self-trapped polarons, and weak and strong coupling regimes, albeit it is not always clear what is the connection between those different classifications of polarons/regimes in terms of the Hamiltonian's parameters. Moreover, discrepancies even exist between the interpretation of polaron states within the same classification. As an example, large and small polarons are sometimes identified with the extended and localized (in space) lattice deformation following an electron motion, respectively. Alternatively, the large polaron is also defined as a quasiparticle that almost freely travels through a crystal, while the notion of small polaron is reserved for the case when the polaron hopping to neighboring lattice sites is very small. In order to avoid any misinterpretations which may result due to the ambiguities related to the polaron physics nomenclature, in the following, we present an (over)simplified classification of polarons that will be used in this thesis.

The parametric space of the model in Eq. (5.1) with the Holstein coupling is spanned by three energy scales: a hopping integral t , characterizing the electron dispersion $\varepsilon_{\mathbf{k}}$, the phonon frequency ω_0 , and the electron-phonon coupling strength g . One of them can always be set as a unit of energy, resulting in two independent dimensionless constants governing the categorization of polarons

$$\kappa = \frac{\omega_0}{t}, \quad \lambda = \frac{g^2}{t\omega_0}. \quad (5.4)$$

The parameter κ is usually used to define different adiabaticity regimes. Analogously, here we identify $\kappa \ll 1$ with the adiabatic and $\kappa \gg 1$ with the antiadiabatic regime. We note that in a more detailed categorization [96] the adiabaticity of polarons actually depends on the electron-phonon coupling strength as well, which we do not take into account here.

Regarding the coupling strength, following Eq. (5.4), it would be natural to further classify polarons based on the parameter λ . However, here we rather exploit the electron-phonon coupling

strength g to simply associate the weak coupling regime, $g \ll 1$, and the strong coupling regime, $g \gg 1$, with the notion of large and small polarons, respectively. This is motivated by the paper [97], where the parameter g was used to distinguish light delocalized polaron states and heavy self-trapped polaron states characterized by the exponentially large effective mass. The former is expected for $g < g_c$, while the latter for $g > g_c$, where g_c is the critical point of self-trapping

$$g_c = \omega_0 + \sqrt{t\omega_0}. \quad (5.5)$$

Without going into further details, our oversimplified classification of polaron states distinguishes only large ($g \ll 1$) and small ($g \gg 1$) polarons, and adiabatic ($\kappa \ll 1$) and antiadiabatic ($\kappa \gg 1$) regimes. It is just worth adding that there exists no phase transition but rather a smooth crossover from large to small polarons in the Holstein model as the coupling strength increases, at least for non-zero phonon frequencies $\omega_0 \neq 0$ [98, 99].

5.4 Theoretical approaches to the polaron problem

Throughout the years, various theoretical techniques, with more or less success, were used to address the polaron problem. For weak and strong electron-phonon coupling regimes, analytical schemes based on the (mostly leading order) perturbation theory gave an initial insight into the polaron physics [40], albeit failed to correctly account for the polaron properties in the intermediate coupling regime. This motivated the adaptation of other approaches to the polaron problem like various variational methods [100, 101], exact (numerical) diagonalization [102], or density matrix renormalization group [103] in order to fill the gap between the weak and the strong electron-phonon coupling cases. Among the non-perturbative computational approaches, we especially highlight Diagrammatic Quantum Monte Carlo simulations [104, 105], which were shown to be very fruitful in studying the polaron problem due to the absence of fermion sign problem [106]. As an example, they were successfully applied to calculate very accurately the optical conductivity [107] and the mobility [108] of polarons for all coupling strengths.

5.4.1 DMFT of polarons - bridging the gap between the polaronic impurity and the polaron problem

One more non-perturbative approach which was shown to be very insightful is the dynamical mean field theory (DMFT) of polarons [109]. We have singled it out from other approaches since it shares a deep connection with the polaronic impurity problem, which we have exactly solved in Part I.

In particular, in the DMFT of polarons one may lift off with the exact solution of the polaronic

impurity model, albeit considering only diagonal matrix elements $\Gamma^{\alpha,\alpha}(\omega)$ in Eq. (2.32) with $\varepsilon_0 = 0$. Specifically, at zero temperature, it is enough to keep only $\Gamma^{0,0}(\omega) \equiv \Sigma^{(0)}(\omega)$, corresponding to the momentum-independent electron self-energy. The translational invariance of the problem, that is of the electron propagator, is then obtained by treating all lattice sites on equal footing by using the self-energy $\Sigma^{(0)}(\omega)$ [110]

$$\mathbf{G}_{\mathbf{i},\mathbf{j}}^{(0)}(\omega) = G_{\mathbf{i},\mathbf{j}}^{(0)}(\omega) + \Sigma^{(0)}(\omega) \sum_{\mathbf{r}} G_{\mathbf{i},\mathbf{r}}^{(0)}(\omega) \mathbf{G}_{\mathbf{r},\mathbf{j}}^{(0)}(\omega). \quad (5.6)$$

The propagator $\mathbf{G}_{\mathbf{i},\mathbf{j}}^{(0)}(\omega)$ is equal [111] to the electron propagator derived in the context of the momentum averaging approximation [112, 113]. In particular, it involves only the processes for which the phonons occupy just one lattice site at the same time [110].

The next step of the DMFT is to iteratively use Eq. (2.32) to account also for other processes involving multiple lattice sites. To be specific, in the n -th step of the iteration one determines the new local propagator

$$\mathcal{G}_{\mathbf{l},\mathbf{l}}^{(n)}(\omega) = G_{\mathbf{l},\mathbf{l}}^{(0)}(\omega) + \Sigma^{(n-1)}(\omega) \sum_{\mathbf{r} \neq \mathbf{l}} G_{\mathbf{l},\mathbf{r}}^{(0)}(\omega) \mathcal{G}_{\mathbf{r},\mathbf{j}}^{(n)}(\omega). \quad (5.7)$$

Such a propagator prevents the double counting of diagrams [114]. Now, this new local propagator can be utilized to calculate $\Sigma^{(n)}(\omega)$ by means of Eq. (2.32), which in turn gives the polaron Green's function in the n -th iteration

$$\mathbf{G}_{\mathbf{i},\mathbf{j}}^{(n)}(\omega) = G_{\mathbf{i},\mathbf{j}}^{(0)}(\omega) + \Sigma^{(n)}(\omega) \sum_{\mathbf{r}} G_{\mathbf{i},\mathbf{r}}^{(0)}(\omega) \mathbf{G}_{\mathbf{r},\mathbf{j}}^{(n)}(\omega). \quad (5.8)$$

This procedure is commonly repeated until the self-consistency condition

$$\left[\mathcal{G}_{\mathbf{l},\mathbf{l}}^{(n)}(\omega) \right]^{-1} = \left[\mathbf{G}_{\mathbf{l},\mathbf{l}}^{(n)}(\omega) \right]^{-1} + \Sigma^{(n)}(\omega), \quad (5.9)$$

is achieved.

Despite the many high-order processes taken into account by the DMFT, it gives an approximate solution to the polaron problem, so it is worth knowing its limitations. Following the arguments presented in [110], the DMFT cannot account for vertex corrections that involve more than one lattice site, which is in accordance with the local nature of the momentum-independent self-energy $\Sigma^{(n)}(\omega)$. However, it becomes that in the limit of infinite dimensional system the self-energy is purely local [109] and correspondingly the DMFT provides the exact solution for that case, with non-local vertex contributions becoming increasingly important with reducing the dimensionality of the system. Moreover, it was also argued [110] that non-local vertex corrections become irrelevant as the adiabaticity parameter $\kappa = \omega_0/t$ increases, rendering the DMFT generally suitable in the antiadiabatic regime. This provides us a clear motivation to study

in more depth the role and properties of vertex corrections in the polaron problem, especially for systems with reduced dimensionality, depending on the adiabaticity parameter.

Electronic properties of polarons

In this Chapter 6, we analyze the polaron problem through the lens of the electron degree of freedom. In particular, we consider the propagation of an electron injected in an otherwise empty band in the presence of the Holstein coupling. Similarly as in the polaronic impurity problem, in that special case, the ground state in Eq. (1.1) contains zero electrons, which allows us to draw all Feynman diagrams in terms of fermion propagators involving only the electron propagation, represented by the dashed line in Fig. 1.1(c). Correspondingly, in all calculations, we may keep only the electron part of the unperturbed fermion Green's function

$$G_0^+(\mathbf{k}, E) = \frac{1}{E - \xi_{\mathbf{k}} + i\eta}. \quad (6.1)$$

Motivated by the discussion in Chapter 5, specifically in Subsection 5.4.1, we are eager to analyze how the (non-)locality of the self-energy manifests in the perturbation theory for low-dimensional systems. Therefore, we put focus on the 1D case with the electron dispersion $\varepsilon_k = 2t(1 - \cos k)$ (with the lattice constant $a = 1$ and $\mathbf{k} \equiv k$), such that the bottom of the band is at $\varepsilon_{k=0} = 0$ and the Fermi level for the non-interacting case equals $\mu = 0$, and consider the electron self-energy in the weak coupling perturbation theory. The strong coupling case is only briefly discussed at the end of Chapter 6.

For starters, we evaluate the electron self-energy in the leading order of the weak coupling perturbation theory and introduce relevant concepts describing the renormalization of electron properties. In particular, we focus on the polaron binding energy, the electron spectral weight, and the electron effective mass. The main actors of Chapter 6 are, however, two next-to-leading order contributions to the electron self-energy, particularly the contribution involving the leading vertex correction. In contrast to the leading order contribution, the two next-to-leading order contributions were rarely studied in the polaron problem in details [115–117], where the non-locality of the vertex correction contribution was only briefly discussed in [115]. Therefore, we contribute by studying in more depth the two contributions and the non-locality of the vertex correction contribution in dependence on the adiabaticity parameter, in the light of the three aforementioned electron properties.

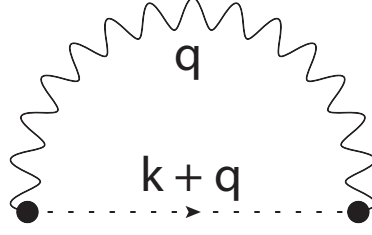


Figure 6.1: Diagrammatic representation of the leading-order contribution in the weak coupling perturbation theory to the electron self-energy in the polaron problem.

6.1 Leading order weak coupling perturbation theory

The leading order contribution in the weak coupling perturbation theory to the electron Green's function comes from the second order contribution in the electron-phonon interaction, with the corresponding electron self-energy being pictorially represented by the Feynman diagram in Fig. 6.1. By using the standard rules [40] for evaluating Feynman diagrams, this self-energy contribution can be written as

$$\Sigma^{(2)}(k, E) = i \frac{g^2}{N} \sum_q \int_{-\infty}^{+\infty} \frac{d\omega}{2\pi} G_0^+(k+q, E+\omega) D_0(q, \omega). \quad (6.2)$$

Here, $D_0(q, \omega)$ corresponds to the Fourier transform of the free phonon Green's function in Eq. (1.9)

$$D_0(q, \omega) = \frac{1}{\omega - \omega_0 + i\eta} - \frac{1}{\omega + \omega_0 - i\eta}. \quad (6.3)$$

By recalling that $G_0^+(k+q, E+\omega)$ only propagates the electron, Eq. (6.1), the integration over the frequency ω can be straightforwardly carried out in the complex plane, giving

$$\Sigma^{(2)}(E) = \frac{g^2}{N} \sum_q \frac{1}{E - \omega_0 - \varepsilon_q + i\eta}. \quad (6.4)$$

The remaining summation over the first Brillouin zone, $\sum_q \rightarrow \sum_{q=-\pi}^{\pi}$, may in the physically relevant regimes of a huge number of lattice sites, $N \rightarrow \infty$, be replaced by the integral, $\sum_{q=-\pi}^{\pi} \rightarrow \frac{N}{2\pi} \int_{-\pi}^{+\pi} dq$. As shown in Appendix A.1, this integration can be carried out analytically, resulting in the momentum-independent, that is local self-energy

$$\text{Re}\Sigma^{(2)}(E) = \begin{cases} -\frac{g^2}{\sqrt{(E-\omega_0)(E-\omega_0-4t)}}, & E < \omega_0, \\ \frac{g^2}{\sqrt{(E-\omega_0)(E-\omega_0-4t)}}, & E > \omega_0 + 4t, \\ 0, & \text{elsewhere,} \end{cases} \quad (6.5)$$

and

$$\text{Im}\Sigma^{(2)}(E) = -\frac{g^2}{\sqrt{(E - \omega_0)(\omega_0 + 4t - E)}}\Theta(E - \omega_0)\Theta(\omega_0 + 4t - E) . \quad (6.6)$$

6.1.1 Electron spectral properties

The influence of this leading order self-energy contribution on electron properties can be most beautifully demonstrated by considering the electron spectral function defined by

$$A(k, E) = -\frac{1}{\pi}G(k, E) . \quad (6.7)$$

By taking advantage of the self-energy $\Sigma(k, E)$, the full electron Green's function can be written as

$$G(k, E) = \frac{1}{E - \xi_k - \text{Re}\Sigma(k, E) + \text{Re}\Sigma(0, 0) + i\text{Im}\Sigma(k, E)} , \quad (6.8)$$

so

$$A(k, E) = -\frac{1}{\pi} \frac{\text{Im}\Sigma(k, E)}{[E - \xi_k - \text{Re}\Sigma(k, E) + \text{Re}\Sigma(0, 0)]^2 + [\text{Im}\Sigma(k, E)]^2} . \quad (6.9)$$

Here, $\text{Re}\Sigma(0, 0)$ accounts for the change of the chemical potential due to the change in the band minimum and brings the zero excitation energy back at $E = 0$. As we shall argue, it can be exploited to calculate the polaron binding energy.

In the absence of interactions ($\text{Re}\Sigma(k, E) = \text{Im}\Sigma(k, E) = 0$), it is easy to see that the spectral function in Eq. (6.9) reduces to the delta peak located at the unperturbed electron energy (measured from the Fermi level)

$$A_0(k, E) = \delta(E - \xi_k) . \quad (6.10)$$

Correspondingly, the total electron spectral weight, obtained by integrating the spectral function over the energy E , is trivially conserved and normalized to unity

$$Z_k = \int_{-\infty}^{+\infty} dE A_0(k, E) = 1 . \quad (6.11)$$

This simple scenario changes with the inclusion of the finite electron-phonon interaction. In particular, in Fig. 6.2, we show a typical electron spectrum in the leading order of the weak coupling perturbation theory. It is immediately evident that polaronic effects drastically render the spectrum even in the lowest order of the perturbation theory, dividing the spectrum into the

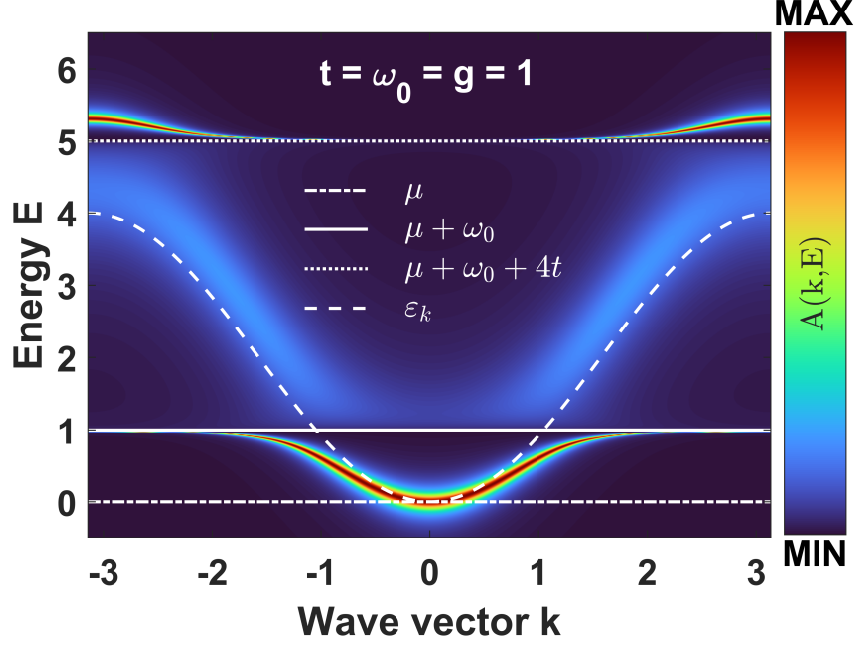


Figure 6.2: Typical electron spectral function in the leading order of the weak coupling perturbation theory. The unperturbed electron dispersion ε_k is shown with the dashed line, while the zero excitation energy, the phonon energy, and the energy $E = \omega_0 + 4t$ (all measured from the Fermi level $\mu = 0$) are shown with the dot-dashed, full, and dotted lines, respectively.

coherent and the incoherent parts, within the energy windows $0 < E < \omega_0$ and $\omega_0 < E < \omega_0 + 4t$, respectively. The structure of the spectrum above $E > \omega_0 + 4t$ is an artifact of the truncation of perturbation theory.

This division of the spectrum can be easily rationalized by looking into the expression for the imaginary part of the self-energy in Eq. (6.6), being zero and finite in the coherent and the incoherent frequency window, respectively, resulting in a smearing of the spectrum in the latter case. Namely, for energies $E > \omega_0$, the electron has enough energy to emit a real phonon, which significantly reduces its lifetime proportional to $\text{Im}\Sigma$ by relaxing its momentum and excitation energy. Accordingly, a state within the incoherent region may be interpreted as a polaron state plus a real phonon, which are not, however, spatially correlated [118].

On the other hand, for energies $E < \omega_0$ the emission of phonons is forbidden by the energy conservation law. Correspondingly, this part of the spectrum is perfectly coherent and only phonons appearing in the system are virtual phonons that coherently follow an electron motion and renormalize its properties. In particular, as can be clearly seen from Fig. 6.2, within the coherent frequency window a polaron band emerges, characterized by the renormalized effective mass m^* and electron spectral weight Z_k , and the shifted band minimum, when compared to the unperturbed band ε_k .

6.1.2 Renormalization effects

Polaron binding energy

To put the zero excitation energy back at $E = 0$ for $g \neq 0$ in Fig. 6.2, it was mandatory to account for the change in the chemical potential due to the shift in the polaron band minimum. Namely, due to the electron-phonon correlations the ground state energy of the unperturbed system $E_0 = \varepsilon_{k=0} = 0$ was lowered $\Delta E_0 < 0$, providing the new ground state energy of the coupled system, $E_G = \Delta E_0$, and defining the new polaron band minimum. Accordingly, the shift ΔE_0 can be interpreted as the polaron binding energy and is given by

$$E_B = \Delta E_0 = \text{Re}\Sigma(0, 0) . \quad (6.12)$$

By recalling our result for $\text{Re}\Sigma^{(2)}(E)$ in Eq. (6.5), we recover the well known result [40] for the leading order contribution to the polaron binding energy

$$E_B^{(2)} = -\frac{g^2}{\sqrt{\omega_0(\omega_0 + 4t)}} \equiv -\alpha\omega_0 , \quad (6.13)$$

where we have introduced the dimensionless parameter

$$\alpha = \frac{g^2}{\omega_0^{3/2}\sqrt{\omega_0 + 4t}} , \quad (6.14)$$

with $\alpha = g^2/\omega_0^2$ and $\alpha \sim g^2/\omega_0^{3/2}t^{1/2}$, in the antiadiabatic and the adiabatic regime, respectively. As shall become evident from our upcoming discussion, the polaron perturbation expansion should rather be viewed as the expansion in α , rather than as the expansion in the coupling strength g .

Electron spectral weight

Following the logic of the division of the spectrum into the coherent and the incoherent parts, we can single out the singular part of the full electron Green's function from the incoherent smooth contribution

$$G(k, E) \approx G_c(k, E) + G_{inc}(k, E) = \frac{Z_k(E)}{E - \xi_k^* + i\eta} + G_{inc}(k, E) . \quad (6.15)$$

Here, $Z_k(E)$ is the electron spectral weight confined within the coherent polaron excitation. In contrast to the non-interacting case, where all of the electron spectral weight was confined within the peak at ξ_k , some of the electron spectral weight is now also distributed among the incoherent contribution $G_{inc}(k, E)$. Since the total electron spectral weight is always conserved,

we generally expect $Z_k(E) \leq 1$.

$Z_k(E)$ can easily be calculated with the knowledge of the electron self-energy [40]

$$Z_k(E) = \left[1 - \frac{\partial \text{Re}\Sigma(k, E)}{\partial E} \right]^{-1}. \quad (6.16)$$

In the leading order we get

$$Z^{(2)}(E) = \frac{1}{1 - g^2 \frac{E - \omega_0 - 2t}{[(E - \omega_0)(E - \omega_0 - 4t)]^{\frac{3}{2}}}}. \quad (6.17)$$

It is now straightforward to estimate how much of the electron spectral weight is confined around the bottom of the polaron band. We simply evaluate

$$Z^{(2)}(E = 0) = \frac{1}{1 + g^2 \frac{\omega_0 + 2t}{[\omega_0(\omega_0 + 4t)]^{\frac{3}{2}}}} \approx 1 - g^2 \frac{\omega_0 + 2t}{[\omega_0(\omega_0 + 4t)]^{\frac{3}{2}}}, \quad (6.18)$$

where we have exploited the assumption that g is small. Correspondingly, the electron spectral weight near the bottom of the polaron band is only slightly lower than in a free electron case, due to the spectral weight of the order g^2 being transferred to the incoherent continuum.

It is particularly interesting to obtain the adiabatic and the antiadiabatic limit of the electron spectral weight in Eq. (6.18). In the adiabatic limit, we get

$$Z^{(2)}(E = 0) \approx 1 - \frac{1}{4} \frac{g^2}{\omega_0^2} \sqrt{\kappa} \approx 1 - \frac{\alpha}{2}, \quad (6.19)$$

while in the antiadiabatic regime we have

$$Z^{(2)}(E = 0) \approx 1 - \frac{g^2}{\omega_0^2} \approx 1 - \alpha. \quad (6.20)$$

We note that in the adiabatic regime the electron spectral weight is less reduced than in the antiadiabatic regime, due to the appearance of the factor $\sqrt{\kappa}$.

The value of $Z_k(E)$, however, decreases dramatically as the polaron band reaches the phonon energy near the Brillouin zone boundaries, where the polaron band peak is barely visible in Fig. 6.2. This readily follows from Eq. (6.17), giving

$$Z^{(2)}(E \rightarrow \omega_0) \approx \frac{4\sqrt{t}}{g^2} (\omega_0 - E)^{\frac{3}{2}} \rightarrow 0. \quad (6.21)$$

As the polaron band approaches the phonon energy, the electron content of the polaron band evidently decreases and the phonon character starts to dominate the polaron state.

This decrease of the electron spectral weight near the phonon energy is accompanied by the

flattening of the polaron band, as is also clearly evident from Fig. 6.2. To quantitatively estimate this flattening, we search for the poles of the electron Green's function

$$G^{(2)}(k, E) = \frac{1}{E - \varepsilon_k - \frac{g^2}{\sqrt{\omega_0(\omega_0+4t)}} + \frac{g^2}{\sqrt{(E-\omega_0)(E-\omega_0-4t)}} + i\eta}, \quad (6.22)$$

providing the equation for the dispersion

$$E - \varepsilon_k - \frac{g^2}{\sqrt{\omega_0(\omega_0+4t)}} + \frac{g^2}{\sqrt{(E-\omega_0)(E-\omega_0-4t)}} = 0. \quad (6.23)$$

Since we are interested in the part of the dispersion just below the phonon energy, $E \approx \omega_0$, we can simplify the above equation to

$$\omega_0 - \tilde{\varepsilon}_k + \frac{g^2}{\sqrt{4t(\omega_0 - E)}} = 0, \quad (6.24)$$

where we introduced $\tilde{\varepsilon}_k \equiv \varepsilon_k + \frac{g^2}{\sqrt{\omega_0(\omega_0+4t)}}$. This simplified equation can now be readily solved, yielding

$$(\tilde{\varepsilon}_k - \omega_0)^2 \approx \frac{g^4}{4t(\omega_0 - E)} \quad \Rightarrow \quad E \approx \omega_0 - \frac{g^4}{4t(\tilde{\varepsilon}_k - \omega_0)^2}. \quad (6.25)$$

Interestingly, E does not decrease with g^2 , but rather with g^4 .

Electron effective mass

The last electron property we consider, which gets renormalized upon the interaction with phonons, is the electron effective mass, which characterizes the polaron band dispersion ξ_k^* in Eq. (6.15). As was the case with the electron spectral weight, the electron effective mass can also be fully calculated by knowing the electron self-energy [40]

$$\frac{m^*}{m} = \lim_{\varepsilon_k \rightarrow 0} \left[\frac{1 - \frac{\partial \text{Re}\Sigma(k, E)}{\partial E}}{1 + \frac{\partial \text{Re}\Sigma(k, E)}{\partial \varepsilon_k}} \right]_{E=0}. \quad (6.26)$$

It is important to note that the results obtained for the electron spectral weight in the leading order can be straightforwardly exploited to calculate the electron effective mass. This is a direct consequence of the locality of the leading order self-energy in Eq. (6.5), resulting in

$$\frac{m^{*(2)}}{m} = 1 - \frac{\partial \text{Re}\Sigma^{(2)}(E)}{\partial E} \Big|_{E=0} = \left[Z^{(2)}(E=0) \right]^{-1} = 1 + g^2 \frac{\hbar\omega_0 + 2t}{[\hbar\omega_0(\hbar\omega_0 + 4t)]^{\frac{3}{2}}} \geq 1. \quad (6.27)$$

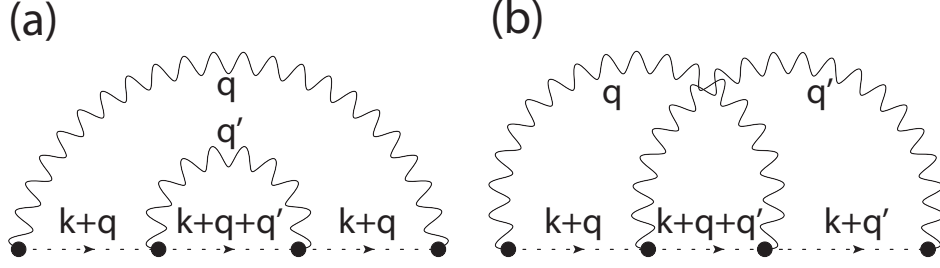


Figure 6.3: Diagrammatic representation of two next-to-leading order contributions to the electron self-energy in the polaron problem. (a) Non-crossing and (b) crossing diagram.

As anticipated, the electron gets heavier, $m^* > m$, due to the virtual cloud of phonons accompanying its motion.

For completeness, we note that in the adiabatic regime the electron effective mass equals

$$\frac{m^{*(2)}}{m} = 1 + \frac{1}{4} \frac{g^2}{(\hbar\omega_0)^2} \sqrt{\kappa} \approx 1 + \frac{\alpha}{2}, \quad (6.28)$$

while in the antiadiabatic regime we have

$$\frac{m^{*(2)}}{m} = 1 + \frac{g^2}{(\hbar\omega_0)^2} \approx 1 + \alpha. \quad (6.29)$$

Evidently, the electron effectively becomes heavier in the latter case. This is easy to rationalize since in the antiadiabatic regime the virtual cloud of phonons is localized on a single site and not smeared over several sites like in the adiabatic case, so the electron hopping demands a shift of the whole lattice deformation.

6.2 Next-to-leading order weak coupling perturbation theory

The leading order electron self-energy in Eq. (6.5) turned out to be momentum independent, so to obtain the leading non-local contribution to the electron self-energy, we have to make a step further and consider the next-to-leading order electron self-energy as well. In particular, in Fig. 6.3, two Feynman diagrams representing the two next-to-leading order contributions to the electron self-energy are shown. Since the two phonon lines in the diagram Fig. 6.3(b) cross each other, and those in the diagram Fig. 6.3(a) do not, we call the diagram in Fig. 6.3(a) the non-crossing diagram, and the diagram in Fig. 6.3(b) the crossing diagram. Obviously, the crossing diagram involves the leading vertex correction and provides us with the anticipated non-local contribution to the electron self-energy.

The two diagrams in Fig. 6.3 are evaluated in Appendix A.2 for finite electron densities, from which the results in the polaron limit may be simply obtained by setting all Fermi-Dirac distributions to zero, $n_{\mathbf{k}} = 0$. As shown in [115], the two resulting contributions can be

computed analytically in the 1D case for energies below the phonon energy, while in [117] they were calculated in the whole relevant energy range. However, since we are interested in the properties of the polaron band, which is anyway located only below the phonon energy due to the leading order contribution, here we just exploit the results in [115] to account for the polaron binding energy, electron spectral weight, and electron effective mass.

6.2.1 Non-crossing diagram

Following [115] and the short derivation in Appendix A.2.4, we have for the electron self-energy coming from the non-crossing diagram

$$\text{Re}\Sigma^{(NC)}(E < \omega_0) = -g^4 \frac{1}{(\omega_0 - E)^{\frac{3}{2}}(4t + \omega_0 - E)^{\frac{3}{2}}} \frac{(2t + \omega_0 - E)}{(2\omega_0 - E)^{\frac{1}{2}}(4t + 2\omega_0 - E)^{\frac{1}{2}}} . \quad (6.30)$$

Since $\Sigma^{(NC)}$ does not have momentum dependence, we conclude that this contribution to the electron self-energy is local.

The corresponding correction to the polaron binding energy can be simply evaluated

$$E_B^{(NC)} = \text{Re}\Sigma^{(NC)}(0) = -\frac{1}{2}\alpha^2\omega_0 \sqrt{\frac{\omega_0 + 2t}{\omega_0 + 4t}} , \quad (6.31)$$

together with the results in the adiabatic

$$E_B^{(NC)} = -\frac{1}{2\sqrt{2}}\alpha^2\omega_0 \approx -0.35\alpha^2\omega_0 , \quad (6.32)$$

and in the antiadiabatic regime

$$E_B^{(NC)} = -\frac{1}{2}\alpha^2\omega_0 . \quad (6.33)$$

On the other hand, the evaluation of the correction to the electron spectral weight, Eq. (6.16), and the electron effective mass, Eq. (6.26), is slightly more complicated. Namely, we have to evaluate the derivative of $\text{Re}\Sigma^{(NC)}(E)$

$$\begin{aligned}
\frac{\partial \text{Re}\Sigma^{(NC)}(E)}{\partial E} &= g^4 \frac{1}{(\omega_0 - E)^{\frac{3}{2}}(4t + \omega_0 - E)^{\frac{3}{2}}} \frac{1}{(2\omega_0 - E)^{\frac{1}{2}}(4t + 2\omega_0 - E)^{\frac{1}{2}}} \times \\
&\times \left[1 + (2t + \omega_0 - E) \left\{ -\frac{3}{2} \left[\frac{1}{\omega_0 - E} + \frac{1}{4t + \omega_0 - E} \right] - \frac{1}{2} \left[\frac{1}{2\omega_0 - E} + \frac{1}{4t + 2\omega_0 - E} \right] \right\} \right] \\
&= \left\{ \frac{1}{E - \omega_0 - 2t} + \frac{3}{2} \left[\frac{1}{\omega_0 - E} + \frac{1}{4t + \omega_0 - E} \right] + \frac{1}{2} \left[\frac{1}{2\omega_0 - E} + \frac{1}{4t + 2\omega_0 - E} \right] \right\} \times \\
&\times \Sigma^{(NC)}(E) ,
\end{aligned} \tag{6.34}$$

so

$$\begin{aligned}
\left. \frac{\partial \text{Re}\Sigma^{(NC)}(E)}{\partial E} \right|_{E=0} &= \left\{ -\frac{1}{2t + \omega_0} + \frac{3}{2} \left[\frac{1}{\omega_0} + \frac{1}{4t + \omega_0} \right] + \frac{1}{2} \left[\frac{1}{2\omega_0} + \frac{1}{4t + 2\omega_0} \right] \right\} \times \\
&\times \left\{ -\frac{1}{2} \alpha^2 \omega_0 \sqrt{\frac{\omega_0 + 2t}{\omega_0 + 4t}} \right\} .
\end{aligned} \tag{6.35}$$

This expression is not particularly suggestive, so we consider its adiabatic and antiadiabatic limits separately. In the adiabatic regime, we have

$$\left. \frac{\partial \text{Re}\Sigma^{(NC)}(E)}{\partial E} \right|_{E=0} = -\frac{7}{8\sqrt{2}} \alpha^2 \approx -0.62\alpha^2 , \tag{6.36}$$

while in the antiadiabatic regime we get

$$\left. \frac{\partial \text{Re}\Sigma^{(NC)}(E)}{\partial E} \right|_{E=0} = -\frac{5}{4} \alpha^2 . \tag{6.37}$$

6.2.2 Crossing diagram

The adaptation of the self-energy contribution coming from the crossing diagram in [115] is not so straightforward and demands a little bit more work. The lengthy, albeit rather simple algebra is again presented in Appendix A.2.4, resulting in

$$\begin{aligned} \text{Re}\Sigma^{(C)}(k, E < \omega_0) = & -g^4 \left[\frac{(2t + \omega_0 - E)^2 - 2t^2}{(\omega_0 - E)(4t + \omega_0 - E)} + \frac{(2t + \omega_0 - E)(2t + 2\omega_0 - E)}{\sqrt{(4t + \omega_0 - E)(\omega_0 - E)(4t + 2\omega_0 - E)(2\omega_0 - E)}} \right] \times \\ & \times \frac{1}{(2t + 2\omega_0 - E) [(2t + \omega_0 - E)^2 - 2t^2] + (2t + \omega_0 - E)\sqrt{(4t + \omega_0 - E)(\omega_0 - E)(4t + 2\omega_0 - E)(2\omega_0 - E)} - 4t^3 \cos k}. \end{aligned} \quad (6.38)$$

Evidently, $\Sigma^{(C)}(k, E)$ represents the leading order non-local contribution to the electron self-energy, due to the momentum dependence coming from $\cos k$ in the denominator.

In order to compare contributions of the non-crossing and the crossing diagram to the renormalized electron properties, we consider the correction to the polaron binding energy due to $\text{Re}\Sigma^{(C)}(k, E < \omega_0)$

$$\begin{aligned} E_B^{(C)} = \text{Re}\Sigma^{(C)}(0, 0) = & -g^4 \left[\frac{(2t + \omega_0)^2 - 2t^2}{\omega_0(4t + \omega_0)} + \frac{(2t + \omega_0)(2t + 2\omega_0)}{\sqrt{(4t + \omega_0)\omega_0(4t + 2\omega_0)2\omega_0}} \right] \times \\ & \times \frac{1}{(2t + 2\omega_0) [(2t + \omega_0)^2 - 2t^2] + (2t + \omega_0)\sqrt{(4t + \omega_0)\omega_0(4t + 2\omega_0)2\omega_0} - 4t^3}, \end{aligned} \quad (6.39)$$

and provide in Appendix A.2.4 its derivatives $\frac{\partial \text{Re}\Sigma^{(C)}(k, E)}{\partial E}$ and $\frac{\partial \text{Re}\Sigma^{(C)}(k, E)}{\partial \varepsilon_k}$.

Due to the complexity of the obtained expressions, it is, however, much more instructive to just consider the results in the adiabatic and the antiadiabatic regime. In particular, in the adiabatic regime, we get

$$E_B^{(C)} = -\frac{2 + \sqrt{2}}{2\sqrt{2}(3 + 2\sqrt{2})} \alpha^2 \omega_0 = \left[-\frac{1}{\sqrt{2}} + \frac{1}{2} \right] \alpha^2 \omega_0 \approx -0.21 \alpha^2 \omega_0, \quad (6.40)$$

and

$$\left. \frac{\partial \text{Re}\Sigma^{(C)}(k, E)}{\partial E} \right|_{0,0} = -\frac{46 + 33\sqrt{2}}{8(3 + 2\sqrt{2})^2} \alpha^2, \quad \left. \frac{\partial \text{Re}\Sigma^{(C)}(k, E)}{\partial \varepsilon_k} \right|_{0,0} = \frac{2 + \sqrt{2}}{4\sqrt{2}(3 + 2\sqrt{2})^2} \alpha^2. \quad (6.41)$$

On the other hand, the antiadiabatic limit yields

$$E_B^{(C)} = -\frac{1}{2} \alpha^2 \omega_0, \quad (6.42)$$

and

$$\left. \frac{\partial \text{Re}\Sigma^{(C)}(k, E)}{\partial E} \right|_{0,0} = -\frac{5}{4}\alpha^2, \quad \left. \frac{\partial \text{Re}\Sigma^{(C)}(k, E)}{\partial \varepsilon_k} \right|_{0,0} = \frac{1}{4\kappa^2}\alpha^2 \sim \mathcal{O}(\kappa^{-2}). \quad (6.43)$$

One striking result is immediately apparent. Namely, in the antiadiabatic regime, $\kappa \gg 1$, the non-local contribution $\left. \frac{\partial \text{Re}\Sigma^{(C)}(k, E)}{\partial \varepsilon_k} \right|_{0,0}$ is suppressed by the factor κ^{-2} . Thus, our analysis, based on the perturbation theory, strongly supports the anticipated result that non-local contributions of the electron self-energy are negligible in the antiadiabatic regime.

6.2.3 Total next-to-leading order contributions to the renormalized electron properties

Finally, we are in a position to evaluate and compare the contributions of both the non-crossing and the crossing diagram to the polaron binding energy, electron spectral weight, and electron effective mass. Following the logic of two precedent Subsections 6.2.1 and 6.2.1, we consider only the results in the adiabatic and the antiadiabatic regime.

Polaron binding energy

By exploiting Eqs. (6.32) and (6.40), we have for the polaron binding energy to the next-to-leading order in the adiabatic regime

$$\begin{aligned} E_B^{(4)} &= E_B^{(2)} + E_B^{(NC)} + E_B^{(C)} = -\alpha\omega_0 - \frac{1}{2\sqrt{2}}\alpha^2\omega_0 - \frac{2-\sqrt{2}}{2\sqrt{2}}\alpha^2\omega_0 \\ &= -\alpha\omega_0 - \left[\frac{3\sqrt{2}}{4} - \frac{1}{2} \right] \alpha^2\omega_0 \approx -\alpha\omega_0 - 0.56\alpha^2\omega_0, \end{aligned} \quad (6.44)$$

while from Eqs. (6.33) and (6.42) in the antiadiabatic regime we get

$$E_B^{(4)} = E_B^{(2)} + E_B^{(NC)} + E_B^{(C)} = -\alpha\omega_0 - \frac{1}{2}\alpha^2\omega_0 - \frac{1}{2}\alpha^2\omega_0 = -\alpha\omega_0 - \alpha^2\omega_0. \quad (6.45)$$

It is interesting to note that both the non-crossing and the crossing diagram contributions take an equally important part in determining the polaron binding energy in both the adiabatic and the antiadiabatic regime, clearly opposing Migdal's result [119] valid in cases with high electron densities. In particular, while the contribution from the crossing diagram slightly subceeds that of the non-crossing diagram in the adiabatic regime, in the antiadiabatic regime both diagrams give an equal correction to the polaron binding energy. This highlights the importance of

vertex corrections in the polaron problem and once more supports the almost local nature of the crossing diagram contribution in the antiadiabatic regime.

Electron spectral weight and electron effective mass

By combining together all contributions in Eqs. (6.19), (6.36), and (6.41), and inserting them into Eq. (6.16), we also get the next-to-leading order result for the electron spectral weight in the adiabatic regime

$$Z_{k \approx 0}^{(4)}(E \approx 0) = 1 - \frac{\alpha}{2} - \frac{185 + 130\sqrt{2}}{8\sqrt{2}(3 + 2\sqrt{2})^2} \alpha^2 \approx 1 - \frac{\alpha}{2} - 0.96\alpha^2. \quad (6.46)$$

In contrast to the leading order scenario, where the inverse of $Z^{(2)}(E \approx 0)$ was sufficient to evaluate the electron effective mass, the inverse of Eq. (6.46) cannot be so simply exploited to calculate $\frac{m^{*(4)}}{m}$ due to the finite non-local contribution of the crossing diagram in Eq. (6.41). Namely, in order to obtain $\frac{m^{*(4)}}{m}$, we have to consider full Eq. (6.26) with both the local and the non-local contribution of Eq. (6.41) in the numerator and the denominator, respectively, resulting in

$$\frac{m^{*(4)}}{m} = \frac{1 + \frac{\alpha}{2} + \frac{185 + 130\sqrt{2}}{8\sqrt{2}(3 + 2\sqrt{2})^2} \alpha^2}{1 + \frac{2 + \sqrt{2}}{4\sqrt{2}(3 + 2\sqrt{2})^2} \alpha^2}. \quad (6.47)$$

By expanding the denominator for small α , we have to the order α^2

$$\begin{aligned} \frac{m^{*(4)}}{m} &= 1 + \frac{\alpha}{2} + \left[\frac{185 + 130\sqrt{2}}{8\sqrt{2}(3 + 2\sqrt{2})^2} - \frac{2 + \sqrt{2}}{4\sqrt{2}(3 + 2\sqrt{2})^2} \right] \alpha^2 \\ &= 1 + \frac{\alpha}{2} + \frac{181 + 128\sqrt{2}}{8\sqrt{2}(3 + 2\sqrt{2})^2} \alpha^2 \approx 1 + \frac{\alpha}{2} + 0.94\alpha^2. \end{aligned} \quad (6.48)$$

Although the overall difference between $[Z^{(4)}]^{-1}$ and $\frac{m^{*(4)}}{m}$ turned out to be rather small, it highlights the distinguished non-local nature of vertex corrections in the adiabatic regime.

The simple leading order scenario, however, continues to hold true in the antiadiabatic regime, for which we have provided the strong argument that the non-local part of the electron self-energy is truly negligible. In particular, in the antiadiabatic regime, we have

$$Z_{k \approx 0}^{(4)}(E \approx 0) = 1 - \alpha - \frac{5}{2}\alpha^2, \quad \frac{m^{*(4)}}{m} = \left[Z_{k \approx 0}^{(4)}(E \approx 0) \right]^{-1} = 1 + \alpha + \frac{5}{2}\alpha^2, \quad (6.49)$$

which we obtained by putting results of Eqs. (6.20), (6.37), and (6.43) into Eq. (6.16). It is worth noting that both contributions from the non-crossing and the crossing diagram to $Z^{(4)}$ are again equal, similarly as were contributions $E_B^{(NC)}$ and $E_B^{(C)}$ to the polaron binding energy.

6.3 Strong coupling perturbation theory

The strong coupling regime demands a conceptually different view of the polaron problem. Rather than assuming that the electron moves freely through the lattice and that the electron-phonon interaction perturbs its motion, it is more natural to assume that an unperturbed electron strongly interacts with a phonon at a given lattice site, with the electron hopping being the perturbation. Accordingly, when referring to this strong coupling scenario, we have in mind the following hierarchy of the energy scales, $g \gg t, \omega_0$, and the perturbation expansion should be viewed as the expansion in t , rather than the expansion in g .

6.3.1 Atomic limit

Specifically, the case with $t = 0$ corresponds to the atomic limit, when the Holstein model reduces to the independent boson model [40]. This celebrated model is especially important since it is one of the few electron-phonon models that can be solved exactly. In particular, the Holstein model with $t = 0$ can be diagonalized by means of the unitary Lang-Firsov transformation [120]

$$U = \exp \left[\sqrt{\alpha} c^\dagger c (a - a^\dagger) \right]. \quad (6.50)$$

The main idea behind the transformation is to shift the phonon operators by a quantity $\sqrt{\alpha}$ to eliminate the electron-phonon interaction. By performing this exact diagonalization, the exact polaron binding energy $E_B = -\alpha\omega_0$ and the energies of excited polaron states $E_B + n\omega_0$ are obtained.

The corresponding exact electron Green's function can also be obtained by means of the Lang-Firsov transformation [40]

$$G(E) = \sum_{n=0}^{\infty} \frac{\alpha^n e^{-\alpha}}{n!} \frac{1}{E - E_B - n\omega_0 + i\eta}, \quad (6.51)$$

which we note is completely local. The resulting spectral function $A(\omega)$ consists of a series of delta peaks, spaced exactly ω_0 apart, with the Poisson distribution of electron spectral weights.

In particular, the electron spectral weight close to the ground state energy is exponentially small in the interaction strength, while it is maximal for excitations involving approximately $n \sim \alpha$ phonons, which is the number of phonons in a virtual cloud surrounding the localized electron.

6.3.2 Small t expansion

The N -fold degeneracy of the atomic limit is lifted by the introduction of the finite hopping term t , resulting in the occurrence of the small polaron band. This is immediately apparent from the electron Green's function, which can be again (approximately) obtained by means of the Lang-Firsov transformation [121] for finite, but small t cases

$$G(k, E) = \frac{e^{-\alpha}}{E - 2te^{-\alpha} \cos k + i\eta} + \sum_{n=1}^{\infty} \frac{1}{N} \sum_q \frac{\alpha^n e^{-\alpha}}{n!} \frac{1}{E - 2te^{-\alpha} \cos k - n\omega_0 + i\eta}. \quad (6.52)$$

Namely, by comparing the Green's function in Eq. (6.52) with the general form of the fermion Green's function in Eq. (6.15), we note that the first contribution in Eq. (6.52) may be attributed to the coherent polaron band with the exponentially narrow bandwidth, while the second term in Eq. (6.52) represents the incoherent part of the electron Green's function.

The direct comparison of the first terms in Eqs. (6.52) and (6.52) also provides us with the electron spectral weight and the electron effective mass in the strong coupling regime. In particular, we have $Z = e^{-\alpha}$ and $\frac{m^*}{m} = e^{\alpha}$. The two quantities are obviously related by the relation, $Z^{-1} = \frac{m^*}{m}$, which, due to the arguments presented in Section 6.2, suggests the antiadiabatic nature of small polarons in the strong coupling regime. This is further supported by the local electron self-energy for strong couplings [109]

$$\text{Re}\Sigma(E) = E_B e^{\alpha} + E(1 - e^{\alpha}), \quad (6.53)$$

contributed equally by non-vertex and vertex contributions. In fact, the situation here is quite similar to the situation we have already met in the polaronic impurity model, where the relevant unperturbed electron Green's function was completely local and where some diagrams in a given order, either without or with vertex corrections, contributed equally to the full Green's function - remember the factor two in Subsection 2.3.5.

6.4 Conclusions

We study the properties of the polaron band up to the next-to-leading order of the perturbation theory in electron-phonon interaction, which includes the leading vertex correction to the electron

self-energy. The special emphasis is put on the momentum dependence of the vertex correction, which influence is best manifested through the difference between the electron effective mass and the inverse of the electron spectral weight in the polaron band. We show that in the antiadiabatic regime the momentum-dependent part of the leading vertex correction is suppressed with the square of the adiabaticity parameter. However, although the non-local part of the vertex contribution becomes vanishingly small in the antiadiabatic regime, the whole vertex contribution is not, and contributes exactly as much as the non-vertex contribution in the next-to-leading order to the renormalization of electron properties for small momenta. On the other hand, the vertex contributions to the renormalization of electron properties for small momenta slightly subceed that of the non-vertex contributions in the adiabatic regime, while for large momenta they become even more suppressed.

Phononic properties of polarons

In this last Chapter 7 of Part II, we complement the picture of the polaron physics from the phonon's point of view. To be specific, in order to treat on an equal footing the phonon and the electron degree of freedom, we consider the perturbation expansion of the phonon Green's function given by Eq. (1.9). Namely, we consider the propagation of the phonon inserted in the system with one electron already present in the lowest energy state $\varepsilon_{\mathbf{k}=0} = 0$ ($\mu \approx 0$). In contrast to the scenario in Chapter 6, where the free fermion propagator in Eq. (6.1) involved only an electron propagation, the free fermion Green's function underlying the forthcoming perturbation expansion reads

$$G_0(\mathbf{k}, E) = G_0^+(\mathbf{k}, E) + G_0^-(\mathbf{k}, E) = \frac{1 - \delta_{\mathbf{k},0}}{E - \varepsilon_{\mathbf{k}} + i\eta} + \frac{\delta_{\mathbf{k},0}}{E - \varepsilon_{\mathbf{k}} - i\eta}, \quad (7.1)$$

due to the permanent electron present in the system. In particular, when compared to Eq. (6.1), the second term in Eq. (7.1) additionally appears, representing the propagation of a hole in the $\mathbf{k} = 0$ state.

The form of the Green's function in Eq. (7.1) has profound implications for the distinguishment of dominant from negligible contributions to the phonon propagator in the perturbation expansion. Technically speaking, due to the Kronecker delta $\delta_{\mathbf{k},0}$ in the hole part of the free fermion Green's function, each hole line with different internal momenta, Fig. 1.1(d), in a Feynman diagram should contribute with the factor $1/N$, with N being the number of lattice sites, to a corresponding contribution in the perturbation expansion. Therefore, the dominant contributions to the perturbation expansion come from the Feynman diagrams which have the least number of hole propagators, making it primarily viewed as the expansion in $1/N$, rather than the expansion in g . As a consequence, the Dyson approach is inferior to the simple addition of irreducible phonon self-energy, hereafter called a phonon polarization, contributions to the full phonon propagator, with the number of contributions kept in the sum determined by the strength of the electron-phonon coupling.

In this context, we derive a few explicit results for the polarization and the phonon spectral function to the next-to-leading order in the weak coupling perturbation theory. Special attention is again devoted to the contributions involving vertex corrections, with a particular emphasis on their treatment in the $1/N$ expansion. To the best of our knowledge, phononic properties of polarons were seldom studied, with the most of analysis being restricted to the leading order perturbation theory [102, 122]. Thus, we may state that the results presented here give

a fresh view of the polaron problem from the perspective of the phonon degree of freedom. However, before exploiting those specific results, we first comment on the consequences of the particle number conservation manifested in terms of the Ward identity [123], which brings robust connections between the non-vertex and vertex corrections to the phonon polarization in the polaron limit, as well as for finite electron density cases.

7.1 Ward identity

The exact phonon polarization $\Pi(\mathbf{q}, \omega)$ has a simple diagrammatic representation shown in Fig. 7.1. Here, the double lines correspond to the full fermion Green's function $G(\mathbf{k}, E)$, while two different symbols are used to distinguish two quite different vertices. In particular, the left vertex in Fig. 7.1 corresponds to the bare electron-phonon vertex g , represented by the full circle as usual, while the right vertex denoted with the full square represents the fully renormalized electron-phonon vertex.

The contributions to the phonon polarization due to the renormalization of a vertex may be represented by the vertex function $\Gamma(\mathbf{k}, E; \mathbf{k} + \mathbf{q}, E + \omega)$ and are correspondingly called vertex contributions. Similarly, since the exact interacting fermion Green's function involves the exact fermion self-energy $\Sigma(\mathbf{k}, E)$

$$G(\mathbf{k}, E) = \frac{1}{E - \varepsilon_{\mathbf{k}} - \Sigma(\mathbf{k}, E)}, \quad (7.2)$$

we call the contributions stemming from the interacting $G(\mathbf{k}, E)$ self-energy contributions. As implied by the Ward identity [40, 123], those two conceptually different contributions to $\Pi(\mathbf{q}, \omega)$ are related by

$$\begin{aligned} \omega \Gamma(\mathbf{k}, E; \mathbf{k} + \mathbf{q}, E + \omega) - |\mathbf{q}| \Gamma(\mathbf{k}, E; \mathbf{k} + \mathbf{q}, E + \omega) &= G^{-1}(\mathbf{k} + \mathbf{q}, E + \omega) - G^{-1}(\mathbf{k}, E) \\ &= \omega + \varepsilon_{\mathbf{k}} - \varepsilon_{\mathbf{k} + \mathbf{q}} + \Sigma(\mathbf{k}, E) - \Sigma(\mathbf{k} + \mathbf{q}, E + \omega). \end{aligned} \quad (7.3)$$

With the use of $G(\mathbf{k}, E)$ and $\Gamma(\mathbf{k}, E; \mathbf{k} + \mathbf{q}, E + \omega)$, we can write the formal expression for the exact phonon polarization in Fig. 7.1

$$\Pi(\mathbf{q}, \omega) = -i \frac{g^2}{N} \sum_{\mathbf{k}} \int_{-\infty}^{+\infty} \frac{dE}{2\pi} G(\mathbf{k}, E) G(\mathbf{k} + \mathbf{q}, E + \omega) \Gamma(\mathbf{k}, E; \mathbf{k} + \mathbf{q}, E + \omega). \quad (7.4)$$

Here, we have kept the momentum-independent Holstein coupling, while we allowed for an arbitrary system dimension, indicated with the vector notation for momenta. Besides the additional factor g^2 , we recognize in Eq. (7.4) the exact (electron) density-density correlation

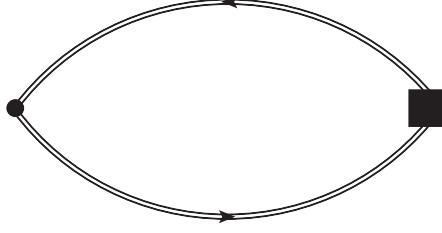


Figure 7.1: The exact phonon polarization diagram. Double lines represent the exact fermion Green's function. The bare electron-phonon vertex is represented by the full circle, whereas the full square denotes the fully renormalized vertex.

function $\chi(\mathbf{q}, \omega)$ [40]

$$\Pi(\mathbf{q}, \omega) = g^2 \chi(\mathbf{q}, \omega) . \quad (7.5)$$

Thus, due to the momentum-independent electron-phonon coupling, the two quantities, $\Pi(\mathbf{q}, \omega)$ and $\chi(\mathbf{q}, \omega)$, are exactly proportional.

Let us now exploit the consequences of the Ward identity in Eq. (7.3). In particular, we consider the dynamic long-wavelength limit of the correlation function $\chi(\mathbf{q}, \omega)$. In that case, the Ward identity reduces to

$$\Gamma(\mathbf{k}, E; \mathbf{k}, E + \omega) = 1 + \frac{\Sigma(\mathbf{k}, E) - \Sigma(\mathbf{k}, E + \omega)}{\omega} , \quad (7.6)$$

and correspondingly we get in the $\mathbf{q} = 0$ limit

$$\begin{aligned} \chi(0, \omega) &= -i \frac{1}{N} \sum_{\mathbf{k}} \int_{-\infty}^{+\infty} \frac{dE}{2\pi} G(\mathbf{k}, E) G(\mathbf{k}, E + \omega) \Gamma(\mathbf{k}, E; \mathbf{k}, E + \omega) \\ &= i \frac{1}{N} \sum_{\mathbf{k}} \int_{-\infty}^{+\infty} \frac{dE}{2\pi} \left[\frac{G(\mathbf{k}, E) - G(\mathbf{k}, E + \omega)}{G^{-1}(\mathbf{k}, E + \omega) - G^{-1}(\mathbf{k}, E)} \right] \left[\frac{\omega + \Sigma(\mathbf{k}, E) - \Sigma(\mathbf{k}, E + \omega)}{\omega} \right] \\ &= i \frac{1}{N} \sum_{\mathbf{k}} \int_{-\infty}^{+\infty} \frac{dE}{2\pi} \left[\frac{G(\mathbf{k}, E) - G(\mathbf{k}, E + \omega)}{\omega + \Sigma(\mathbf{k}, E) - \Sigma(\mathbf{k}, E + \omega)} \right] \left[\frac{\omega + \Sigma(\mathbf{k}, E) - \Sigma(\mathbf{k}, E + \omega)}{\omega} \right] \\ &= i \frac{1}{N\omega} \sum_{\mathbf{k}} \int_{-\infty}^{+\infty} \frac{dE}{2\pi} [G(\mathbf{k}, E) - G(\mathbf{k}, E + \omega)] = 0 . \end{aligned} \quad (7.7)$$

Evidently, due to the Ward identity, the correlation function $\chi(\mathbf{q}, \omega)$ vanishes in the dynamic long-wavelength limit implying the same behavior for the phonon polarization, $\Pi(0, \omega) = 0$. Since this simple exact result would not be achievable by not taking into account vertex corrections, it beautifully highlights the importance of vertex corrections on phonon properties,

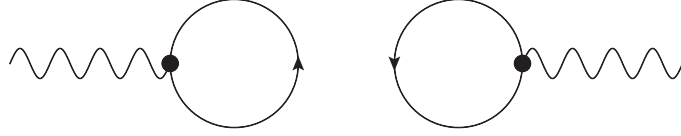


Figure 7.2: Diagrammatic representation of a typical contribution to the phonon propagator for $\mathbf{q} = 0$.

which are oftentimes neglected in comparison to self-energy contributions.

7.1.1 The $\mathbf{q} = 0$ mode

Regarding the $\mathbf{q} = 0$ mode, the only question remains what happens with the phonon propagator in the static limit, $\omega = 0$? As shown in [118], the $\mathbf{q} = 0$ part of the Holstein Hamiltonian is decoupled from the $\mathbf{q} \neq 0$ part and describes the coupling of the (homogeneous) $\mathbf{q} = 0$ phonon mode with the total electron density n . A typical contribution in the perturbation expansion to the phonon propagator, in that case, is shown in Fig. 7.2, where the single closed fermion loop corresponds to the total electron density. However, all the trouble which comes along with the perturbation expansion for the $\mathbf{q} = 0$ case can be avoided since the exact solution for the phonon propagator may be obtained by exploiting the Lehmann representation of the Green's function [40]. Namely, the eigenstates of the $\mathbf{q} = 0$ phonon mode are coherent states, which yields for the full phonon propagator

$$D(\mathbf{q} = 0, \omega) = D_0(\mathbf{q} = 0, \omega) - i8nN_{el} \frac{g^2}{\omega_0^2} \delta(\omega), \quad (7.8)$$

with the details of the derivation left for Appendix B.1.

7.2 Diagrammatic expansion of polarization

For finite momenta \mathbf{q} , such an exact solution for the phonon propagator can no longer be obtained. We are then left with no other choice but to seek the best possible approximation for the phonon propagator depending on the model parameters (t, ω_0, g). In particular, here we concentrate on the weak coupling regime, $g \ll 1$, and consider the expansion of the phonon polarization in the weak coupling perturbation theory.

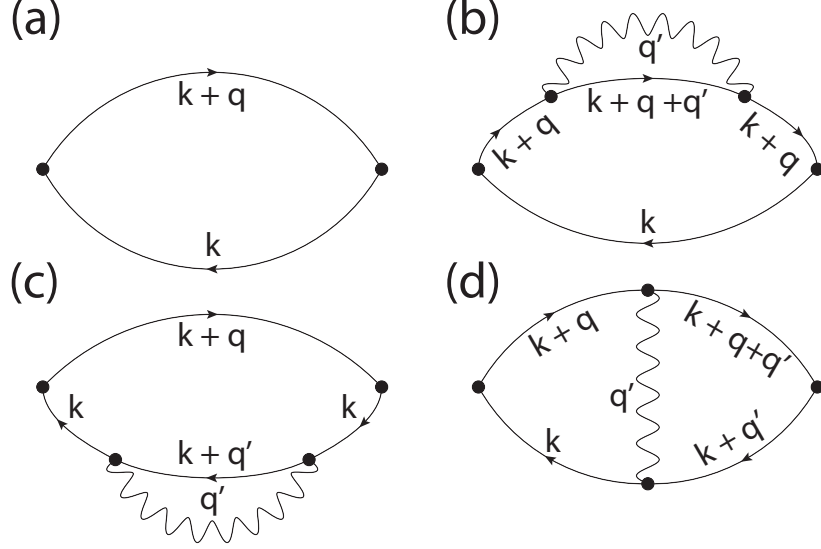


Figure 7.3: Diagrammatic representation of the phonon polarization to the fourth order of the weak coupling perturbation theory. (a) Leading order contribution, (b) and (c) leading self-energy contributions, and (d) leading vertex contribution.

7.2.1 Leading order and leading self-energy corrections

Leading order polarization

The leading order contribution in the weak coupling perturbation theory to the phonon polarization is diagrammatically presented in Fig. 7.3(a). Physically, it represents the creation of a single electron-hole pair. Note that all fermion lines in Fig. 7.3 are full, and not dotted, giving a hint that we will immediately consider the polarization for finite electron density cases, and simply extract the polaron limit results by setting $n_{\mathbf{k}} = \delta_{\mathbf{k},0}$ in the obtained expressions.

To demonstrate how this works, we use Feynman rules [40] for the leading order polarization diagram in Fig. 7.3(a), giving

$$\begin{aligned} \Pi^{(2)}(\mathbf{q}, \omega) &= -i \frac{g^2}{N} \sum_{\mathbf{k}} \int_{-\infty}^{+\infty} \frac{dE}{2\pi} G_0(\mathbf{k}, E) G_0(\mathbf{k} + \mathbf{q}, E + \omega) \\ &= -i \frac{g^2}{N} \sum_{\mathbf{k}} \int_{-\infty}^{+\infty} \frac{dE}{2\pi} \left[\frac{1 - n_{\mathbf{k}}}{E - \varepsilon_{\mathbf{k}} + i\eta} + \frac{n_{\mathbf{k}}}{E - \varepsilon_{\mathbf{k}} - i\eta} \right] \left[\frac{1 - n_{\mathbf{k}+\mathbf{q}}}{E + \omega - \varepsilon_{\mathbf{k}+\mathbf{q}} + i\eta} + \frac{n_{\mathbf{k}+\mathbf{q}}}{E + \omega - \varepsilon_{\mathbf{k}+\mathbf{q}} - i\eta} \right]. \end{aligned} \quad (7.9)$$

The integration over the energy E yields non-vanishing contributions only when two poles are located in different halves of the complex plane, resulting in

$$\Pi^{(2)}(\mathbf{q}, \omega) = \frac{g^2}{N} \sum_{\mathbf{k}} \left[\frac{n_{\mathbf{k}} (1 - n_{\mathbf{k}+\mathbf{q}})}{\omega + \varepsilon_{\mathbf{k}} - \varepsilon_{\mathbf{k}+\mathbf{q}} + i\eta} - \frac{n_{\mathbf{k}+\mathbf{q}} (1 - n_{\mathbf{k}})}{\omega + \varepsilon_{\mathbf{k}} - \varepsilon_{\mathbf{k}+\mathbf{q}} - i\eta} \right]. \quad (7.10)$$

For $\mathbf{q} = 0$, the Fermi-Dirac distributions in the numerators ensure $\Pi^{(2)}(0, \omega) = 0$, in accordance with the discussion in Section 7.1.

By putting now $n_{\mathbf{k}} = \delta_{\mathbf{k},0}$ in Eq. (7.10), and by remembering that we consider the case with the electron dispersion, $\varepsilon_{\mathbf{k}=0} = 0$, we get in the polaron limit

$$\Pi^{(2)}(\mathbf{q}, \omega) = \frac{g^2}{N} \left[\frac{1}{\omega - \varepsilon_{\mathbf{q}} + i\eta} - \frac{1}{\omega + \varepsilon_{\mathbf{q}} - i\eta} \right]. \quad (7.11)$$

It is interesting to note that $\Pi^{(2)}(\mathbf{q}, \omega)$ in Eq. (7.11) resembles the form of the free phonon Green's function in Eq. (6.3), with the phonon energy replaced by the electron dispersion, $\omega_0 \rightarrow \varepsilon_{\mathbf{q}}$. For future conveniences, we introduce

$$\Pi^{(2)\pm}(\mathbf{q}, \omega) = \pm \frac{g^2}{N} \frac{1}{\omega \mp \varepsilon_{\mathbf{q}} \pm i\eta}, \quad (7.12)$$

in terms of which we can write

$$\Pi^{(2)}(\mathbf{q}, \omega) = \Pi^{(2)+}(\mathbf{q}, \omega) + \Pi^{(2)-}(\mathbf{q}, \omega). \quad (7.13)$$

Leading self-energy contributions

Such simplicity is no longer present when the leading self-energy contributions to the polarization, shown in Figs. 7.3(b) and (c), are taken into account. Their evaluation for finite electron density cases, as well as in the polaron limit, is due to the long derivation procedure presented in Appendix B.2, with the end result in the polaron case reading

$$\begin{aligned} \Pi^{(4b)}(\mathbf{q}, \omega) = \frac{g^4}{N^2} \sum_{\mathbf{k}} \left[\frac{1}{(\varepsilon_{\mathbf{k}} + \omega_0 - i\eta)^2 (\omega - \varepsilon_{\mathbf{k}+\mathbf{q}} - \omega_0 + i\eta)} - \frac{1}{(\varepsilon_{\mathbf{k}} + \omega_0 - i\eta)^2 (\omega - \varepsilon_{\mathbf{q}} + i\eta)} + \right. \\ \left. + \frac{1}{(\varepsilon_{\mathbf{k}} + \omega_0 - i\eta) (\omega - \varepsilon_{\mathbf{q}} + i\eta)^2} - \frac{1}{(\omega + \varepsilon_{\mathbf{q}} - i\eta)^2 (\omega + \varepsilon_{\mathbf{k}} + \omega_0 - i\eta)} \right] = \Pi^{(4c)}(-\mathbf{q}, -\omega). \end{aligned} \quad (7.14)$$

Strictly speaking, in the summation over \mathbf{k} , the states $\mathbf{k} = 0, -\mathbf{q}$ should be omitted. However, this introduces a negligible effect of the order $\mathcal{O}(1/N^2)$.

7.2.2 Leading vertex contribution

Lastly, we consider the leading vertex contribution to the polarization, shown in Fig. 7.3(d). As commented in Section 7.1, all vertex contributions can be expressed in terms of the vertex

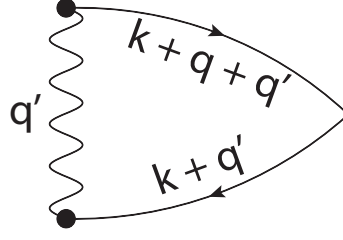


Figure 7.4: Diagrammatic representation of the leading order contribution to the vertex function.

function $\Gamma(\mathbf{k}, E; \mathbf{k} + \mathbf{q}, E + \omega)$. Here in particular, in order to account for the leading vertex contribution to the polarization, it is sufficient to keep only the leading order contribution of the full vertex function, shown diagrammatically in Fig. 7.4. By using the Feynman rules [40], we can write for this leading order contribution

$$\Gamma^{(2)}(\mathbf{k}, E; \mathbf{k} + \mathbf{q}, E + \omega) = i \frac{g^2}{N} \sum_{\mathbf{q}'} \int_{-\infty}^{+\infty} \frac{d\omega'}{2\pi} G_0(\mathbf{k} + \mathbf{q}', E + \omega') D_0(\mathbf{q}', \omega') \times \quad (7.15)$$

$$\times G_0(\mathbf{k} + \mathbf{q} + \mathbf{q}', E + \omega + \omega') ,$$

with the details of the integration over ω' in the complex plane presented in Appendix A.2.2.

With $\Gamma^{(2)}(\mathbf{k}, E; \mathbf{k} + \mathbf{q}, E + \omega)$ known, we can go back to Eq. (7.4) and calculate the leading vertex contribution to the polarization in Fig. 7.3(d)

$$\Pi^{(4d)}(\mathbf{q}, \omega) = -i \frac{g^2}{N} \sum_{\mathbf{k}} \int_{-\infty}^{+\infty} \frac{dE}{2\pi} G_0(\mathbf{k}, E) G_0(\mathbf{k} + \mathbf{q}, E + \omega) \Gamma^{(2)}(\mathbf{k}, E; \mathbf{k} + \mathbf{q}, E + \omega) . \quad (7.16)$$

The details of the derivation are again left for Appendix B.2.4, with the final result in the polaron limit

$$\Pi^{(4d)}(\mathbf{q}, \omega) = -2 \frac{g^4}{N^2} \sum_{\mathbf{k}} \left[\frac{1}{(\omega - \varepsilon_{\mathbf{q}} + i\eta)(\omega - \omega_0 - \varepsilon_{\mathbf{k}+\mathbf{q}} + i\eta)(\omega_0 + \varepsilon_{\mathbf{k}})} \right. \quad (7.17)$$

$$\left. + \frac{1}{(\omega + \varepsilon_{\mathbf{q}} - i\eta)(\omega + \omega_0 + \varepsilon_{\mathbf{k}} - i\eta)(\omega_0 + \varepsilon_{\mathbf{k}+\mathbf{q}})} \right] .$$

Interestingly, in terms of the leading order polarization, Eq. (7.12), $\Pi^{(4d)}(\mathbf{q}, \omega)$ can be written as

$$\Pi^{(4d)}(\mathbf{q}, \omega) = 2\Pi^{(2)+}(\mathbf{q}, \omega)\Theta^{(2)}(\mathbf{q}, \omega) + 2\Pi^{(2)-}(\mathbf{q}, \omega)\Theta^{(2)}(-\mathbf{q}, -\omega) , \quad (7.18)$$

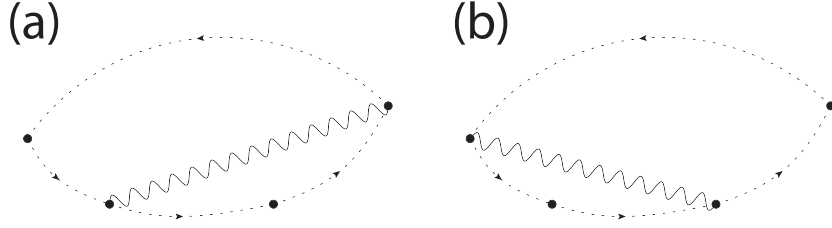


Figure 7.5: Two possible time-ordered diagrams for the leading vertex contribution to the polarization involving at most one hole line.

where Θ denotes the part of the vertex function involving only electron-electron processes, see Appendix A.2.4. Accordingly, $\Theta^{(2)}(\mathbf{q}, \omega)$ can be evaluated by keeping only the electron parts of fermion Green's functions in Eq. (7.15)

$$\begin{aligned}
\Theta^{(2)}(\mathbf{q}, \omega) &= i \frac{g^2}{N} \sum_{\mathbf{q}'} \int_{-\infty}^{+\infty} \frac{d\omega'}{2\pi} G_0^+(\mathbf{q}', \omega') G_0^+(\mathbf{q} + \mathbf{q}', \omega + \omega') D_0(\mathbf{q}', \omega') \\
&= i \frac{g^2}{N} \sum_{\mathbf{q}'} \int_{-\infty}^{+\infty} \frac{d\omega'}{2\pi} \frac{1}{\omega' - \varepsilon_{\mathbf{q}'} + i\eta} \frac{1}{\omega + \omega' - \varepsilon_{\mathbf{q}+\mathbf{q}'} + i\eta} \left[\frac{1}{\omega' - \omega_0 + i\eta} - \frac{1}{\omega' + \omega_0 - i\eta} \right] \\
&= -\frac{g^2}{N} \sum_{\mathbf{q}'} \frac{1}{(\omega - \omega_0 - \varepsilon_{\mathbf{q}+\mathbf{q}'} + i\eta)(\omega_0 + \varepsilon_{\mathbf{q}'})}.
\end{aligned} \tag{7.19}$$

We note that Θ lacks the \mathbf{k} and E dependence since one of its external fermion lines necessarily involves the $\mathbf{k} = 0$ hole state in the polaron limit. Moreover, $\Theta^{(2)}(\mathbf{q}, \omega)$ satisfies the Ward identity in Eq. (7.6) in the leading order

$$1 + \Theta^{(2)}(0, \omega) = 1 + \frac{\Sigma^{(2)}(0) - \Sigma^{(2)}(\omega)}{\omega}, \tag{7.20}$$

where $\Sigma^{(2)}$ is the leading order electron self-energy, Eq. (6.4).

Exploitation of the $1/N$ expansion

So far, all four polarization diagrams in Fig. (7.3) were considered exclusively in the (standardized) frequency domain. Accordingly, we could not distinguish whether corresponding fermion lines denote the propagation of an electron or the propagation of a hole. However, in polaron physics this turns out to be important since dominant contributions to the phonon polarization should contain as few as possible hole lines with different internal momenta, as discussed at the beginning of Chapter 7. Therefore, in what follows, we consider the diagrammatic representation of the polarization in the time domain, with the focus being put on the vertex contribution.

In particular, as shown in Fig. 7.5, in the polaron limit there are just two different time-ordered polarization diagrams with the leading vertex correction involving at most one hole line.

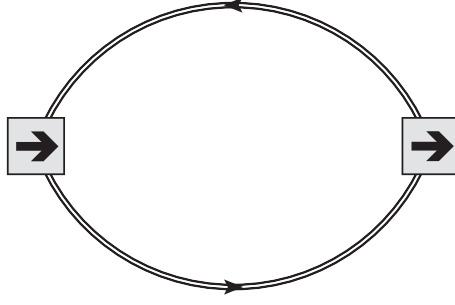


Figure 7.6: Phonon polarization with both vertices renormalized, albeit with the vertex function involving only the electron part of fermion Green's functions.

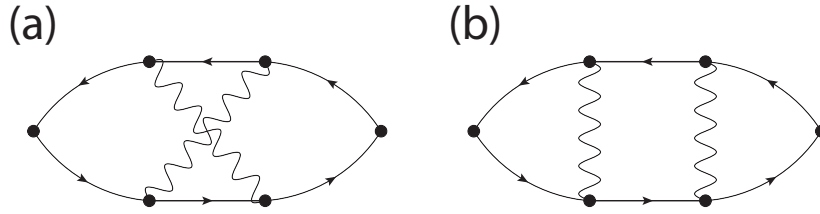


Figure 7.7: Two higher-order vertex polarization diagrams. Diagram (a) involves the crossing of phonon propagators, while diagram (b) represents a contribution to the ladder series.

Following Fig. 7.1, that is by assuming that the right vertex is being renormalized, we conclude that the diagram in Fig. 7.5(a) involves the vertex correction with two electron propagators, whereas the diagram in Fig. 7.5(b) involves the vertex correction with an electron-hole process. However, the diagram in Fig. 7.5(b) as a whole may just be equally interpreted in terms of the leading correction of the left vertex, with a purely electron-electron process. This interpretation also rationalizes the appearance of the vertex function Θ in Eq. (7.18), as well as the factor 2, accounting for two diagrams in Fig. 7.5.

Based on this observation, we propose that in the polaron limit we may renormalize both vertices in the exact phonon polarization, albeit with the vertex function involving only the electron part of fermion Green's functions. This is diagrammatically presented in Fig. 7.6, where the renormalized vertex is denoted with the square with an arrow pointing to the right, emphasizing the fact that the vertex function involves only electron propagators, while the formal expression for the exact phonon polarization in Eq. (7.4) according to Fig. 7.6 becomes

$$\Pi(\mathbf{q}, \omega) = -i \frac{g^2}{N} \int_{-\infty}^{+\infty} \frac{dE}{2\pi} G(0, E) G(\mathbf{q}, E + \omega) [\Theta(\mathbf{q}, \omega)]^2 . \quad (7.21)$$

This analysis based on the next-to-leading order polarization seems so convincing that we are tempted to proclaim the polarization in Fig. 7.6 the exact polarization in the polaron limit. However, we should be very careful before jumping to a such firm conclusion. Here we do not provide any rigorous mathematical proof, but we rather base our statements on intuitive grounds. In particular, we consider two higher order vertex diagrams in Fig. 7.7. It is obvious that if we

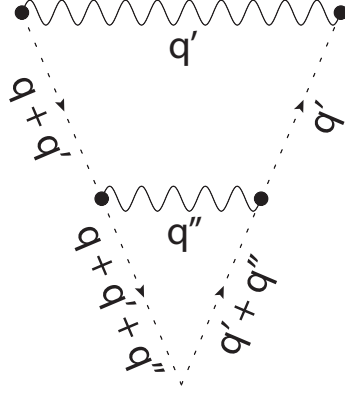


Figure 7.8: Next-to-leading order time-ordered ladder vertex function.

would take that one of the middle (straight) fermion lines in the diagram in Fig. 7.7(a), with the crossed phonon propagators, corresponds to the hole propagator, then we would not be able to disentangle the renormalization of the right and the left vertex. In other words, the polarization in Fig. (7.6) cannot fully account for the vertex diagram in Fig. 7.7(a). In contrast, it is quite intuitive that the renormalization of both vertices would work fine with the ladder diagram in Fig. 7.7(b). In fact, we expect it to work fine with the infinite series of ladder diagrams, for which we show that the exact vertex function Θ_L can be obtained in the closed form.

7.2.3 Ladder approximation

We start by considering the next-to-leading order contribution to the ladder vertex function $\Theta_L^{(4)}$, shown diagrammatically in Fig. 7.8. With the Feynman rules [40], we have

$$\begin{aligned} \Theta_L^{(4)}(\mathbf{q}, \omega) &= i \frac{g^2}{N} \sum_{\mathbf{q}'} \int_{-\infty}^{+\infty} \frac{d\omega'}{2\pi} G_0^+(\mathbf{q}', \omega') G_0^+(\mathbf{q} + \mathbf{q}', \omega + \omega') D_0(\mathbf{q}', \omega') \\ &\times i \frac{g^2}{N} \sum_{\mathbf{q}''} \int_{-\infty}^{+\infty} \frac{d\omega''}{2\pi} G_0^+(\mathbf{q}' + \mathbf{q}'', \omega' + \omega'') G_0^+(\mathbf{q} + \mathbf{q}' + \mathbf{q}'', \omega + \omega' + \omega'') D_0(\mathbf{q}'', \omega''). \end{aligned} \quad (7.22)$$

First, we compute the integral over ω'' . Since all fermion propagators have poles only in the lower half of the complex plane, the integration is easy to evaluate

$$\begin{aligned}
& \int_{-\infty}^{+\infty} \frac{d\omega''}{2\pi} G_0^+(\mathbf{q}' + \mathbf{q}'', \omega' + \omega'') G_0^+(\mathbf{q} + \mathbf{q}' + \mathbf{q}'', \omega + \omega' + \omega'') D_0(\mathbf{q}'', \omega'') \\
&= \int_{-\infty}^{+\infty} \frac{d\omega''}{2\pi} \left[\frac{1}{\omega' + \omega'' - \varepsilon_{\mathbf{q}' + \mathbf{q}''} + i\eta} \right] \left[\frac{1}{\omega + \omega' + \omega'' - \varepsilon_{\mathbf{q} + \mathbf{q}' + \mathbf{q}''} + i\eta} \right] \times \\
&\times \left[\frac{1}{\omega'' - \omega_0 + i\eta} - \frac{1}{\omega'' + \omega_0 - i\eta} \right] \\
&= -i \frac{1}{(\omega' - \omega_0 - \varepsilon_{\mathbf{q}' + \mathbf{q}''} + i\eta)(\omega + \omega' - \omega_0 - \varepsilon_{\mathbf{q} + \mathbf{q}' + \mathbf{q}''} + i\eta)}.
\end{aligned} \tag{7.23}$$

The remaining integration over ω' can be carried out in the similar fashion, giving ($\mathbf{q}'' \rightarrow \mathbf{q}'' - \mathbf{q}'$)

$$\begin{aligned}
\Theta_L^{(4)}(\mathbf{q}, \omega) &= i \frac{g^4}{N^2} \sum_{\mathbf{q}'} \sum_{\mathbf{q}''} \int_{-\infty}^{+\infty} \frac{d\omega'}{2\pi} \frac{1}{(\omega' - \omega_0 - \varepsilon_{\mathbf{q}''} + i\eta)(\omega + \omega' - \omega_0 - \varepsilon_{\mathbf{q} + \mathbf{q}''} + i\eta)} \\
&\times \left[\frac{1}{\omega + \omega' - \varepsilon_{\mathbf{q} + \mathbf{q}'} + i\eta} \right] \left[\frac{1}{\omega' - \varepsilon_{\mathbf{q}'} + i\eta} \right] \left[\frac{1}{\omega' - \omega_0 + i\eta} - \frac{1}{\omega' + \omega_0 - i\eta} \right] \\
&= \frac{g^2}{N} \sum_{\mathbf{q}'} \frac{(-1)}{(\omega - \omega_0 - \varepsilon_{\mathbf{q} + \mathbf{q}'} + i\eta)(\omega_0 + \varepsilon_{\mathbf{q}'})} \times \frac{g^2}{N} \sum_{\mathbf{q}''} \frac{(-1)}{(\omega - 2\omega_0 - \varepsilon_{\mathbf{q} + \mathbf{q}''} + i\eta)(2\omega_0 + \varepsilon_{\mathbf{q}''})}.
\end{aligned} \tag{7.24}$$

We recognize the expression for the leading order vertex function $\Theta^{(2)}(\mathbf{q}, \omega)$, Eq. (7.19), in both factors in the final expression for $\Theta_L^{(4)}(\mathbf{q}, \omega)$. However, the phonon energy ω_0 is being replaced by $2\omega_0$ in the second factor. Therefore, by introducing

$$\Theta^{(2)}(\mathbf{q}, \omega | n\omega_0) = -\frac{g^2}{N} \sum_{\mathbf{q}'} \frac{1}{(\omega - n\omega_0 - \varepsilon_{\mathbf{q} + \mathbf{q}'} + i\eta)(n\omega_0 + \varepsilon_{\mathbf{q}'})}, \tag{7.25}$$

we can write $\Theta_L^{(4)}(\mathbf{q}, \omega)$ in a particularly convenient form

$$\Theta_L^{(4)}(\mathbf{q}, \omega) = \Theta^{(2)}(\mathbf{q}, \omega | \omega_0) \Theta^{(2)}(\mathbf{q}, \omega | 2\omega_0). \tag{7.26}$$

Each higher-order contribution in the ladder approximation adds an additional phonon line, parallel to the phonon lines in Fig. 7.8, to the ladder vertex, so analogously as with the result for $\Theta_L^{(4)}(\mathbf{q}, \omega)$, we can write for the ladder vertex function in the $2n$ -th order

$$\Theta_L^{(2n)}(\mathbf{q}, \omega) = \prod_{k=1}^n \Theta^{(2)}(\mathbf{q}, \omega | k\omega_0). \tag{7.27}$$

Thus, in the ladder approximation, the full vertex function is given by the infinite sum

$$\begin{aligned}
\Theta_L(\mathbf{q}, \omega) &= \sum_{n=1}^{\infty} \Theta_L^{(2n)}(\mathbf{q}, \omega) = \sum_{n=1}^{\infty} \prod_{k=1}^n \Theta^{(2)}(\mathbf{q}, \omega|k\omega_0) \\
&= \Theta^{(2)}(\mathbf{q}, \omega|\omega_0) \left(1 + \Theta^{(2)}(\mathbf{q}, \omega|2\omega_0) \left(1 + \Theta^{(2)}(\mathbf{q}, \omega|3\omega_0) (1 + \dots) \right) \right) .
\end{aligned} \tag{7.28}$$

7.3 Phonon spectral properties

The phonon polarization is a powerful theoretical tool, however, it is not particularly useful from the experimental point of view. Therefore, to conclude the polaron Part II of the thesis, we also consider the more experimentally relatable phonon spectral function defined by

$$B(\mathbf{q}, \omega > 0) = -\frac{1}{\pi} \text{Im} D(\mathbf{q}, \omega > 0) . \tag{7.29}$$

We restrict $B(\mathbf{q}, \omega)$ to positive frequencies only, since $D(\mathbf{q}, \omega)$ is symmetric in ω . For the free phonon Green's function in Eq. (6.3), $B(\mathbf{q}, \omega > 0)$ has a simple delta peak structure

$$B_0(\mathbf{q}, \omega > 0) = \delta(\omega - \omega_0) , \tag{7.30}$$

accounting for all of the phonon spectral weight

$$z_{\mathbf{q}} = \int_0^{+\infty} d\omega B_0(\mathbf{q}, \omega > 0) = 1 . \tag{7.31}$$

Following the reasonings from the introduction to Chapter 7, in the polaron limit, we may obtain the full phonon Green's function by simply summing irreducible polarization contributions, rather than by solving the Dyson equation. That is, we may write for the phonon Green's function

$$D(\mathbf{q}, \omega) = D_0(\mathbf{q}, \omega) + \Pi_{IRR}(\mathbf{q}, \omega) [D_0(\mathbf{q}, \omega)]^2 , \tag{7.32}$$

where $\Pi_{IRR}(\mathbf{q}, \omega)$ is the sum of irreducible polarization contributions. Correspondingly,

$$\text{Im} D(\mathbf{q}, \omega) = \text{Im} D_0(\mathbf{q}, \omega) + \text{Im} \Pi_{IRR}(\mathbf{q}, \omega) \text{Re} [D_0(\mathbf{q}, \omega)]^2 + \text{Im} [D_0(\mathbf{q}, \omega)]^2 \text{Re} \Pi_{IRR}(\mathbf{q}, \omega) , \tag{7.33}$$

with

$$\text{Re} [D_0(\mathbf{q}, \omega)]^2 = \frac{4\omega_0^2}{[\omega^2 - \omega_0^2]^2} , \tag{7.34}$$

and

$$\begin{aligned} \text{Im} [D_0(\mathbf{q}, \omega)]^2 = & -\pi\delta(\omega - \omega_0)\frac{d}{d\omega} + \pi\delta(\omega + \omega_0)\frac{d}{d\omega} \\ & + 2\pi\frac{1}{\omega + \omega_0}\delta(\omega - \omega_0) - 2\pi\frac{1}{\omega - \omega_0}\delta(\omega + \omega_0), \end{aligned} \quad (7.35)$$

where we have used the identity $\frac{1}{(\omega \pm i\eta)^2} = \frac{1}{\omega^2} \mp i\pi\delta(\omega)\frac{d}{d\omega}$ [124].

7.3.1 Phonon transfer and phonon production

Let us now consider the phonon spectral function to the leading order, when $\Pi_{IRR}(\mathbf{q}, \omega) \approx \Pi^{(2)}(\mathbf{q}, \omega)$, given by Eq. (7.12). In that case we have

$$\text{Re}\Pi^{(2)}(\mathbf{q}, \omega) = \frac{g^2}{N} \frac{2\varepsilon_{\mathbf{q}}}{\omega^2 - \varepsilon_{\mathbf{q}}^2}, \quad \text{Im}\Pi^{(2)}(\mathbf{q}, \omega) = -\pi\frac{g^2}{N} [\delta(\omega - \varepsilon_{\mathbf{q}}) + \delta(\omega + \varepsilon_{\mathbf{q}})], \quad (7.36)$$

resulting in

$$B^{(2)}(\mathbf{q}, \omega > 0) = \left[1 - \frac{g^2}{N} \frac{4\varepsilon_{\mathbf{q}} (2\omega^2 + \omega_0\omega - \varepsilon_{\mathbf{q}}^2)}{(\omega + \omega_0) [\omega^2 - \varepsilon_{\mathbf{q}}^2]^2} \right] \delta(\omega - \omega_0) + \frac{g^2}{N} \frac{4\omega_0^2}{[\omega^2 - \omega_0^2]^2} \delta(\omega - \varepsilon_{\mathbf{q}}). \quad (7.37)$$

There are two important novelties to notice in comparison to the non-interacting case. First, some of the phonon spectral weight has been transferred from the pole at $\omega = \omega_0$ to the new pole at $\omega = \varepsilon_{\mathbf{q}}$ - the effect we dub a phonon transfer. The phonon spectral weight at the pole $\omega = \varepsilon_{\mathbf{q}}$ corresponds to the phonon spectral weight in the polaron band, introduced in Chapter 6, located below the phonon energy, $\varepsilon_{\mathbf{q}} < \omega_0$. Second, the sum rule in Eq. (7.31) is violated and the additional phonon spectral weight appears - we dub this effect a phonon production

$$\Delta B^{(2)}(\mathbf{q}, \omega > 0) = \int_0^{+\infty} d\omega B^{(2)}(\mathbf{q}, \omega > 0) - 1 = \frac{g^2}{N} \frac{2(2\omega_0 + \varepsilon_{\mathbf{q}})}{\omega_0(\omega_0 + \varepsilon_{\mathbf{q}})^2}. \quad (7.38)$$

The additional phonon spectral weight is a consequence of the lattice deformation that accompanies the polaron formation [102]. In particular, in the long-wavelength limit, $\Delta B(\mathbf{q}, \omega > 0) \sim \bar{n}_{ph}$, where \bar{n}_{ph} is the mean number of phonons in the ground state. Both those effects are actually very weak, scaling as $1/N$.

By going to the next-to-leading order, we expect no new qualitative effects, however, we

can for example study how is the phonon spectral weight in the polaron band affected by including the self-energy and vertex contributions in Figs. 7.3 (b), (c), and (d). As shown in Appendix B.2.4, the total imaginary part of the polarization in the next-to-leading order, $\Pi^{(4)}(\mathbf{q}, \omega) = \Pi^{(4b)}(\mathbf{q}, \omega) + \Pi^{(4c)}(\mathbf{q}, \omega) + \Pi^{(4d)}(\mathbf{q}, \omega)$, relevant for the pole at $\omega = \varepsilon_{\mathbf{q}}$ reads

$$\text{Im}\Pi^{(4)}(\mathbf{q}, \omega < \omega_0) = -\pi \frac{g^2}{N} F_{\mathbf{q}} \left[\delta(\omega - \varepsilon_{\mathbf{q}}) + \delta(\omega + \varepsilon_{\mathbf{q}}) \right] , \quad (7.39)$$

where

$$F_{\mathbf{q}} = \sum_{\mathbf{q}'} \left[\frac{1}{\omega_0 + \varepsilon_{\mathbf{q}'}} - \frac{1}{\omega_0 + \varepsilon_{\mathbf{q}+\mathbf{q}'} - \varepsilon_{\mathbf{q}}} \right]^2 . \quad (7.40)$$

Each term of $F_{\mathbf{q}}$ can be mapped one-to-one to the fourth order polarization diagrams in Figs. 7.3 (b), (c), and (d). Particularly, when squared, each term in the bracket characterizes the renormalization of one of the fermion lines, $Z_{\mathbf{q}}^{(2)}$ and $Z_0^{(2)}$, coming from the self-energy diagrams in Figs. 7.3(b) and (c), respectively. On the other hand, the product of these two terms corresponds to the vertex polarization diagram, Fig. 7.3(d), and is given by $\Theta^{(2)}(\mathbf{q}, \varepsilon_{\mathbf{q}})$. Therefore, in the next-to-leading order, the phonon spectral weight in the polaron band reads

$$B^{(4)}(\mathbf{q}, \omega = \varepsilon_{\mathbf{q}}) = \frac{g^2}{N} \frac{4\omega_0^2}{[\varepsilon_{\mathbf{q}}^2 - \omega_0^2]^2} [1 + F_{\mathbf{q}}] . \quad (7.41)$$

In the 1D case, the expression for F_q can be obtained in the closed form. The details of derivations of all contributions to F_q can be found in Appendices A.2.4 and B.2.4, giving

$$Z_q^{(2)} = \sum_{q'} \left[\frac{1}{\omega_0 + \varepsilon_{q+q'} - \varepsilon_q} \right]^2 = -g^2 \frac{(\omega_0 + 2t - \varepsilon_q)}{[(\omega_0 - \varepsilon_q)(\omega_0 + 4t - \varepsilon_q)]^{\frac{3}{2}}} < 0 , \quad (7.42)$$

and

$$\Theta^{(2)}(q, \varepsilon_q) = \frac{g^2}{2t^2} \left[\frac{\frac{\gamma_1}{\sqrt{\gamma_1^2 - 1}} + \frac{\gamma_2}{\sqrt{\gamma_2^2 - 1}}}{\gamma_1 \gamma_2 + \sqrt{(\gamma_1^2 - 1)(\gamma_2^2 - 1)} - \cos q} \right] > 0 , \quad (7.43)$$

where $\gamma_1 = 1 + \frac{\omega_0}{2t}$ and $\gamma_2 = 1 + \frac{\omega_0 - \omega}{2t}$. Since $Z_q^{(2)}$ is negative, self-energy corrections suppress the phonon spectral weight in the polaron band pole due to dressing effects. On the other hand, the vertex function $\Theta^{(2)}(q, \varepsilon_q)$ given by Eq. (7.43) is always positive, enhancing the phonon spectral weight in the polaron band pole by enhancing the bare vertex contribution

$$g^2 \rightarrow g^2 \left(1 + \Theta^{(2)}(q, \varepsilon_q) \right)^2 \approx g^2 \left(1 + 2\Theta^{(2)}(q, \varepsilon_q) \right) . \quad (7.44)$$

7.3.2 Renormalized electron propagator

By inspecting Eq. (7.37), there are, however, two evident issues that need to be addressed. First, the polaron band pole is located at the free electron energy $\varepsilon_{\mathbf{q}}$, while according to Chapter 6 it should be located at the renormalized energy $\varepsilon_{\mathbf{q}}^*$. Second, which is more severe, the spectral weights in Eq. (7.37) diverge as the electron energy approaches the phonon energy, $\varepsilon_{\mathbf{q}} \rightarrow \omega_0$. This latter issue is a general property of a perturbation theory when two energy levels are degenerate. To cure both of these problems, we thus have to renormalize the electron dispersion by means of the Dyson equation.

In particular, we use the renormalized fermion Green's function in the spirit of Chapter 6 to calculate the leading order polarization in Fig. 7.3(a). To be specific, we rederive Eq. (7.11) by replacing G_0 in Eq. (7.9) by the renormalized fermion Green's function

$$G_{pol}(\mathbf{k}, E) \approx \frac{Z_{\mathbf{k}}(1 - n_{\mathbf{k}})}{E - \varepsilon_{\mathbf{k}}^* + i\eta} + \frac{Z_{\mathbf{k}}n_{\mathbf{k}}}{E - \varepsilon_{\mathbf{k}}^* - i\eta}, \quad (7.45)$$

with $Z_{\mathbf{k}}$ and $\varepsilon_{\mathbf{k}}^*$ being the electron spectral weight and the polaron band dispersion, respectively, from Chapter 6. Here, we neglected the incoherent contribution to the fermion Green's function. Moreover, we assume that differences between the fermion Green's functions calculated for cases when an electron is injected in an empty band or a band with one electron already present are negligible.

The new form of the fermion Green's function in Eq. (7.45) does not change the actual derivation of $\Pi^{(2)}(\mathbf{q}, \omega)$ presented earlier. The only difference is that $\varepsilon_{\mathbf{q}}^*$ replaces $\varepsilon_{\mathbf{q}}$ and that additional factors Z_0 and $Z_{\mathbf{q}}$ appear, resulting in

$$\Pi^{(2)}(\mathbf{q}, \omega) = \frac{g^2}{N} \left[\frac{Z_0 Z_{\mathbf{q}}}{\omega - \varepsilon_{\mathbf{q}}^* + i\eta} - \frac{Z_0 Z_{\mathbf{q}}}{\omega + \varepsilon_{\mathbf{q}}^* - i\eta} \right]. \quad (7.46)$$

The corrected corresponding phonon spectral function now reads

$$B^{(2)}(\mathbf{q}, \omega > 0) = \left[1 - \frac{g^2 4Z_0 Z_{\mathbf{q}} \varepsilon_{\mathbf{q}}^* (2\omega^2 + \omega_0 \omega - \varepsilon_{\mathbf{q}}^{*2})}{N (\omega + \omega_0) [\omega^2 - \varepsilon_{\mathbf{q}}^{*2}]^2} \right] \delta(\omega - \omega_0) + \frac{g^2 4Z_0 Z_{\mathbf{q}} \omega_0^2}{N [\omega^2 - \omega_0^2]^2} \delta(\omega - \varepsilon_{\mathbf{q}}^*). \quad (7.47)$$

By recalling the results (we expect they hold also for $D > 1$) for the polaron band dispersion near the phonon energy in Eqs. (6.21) and (6.25), we note that true divergencies in Eq. (7.47) never appear. Moreover, $Z_{\mathbf{q}}$ smoothly vanishes as the phonon energy is approached, so the spectral weight at the polaron band pole vanishes too, as well as all the phonon transfer and phonon production effects. Evidently, the polaron band pole is located at the right energy $\varepsilon_{\mathbf{q}}^*$ just as well.

7.3.3 Small polaron

As our final result related to the polaron physics, we diagrammatically recover the well-known result for the phonon spectral weight in the polaron band pole in the small polaron case. As commented in Section 6.3, the electron self-energy in the small polaron case is momentum independent $\Sigma(E) = E_B/Z + E(1 - 1/Z)$ and the polaron band exponentially narrow $\varepsilon_{\mathbf{q}}^* = Z\varepsilon_{\mathbf{q}}$, with $Z = \exp(-g^2/\omega_0^2)$. The Ward identity, Eq. (7.6), therefore gives for the time-ordered vertex function

$$\Theta(|\mathbf{q}| \rightarrow 0, \omega) = 1 + \frac{E_B/Z - E_B/Z - \omega(1 - 1/Z)}{\omega} = \frac{1}{Z}, \quad (7.48)$$

while the fermion Green's function can be expressed in terms of the scaled free fermion Green's function $G_{pol}(\mathbf{k}, E) = G_0(\mathbf{k}, E/Z)$.

By exploiting those two expressions in Eq. (7.21) for the phonon polarization, a simple result readily follows

$$\text{Im}\Pi(\mathbf{q}, \omega < \omega_0) = -\pi \frac{g^2}{N} [\delta(\omega - Z\varepsilon_{\mathbf{q}}) + \delta(\omega + Z\varepsilon_{\mathbf{q}})] . \quad (7.49)$$

In other words, in the small polaron limit, for small frequencies, the exact polarization has the same form as the polarization obtained in the leading order of the perturbation theory, Eq. (7.36). The only difference is that the free electron dispersion $\varepsilon_{\mathbf{q}}$ is replaced by the small polaron dispersion $Z\varepsilon_{\mathbf{q}}$. Although this result has been obtained previously by other methods, it is quite fascinating to see how the diagrammatic expansion, when summed to the infinite order, recovers the simple $\text{Im}\Pi(\mathbf{q}, \omega) \propto \frac{g^2}{N}$ behavior. In particular, for future works it would be interesting to study in more detail how is the exact result in the small polaron limit obtained by the approximate form for the phonon polarization in Eq. (7.21).

7.4 Conclusions

We calculate the phonon polarization in the leading order and the next-to-leading order in electron-phonon coupling for cases with finite electron densities. For very low electron densities, we exploit the fact that in the polaron problem only one hole with the momentum $\mathbf{k} = 0$ may appear in order to obtain the dominant contributions to the polarization of the order $\mathcal{O}(1/N)$, with N being the number of lattice sites. By taking a closer look at the polarization diagram with the leading vertex correction in the time domain, we propose an approximate two-vertices renormalization scheme with the vertex function involving only the electron processes. Here, the crucial thing is to observe that the leading order vertex function of the order $\mathcal{O}(1/N)$, involving the hole $\mathbf{k} = 0$ line, can be interpreted as it renormalizes the left vertex in Fig. 7.5(b), albeit rather with only the electron processes. We argue that such a scheme gives the exact solution

for the phonon polarization in the ladder approximation and provides the analytical expression for the corresponding vertex function to the infinite order.

By further exploiting the $1/N$ expansion, we argue that the Dyson approach is inferior to the simple addition of irreducible polarizations in determining the full phonon propagator. Consequently, the renormalization of the phonon frequency is negligible, albeit some of its phonon spectral weight is nevertheless being transferred to the polaron band. The phonon spectral weight in the polaron band is calculated up to the next-to-leading order of the perturbation theory in electron-phonon interaction. Apart from the phonon transfer effects, we note a phonon production contribution, accounting for an additional, enhanced total phonon spectral weight. It can be attributed to the virtual cloud of phonons accompanying the electron in the polaron ground state.

Part III

Spectral properties of moderately to heavily doped polar systems

Electron spectral properties

Parts of Chapter 8 have been published in [125]. Some of the results discussed here were performed in collaboration with A. S. Mishchenko.

In the previous two Parts I and II of the thesis, we considered systems with very low electron densities. In such situations, correlations between dilute electrons are arguably negligible and charge carriers behave as a non-degenerate gas coupled to a crystal lattice. As the electron concentration starts increasing, the correlations, however, become growingly important, giving rise to novel phenomena in combination with the electron-phonon interaction. In metallic systems, for instance, the electron-phonon interaction may lead to a transition to a conventional BCS superconducting [126] or a charge density wave state accompanied by the Peierls instability [127–129]. Profound influences of the electron-phonon interaction are noticeable in spectral features of moderately to heavily doped polar semiconductors as well. In particular, while the ARPES spectra feature phonon sidebands below the quasiparticle band [84, 87, 125, 130, 131], both the Raman and the infrared spectroscopy measurements on doped polar semiconductors contain fingerprints of a phonon-plasmon coupling [132–143]. Here, we put a major of focus on latter systems and it is the task of Part III of the thesis to shed some light on some of electron and phonon spectral properties.

8.1 Leading order weak coupling perturbation theory

Following the same approach as in Part II, we start the discussion by considering electron spectral properties of polar systems with finite electron densities ($\mu \neq 0$) within the perturbation theory in the electron-phonon coupling. In particular, we consider the weak coupling expansion of the fermion self-energy, with the leading order contribution shown diagrammatically in Fig. 8.1. The diagrams in Figs. 6.1 and 8.1 are topologically equivalent, with the important difference that the fermion line in Fig. 8.1 goes in both directions of time, representing either the electron or the hole propagation, while in Fig. 6.1 it strictly represents the electron propagation. From the technical point of view, this implies that in all our forthcoming calculations we have to keep both contributions to the fermion Green's function in Eq. (1.7).

By using the standard Feynman rules [40], we can write the expression for the leading order fermion self-energy in Fig. 8.1

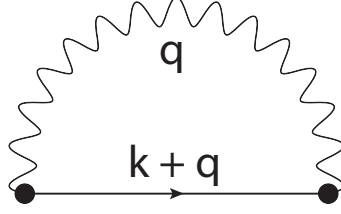


Figure 8.1: Diagrammatic representation of the leading order fermion self-energy in the weak coupling perturbation theory in cases with finite electron densities.

$$\Sigma^{(2)}(\mathbf{k}, E) = \sum_{\mathbf{q}} |g(\mathbf{q})|^2 i \int_{-\infty}^{+\infty} \frac{d\omega}{2\pi} G_0(\mathbf{k} + \mathbf{q}, E + \omega) D_0(\mathbf{q}, \omega) . \quad (8.1)$$

The integration over the energy ω gives

$$\begin{aligned} & i \int_{-\infty}^{+\infty} \frac{d\omega}{2\pi} G_0(\mathbf{k} + \mathbf{q}, E + \omega) D_0(\mathbf{q}, \omega) = \\ & = i \int_{-\infty}^{+\infty} \frac{d\omega}{2\pi} \left[\frac{1 - n_{\mathbf{k}+\mathbf{q}}}{E + \omega - \xi_{\mathbf{k}+\mathbf{q}} + i\eta} + \frac{n_{\mathbf{k}+\mathbf{q}}}{E + \omega - \xi_{\mathbf{k}+\mathbf{q}} - i\eta} \right] \left[\frac{1}{\omega - \omega_0 + i\eta} - \frac{1}{\omega + \omega_0 - i\eta} \right] \\ & = \left[\frac{1 - n_{\mathbf{k}+\mathbf{q}}}{E - \omega_0 - \xi_{\mathbf{k}+\mathbf{q}} + i\eta} + \frac{n_{\mathbf{k}+\mathbf{q}}}{E + \omega_0 - \xi_{\mathbf{k}+\mathbf{q}} - i\eta} \right] . \end{aligned} \quad (8.2)$$

As a result, the expression for the leading order self-energy reads

$$\Sigma^{(2)}(\mathbf{k}, E) = \sum_{\mathbf{q}} |g(\mathbf{q})|^2 \left[\frac{1 - n_{\mathbf{k}+\mathbf{q}}}{E - \omega_0 - \xi_{\mathbf{k}+\mathbf{q}} + i\eta} + \frac{n_{\mathbf{k}+\mathbf{q}}}{E + \omega_0 - \xi_{\mathbf{k}+\mathbf{q}} - i\eta} \right] . \quad (8.3)$$

8.1.1 First phonon sideband

The expression in Eq. (8.3) is completely general, in the sense that it holds irrespectively to the system dimension, and we did not specify the exact form of the electron-phonon interaction. This allows us to exploit the properties of Eq. (8.3) in both the 2D and the 3D cases, with both short-range and long-range electron-phonon interactions, in order to model ARPES spectra of real materials. However, it is instructive to also consider properties of the leading order fermion self-energy in some simpler cases, when both the real and the imaginary part of Eq. (8.3) can be evaluated analytically. In particular, the exact evaluation of the summation/integration over q is presented in Appendix A.1.1 in the 1D case with the electron dispersion $\varepsilon_k = 2t(1 - \cos k)$ and the Holstein coupling. The final result for the real part of Eq. (8.3) in that case reads

$$\text{Re}\Sigma^{(2)}(E) = \begin{cases} -\frac{g^2}{\sqrt{(E+\omega_0+\mu)(E+\omega_0+\mu-4t)}} \left\{ \frac{2}{\pi} \arctan \left[\sqrt{\frac{E+\omega_0+\mu-4t}{E+\omega_0+\mu}} \sqrt{\frac{\mu}{4t-\mu}} \right] \right\}, & E < -\omega_0 - \mu, \\ \frac{g^2}{\sqrt{(E+\omega_0+\mu)(E+\omega_0+\mu-4t)}} \left\{ \frac{2}{\pi} \arctan \left[\sqrt{\frac{E+\omega_0+\mu-4t}{E+\omega_0+\mu}} \sqrt{\frac{\mu}{4t-\mu}} \right] \right\}, & E > -\omega_0 - \mu + 4t \\ \frac{g^2}{\sqrt{(E+\omega_0+\mu)(4t-\omega_0-\mu-E)}} \left\{ \frac{1}{\pi} \ln \left| \frac{\sqrt{4t-\omega_0-\mu-E} \sqrt{\frac{\mu}{4t-\mu}} + \sqrt{E+\omega_0+\mu}}{\sqrt{4t-\omega_0-\mu-E} \sqrt{\frac{\mu}{4t-\mu}} - \sqrt{E+\omega_0+\mu}} \right| \right\}, & -\omega_0 - \mu < E < -\omega_0 - \mu + 4t, \\ -\frac{g^2}{\sqrt{(E-\omega_0+\mu)(E-\omega_0+\mu-4t)}} \left\{ 1 - \frac{2}{\pi} \arctan \left[\sqrt{\frac{E-\omega_0+\mu-4t}{E-\omega_0+\mu}} \sqrt{\frac{\mu}{4t-\mu}} \right] \right\}, & E < \omega_0 - \mu, \\ \frac{g^2}{\sqrt{(E-\omega_0+\mu)(E-\omega_0+\mu-4t)}} \left\{ 1 - \frac{2}{\pi} \arctan \left[\sqrt{\frac{E-\omega_0+\mu-4t}{E-\omega_0+\mu}} \sqrt{\frac{\mu}{4t-\mu}} \right] \right\}, & E > \omega_0 + 4t - \mu, \\ -\frac{g^2}{\sqrt{(E-\omega_0+\mu)(4t+\omega_0-\mu-E)}} \left\{ \frac{1}{\pi} \ln \left| \frac{\sqrt{4t+\omega_0-\mu-E} \sqrt{\frac{\mu}{4t-\mu}} + \sqrt{E-\omega_0+\mu}}{\sqrt{4t+\omega_0-\mu-E} \sqrt{\frac{\mu}{4t-\mu}} - \sqrt{E-\omega_0+\mu}} \right| \right\}, & \omega_0 - \mu < E < \omega_0 + 4t - \mu, \\ 0, & \text{elsewhere,} \end{cases} \quad (8.4)$$

while its imaginary part equals

$$\text{Im}\Sigma^{(2)}(E) = g^2 \left\{ -\frac{\Theta(E-\omega_0)\Theta(4t+\omega_0-\mu-E)}{\sqrt{(E-\omega_0+\mu)(4t+\omega_0-\mu-E)}} + \frac{\Theta(E+\omega_0+\mu)\Theta(-\omega_0-E)}{\sqrt{(E+\omega_0+\mu)(4t-\omega_0-\mu-E)}} \right\}. \quad (8.5)$$

By simply putting Fermi level to zero, $\mu \rightarrow 0$, in Eqs. (8.4) and (8.5), the results in Eqs. (6.5) and (6.6), corresponding to the polaron limit, are straightforwardly recovered.

In contrast to the polaron case where we were most interested in the renormalization effects coming from the real part of the self-energy, here we put more attention on its imaginary part. By inspecting Eq. (8.5), we see that the imaginary part of the self-energy is zero in the energy window around the Fermi level $-\omega_0 < E < \omega_0$ (E is measured from the Fermi energy), suggesting that electron excitations around the Fermi level stay perfectly coherent despite the interaction with the optical phonon, at least to the leading order. This changes, however, as soon as the phonon energy is surpassed, as indicated by non-zero values of the imaginary part of the self-energy in the energy window $\omega_0 < E < 4t + \omega_0 - \mu$, present already in the polaron case ($\mu = 0$), but also within the new energy range $-\omega_0 - \mu < E < -\omega_0$. In those two energy windows, electron spectral functions exhibit non-trivial incoherent structures, which we call first phonon sidebands.

8.1.2 Comment on the leading order diagram in the time domain

Before the study of the structure of the imaginary part of the fermion self-energy in the next-to-leading order of the weak coupling perturbation theory, it is instructive to discuss the leading order contribution from the point of view of time-ordered diagrams. In particular, since in Fig. 8.1 the fermion line represents either the electron or the hole, the propagation of an electron in the leading order can be diagrammatically sketched by two processes shown in Fig. 8.2.

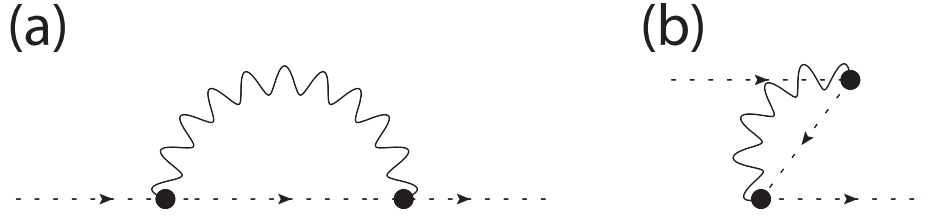


Figure 8.2: Two possible time-ordered Feynman diagrams that represent the leading order electron Green's function in cases with finite electron densities.

Obviously, the diagram in Fig. 8.2(a) represents the electron scattered in the intermediate state with one phonon in the system. However, the more intriguing is the diagram in Fig. 8.2(b) involving the formation of an electron-hole pair and the subsequent annihilation of the hole with the incoming electron. During the intermediate process in Fig. 8.2(b), it appears that two electrons with the same momentum and spin are present, violating thus the Pauli exclusion principle.

The resolution to the apparent breakdown of the Pauli exclusion principle in the process shown in Fig. 8.2(b) consists of two parts. First, we note that this process actually raises, rather than lowers, the energy of the electron [144]. Namely, in the ground state, there are virtual fluctuations that lower the ground state energy. However, by adding the electron with the momentum \mathbf{k} , the vacuum fluctuations with $\mathbf{k}' = \mathbf{k}$ are prevented and the elimination of those vacuum fluctuations raises the energy of the electron. Accordingly, the time-ordered diagram in Fig. 8.2(b) violating the Pauli exclusion principle actually describes the suppression of vacuum fluctuations.

Following this interpretation, the time-ordered self-energy contribution in Fig. 8.2(b) cancels with some vacuum fluctuation, meaning that in the formal expansion of the Green's function this contribution vanishes. However, when doing the standard Green's function expansion by keeping only irreducible connected diagrams, all vacuum fluctuations are already canceled since they are represented by disconnected diagrams, leaving no choice but to keep in the expansion all time-ordered connected diagrams which violate the Pauli exclusion principle. For more details see Appendix C. The point here is that only the Green's function as a whole represents a physical process, while its parts, like one in Fig. 8.2(b) may or may not be physical [145]. Those non-physicalities are the consequence of the mathematical regrouping in the perturbation theory, that is, of the decomposition of the whole physical process into its simpler parts, which are not necessarily physical.

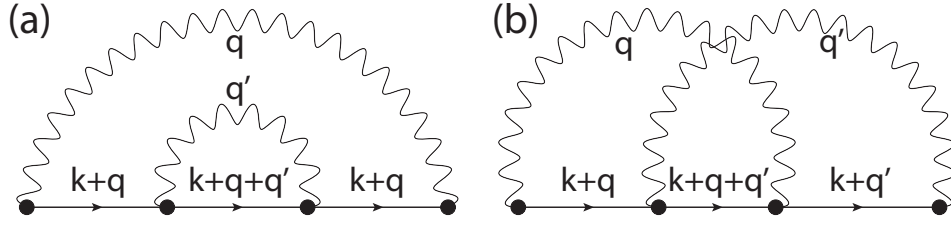


Figure 8.3: Diagrammatic representation of two next-to-leading order contributions in the electron-phonon coupling to the fermion self-energy in cases with finite electron densities. (a) Non-crossing and (b) crossing diagram.

8.2 Next-to-leading order weak coupling perturbation theory

Similar to the polaron case, two contributions to the fermion self-energy in the next-to-leading order in cases with finite electron densities are represented by the non-crossing and the crossing diagram shown in Figs. 8.3(a) and (b), respectively. Both diagrams are straightforward, although tedious to evaluate, with the details of calculations given in Appendices A.2.1 and A.2.2. The final expression for the fermion self-energy corresponding to the non-crossing diagram can be represented as a sum of six contributions

$$\Sigma^{(NC)}(\mathbf{k}, E) = \sum_{\mathbf{q}, \mathbf{q}'} |g(\mathbf{q})|^2 |g(\mathbf{q}')|^2 \sum_{i=1}^6 \sigma_i^{(NC)}, \quad (8.6)$$

while the correction to the fermion self-energy stemming from the crossing diagram as a sum of eighteen contributions

$$\Sigma^{(C)}(\mathbf{k}, E) = \sum_{\mathbf{q}, \mathbf{q}'} |g(\mathbf{q})|^2 |g(\mathbf{q}')|^2 \sum_{i=1}^{18} \sigma_i^{(C)}, \quad (8.7)$$

with all $\sigma_i^{(NC)}$ and $\sigma_i^{(C)}$ listed in Appendices A.2.1 and A.2.2.

Evidently, the number of contributions to the fermion self-energy in the next-to-leading order is enormous and the whole analysis of the fermion self-energy can be a bit overwhelming. Therefore, we put focus only on imaginary parts of the calculated self-energy contributions, which is, as we shall argue, sufficient to study the structure of phonon sidebands and the lifetime of excitations in the vicinity of the Fermi level. In particular, we distinguish electron ($E > 0$) and hole ($E < 0$) part of spectra, and electron and hole phonon sidebands located above and below $E = 0$, respectively, and analyze only the latter. In that regard, we note that whenever $n_{\mathbf{k}}$ appears in the numerator of $\sigma_i^{(NC)}$ or $\sigma_i^{(C)}$, in the denominator we have $\xi_{\mathbf{k}} < 0$. Analogously, for $1 - n_{\mathbf{k}}$ in the numerator, $\xi_{\mathbf{k}} > 0$ holds in the denominator.

With that in mind, we can start extracting imaginary parts of the self-energy expressions in Eqs. (8.6) and (8.7) by recalling the identity $\frac{1}{\omega \pm i\eta} = \frac{1}{\omega} \mp i\pi\delta(\omega)$. For starters, we note that

both the non-crossing and the crossing diagram give non-vanishing contributions in the energy window of the first hole phonon sideband, $-\omega_0 - \mu < E < -\omega_0$. In particular, we see that two contributions $\sigma_i^{(NC)}$ of the non-crossing diagram given by Eqs. (A.38) and (A.39) satisfy $\text{Im}\sigma_i^{(NC)} \propto \sum_{\mathbf{q}} n_{\mathbf{k}+\mathbf{q}} \delta(E + \omega_0 - \varepsilon_{\mathbf{k}+\mathbf{q}})$, while the same holds true for the contributions $\sigma_i^{(C)}$ of the crossing diagram given by Eqs. (A.52), (A.55), (A.56), (A.57), (A.58), (A.61), (A.64), (A.65), (A.66), and (A.67). Nevertheless, we anticipate that the contributions of $\text{Im}\Sigma^{(C)}$ and $\text{Im}\Sigma^{(NC)}$ to the first hole phonon sideband are very small in comparison to the leading order contribution coming from $\text{Im}\Sigma^{(2)}$, at least for weak electron-phonon couplings, so we exclude them from our further discussions.

There are, however, two novelties that were not present in the leading order case. Namely, by inspecting the contributions $\text{Im}\sigma_i^{(NC)}$ of the non-crossing diagram coming from Eqs. (A.35) and (A.38), and the contributions $\text{Im}\sigma_i^{(C)}$ of the crossing diagram coming from Eqs. (A.59), (A.61), (A.65), and (A.67), we see that they additionally have non-vanishing values in the energy region $-2\omega_0 - \mu < E < -2\omega_0$. In other words, the next-to-leading order fermion self-energy gives rise to the leading order contribution to the second hole phonon sideband. In particular, in the corresponding energy window, $-2\omega_0 - \mu < E < -2\omega_0$, the imaginary part of $\Sigma^{(NC)}(\mathbf{k}, E)$ reads

$$\begin{aligned} \text{Im}\Sigma^{(NC)}(\mathbf{k}, E) &= \pi \sum_{\mathbf{q}, \mathbf{q}'} |g(\mathbf{q})|^2 |g(\mathbf{q}')|^2 \delta(E + 2\omega_0 - \xi_{\mathbf{k}+\mathbf{q}+\mathbf{q}'}) \times \\ &\times \left[\frac{(1 - n_{\mathbf{k}+\mathbf{q}})^2 n_{\mathbf{k}+\mathbf{q}+\mathbf{q}'}}{(\xi_{\mathbf{k}+\mathbf{q}} + \omega_0 - \xi_{\mathbf{k}+\mathbf{q}+\mathbf{q}'})^2} + \frac{(n_{\mathbf{k}+\mathbf{q}})^2 n_{\mathbf{k}+\mathbf{q}+\mathbf{q}'}}{(\xi_{\mathbf{k}+\mathbf{q}+\mathbf{q}'} - \omega_0 - \xi_{\mathbf{k}+\mathbf{q}})^2} \right] \\ &= \pi \sum_{\mathbf{q}, \mathbf{q}'} |g(\mathbf{q})|^2 |g(\mathbf{q}')|^2 \frac{n_{\mathbf{k}+\mathbf{q}+\mathbf{q}'}}{(\xi_{\mathbf{k}+\mathbf{q}+\mathbf{q}'} - \omega_0 - \xi_{\mathbf{k}+\mathbf{q}})^2} \delta(E + 2\omega_0 - \xi_{\mathbf{k}+\mathbf{q}+\mathbf{q}'}), \end{aligned} \quad (8.8)$$

while $\Sigma^{(C)}(\mathbf{k}, E)$ contributes to the second hole phonon sideband with

$$\begin{aligned} \text{Im}\Sigma^{(C)}(\mathbf{k}, E) &= \pi \sum_{\mathbf{q}, \mathbf{q}'} |g(\mathbf{q})|^2 |g(\mathbf{q}')|^2 \delta(E + 2\omega_0 - \xi_{\mathbf{k}+\mathbf{q}+\mathbf{q}'}) \times \\ &\times \left[\frac{(1 - n_{\mathbf{k}+\mathbf{q}}) n_{\mathbf{k}+\mathbf{q}+\mathbf{q}'} (1 - n_{\mathbf{k}+\mathbf{q}'})}{(\xi_{\mathbf{k}+\mathbf{q}+\mathbf{q}'} - \omega_0 - \xi_{\mathbf{k}+\mathbf{q}})(\xi_{\mathbf{k}+\mathbf{q}+\mathbf{q}'} - \omega_0 - \xi_{\mathbf{k}+\mathbf{q}'})} + \frac{n_{\mathbf{k}+\mathbf{q}} n_{\mathbf{k}+\mathbf{q}+\mathbf{q}'} (1 - n_{\mathbf{k}+\mathbf{q}'})}{(\xi_{\mathbf{k}+\mathbf{q}+\mathbf{q}'} - \omega_0 - \xi_{\mathbf{k}+\mathbf{q}})(\xi_{\mathbf{k}+\mathbf{q}+\mathbf{q}'} - \omega_0 - \xi_{\mathbf{k}+\mathbf{q}'})} \right] \\ &\frac{(1 - n_{\mathbf{k}+\mathbf{q}}) n_{\mathbf{k}+\mathbf{q}+\mathbf{q}'} n_{\mathbf{k}+\mathbf{q}'}}{(\xi_{\mathbf{k}+\mathbf{q}+\mathbf{q}'} - \omega_0 - \xi_{\mathbf{k}+\mathbf{q}})(\xi_{\mathbf{k}+\mathbf{q}+\mathbf{q}'} - \omega_0 - \xi_{\mathbf{k}+\mathbf{q}'})} + \frac{n_{\mathbf{k}+\mathbf{q}} n_{\mathbf{k}+\mathbf{q}+\mathbf{q}'} n_{\mathbf{k}+\mathbf{q}'}}{(\xi_{\mathbf{k}+\mathbf{q}+\mathbf{q}'} - \omega_0 - \xi_{\mathbf{k}+\mathbf{q}})(\xi_{\mathbf{k}+\mathbf{q}+\mathbf{q}'} - \omega_0 - \xi_{\mathbf{k}+\mathbf{q}'})} \\ &= \pi \sum_{\mathbf{q}, \mathbf{q}'} |g(\mathbf{q})|^2 |g(\mathbf{q}')|^2 \frac{n_{\mathbf{k}+\mathbf{q}+\mathbf{q}'}}{(\xi_{\mathbf{k}+\mathbf{q}+\mathbf{q}'} - \omega_0 - \xi_{\mathbf{k}+\mathbf{q}})(\xi_{\mathbf{k}+\mathbf{q}+\mathbf{q}'} - \omega_0 - \xi_{\mathbf{k}+\mathbf{q}'})} \delta(E + 2\omega_0 - \xi_{\mathbf{k}+\mathbf{q}+\mathbf{q}'}). \end{aligned} \quad (8.9)$$

giving in total

$$\begin{aligned} \text{Im}\Sigma^{(4)}(\mathbf{k}, E) = & \pi \sum_{\mathbf{q}, \mathbf{q}'} |g(\mathbf{q})|^2 |g(\mathbf{q}')|^2 \frac{n_{\mathbf{k}+\mathbf{q}+\mathbf{q}'}}{\xi_{\mathbf{k}+\mathbf{q}+\mathbf{q}'} - \omega_0 - \xi_{\mathbf{k}+\mathbf{q}}} \delta(E + 2\omega_0 - \xi_{\mathbf{k}+\mathbf{q}+\mathbf{q}'}) \times \\ & \times \left[\frac{1}{\xi_{\mathbf{k}+\mathbf{q}+\mathbf{q}'} - \omega_0 - \xi_{\mathbf{k}+\mathbf{q}}} + \frac{1}{\xi_{\mathbf{k}+\mathbf{q}+\mathbf{q}'} - \omega_0 - \xi_{\mathbf{k}+\mathbf{q}'}} \right]. \end{aligned} \quad (8.10)$$

8.2.1 Exchange processes

The second novelty appearing in the next-to-leading order is related to the excitations' lifetime in the vicinity of the Fermi level. Namely, we have shown that the imaginary part of the leading order self-energy has non-vanishing values only in the energy regions corresponding to phonon sidebands, leaving the energy window around the Fermi level perfectly coherent. The same holds true for the non-crossing diagram contributions, however, on closer inspection of the crossing diagram contributions, we note that the imaginary parts of $\sigma_i^{(C)}$ given by Eqs. (A.53), (A.55), (A.56), (A.58), (A.59), (A.60), (A.62), and (A.63), have non-zero values arbitrarily close to the Fermi level. Specifically, the former four contribute to the hole, while the latter four to the electron side of spectra. By focusing only on the hole side, we have for energies E around the Fermi level

$$\begin{aligned} \text{Im}\Sigma^{(C)}(\mathbf{k}, E) = & \pi \sum_{\mathbf{q}, \mathbf{q}'} |g(\mathbf{q})|^2 |g(\mathbf{q}')|^2 n_{\mathbf{k}+\mathbf{q}} (1 - n_{\mathbf{k}+\mathbf{q}+\mathbf{q}'}) n_{\mathbf{k}+\mathbf{q}'} \delta(E - \xi_{\mathbf{k}+\mathbf{q}} - \xi_{\mathbf{k}+\mathbf{q}'} + \xi_{\mathbf{k}+\mathbf{q}+\mathbf{q}'}) \times \\ & \times \left[\frac{1}{(\xi_{\mathbf{k}+\mathbf{q}'} - \omega_0 - \xi_{\mathbf{k}+\mathbf{q}+\mathbf{q}'}) (\xi_{\mathbf{k}+\mathbf{q}} + \omega_0 - \xi_{\mathbf{k}+\mathbf{q}+\mathbf{q}'})} + \frac{1}{(\xi_{\mathbf{k}+\mathbf{q}} - \omega_0 - \xi_{\mathbf{k}+\mathbf{q}+\mathbf{q}'}) (\xi_{\mathbf{k}+\mathbf{q}'} + \omega_0 - \xi_{\mathbf{k}+\mathbf{q}+\mathbf{q}'})} \right. \\ & \left. - \frac{1}{(\xi_{\mathbf{k}+\mathbf{q}} - \omega_0 - \xi_{\mathbf{k}+\mathbf{q}+\mathbf{q}'}) (\xi_{\mathbf{k}+\mathbf{q}'} - \omega_0 - \xi_{\mathbf{k}+\mathbf{q}+\mathbf{q}'})} - \frac{1}{(\xi_{\mathbf{k}+\mathbf{q}} + \omega_0 - \xi_{\mathbf{k}+\mathbf{q}+\mathbf{q}'}) (\xi_{\mathbf{k}+\mathbf{q}'} + \omega_0 - \xi_{\mathbf{k}+\mathbf{q}+\mathbf{q}'})} \right] \\ & = -\pi \sum_{\mathbf{q}, \mathbf{q}'} |g(\mathbf{q})|^2 |g(\mathbf{q}')|^2 \frac{4\omega_0^2}{[(\xi_{\mathbf{k}+\mathbf{q}} - \xi_{\mathbf{k}+\mathbf{q}+\mathbf{q}'})^2 - \omega_0^2] [(\xi_{\mathbf{k}+\mathbf{q}'} - \xi_{\mathbf{k}+\mathbf{q}+\mathbf{q}'})^2 - \omega_0^2]} \\ & \times n_{\mathbf{k}+\mathbf{q}} (1 - n_{\mathbf{k}+\mathbf{q}+\mathbf{q}'}) n_{\mathbf{k}+\mathbf{q}'} \delta(E - \xi_{\mathbf{k}+\mathbf{q}} - \xi_{\mathbf{k}+\mathbf{q}'} + \xi_{\mathbf{k}+\mathbf{q}+\mathbf{q}'}). \end{aligned} \quad (8.11)$$

Since the excitation's lifetime is determined by $\tau^{-1}(\mathbf{k}, E) = |\text{Im}\Sigma(\mathbf{k}, E)|$, we may conclude that the leading vertex contribution to the fermion self-energy influences the damping of excitations in the vicinity of the Fermi level.

We should carefully interpret this intriguing result, because for finite electron densities there exists one more fermion self-energy contribution in the next-to-leading order shown diagrammatically in Fig. 8.4. The process depicted by the corresponding diagram can be interpreted either as the phonon-mediated electron/hole scattering on the electron-hole continuum or as the electron/hole emitting and absorbing a phonon dressed by an electron-hole pair. Anyhow, the evaluation of the self-energy diagram in Fig. 8.4 is presented in Appendix A.2.3, where the final

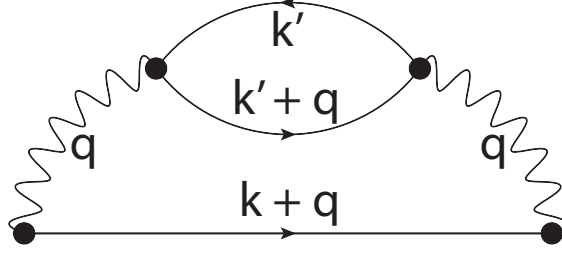


Figure 8.4: Next-to-leading order fermion self-energy diagram representing the phonon-mediated electron scattering on the electron-hole continuum.

result has been expressed as the sum of fourteen contributions $\sigma_i^{(B)}$

$$\Sigma^{(B)}(\mathbf{k}, E) = \sum_{\mathbf{q}, \mathbf{q}'} |g(\mathbf{q})|^4 \sum_{i=1}^{14} \sigma_i^{(B)}. \quad (8.12)$$

By inspecting the imaginary parts of $\sigma_i^{(B)}$, we can see that $\text{Im}\Sigma^{(B)}(\mathbf{k}, E)$ contributes only to the first phonon sidebands and not to the second. More importantly, $\text{Im}\Sigma^{(B)}(\mathbf{k}, E)$ does not vanish in the vicinity of the Fermi level, but rather reads, see Appendix A.2.3,

$$\begin{aligned} \text{Im}\Sigma^{(B)}(\mathbf{k}, E) &= \pi \sum_{\mathbf{q}, \mathbf{q}'} |g(\mathbf{q})|^4 \frac{4\omega_0^2}{\left[(\xi_{\mathbf{k}+\mathbf{q}'} - \xi_{\mathbf{k}+\mathbf{q}+\mathbf{q}'})^2 - \omega_0^2 \right]^2} \\ &\times n_{\mathbf{k}+\mathbf{q}} (1 - n_{\mathbf{k}+\mathbf{q}+\mathbf{q}'}) n_{\mathbf{k}+\mathbf{q}'} \delta(E - \xi_{\mathbf{k}+\mathbf{q}} - \xi_{\mathbf{k}+\mathbf{q}'} + \xi_{\mathbf{k}+\mathbf{q}+\mathbf{q}'}), \end{aligned} \quad (8.13)$$

in the relevant energy window around the Fermi energy.

Evidently, in both Eqs. (8.11) and (8.13) the following factor appears

$$\text{Im}\Sigma^{(B,C)}(\mathbf{k}, E) \propto \sum_{\mathbf{q}, \mathbf{q}'} n_{\mathbf{k}+\mathbf{q}} (1 - n_{\mathbf{k}+\mathbf{q}+\mathbf{q}'}) n_{\mathbf{k}+\mathbf{q}'} \delta(E - \xi_{\mathbf{k}+\mathbf{q}} - \xi_{\mathbf{k}+\mathbf{q}'} + \xi_{\mathbf{k}+\mathbf{q}+\mathbf{q}'}), \quad (8.14)$$

determining the available phase space for the excitations' relaxation. In fact, this is the same phase space factor that appears in Landau's general argument regarding the relaxation rate of excitations near the Fermi level in a Fermi liquid [145]. It states that the relaxation rate of excitations becomes smaller and eventually vanishes as the Fermi level is approached.

It is not so unexpected that the process in Fig. 8.4 leads to the Fermi liquid behavior since we have already argued that it can be interpreted as the phonon-mediated electron/hole scattering on the electron-hole continuum. Namely, the applicability of Landau's original result depends only on the phase space available for the scattering on the electron-hole continuum and not on the specific details of the effective electron-electron interaction. What is more exciting is that

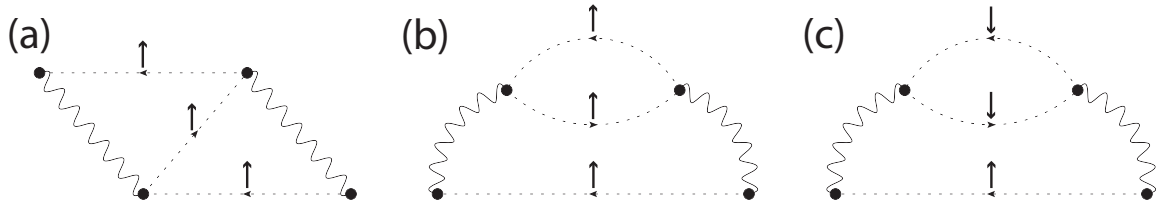


Figure 8.5: (a) Time-ordered crossing diagram influencing the hole relaxation rate near the Fermi level. While in the crossing diagram all fermion lines necessarily possess the same projection of spin, denoted with up/down arrows, as the incident hole, the closed loop in the bubble diagram may have both projections of spin (b) and (c).

the same phase space factor stems from the processes involving the leading vertex correction as well. On top of that, the two contributions $\text{Im}\Sigma^{(B,C)}(\mathbf{k}, E)$ are of the opposite sign, meaning that leading vertex correction processes tend to suppress the electron/hole scattering on the electron-hole continuum.

In order to fully rationalize this result, one should take into account and fermionic spin degree of freedom. In particular, for an incoming hole with a spin $s = +\frac{1}{2}$, which we denote with an up arrow, the relevant time-ordered self-energy diagrams with non-vanishing imaginary parts around the Fermi level are shown in Fig. 8.5. Following Fig. 8.5(a), the corresponding time-ordered leading vertex contribution can be interpreted as an exchange process, in which an incoming hole is exchanged with a hole created from a vacuum fluctuation. Because the electron-phonon interaction in Eq. (5.1) cannot flip the fermion spin, all fermion propagators in the vertex correction diagram in Fig. 8.5(a) necessarily possess the same projection of spin. This is not the case with the bubble diagram, where the fermion propagators contributing to the closed loop may possess both projections of spin, Figs. 8.5(b) and (c). Obviously, the exchange process depicted in Fig. 8.5(a) suppresses only the scattering of holes with the same projections of spin s , Fig. 8.5(b).

Finally, we note that in the case with the momentum-independent Holstein coupling the two contributions given by Eqs. (8.11) and (8.13), that is, the contributions of the diagrams in Figs. 8.5(a) and (b), respectively, cancel exactly in the adiabatic regime when there are no retardation effects. This scenario is analogous to the scenario in the Hubbard model [83], where electrons mutually interact with the short-range instantaneous electron-electron interaction. Due to this specific nature of the Hubbard interaction, the scattering between electrons with the same projections of spin is forbidden by the Pauli exclusion principle, meaning that the topologically equivalent diagrams to the ones in Figs. 8.5(a) and (b), with the phonon lines replaced by the Hubbard interaction lines, are absent, and that the electron/hole scattering on the electron-hole continuum is fully determined by the process in Fig. 8.5(c). This points to the fact that the suppression/cancellation of the diagrams in Fig. 8.5(a) and (b) is a diagrammatic way of obeying the Pauli exclusion principle [40]. However, since the electron-phonon interaction is

generally retarded, the cancellation of diagrams in Fig. 8.5(a) and (b) is not fully complete and the scattering between electron/holes with the same projection of spin becomes only partially suppressed by the exchange processes. Nevertheless, it is interesting to find that the Fermi liquid behavior, $\text{Im}\Sigma(E \rightarrow 0) \rightarrow E^2$, may be obtained in the context of the electron-phonon model alone.

8.3 Determination of electron-phonon interaction range from ARPES spectra

To show that the presented thorough analytical evaluations of the self-energy to the next-to-leading order are not interesting only from the point of view of theoretical considerations *per se*, in what follows we exploit the results obtained in Sections 8.1 and 8.2 to simulate ARPES spectra measured on real materials. Namely, in an ARPES measurement one expels an electron from a material and *de facto* engages a propagation of a hole. Therefore, the spectral function of the hole is measured, which in turn can be theoretically simulated by knowing the hole's self-energy.

As has been well established [146], and shown in our calculations, an ARPES spectrum of materials with significant polaronic correlations exhibits hole phonon sidebands below the quasiparticle band. Indeed, this was confirmed in a great number of experiments on 2D and 3D materials [84–87, 147–150] characterized by the significant electron-phonon interaction, see Fig. 8.6. Soon after, these experimental observations of hole phonon sidebands were followed by numerous *ab initio* simulations of measured spectra [130, 149, 151], reproducing the occurrence of hole phonon sidebands below the quasiparticle band. Due to limited resolutions, only two hole phonon sidebands are usually well captured in ARPES experiments. This is also the reason to stop at the next-to-leading order of the perturbation theory, giving the leading order contributions to second phonon sidebands.

With the powerful *ab initio* computations available, one can ask why even bother with toy models and complicated next-to-leading order analytical calculations? There are two main reasons for that. First, *ab initio* computations of the self-energy are exact only in the leading order of the perturbation theory [152, 153], while higher order contributions are obtained via the cumulant expansion [130, 149, 154]. On the one hand, the cumulant expansion captures contributions of all orders to the self-energy. However, it is restricted to self-energy diagrams in which fermion Green's functions move only in one direction of time [155]. For example, it cannot capture the diagram in Fig. 8.5(a), that is all the effects coming from the next-to-leading (and higher) order of the perturbation theory. Contrary to that, our calculations capture exactly all such effects, including the exact leading vertex contribution to second phonon sidebands.

Moreover, *ab initio* simulations are restricted to specific materials and they seldom unravel

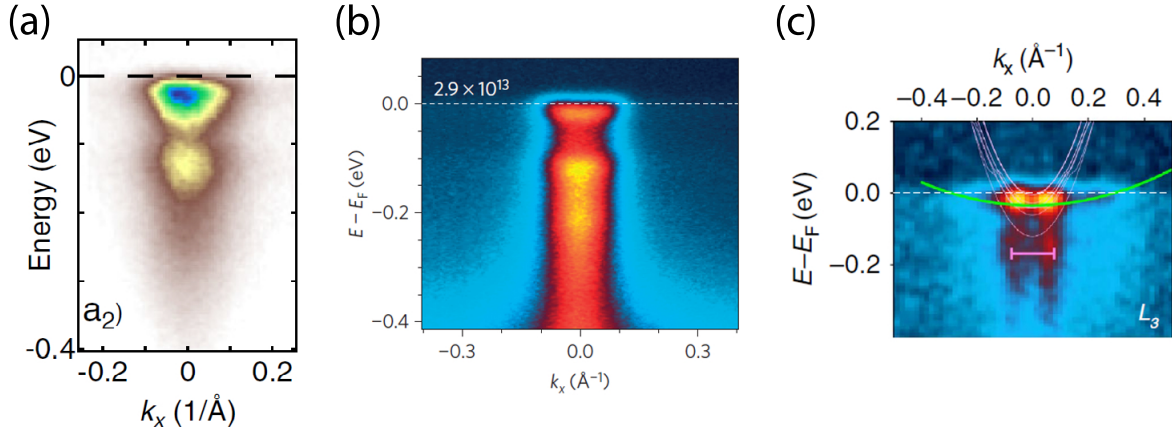


Figure 8.6: Measured ARPES spectra containing phonon sidebands below the quasiparticle band located at the integer number of phonon energies $n\hbar\omega_{LO}$ measured from the Fermi level E_F . (a) Anatase TiO_2 with $\hbar\omega_{LO} = 108$ meV [84], (b) $\text{SrTiO}_3(001)$ with $\hbar\omega_{LO} \sim 100$ meV [147], and (c) $\text{LaAlO}_3/\text{SrTiO}_3$ interface with $\hbar\omega_{LO} \sim 100$ meV [87].

qualitative effects governing the structure of generic spectra. For example, it is not clear to what extent the range of the electron-phonon interaction determines energy and momentum intensity distributions of phonon sidebands. Therefore, our analysis focuses on identifying different behaviors of phonon sidebands across all ranges of the electron-phonon interaction and provides a general procedure for the estimation of the electron-phonon interaction range from experimental data, prior to material-specific calculations.

8.3.1 Modeling prerequisites

In order to account for cases with very different ranges of the electron-phonon interaction, we assume the following form of the electron-phonon interaction in Eq. (5.1)

$$|g(\mathbf{q})|^2 = \frac{a_D}{|\mathbf{q}|^{D-1} + q_{TF}^{D-1}}, \quad (8.15)$$

with $a_{D=3} = 2\sqrt{2}\pi\alpha$ for 3D and $a_{D=2} = \sqrt{2}\pi\alpha$ for 2D systems [156], and α characterizing the strength of the interaction [157]. One way to rationalize the choice of interaction in Eq. (8.15) is by noting that it corresponds to the Fröhlich interaction, albeit statically screened by electrons. This static screening is characterized by the Thomas-Fermi wave vector q_{TF} and $r_{TF} = \pi/q_{TF}$, the latter roughly giving the screening range in the lattice constant units. Therefore, by varying q_{TF} , the screening and the range of the electron-phonon interaction can be tuned. In particular, $q_{TF} \rightarrow 0$ ($q_{TF} \rightarrow \infty$) corresponds to the long-(short-) range Fröhlich (Holstein) electron-phonon interaction.

To further specify the parameters of the Hamiltonian in Eq. (5.1), we set $\omega_0 = 1$ and consider the dispersion of a simple cubic/square lattice in 3D/2D cases, $\varepsilon_{\mathbf{k}} = 2t \sum_{i=1}^D (1 - \cos k_i)$, where

t is the nearest neighbor hopping. With the lattice constant $a = 1$, the effective mass of the unperturbed electron at the bottom of the band reads $m_0 = 1/2t$. To search for general properties of ARPES phonon sidebands components in various systems, we use two very different sets of parameters for the broad and the narrow electron band: S1 (S2) denotes $\mu = 0.5$ ($\mu = 0.1$) and $t = 1$ ($t = 1/24$), with the effective mass $m_0 = 0.5$ ($m_0 = 12$). In both these cases, only a small fraction of the lowest band states are occupied, such that the condition $\mu < \omega_0$ is always satisfied. This ensures a pattern of spectrally separated phonon sidebands, the situation observed in numerous experiments [84–86, 149].

In accordance with the interpretation of ARPES measurements, we are interested only in the hole spectral function given by

$$\begin{aligned} A(\mathbf{k}, E < 0) &= \frac{1}{\pi} \text{Im}G(\mathbf{k}, E < 0) \\ &= \frac{1}{\pi} \frac{\text{Im}\Sigma(\mathbf{k}, E < 0)}{[E - \xi_{\mathbf{k}} - \text{Re}\Sigma(\mathbf{k}, E < 0) + \text{Re}\Sigma(0, 0)]^2 + [\text{Im}\Sigma(\mathbf{k}, E < 0)]^2} . \end{aligned} \quad (8.16)$$

When the electron-phonon interaction is weak, the self-energy contributions in the denominator may be neglected, simplifying Eq. (8.16) to

$$A(\mathbf{k}, E < 0) \approx \frac{1}{\pi} \frac{\text{Im}\Sigma(\mathbf{k}, E < 0)}{[E - \xi_{\mathbf{k}}]^2} . \quad (8.17)$$

On the other hand, for a stronger electron-phonon interaction, the real part of the self-energy leads to a renormalized dispersion, $\tilde{\varepsilon}_{\mathbf{k}} = \varepsilon_{\mathbf{k}} + \text{Re}\Sigma(\mathbf{k}, \tilde{\varepsilon}_{\mathbf{k}})$. This facilitates experimental analysis because $\tilde{\varepsilon}_{\mathbf{k}}$ is the quantity that is actually measured in an experiment, rather than the bare dispersion $\varepsilon_{\mathbf{k}}$. Moreover, we argue that the imaginary part of the self-energy in the denominator of Eq. (8.16) can be neglected since it barely affects the \mathbf{k} and E dependence of the spectral function $A(\mathbf{k}, E)$, giving finally for stronger couplings

$$A(\mathbf{k}, E < 0) \approx \frac{1}{\pi} \frac{\text{Im}\Sigma(\mathbf{k}, E < 0)}{[E - \tilde{\xi}_{\mathbf{k}}]^2} . \quad (8.18)$$

In any case, here we consider only weak interaction scenarios when it is sufficient to evaluate the imaginary part of the self-energy to simulate ARPES spectra in accordance with Eq. (8.17). In particular, by recalling Eqs. (8.3) and (8.10), the expressions for the leading order contributions of $\text{Im}\Sigma$ in the energy windows of the first and the second hole phonon sidebands read

$$\text{Im}\Sigma^{(2)}(\mathbf{k}, E) = \pi \sum_{\mathbf{q}} |g(\mathbf{q})|^2 n_{\mathbf{k}+\mathbf{q}} \delta(E + \omega_0 - \xi_{\mathbf{k}+\mathbf{q}}) , \quad (8.19)$$

and

$$\text{Im}\Sigma^{(4)}(\mathbf{k}, E) = \pi \sum_{\mathbf{q}, \mathbf{q}'} |g(\mathbf{q})|^2 |g(\mathbf{q}')|^2 \frac{n_{\mathbf{k}+\mathbf{q}+\mathbf{q}'}}{\xi_{\mathbf{k}+\mathbf{q}+\mathbf{q}'} - \omega_0 - \xi_{\mathbf{k}+\mathbf{q}}} \delta(E + 2\omega_0 - \xi_{\mathbf{k}+\mathbf{q}+\mathbf{q}'}) \times \left[\frac{1}{\xi_{\mathbf{k}+\mathbf{q}+\mathbf{q}'} - \omega_0 - \xi_{\mathbf{k}+\mathbf{q}}} + \frac{1}{\xi_{\mathbf{k}+\mathbf{q}+\mathbf{q}'} - \omega_0 - \xi_{\mathbf{k}+\mathbf{q}'}} \right], \quad (8.20)$$

respectively. The required wave vector summations over the whole Brillouin zone generally cannot be carried out analytically. Moreover, even the brute force numerical evaluations of summations are extremely time-consuming for 2D and 3D systems. Therefore, the required summations were performed by the importance sampling similar to that used for a fixed diagram order integration within the Diagrammatic Monte Carlo approach [105].

8.3.2 Short-range interaction

We first consider the behaviors of ARPES spectra when the screening is strong and the electron-phonon interaction is short-ranged. An example of a typical ARPES spectrum in the energy window of the first hole phonon sideband, in that case, is shown in Fig. 8.7(a). We can see that the majority of the spectrum is confined within the Fermi surface, left of the vertical dashed line denoting the Fermi wave vector. In experimental works, it is often concluded that this accumulation of the spectral weight stems due to the weakly screened Fröhlich interaction, however, our results evidently do not support that hypothesis.

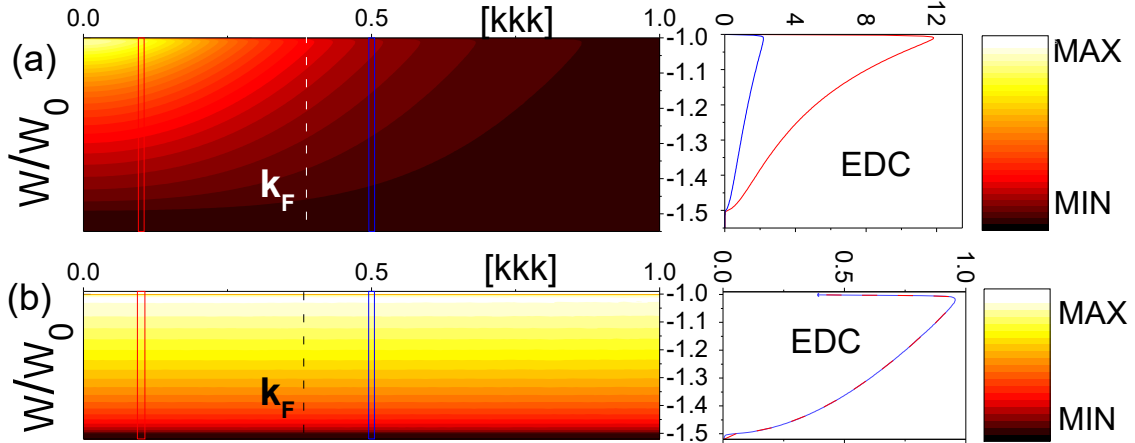


Figure 8.7: Contour plot of the (a) ARPES spectrum $A^{(2)}(\mathbf{k}, E)$ and (b) $\text{Im}\Sigma^{(2)}(\mathbf{k}, E)$ in the energy window of the first hole phonon sideband for the 3D parameter set S1 and strong screening $r_{TF} = 0.1$. The right panels show EDCs for the corresponding cuts in the left panels.

Therefore, in order to elaborate on that finding, in Fig. 8.7(b) we show the imaginary part of the self-energy in the same energy window. Clearly, it is uniformly spread and momentum independent throughout the whole Brillouin zone. This is further supported by the energy

distribution curves (EDCs), being equal for two choices of momenta, one inside and one outside the Fermi surface. In fact, the energy dependence of $\text{Im}\Sigma^{(2)}(\mathbf{k}, E)$ is determined solely by the density of occupied electron states at the bottom of the band, which is readily seen by assuming the momentum-independent interaction in Eq. (8.19). We note that this behavior also agrees with the local nature of the leading order self-energy in cases with the Holstein coupling.

By inspecting Eq. (8.17), it is then natural to conclude that the strong momentum dependence of the ARPES spectrum comes from the denominator $[E - \xi_{\mathbf{k}}]^2$, and is not the result of the range of the electron-phonon interaction. Actually, since the factor $[E - \xi_{\mathbf{k}}]^2$ is always present in the spectral function, we may suggest that the confinement of spectral weight within the Fermi surface is a generic behavior of ARPES spectra, which is indeed generally found in the ARPES experiments [84–86, 149]. In contrast, the same obviously does not hold true for the imaginary part of the self-energy corresponding to the first hole phonon sideband. Therefore, the momentum dependence, that is the confinement in the momentum space of the imaginary part of the self-energy within the energy window of the first hole phonon sideband potentially serves as a more suitable estimator of the electron-phonon interaction range.

8.3.3 Long-range interaction

Following the above reasonings, in Fig. 8.8 we show the imaginary part of the self-energy in the energy regions of the quasiparticle band and the first two hole phonon sidebands when the screening is weak and the electron-phonon interaction long-range. Clearly, in sharp contrast to

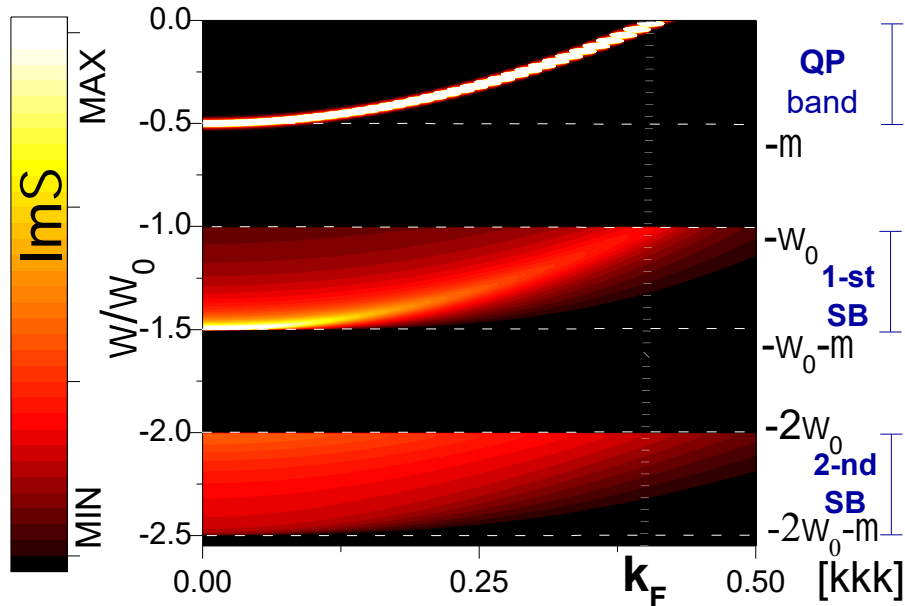


Figure 8.8: Contour plot of $\text{Im}\Sigma$ in the energy regions of the quasiparticle band and the first two hole phonon sidebands for the 3D parameter set S1 and weak screening $r_{TF} = 100$.

the short-range interaction case, $\text{Im}\Sigma$ corresponding to the first hole phonon sideband exhibits

maxima that approximately follow the quasiparticle dispersion. Using this property, the cases with the long-range interaction can be unambiguously identified and differentiated from the cases with short-range interactions. In particular, while for the short-range interaction $\text{Im}\Sigma$ corresponding to the first hole phonon sideband is momentum independent and uniformly spread over the Brillouin zone, for long-range interactions its maxima follow the quasiparticle dispersion.

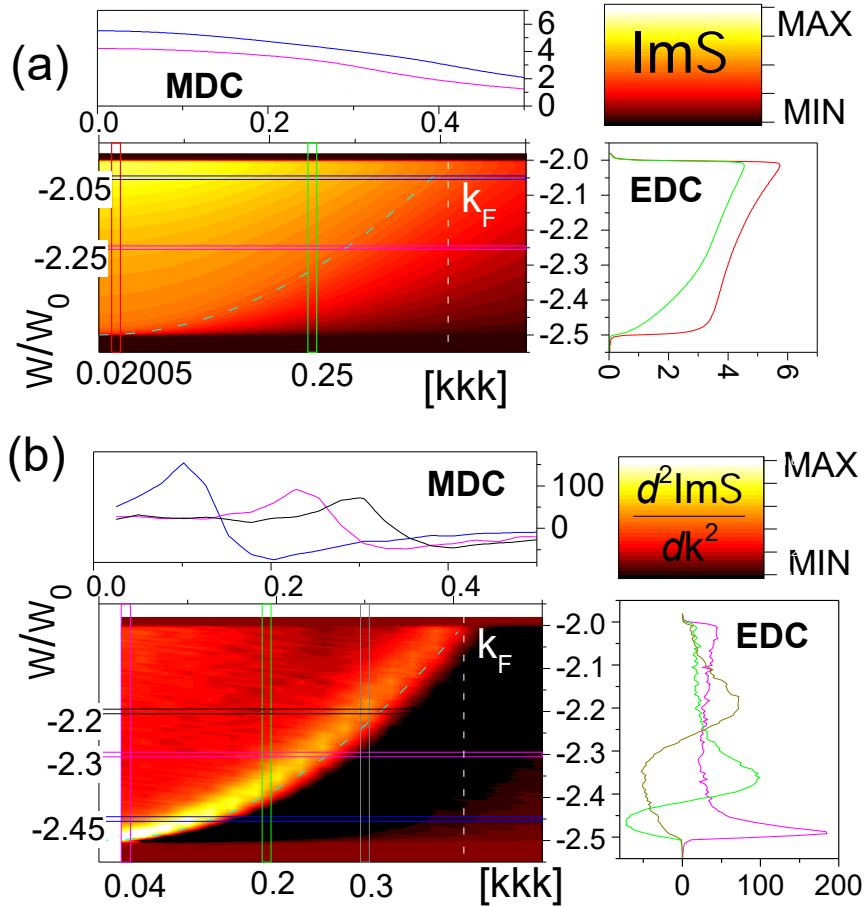


Figure 8.9: Contour plot of (a) $\text{Im}\Sigma^{(4)}(\mathbf{k}, E)$ and (b) its second derivative $d^2\text{Im}\Sigma^{(4)}(\mathbf{k}, E)/dk^2$ for the 3D parameter set S1 and $r_{TF} = 100$. Right panels in (a) and (b) show the EDCs and the upper panels show the MDCs along the cuts highlighted in the left-bottom panels of (a) and (b). The dashed curves represent the quasiparticle dispersion shifted by $2\omega_0$.

Regarding the second hole phonon sideband in Fig. 8.8, our analysis of the EDCs and the momentum distribution curves (MDCs) is presented in Fig. 8.9(a) together with the contour plot of $\text{Im}\Sigma$. It shows no particular maxima of $\text{Im}\Sigma$ in the corresponding energy region. However, as can be seen in Fig. 8.9(b), by taking the second derivative $d^2\text{Im}\Sigma^{(2)}(\mathbf{k}, \omega)/dk^2$, a dispersion resembling to that of the quasiparticle dispersion is recovered.

8.3.4 Anomalous phonon sideband structures

Between the regimes with strong and weak screenings, with the short-range and the long-range electron-phonon interaction, respectively, characterized by the different and characteristic behaviors of $\text{Im}\Sigma$ in the energy region of the first hole phonon sideband, an intermediate regime sets in, which we estimate to be found for $3 \leq r_{TF} \leq 20$. For corresponding interaction ranges, $\text{Im}\Sigma$ in the energy region of the first hole phonon sideband shows anomalous behaviors which are very sensitive to system parameters, as shown in Fig. 8.10. In particular, while for long-

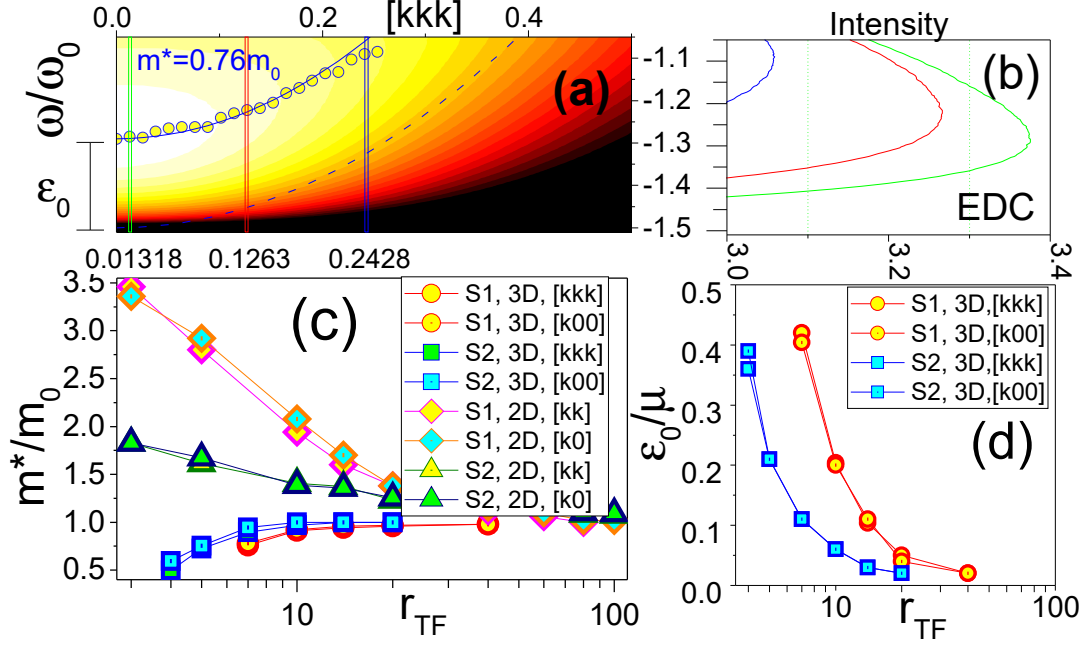


Figure 8.10: (a) Contour plot of $\text{Im}\Sigma^{(2)}(\mathbf{k}, E)$ for the 3D parameter set S1 and $r_{TF} = 7$. The dashed curve represents the quasiparticle dispersion $\varepsilon_{\mathbf{k}}$ shifted downward by ω_0 . The circles follow the maxima of EDCs, fitted by a parabola (solid line) that gives the effective mass $m^* = 0.76 m_0$. (b) EDCs for cuts shown in panel (a). (c) m^* derived from EDCs maxima of $\text{Im}\Sigma^{(2)}(\mathbf{k}, E)$. (d) Upward shifts ε_0 characterizing the EDCs maxima of $\text{Im}\Sigma^{(2)}(\mathbf{k}, E)$.

range interactions the EDCs maxima of $\text{Im}\Sigma$ follow closely the quasiparticle dispersion, in the intermediate regime the dispersion of EDCs maxima appears to be shifted upward from the lower edge of the sideband by ε_0 . Moreover, the parabolic fit yields an effective mass different than that characterizing the quasiparticle dispersion. Such anomalies are found for all parameter sets considered here, with the emphasis that the anomalies in 3D and 2D cases behave quite differently. Namely, Figs. 8.10(c) and 8.10(d) show that m^* is smaller (larger) in 3D (2D) and ε_0 varies (being zero) in 3D (2D). While in the 3D cases the EDCs maxima follow the parabolic dispersion over the whole sideband, in the 2D cases the parabolic dispersion exhibits a jump toward large momenta.

A similar anomalous structure characterizes the ARPES spectrum in the energy region of

the first hole phonon sideband as well, as presented in Fig. 8.11. However, the shifts ε_0 and the effective masses m^* characterizing the anomalous dispersion of EDCs maxima of $\text{Im}\Sigma$ and the ARPES spectrum are generally different. Lastly, from Fig. 8.11 it is also clear that the

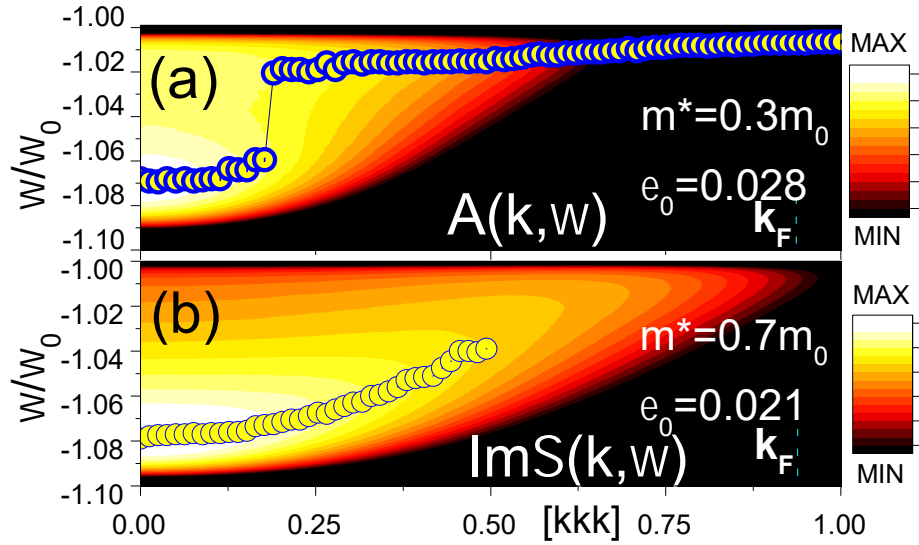


Figure 8.11: Contour plot of (a) $A^{(2)}(\mathbf{k}, E)$ and (b) $\text{Im}\Sigma^{(2)}(\mathbf{k}, E)$ for the 3D parameter set S2 and $r_{TF} = 5$. Circles follow the maxima of EDCs. These are fitted by parabolas, giving corresponding effective masses m^* and shifts ε_0 of anomalous phonon sideband dispersions.

confinement of spectral weight within the Fermi surface of the ARPES spectrum is enhanced in comparison to that obtained from $\text{Im}\Sigma$, being reduced to momenta, $k < k_r$, where k_r is considerably smaller than k_F . This effect is experimentally observed as well [84, 87, 149], as can be seen in Fig. 8.6.

8.3.5 Confinement estimators

We have seen how different interaction regimes can be simply identified by considering the structure of $\text{Im}\Sigma$ in the energy region of the first hole phonon sideband. In particular, based on our qualitative arguments, we saw how the confinement of $\text{Im}\Sigma$ within the Fermi surface varies with the electron-phonon interaction range. In what follows, we give a more robust, quantitative mean to determine the electron-phonon interaction range based on that confinement.

For that purpose, we introduce several confinement estimators. First, we consider the $\text{Im}\Sigma$ intensity integrated over the energies within the n -th hole phonon sideband for a given \mathbf{k}

$$\mathcal{R}_n(\mathbf{k}) = \int_{-n\omega_0 - \mu}^{-n\omega_0} dE \text{Im}\Sigma^{(n)}(\mathbf{k}, E). \quad (8.21)$$

Now, by using $\mathcal{R}_n(\mathbf{k})$, the confinement of $\text{Im}\Sigma$ within the Fermi surface may be expressed by a confinement estimator corresponding to the ratio of the $\mathcal{R}_n(\mathbf{k})$ intensity within and outside the

Fermi surface

$$R_n = \left(\int_0^{k_F} dk \frac{\mathcal{R}_n(\mathbf{k})}{k_F} \right) / \left(\int_{k_F}^{\pi} dk \frac{\mathcal{R}_n(\mathbf{k})}{\pi - k_F} \right). \quad (8.22)$$

Such an estimator of the confinement is particularly suitable for an analysis of the experimental data since it involves averaging over energy and momenta intervals, reducing the inevitable effects of noise in experimental ARPES spectra. Moreover, it is unaffected by the arbitrariness in the normalization of the experimental ARPES intensity, as well as it is independent of the coupling strength α . Furthermore, the case with the short-range interaction, when $\text{Im}\Sigma$ is momentum independent, may be identified directly from R_n . In particular, when $r_{TF} \rightarrow 0$, we have $R_n \rightarrow 1$.

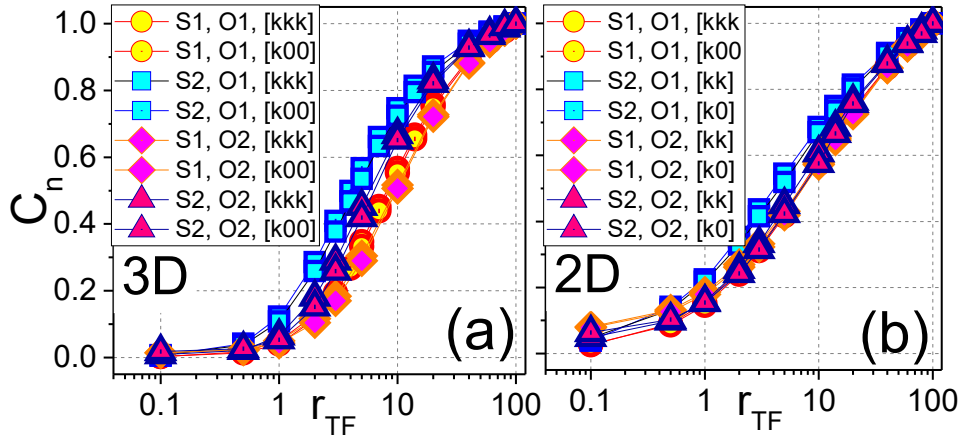


Figure 8.12: Confinement estimator $C_n(r_{TF})$ defined by Eq. (8.23) for the parameter sets S1 and S2, the first O1 and the second O2 phonon sidebands in (a) 3D and (b) 2D cases.

Except for the $r_{TF} \rightarrow 0$ limit, the confinement estimator R_n may vary by an order of magnitude for different systems. This motivates us to introduce the third confinement estimator

$$C_n(r_{TF}) = [R_n(r_{TF}) - 1] [R_n(\infty) - 1]^{-1}. \quad (8.23)$$

As shown in Fig. 8.12, for all cases (parameter sets S1 and S2, 3D and 2D cases, diagonal $[k'k'k']/[k'k']$ and non-diagonal $[k'00]/[k', 0]$ directions) considered and for the both phonon sidebands, the confinement estimator $C_n(r_{TF})$ exhibits a fairly universal behavior. This suggests that one can unambiguously determine the electron-phonon interaction range in a real material by evaluating solely the confinement estimator $C_n(r_{TF})$ from experimental data, irrespectively of the peculiarities of the experimental setup and the material.

However, in order to evaluate $C_n(r_{TF})$ one should know the value $R_n(\infty)$ specific for the material of interest. As we show, it can always be computed numerically, at least for the first hole phonon sideband. In particular, with the details shown in Appendix A.1.1, we can evaluate

exactly the summation/integration in Eq. (8.19) in the limit $r_{TF} \rightarrow \infty$. In the 3D case, we have

$$\text{Im}\Sigma^{(2)}(\mathbf{k}, E) = \frac{\alpha}{2\sqrt{2}t\varepsilon_{\mathbf{k}}} \ln \left| \frac{(\sqrt{\varepsilon_{\mathbf{k}}} - \sqrt{E + \omega_0 + \mu})^2}{(\sqrt{\varepsilon_{\mathbf{k}}} + \sqrt{E + \omega_0 + \mu})^2} \right| \Theta(-E - \omega_0) \Theta(E + \mu + \omega_0), \quad (8.24)$$

while in the 2D case

$$\begin{aligned} \text{Im}\Sigma^{(2)}(\mathbf{k}, E) &= \frac{\alpha}{\sqrt{2}t(\sqrt{\varepsilon_{\mathbf{k}}} + \sqrt{E + \omega_0 + \mu})} K \left(\frac{2[\varepsilon_{\mathbf{k}}(E + \omega_0 + \mu)]^{\frac{1}{4}}}{\sqrt{\varepsilon_{\mathbf{k}}} + \sqrt{E + \omega_0 + \mu}} \right) \times \\ &\times \Theta(-E - \omega_0) \Theta(E + \mu + \omega_0). \end{aligned} \quad (8.25)$$

The remaining integrations in Eq. (8.22) can be easily carried out numerically, yielding finally the numerical value for $R_1(\infty)$. The only data needed for its concrete evaluation are the effective mass characterizing the quasiparticle dispersion, Fermi energy, and Fermi wave vector. All those data can be read out from an experimental ARPES spectrum.

8.3.6 Application to real experimental ARPES data

To conclude this Chapter 8, we provide an illustrative example of determining the electron-phonon interaction range from the real ARPES data by using our developed formalism. In particular, we consider the ARPES spectrum of oxygen-deficient $\text{LaAlO}_3/\text{SrTiO}_3$ interface [158], involving different phonons and the limited experimental resolution (0.04 eV), making the theoretical modeling very challenging. Yet, even in such circumstances, our approach based on confinement estimators and integrated spectra may provide valuable insights into the range of the electron-phonon interaction.

The corresponding ARPES spectrum with the constant background removed is shown in Fig. 8.13(a). In particular, always present lattice imperfections cause a scattering of electrons, giving a finite constant contribution B to the imaginary part of the self-energy. For weak electron-phonon interactions, this constant contribution may easily dominate over the self-energy contributions arising due to the interaction with the phonon, and in such circumstances, we need to adapt our expression for the ARPES spectrum in Eq. (8.17). According to Eq. (8.16), for finite B we have

$$A(\mathbf{k}, E < 0) \approx \frac{1}{\pi} \frac{\text{Im}\Sigma(\mathbf{k}, E < 0)}{[E - \xi_{\mathbf{k}}]^2 + B^2} + \frac{1}{\pi} \frac{B}{[E - \xi_{\mathbf{k}}]^2 + B^2}. \quad (8.26)$$

First, the value $B = 0.15$ eV was determined by fitting Gaussian-like peaks to the quasiparticle band signal and by evaluating the average value of the full width at half the maximum of the

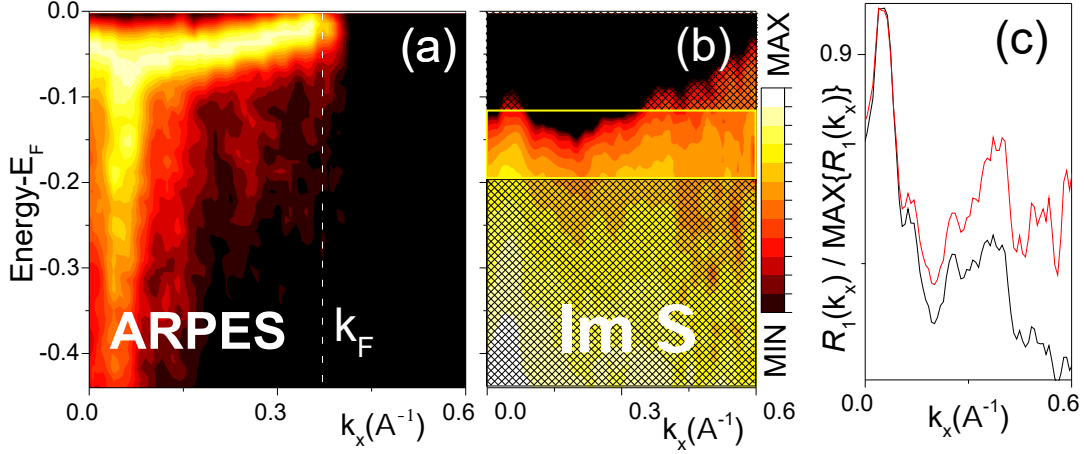


Figure 8.13: (a) Raw ARPES data [158] with the constant background removed. (b) $\text{Im}\Sigma$ corresponding to (a). (c) Measure of confinement $\mathcal{R}_1(k_x)/\text{MAX}\{\mathcal{R}_1(k_x)\}$ for data in (a) (black) and (b) (red) panel.

Gaussian-like peaks. From the same fits, peculiarities of the dispersion $\xi_{\mathbf{k}}$ have been extracted as well. In the next step, the minimal value of the ARPES signal has been removed as a constant background, and the remaining ARPES intensity was normalized for each given momentum to the maximum of the quasiparticle peak, resulting finally in the spectrum shown in Fig. 8.13(a). From Fig. 8.13(a), $k_F \approx 0.37 \text{ \AA}^{-1}$ and $\mu \approx 0.07 \text{ eV}$ were easily read out.

In the last step, the $\text{Im}\Sigma$ intensity was extracted from the resulting ARPES spectrum. In particular, the quasiparticle band signal was subtracted in order to obtain the signal corresponding purely to phonon sidebands, after which $\text{Im}\Sigma$ was obtained by means of Eq. (8.26) (without the second term). The resulting $\text{Im}\Sigma$ intensity is shown in Fig. 8.13(b). Here, we assumed that electrons dominantly couple to the LO3 phonon, with the energy $\hbar\omega_{LO3} \approx 0.12 \text{ eV}$ [87].

Once the imaginary part of the self-energy is known, it is straightforward to calculate the confinement estimators. Namely, by averaging $\text{Im}\Sigma$ over the energy interval $-\mu - \hbar\omega_{LO3} \leq E \leq -\hbar\omega_{LO3}$, the value of $R_1 = 1.03$ was obtained. This is almost the minimal value that this estimator can attain, pointing to the short-range nature of the electron-phonon interaction, without the need of referencing to the estimator $C_n(r_{TF})$.

For such short-ranges couplings, $\text{Im}\Sigma$ should be almost momentum independent in the energy region of the first hole phonon sideband, which is ungrateful to estimate from Fig. 8.13(b) due to the limited experimental resolution. However, it is quite clear that $\text{Im}\Sigma$ is approximately evenly spread over the whole momentum range shown. On the other hand, the ARPES intensity is almost completely confined deeply within the Fermi surface, which is, as we argued, the general property of all ARPES spectra. The confinement estimator of the ARPES intensity can also be calculated and reads $R_1 = 1.85$. Based on that value one would obviously overestimate the range of the electron-phonon interaction.

8.4 Conclusions

We perform the evaluation of the fermion self-energy up to the next-to-leading order of the electron-phonon interaction perturbation theory, including the leading vertex correction and the correction involving the renormalization of the phonon line, in cases with finite electron densities. While we briefly comment on the influence of the retarded electron-phonon interaction and exchange processes on the excitations' lifetime in the vicinity of the Fermi level, the major focus is put on the self-energy corrections away from the Fermi level in the energy windows of phonon sidebands. Based on the momentum and energy structure of phonon sidebands, we provide means to estimate the effective electron-phonon interaction range from measured ARPES spectra. Our reasonings are based on the confinement in the momentum space of the imaginary part of the self-energy intensity in the regions of phonon sidebands, which is experiencing significant change as the interaction range is varied. Based on that confinement, a few confinement estimators involving integrated spectra are introduced, which provide a robust estimate of the effective interaction range even when the experimental resolution is very limited.

Phonon-plasmon coupling

Some results of Chapter 9 have been published in [159].

9.1 Introduction

In the previous Chapter 8, the electron-electron interaction was only implicitly taken into account through the static screening of the electron-phonon interaction. We change that here by explicitly introducing the Coulomb interaction between electrons, which long-range nature results in the collective electron excitation called plasmon [40]. In polar materials, the longitudinal plasma oscillation may strongly couple with the longitudinal optical (LO) phonon resulting in a hybridization of those two boson modes. This coupling in 3D polar semiconductors has been addressed as early as in the 1960s in seminal works by Yokota [160], Varga [161], Singwi *et al.* [162], and Cochran *et al.* [163]. Since the long-wavelength plasma energy directly depends on the electron density, it may be easily controlled. In particular, a resonance with the phonon energy may be achieved, which results in a level repulsion of two boson modes. This phenomenon was oftentimes observed experimentally in the Raman [132–137] and infrared spectroscopy [138–140] measurements of a highly doped GaAs, as well as of some transition metal oxides [141–143], giving an excellent agreement with theoretical predictions [164]. In the past decade, the level repulsion of modes was captured in ultrafast transient reflectivity measurements of III-IV semiconductors [165–168] as well, leading to the renewed interest in studying the phonon-plasmon coupled excitations in 3D systems.

A scenario in 2D cases is radically different since the energy of long-wavelength plasma oscillations vanishes [169]. Peculiarities of the 2D case were seldom discussed until recently when the renewed interest in 2D systems emerged due to the synthesis of mono- to few-layer materials. The relevance of the phonon-plasmon coupling in monolayer graphene was pointed out in several experiments showing clear signatures of the coupling of graphene's plasmon with the substrate's phonon [170–175], while the interaction of the intrinsic phonon with the plasmon in bilayer graphene was recorded in [176]. The important role of the electron-phonon interaction was recognized in transition metal dichalcogenides (TMDs) as well, where it is frequently invoked to explain spectral and transport properties of monolayer TMDs [177–181]. Experimental evidence also exist for the coupling of a monolayer MoS₂ plasmon with a substrate phonon [182], albeit, to the best of our knowledge, no coupling of an intrinsic phonon to a

plasmon has been observed in monolayer TMDs to our knowledge. Indeed, for most monolayer TMDs, a polar coupling is expected to be rather weak [183]. However, experiments and *ab initio* calculations suggest a large ionic character of bonds and a strong polar coupling for monolayer TMDs with the 1T polytype structure [183–185], given by the chemical formula MX_2 with $\text{M} = \text{Hf}, \text{Zr}$ and $\text{X} = \text{S}, \text{Se}$. It is for these materials that a strong hybridization of a 2D plasmon with intrinsic phonon modes is expected, demanding a thorough analysis of the effects of the phonon-plasmon coupling on the spectral properties of 2D materials.

Apart from the examination of the phonon-plasmon coupled excitations in the long-wavelength limit, several studies analyzed the dispersions of coupled modes outside the electron-hole continuum, examined by considering zeros of the longitudinal dielectric function or extracted from the simulated EELS spectra in 3D [161, 163, 164, 186, 187] and 2D [188–193] cases. The level of influence of the continuum on coupled modes remained thus unclear, which was tried to be reconciled by considering the scattering of electrons on collective excitations [194, 195]. However, the definite answer about excitations' damping is still not provided.

Another important problem of the excitations' character was addressed in [164, 188, 189, 192, 195] by considering phonon and plasmon strengths in the total dielectric function and EELS spectra. These results were further supplemented by considering phonon strengths of coupled modes in the long-wavelength limit [161, 162, 194]. However, the full phonon spectrum in the presence of the phonon-plasmon coupling was seldom analyzed. We may mention a work by Yi *et al.* [196] considering phonon spectra in the 3D case, which, however, overlooks the spectral weight of collective excitations outside the continuum and lacks a very interesting resonant regime. Actually, in all of the works, to the best of our knowledge, only the adiabaticity parameter, that is, the electron density, was considered as a quantity that separates quantitatively different coupling regimes, while the influence of the electron-phonon interaction strength was not discussed at all. We shall also add that in the context of the phonon degree of freedom, the interest in investigating phonon spectral properties recently increased due to the potential impact of nonadiabatic effects in *ab initio* modeling of phonon spectra of highly doped monolayer TMDs [180, 181, 197].

Here, we provide a systematic and thorough analysis of phonon-plasmon coupled excitations in the whole two-dimensional parametric space, spanned by both the adiabaticity parameter and the electron-phonon interaction strength. In particular, we distinguish six very different regimes, which come as a product of three adiabaticity regimes: (a) antiadiabatic, (b) resonant, and (c) adiabatic, and two electron-phonon interaction strength cases: (A) weak and (B) strong. Characteristics of all the regimes are studied by means of fully momentum and energy resolved raw and integrated EELS and phonon (corresponding to the LO phonon) spectra, providing an original side-by-side comparison of coupled excitations' projections onto the electron and the phonon degree of freedom. To cover all of the experimentally relevant parametric space, we refer to four semiconducting materials that are of particular interest. Namely, we consider the

bulk GaAs, which is on the weak electron-phonon interaction side of the phase diagram, and TiO₂ with the considerably stronger electron-phonon interaction. When it comes to the 2D case, we refer to the monolayer MoS₂, which is assumed to be weakly polar, and ZrS₂ which should be a much more polar system.

Both the momentum and energy resolved EELS and phonon spectra may be probed experimentally. In particular, when a high-energy electron beam is directed onto a material, by measuring the energy loss of transmitted electrons the EELS spectrum is formed. It shows peaks at excitations' energies with spectral weights proportional to the rate at which electrons inelastically scatter by corresponding excitations. EELS measurements are regularly used to experimentally determine plasmon energies in metals [198–200] and are recently exploited to study plasmon dispersions in heavily doped semiconductors [201, 202]. The EELS measurements should in principle capture phonon-plasmon coupled excitations as well. However, at the present time the energy resolution $\Delta E \sim 30 - 100$ meV is not high enough to fully spectrally resolve characteristic energies of coupled modes. While new techniques that overcome these technical difficulties are appearing [203], our analysis based on integrated spectra may circumvent the problem of the limited experimental resolutions to a great extent.

Besides the standard Raman and the infrared spectroscopy for momenta close to the center of the Brillouin zone, an alternative with a sufficient energy resolution to capture [204] dispersions of phonon-plasmon coupled modes are experiments based on the inelastic neutron scattering [205, 206]. The coupling strength of a neutron to material excitations is directly proportional to the amount of ionic motion present in corresponding excitations, highlighting the importance of the projection of coupled excitations on the phonon degree of freedom. By conducting an in-depth analysis of phonon spectral features, we show that the strong coupling case is accompanied by large phonon production contributions, which makes us especially emphasize the importance of a distinction between phonon softening effects and effects caused by a cloud of phonons attached to charge fluctuations.

9.2 Random phase approximation

To be able at all to account for the plasmon excitation, we need to complement the electron-phonon Hamiltonian in Eq. (5.1) with the electron-electron interaction, $\hat{H}_{el-el} = \frac{1}{2} \sum_{\mathbf{q}} v_{\mathbf{q}}^{\infty} \hat{\rho}_{\mathbf{q}} \hat{\rho}_{-\mathbf{q}}$. Here, $\hat{\rho}_{\mathbf{q}} = \sum_{\mathbf{k}} c_{\mathbf{k}+\mathbf{q}}^{\dagger} c_{\mathbf{k}}$ is the charge density operator, while $v_{\mathbf{q}}^{\infty} = v_{\mathbf{q}}/\epsilon_{\infty}$ characterizes the interaction between electrons, with $v_{\mathbf{q}} = e^2/\epsilon_0 q^{D-1} V$ the Coulomb potential, where ϵ_0 is the vacuum permittivity. The screening from high-energy excitations across band gaps is taken into account through the high-frequency dielectric constant ϵ_{∞} . Due to this screening, the interband excitations renormalize the plasmon frequency, $\Omega_{PL}^{\infty} = \Omega_{PL}/\sqrt{\epsilon_{\infty}}$, where Ω_{PL} would be the plasmon frequency in the absence of other bands. With these necessary inclusions, our minimal model capturing the essences of the phonon-plasmon coupling reads

$$\hat{H} = \sum_{\mathbf{k}} \varepsilon_{\mathbf{k}} c_{\mathbf{k}}^{\dagger} c_{\mathbf{k}} + \hbar\omega_0 \sum_{\mathbf{k}} a_{\mathbf{k}}^{\dagger} a_{\mathbf{k}} + \frac{1}{2} \sum_{\mathbf{q}} v_{\mathbf{q}}^{\infty} \hat{\rho}_{\mathbf{q}} \hat{\rho}_{-\mathbf{q}} + \sum_{\mathbf{q}} g(\mathbf{q}) \hat{\rho}_{\mathbf{q}} \left[a_{\mathbf{q}}^{\dagger} + a_{-\mathbf{q}} \right]. \quad (9.1)$$

Hereafter, we recover the full \hbar .

We are interested in a single band model that describes a semiconductor with a bottom/top of conduction/valence band doped, such that dispersion of electrons/holes may be assumed quadratic $\varepsilon_{\mathbf{k}} = \frac{\hbar^2 k^2}{2m^*}$, characterized by an effective mass m^* . In addition to the Coulomb interaction between itinerant charges, we investigate the effects of the electron/hole interaction with lattice phonons, assuming that the latter is dominated by the polar coupling to a dispersionless LO phonon branch with the frequency $\omega_0 = \omega_{LO}$. Regarding the electron-phonon interaction, corresponding to the last term in Eq. (9.1), we assume a polar coupling described by the Fröhlich model [207]

$$g(\mathbf{q}) = -i\sqrt{v_{\mathbf{q}}^{\infty}} \sqrt{\frac{\hbar\omega_{LO}}{2}} \sqrt{1 - \frac{\varepsilon_{\infty}}{\varepsilon_0}}. \quad (9.2)$$

Here, ε_0 is the static dielectric constant of a polar crystal, measured well below the phonon frequency ω_{LO} (not to be confused with ϵ_0). In the spirit of the earlier introduced polaron theory, we take a dimensionless electron-phonon coupling constant [207]

$$\alpha = \frac{e^2}{4\pi\epsilon_0\hbar} \sqrt{\frac{m^*}{2\hbar\omega_{LO}}} \left(\frac{1}{\varepsilon_{\infty}} - \frac{1}{\varepsilon_0} \right), \quad (9.3)$$

as a measure of the electron-phonon interaction strength. In particular, values $\alpha \ll 1$ and $\alpha \approx 1$ correspond to the weak and the strong electron-phonon interaction case, respectively, as found in standard semiconducting materials. It should be emphasized that all the bare model parameters in Eq. (9.1) may be determined either from experiments or by performing *ab initio* calculations for the undoped polar semiconductor of interest.

9.2.1 EELS spectrum

The inelastic scattering cross section of electrons measured in an EELS experiment is related via the fluctuation-dissipation theorem to the system's charge density-density correlation function [83] and hence an EELS spectrum is directly proportional to the imaginary part of the inverse of system's total dielectric function

$$\begin{aligned}
S(\mathbf{q}, \omega) &\propto -\pi^{-1} \text{Im} [\varepsilon^{-1}(\mathbf{q}, \omega)] \\
&= \pi^{-1} \frac{\text{Im} \varepsilon(\mathbf{q}, \omega)}{[\text{Re} \varepsilon(\mathbf{q}, \omega)]^2 + [\text{Im} \varepsilon(\mathbf{q}, \omega)]^2}.
\end{aligned} \tag{9.4}$$

In order to simulate EELS spectra, we adopt the RPA kind of scheme for the total dielectric function of the system. Within this scheme, the electron and the phonon contributions to the dielectric function are additive, yielding [40]

$$\begin{aligned}
\varepsilon(\mathbf{q}, \omega) &= \varepsilon_\infty - v_{\mathbf{q}} \chi_0(\mathbf{q}, \omega) + \varepsilon_\infty \frac{\omega_{pl}^2}{\omega_{TO}^2 - \omega^2} \\
&= \varepsilon_\infty \left[\varepsilon_{RPA}(\mathbf{q}, \omega) + \frac{\omega_{pl}^2}{\omega_{TO}^2 - \omega^2} \right].
\end{aligned} \tag{9.5}$$

The first term in the first row of Eq. (9.5) accounts for the high-energy interband excitations, the second term for the intraband excitations, and the last term for the phonon contribution. In the second row of Eq. (9.5), we simply exploited the standard RPA form for the electron dielectric function [40]

$$\varepsilon_{RPA}(\mathbf{q}, \omega) = 1 - v_{\mathbf{q}}^\infty \chi_0(\mathbf{q}, \omega). \tag{9.6}$$

Here, as well as in Eq. (9.5), $\chi_0(\mathbf{q}, \omega)$ is the density-density correlation function of a free electron system, that is the Lindhard function [40]

$$\chi_0(\mathbf{q}, \omega) = \frac{2}{V} \sum_{\mathbf{k}} \frac{n_{\mathbf{k}} - n_{\mathbf{k}+\mathbf{q}}}{\hbar\omega - \varepsilon_{\mathbf{k}+\mathbf{q}} + \varepsilon_{\mathbf{k}} + i\eta}, \tag{9.7}$$

where factor 2 accounts for the electron spin degeneracy. The frequency of the transversal optical (TO) phonon is given by the LO phonon frequency through the Lydanne-Sachs-Teller (LST) relation $\omega_{TO}^2 = \omega_{LO}^2 \varepsilon_\infty / \varepsilon_0$, or through the ionic plasma frequency $\omega_{pl}^2 = \omega_{LO}^2 - \omega_{TO}^2$ [40].

Outside the electron-hole continuum, $\text{Im}\varepsilon(\mathbf{q}, \omega)$ is zero and $S(\mathbf{q}, \omega)$ is contributed only by delta peaks at frequencies of system collective excitations ω_i , with the corresponding spectral weights given by

$$s_i(\mathbf{q}) = \hbar \left[\frac{\partial \varepsilon(\mathbf{q}, \omega)}{\partial \omega} \right]^{-1} \Big|_{\omega=\omega_i}. \tag{9.8}$$

Once the continuum is reached, the EELS spectrum acquires an incoherent contribution from electron-hole pair excitations $s_{e-h}(\mathbf{q}, \omega)$ as well. By integrating the spectrum over frequencies,

one obtains the total spectral weight as a function of \mathbf{q}

$$\begin{aligned} s_{tot}(\mathbf{q}) &= \int_0^{+\infty} d\omega \{ -\pi^{-1} \text{Im} [\varepsilon^{-1}(\mathbf{q}, \omega)] \} \\ &= \sum_i s_i(\mathbf{q}) + s_{e-h}(\mathbf{q}) . \end{aligned} \quad (9.9)$$

In the long-wavelength limit and in the absence of the electron-phonon interaction, the EELS spectrum is dominated by plasmon excitation. The corresponding EELS spectral weight may be easily derived by noting that, in that case, the long-wavelength form of the dielectric function reads ($|\mathbf{q}| \equiv q$)

$$\varepsilon(q \rightarrow 0, \omega) = \varepsilon_\infty - \frac{\Omega_{PL}^2}{\omega^2} , \quad (9.10)$$

resulting in

$$s_{tot}(q \rightarrow 0) \approx s_{\Omega_{PL}^\infty}(q \rightarrow 0) = \frac{\hbar \Omega_{PL}^\infty}{2\varepsilon_\infty} . \quad (9.11)$$

With the introduction of finite electron-phonon interaction, the electrons scatter on phonons at a rate proportional to the strength of the interaction. Correspondingly, the EELS spectral weight at $\omega = \omega_{LO}$, characterizing this scattering, is given by

$$s_{\omega_{LO}}(q \rightarrow 0) = \frac{\hbar \omega_{LO}}{2} \left(\frac{1}{\varepsilon_\infty} - \frac{1}{\varepsilon_0} \right) . \quad (9.12)$$

This result was derived by noting that in the cases with the finite electron-phonon interaction the long-wavelength form of the dielectric function in Eq. (9.10) acquires an additional term according to Eq. (9.5)

$$\varepsilon(q \rightarrow 0, \omega) = \varepsilon_\infty - \frac{\Omega_{PL}^2}{\omega^2} + \varepsilon_\infty \frac{\omega_{pl}^2}{\omega_{TO}^2 - \omega^2} , \quad (9.13)$$

which derivative's inverse reads

$$\left[\frac{\partial \varepsilon(q \rightarrow 0, \omega)}{\partial \omega} \right]^{-1} = \frac{1}{2} \frac{[\omega_{TO}^2 - \omega^2]^2 \omega^3}{\Omega_{PL}^2 [\omega_{TO}^2 - \omega^2]^2 + \varepsilon_\infty \omega^4 \omega_{pl}^2} . \quad (9.14)$$

In the limit when the ionic plasma frequency ω_{pl} exceeds that of the electron plasma Ω_{pl} , we get

$$\left[\frac{\partial \varepsilon(q \rightarrow 0, \omega)}{\partial \omega} \right]^{-1} \Big|_{\omega=\omega_{LO}} \stackrel{\Omega_{PL} \ll \omega_{pl}}{\approx} \frac{1}{2} \frac{\omega_{LO}^2 - \omega_{TO}^2}{\varepsilon_{\infty} \omega_{LO}} = \frac{1}{2} \frac{\omega_{LO}^2 - \omega_{LO}^2 \frac{\varepsilon_{\infty}}{\varepsilon_0}}{\varepsilon_{\infty} \omega_{LO}} \quad (9.15)$$

$$= \frac{\omega_{LO}}{2} \left(\frac{1}{\varepsilon_{\infty}} - \frac{1}{\varepsilon_0} \right),$$

giving the desired result. As an immediate consequence of Eq. (9.14), we note that the EELS spectral weight at the frequency of the TO phonon vanishes, $s_{\omega_{TO}}(q \rightarrow 0) = 0$.

However, for the itinerant charge concentrations when the plasmon and the phonon energies become comparable, the two excitations are strongly coupled, resulting in significantly renormalized energies of coupled excitations. They do not necessarily have predominantly a phonon nor a plasmon character, but rather a hybridization of excitations is generally expected. In such circumstances, in the long-wavelength limit, the EELS spectrum shows two peaks at frequencies ω_- and ω_+ , hereafter referred to the lower frequency excitation (LFE) and higher frequency excitation (HFE), respectively. With s_- and s_+ , we denote the corresponding spectral weights of the two coupled excitations in EELS spectra.

9.2.2 Phonon spectral function

In parallel to the EELS spectrum, we also consider the experimentally relevant phonon spectral function that may be investigated by neutron scattering experiments, defined by Eq. (7.29), where $D(\mathbf{q}, \omega)$ now corresponds to the LO phonon propagator. The spectral function of the unperturbed LO phonon propagator

$$D_0(\mathbf{q}, \omega) = \frac{1}{\hbar\omega - \hbar\omega_{LO} + i\eta} - \frac{1}{\hbar\omega + \hbar\omega_{LO} - i\eta}, \quad (9.16)$$

is characterized by the LO phonon frequency only

$$B_0(\mathbf{q}, \omega) = [\delta(\hbar\omega - \hbar\omega_{LO}) + \delta(\hbar\omega + \hbar\omega_{LO})], \quad (9.17)$$

satisfying the sum rule

$$\hbar \int_0^{+\infty} d\omega B_0(\mathbf{q}, \omega) = 1, \quad (9.18)$$

where we again restrict the analysis to positive frequencies only. For the upcoming discussion, it is convenient to exploit Eq. (1.8) to write for the total LO phonon spectral weight

$$\hbar \int_{-\infty}^{\infty} B(\mathbf{q}, \omega) d\omega = \frac{2M\omega_{LO}}{\hbar} \langle \Omega | \hat{x}_{\mathbf{q}} \hat{x}_{-\mathbf{q}} | \Omega \rangle. \quad (9.19)$$

According to Eq. (9.19), the total phonon spectral weight is defined by the lattice quantum fluctuations in the ground state of the interacting system $|\Omega\rangle$. In general, this spectral weight may be distributed among different excitations of the system.

Specifically, with the interactions included, in contrast to the polaron case, the renormalized LO phonon propagator can be obtained by means of the Dyson equation

$$[D(\mathbf{q}, \omega)]^{-1} = [D_0(\mathbf{q}, \omega)]^{-1} - \Pi(\mathbf{q}, \omega) , \quad (9.20)$$

and the phonon spectral function develops new peaks corresponding to collective system excitations, given by the poles of Eq. (9.20). This is accompanied by the appearance of an incoherent contribution from electron-hole pair excitations, yielding

$$D(\mathbf{q}, \omega > 0) = \sum_i \frac{z_i(\mathbf{q})}{\hbar\omega - \hbar\omega_i(\mathbf{q}) + i\eta} + D_{e-h}(\mathbf{q}, \omega > 0) . \quad (9.21)$$

Here, z_i measures directly the projection of system excitations to the unperturbed phonon, providing information about their phonon character. Similarly as in the polaron problem, it is crucial to observe that in addition to the spectral weight redistribution among excitations and the incoherent continuum (phonon transfer), an additional spectral weight might appear (phonon production)

$$\hbar \int_0^{+\infty} d\omega B(\mathbf{q}, \omega) = \sum_i z_i(\mathbf{q}) + z_{e-h}(\mathbf{q}) \geq 1 , \quad (9.22)$$

where $z_{e-h}(\mathbf{q}, \omega > 0)$ denotes the phonon spectral weight associated with the incoherent continuum. This additional spectral weight, as we show, heavily depends on the electron-phonon interaction strength and may be of very different physical origins.

In analogy to the EELS spectrum, due to the phonon-plasmon coupling, in the long-wavelength limit two excitations with finite frequencies, ω_{\pm} , appear in the phonon spectral function. Each of these two excitations is characterized by its own spectral weight z_{\pm} . The cases with the phonon production, $z_+ + z_- > 1$, deserve special attention since they may be caused by different physical mechanisms, ranging from the standard phonon frequency softening to a presence of a permanent, yet dynamic lattice deformation that does not break the translational symmetry. In the context of phonon-plasmon coupled systems, to the best of our knowledge, phonon production has not been discussed previously, with the exception of seminal work by Varga [161].

To treat on an equal footing EELS and phonon spectra, we adopt the RPA kind of scheme for calculations of the phonon propagator. Diagrammatically, this scheme is shown in Fig. 9.1. The first row in Fig. 9.1 represents the Dyson equation for the phonon propagator, with the polarization being represented by the bubble denoted with double fermion lines ending by the pair

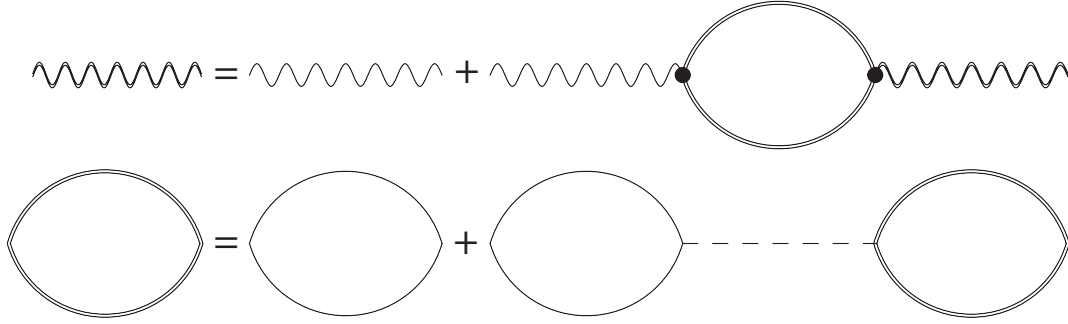


Figure 9.1: Diagrammatic representation of the RPA kind of scheme for the phonon propagator. The corresponding polarization consists of the density-density correlation function (bubble with double solid lines) ending with the electron-phonon interaction vertices. In the RPA, the density-density correlation function can be pictorially represented by the infinite chain of bubble diagrams coupled with the Coulomb interaction, as shown in the second row.

of electron-phonon vertices (dots). The bubble in the first row stands for the standard RPA for the density-density correlation function in a system with the electron-electron interaction, shown in the second row in Fig. 9.1, with the dashed line representing the instantaneous electron-electron interaction. It is easy to verify that the scheme in Fig. 9.1 corresponds to an infinite series of diagrams for the phonon propagator, where the series consists of the diagrams with all different numbers of polarization bubbles connected either with phonon or electron-electron interaction lines in all possible combinations. It is worth mentioning that the scheme in Fig. 9.1 can be utilized to obtain the total dielectric function in Eq. (9.5), simply by reinterpreting the double wavy line as the effective electron-electron interaction and interchanging the phonon (together with the electron-phonon interaction vertices) and the Coulomb interaction propagators.

By recalling that the electron dielectric function in the standard RPA takes the form given by Eq. (9.6), the polarization corresponding to that in Fig. 9.1 may be written as

$$\Pi(\mathbf{q}, \omega) = \frac{|g(\mathbf{q})|^2}{v_{\mathbf{q}}^{\infty}} \left[\frac{1}{\varepsilon_{RPA}(\mathbf{q}, \omega)} - 1 \right]. \quad (9.23)$$

This expression is especially appealing since it readily allows for the calculation of polarization beyond the RPA. Namely, replacing $\chi_0(\mathbf{q}, \omega)$ with $\chi_{irr}(\mathbf{q}, \omega)$ in $\varepsilon_{RPA}(\mathbf{q}, \omega)$, where $\chi_{irr}(\mathbf{q}, \omega)$ denotes the sum of irreducible density-density correlation function diagrams, allows for the inclusion of some fermion self-energy and vertex corrections due to both the electron-electron and the electron-phonon interaction.

However, we emphasize that the RPA kind of scheme used here is generally valid in describing high electron density liquids such as in heavily doped semiconductors. In particular, in doped semiconductors, an actual density of itinerant charge carriers is usually quite low in comparison to metals, albeit due to the smallness of effective masses and large values of effective Bohr radii,

effective carrier densities may be even larger than in metals, making many semiconductors a suitable environment to implement the RPA [40]. The use of the RPA for the phonon propagator is further supported by Migdal's theorem [119], which justifies the omission of electron-phonon vertex corrections for sufficiently high electron densities and high momenta. Moreover, as long as Migdal's theorem may be applied, it may be argued that fermion self-energy contributions bring only quantitative corrections to spectra, for example through the (weak) renormalization of effective masses or damping of excitations [208], while qualitatively no new features should be expected.

9.2.3 Adiabaticity parameter and limiting behaviors

The complex mixing of a phonon and a plasmon is captured by Eqs. (9.5) and (9.23), accounting for the full dynamic treatment of the total dielectric function and the polarization in the presence of electrons coupled to the crystal lattice. However, for a better understanding of the interplay between the lattice and the electron subsystem, it is particularly useful to consider some limiting cases.

First, we redefine the adiabaticity parameter introduced in Part II of the thesis $\kappa = \omega_0/t$. Namely, now the plasmon frequency Ω_{pL}^∞ naturally sets the frequency scale for the electron subsystem, similarly to the way the phonon frequency ω_{LO} characterizes the lattice subsystem. Therefore, we redefine the adiabaticity parameter as the ratio of those two frequency scales $\kappa = \omega_{LO}/\Omega_{pL}^\infty$ in the long-wavelength limit. Depending on the value of κ , three different regimes may be distinguished, followed by the three limiting choices for the electron dielectric function $\epsilon_{RPA}(\mathbf{q}, \omega)$ in Eqs. (9.5) and (9.23).

The case $\kappa \gg 1$ corresponds to the antiadiabatic regime when the plasmon frequency significantly subceeds that of the phonon. Apart from the polaronic effects described in Part II, the phonon remains unrenormalized, since the slow electron plasma oscillations cannot influence the fast lattice vibrations. This readily follows from Eq. (9.23), by noting that only the high-frequency part of the electron dielectric function $\epsilon_{RPA}(\mathbf{q}, \omega \approx \infty) \rightarrow 1$ contributes to the frequency window situated around the phonon frequency.

When the plasmon frequency is tuned so that it approximately matches that of the phonon, the resonant regime with $\kappa \approx 1$ is reached. In such situations, the full frequency dependence of the electron dielectric function should be kept.

Lastly, for small κ , corresponding to the adiabatic regime, the electron degrees of freedom are much faster than the phonon. Correspondingly, the electron dielectric function in Eqs. (9.5) and (9.23) may be approximated by its static value $\epsilon_{RPA}(\mathbf{q}, \omega \approx 0)$. This suggests that the correct way of approximating the total dielectric function or the polarization is to first determine their dynamic properties through the electron dielectric function $\epsilon_{RPA}(\mathbf{q}, \omega)$, depending on the adiabaticity parameter κ , and only after that eventual approximations on their momentum

dependence can be made.

Resonant regime

The resonant regime naturally serves as a starting playground for studying the phonon-plasmon mixing, since then the frequencies of two excitations are nearly degenerate. In particular, in the long-wavelength limit, the physics of the resonant regime reduces solely to the phonon-plasmon coupling due to the absence of the continuum and the corresponding polaronic effects. Namely, the dynamic long-wavelength limit of the electron dielectric function takes the form $\epsilon_{RPA}(q \rightarrow 0, \omega) = 1 - (\Omega_{PL}^\infty)^2/\omega^2$, yielding for the polarization

$$\Pi(q \rightarrow 0, \omega) = \frac{\hbar\Omega_{PL}^\infty |g(\mathbf{q})|^2}{2v_{\mathbf{q}}^\infty} \frac{2\hbar\Omega_{PL}^\infty}{(\hbar\omega)^2 - (\hbar\Omega_{PL}^\infty - i\eta)^2}. \quad (9.24)$$

We note that the second factor on the right-hand side of Eq. (9.24) has the form of the free plasmon propagator, while the first factor may be interpreted as the effective matrix element of phonon-plasmon coupling $|\tilde{g}(\mathbf{q})|^2$.

By inserting Eq. (9.24) into the Dyson equation in Eq. (9.20) and by looking for the poles of the phonon propagator, the biquadratic equation is obtained, describing the coupling of two boson modes. Its solutions are given by

$$2\omega_\pm^2 = \omega_{LO}^2 + [\Omega_{PL}^\infty]^2 \pm \sqrt{\left(\omega_{LO}^2 - [\Omega_{PL}^\infty]^2\right)^2 + 16|\tilde{g}(\mathbf{q})|^2\omega_{LO}\Omega_{PL}^\infty/\hbar^2}, \quad (9.25)$$

corresponding to the frequencies of the collective excitations of the coupled phonon-plasmon system. The same solutions are obtained from the zeros of Eq. (9.5), assuming in Eq. (9.25) the polar coupling given by Eq. (9.2). Here, it should be stressed that in describing the phonon-plasmon coupled system via the total dielectric function, Eq. (9.5), the polar coupling is explicitly assumed. On the other hand, the approach involving the phonon propagator allows for a general type of the electron-phonon interaction matrix element $g(\mathbf{q})$.

Although Eq. (9.25) is strictly speaking obtained in the resonant regime, as we shall show, it provides the excitations' frequencies of the phonon-plasmon coupled system around $q \approx 0$ irrespectively of the adiabaticity parameter. In particular, we first consider the 3D case with $\Omega_{PL}^2(q \rightarrow 0) = \text{const} \propto n$ in the antiadiabatic $\kappa \gg 1$ regime, when two solutions of Eq. (9.25) are $\omega_+ = \omega_{LO}$ and $\omega_- = \Omega_{PL}^0 = \Omega_{PL}/\sqrt{\epsilon_0}$. That is, the phonon frequency remains unchanged, while the plasmon gets screened by both the interband excitations and the lattice vibrations. By exploiting Eq. (9.14) and the inequality $\Omega_{PL}^0 \ll \omega_{TO}$, the corresponding plasmon spectral weight in an EELS spectrum then equals

$$s_{\Omega_{PL}^0}(q \rightarrow 0) = \frac{\hbar \Omega_{PL}^0}{2\varepsilon_0}. \quad (9.26)$$

For higher electron densities when the adiabatic regime is reached, the electron subsystem completely screens long-range interactions between ions. This reduces the frequency of the LO phonon to that of the TO phonon. Accordingly, for $\kappa \ll 1$, two solutions of Eq. (9.25) read $\omega_- = \omega_{TO}$ and $\omega_+ = \Omega_{PL}^\infty$. Since only the interband excitations are fast enough to screen the plasmon, ω_+ is characterized by ε_∞ .

In addition, we can obtain the momentum dependence of the ω_- mode in the adiabatic regime by taking the static limit of the electron dielectric function in Eq. (9.23). In particular, with $\varepsilon_{RPA}(q \rightarrow 0, \omega \approx 0) = 1 + q_{TF}^2/q^2$ giving $1/\varepsilon_{RPA}(q \rightarrow 0, \omega \approx 0) \approx q^2/q_{TF}^2$ in Eq. (9.23), where q_{TF} is the Thomas-Fermi wave vector, we obtain by solving the Dyson equation, Eq. (9.20), for the LFE

$$\omega_- = \sqrt{\omega_{TO}^2 + \omega_{pl}^2 \frac{q^2}{q_{TF}^2}}. \quad (9.27)$$

For metals in the jellium model ε_0 diverges [209] and Eq. (9.27) may be used to obtain ω_- by setting $\omega_{TO} = 0$. The ionic plasma oscillations get screened, acquiring an acoustic dispersion $\omega_-/\omega_{pl} = q/q_{TF}$, with $\omega_{pl} = \omega_{LO}$.

Such analysis of the phonon-plasmon coupling in 2D cases requires a bit more attention. In particular, in 2D systems the plasmon is gapless and its frequency vanishes in the long-wavelength limit $\Omega_{PL}^\infty(q \rightarrow 0) = \sqrt{\frac{e^2 n}{2\varepsilon_0 \varepsilon_\infty m^*}} q$ [169], raising the question whether the different adiabaticity regimes are well defined at all. Thus, we argue that it is unimportant to study Eq. (9.25) for different limits of κ , but rather for various strengths of the electron-phonon interaction.

With the polar coupling given by Eq. (9.2) substituted in Eq. (9.25), the frequencies of phonon-plasmon coupled excitations in the long-wavelength limit read

$$\omega_\pm^2 = \frac{\omega_{LO}^2 + [\Omega_{PL}^\infty]^2}{2} \pm \frac{1}{2} \sqrt{(\omega_{LO}^2 - [\Omega_{PL}^\infty]^2)^2 + 4\lambda \omega_{LO}^2 [\Omega_{PL}^\infty]^2}, \quad (9.28)$$

where $\lambda = 1 - \frac{\varepsilon_\infty}{\varepsilon_0}$. In the weak coupling case $\varepsilon_\infty \approx \varepsilon_0 \Rightarrow \lambda \rightarrow 0$, so

$$\omega_-^2 \approx [\Omega_{PL}^\infty]^2 - \lambda [\Omega_{PL}^\infty]^2 = \frac{\varepsilon_\infty}{\varepsilon_0} [\Omega_{PL}^\infty]^2 = [\Omega_{PL}^0]^2, \quad \omega_+^2 \approx \omega_{LO}^2 + \lambda [\Omega_{PL}^\infty]^2 \approx \omega_{LO}^2. \quad (9.29)$$

On the other hand, for a much stronger coupling holds $\varepsilon_\infty \ll \varepsilon_0 \Rightarrow \lambda \rightarrow 1$. With the introduction

of $\tilde{\lambda} \equiv 1 - \lambda = \frac{\varepsilon_\infty}{\varepsilon_0}$, Eq. (9.25) can be written as

$$\omega_\pm^2 = \frac{\omega_{LO}^2 + [\Omega_{PL}^\infty]^2}{2} \pm \frac{1}{2} \sqrt{\left(\omega_{LO}^2 + [\Omega_{PL}^\infty]^2\right)^2 - 4\tilde{\lambda}\omega_{LO}^2 [\Omega_{PL}^\infty]^2}, \quad (9.30)$$

giving in the strong coupling case ($\tilde{\lambda} \rightarrow 0$)

$$\omega_-^2 \approx \tilde{\lambda} [\Omega_{PL}^\infty]^2 = \frac{\varepsilon_\infty}{\varepsilon_0} [\Omega_{PL}^\infty]^2 = [\Omega_{PL}^0]^2, \quad \omega_+^2 \approx \omega_{LO}^2 + (1 - \tilde{\lambda}) [\Omega_{PL}^\infty]^2 \approx \omega_{LO}^2 + [\Omega_{PL}^\infty]^2. \quad (9.31)$$

In both cases, the LFE follows the plasmon dispersion screened by both interband excitations and the phonon. However, the HFE retains the constant frequency situated at ω_{LO} for weak couplings, while it starts developing the linear dispersion, $\omega_+ \approx \omega_{LO} + \frac{e^2 n}{4\varepsilon_0 \varepsilon_\infty m^* \omega_{LO}} q$, as the coupling increases, with the slope directly proportional to the electron density.

The behaviors discussed above correspond to the long-wavelength limit, with nothing said about the large- q behaviors nor a character of the corresponding excitations. Without the electron-hole continuum in Eq. (9.25), the damping effects are absent as well. To overcome these limitations, by preserving the full momentum and frequency dependence in Eqs. (9.4) and (9.23), we investigate in detail the structure of EELS spectra and phonon spectral functions, along with the distribution of corresponding spectral weights among different excitations. Our results show that in addition to the adiabaticity parameter, the electron-phonon interaction strength is essentially important for the shape of spectra of phonon-plasmon coupled systems, motivating us to discuss regimes, with the experimentally relevant weak and strong electron-phonon interaction separately. From the technical point of view, we use the analytical expression for the 3D and the 2D Lindhard function $\chi_0(\mathbf{q}, \omega)$ [210], which simplifies the numerical work.

9.3 3D case

9.3.1 Weak coupling

All our calculated spectra correspond to actual materials. As a first model of a bulk polar semiconductor, we consider the frequently studied GaAs. With the effective mass $m^* = 0.0657m$, the energy of the LO phonon $\hbar\omega_{LO} = 36.77$ meV, and the dielectric constants $\varepsilon_\infty = 10.9$ and $\varepsilon_0 = 12.83$ [211], it qualifies as a material with a weak polar coupling $\alpha \approx 0.07$.

Spectral functions

In Fig. 9.2, we show the calculated EELS spectra, Figs. 9.2(a)-9.2(c), and the phonon spectral functions of the LO phonon, Figs. 9.2(d)-9.2(f), of the doped bulk GaAs for three different

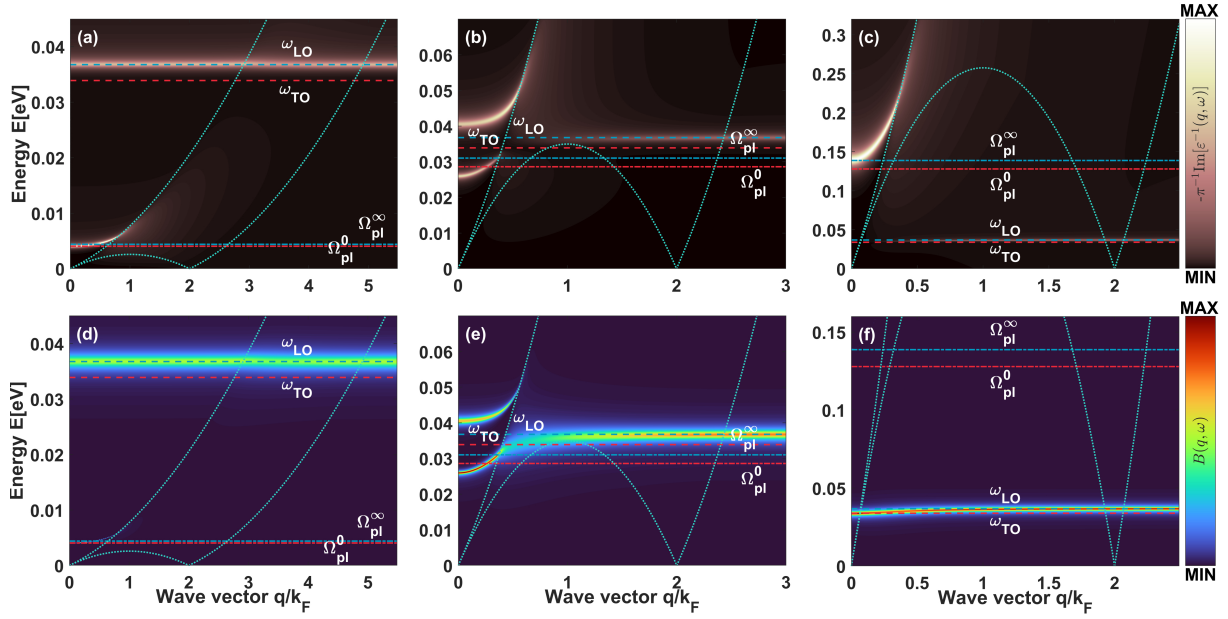


Figure 9.2: EELS spectra (upper row) and phonon spectral functions (corresponding to the LO phonon) (lower row) of the bulk GaAs for three different electron densities n . The first column corresponds to $n = 10^{16} \text{ cm}^{-3}$, the second to $n = 5 \cdot 10^{17} \text{ cm}^{-3}$, and the third to $n = 10^{19} \text{ cm}^{-3}$, depicting the antiadiabatic ($\kappa \gg 1$), resonant ($\kappa \approx 1$), and adiabatic ($\kappa \ll 1$) regime, respectively. Note that MAX on the intensity scale takes a different absolute value for each of the panels.

electron densities $n = 10^{16} \text{ cm}^{-3}$ ($k_F = 6.6 \cdot 10^{-3} \text{ \AA}^{-1}$), $5 \cdot 10^{17} \text{ cm}^{-3}$ ($k_F = 2.4 \cdot 10^{-2} \text{ \AA}^{-1}$), and 10^{19} cm^{-3} ($k_F = 6.6 \cdot 10^{-2} \text{ \AA}^{-1}$). In all the figures, the red and blue dashed lines denote the phonon frequencies ω_{TO} and ω_{LO} , respectively. The plasmon frequencies Ω_{PL}^0 and Ω_{PL}^∞ in the long-wavelength limit are denoted by the dot-dashed red and blue lines, respectively, while the boundaries of the electron-hole continuum are denoted by the turquoise dotted lines.

From Figs. 9.2(a) and 9.2(d), for $q = 0$ we see two well-defined excitations at frequencies Ω_{PL}^0 and ω_{LO} , indicating clearly that the electron density $n = 10^{16} \text{ cm}^{-3}$ corresponds to the antiadiabatic regime. As q increases, the LFE follows a plasmon-like dispersion and gets Landau damped upon entering the continuum. The HFE stays a well-defined excitation of constant frequency ω_{LO} up to the highest values of q shown.

Upon increasing the electron density, the resonant regime is reached, with the corresponding spectra shown in Figs. 9.2(b) and 9.2(e). The strong level repulsion of coupled excitations is evident for small momenta $q < k_F$, because of which neither of the two excitations in Figs. 9.2(b) and 9.2(e) exhibit long-wavelength limiting behaviors denoted by the horizontal lines. With increasing q , both excitations develop a considerable dispersion and the HFE gets completely Landau damped by the continuum. The frequency of the LFE monotonically increases from the minimum value at $q = 0$ to the frequency of the LO phonon ω_{LO} for $q \gtrsim k_F$. Upon reaching the continuum roughly at $\omega \approx \omega_{TO}$, it gets strongly damped and ceases to be a well-defined excitation. However, with the further increase of q , the spectral weight corresponding to the

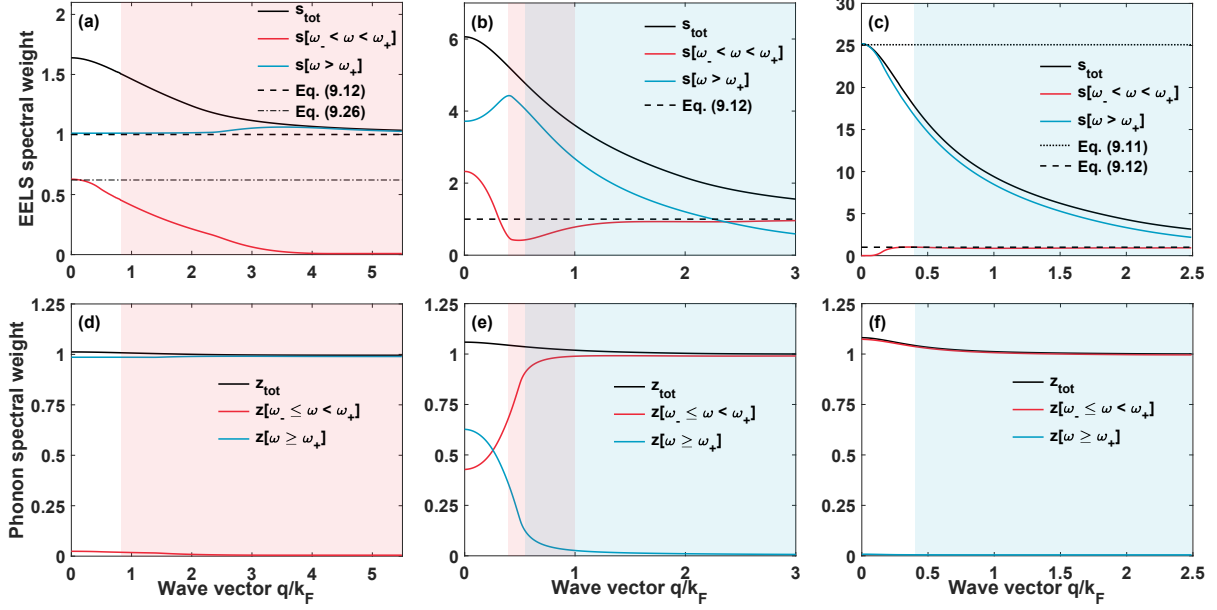


Figure 9.3: Integrated EELS spectra (upper row) and integrated phonon spectra (lower row) shown in Fig. 9.2.

LFE sharpens again, forming a well-defined excitation characterized by a lifetime that becomes longer as q increases.

For the highest electron density considered, the EELS spectrum shows only the HFE for low q , Fig. 9.2(c). The LFE is, however, well captured by the phonon spectral function in Fig. 9.2(f), with exactly the frequency of the TO phonon for $q \approx 0$, suggesting the adiabatic behavior of the system for the corresponding electron density. The absence of the LFE's spectral weight around $q \approx 0$ in the EELS spectrum is in accordance with the vanishing spectral weight at ω_{TO} , when the total dielectric function diverges. In Fig. 9.2(c), the HFE evidently follows the plasmon dispersion Ω_{PL}^{∞} unaffected by the phonon and gets Landau damped in the continuum. As seen from Fig. 9.2(f), the frequency of the LFE continuously increases from ω_{TO} to ω_{LO} and remains a well-defined excitation for all momenta, although weakly damped upon entering the continuum (the large energy scale set by the HFE partially hinders these details in Fig. 9.2(f)).

Integrated spectra

In order to get a better insight into the nature of excitations in Fig. 9.2 as a function of q , in Fig. 9.3 we consider EELS and phonon spectral weights given by Eqs. (9.9) and (9.22), respectively, obtained by integrating the spectra in Fig. 9.2. In particular, aside from the total spectral weight, we consider spectral weights in two specific frequency regions. The first corresponds to the frequency window $\omega_- < \omega < \omega_+$, while the second to $\omega > \omega_+$. This should provide an estimation of the spectral weights s_{\pm} and z_{\pm} even in the presence of a strong damping or a limited experimental resolution. For example, to capture the total spectral weight in the

HFE, s_+ or z_+ , the integration cutoff is defined below ω_+ such that it correctly reproduces the corresponding spectral weight in the long-wavelength limit. In the resonant regime, a weakly momentum-dependent integration cutoff has been taken. The spectral weights corresponding to the reference limiting behaviors, Eqs. (9.11), (9.12) and (9.26), are indicated by the straight lines in Fig. 9.3, normalized to the spectral weight at $\omega = \omega_{LO}$. Momenta for which in Fig. 9.2 the LFE and the HFE get damped are shaded by the red and blue color, respectively. These two shaded areas overlap in Figs. 9.3(b) and 9.3(e), that is, in the resonant regime.

For small momenta q , it is clear from Fig. 9.3(a) that in the antiadiabatic regime both the LFE and the HFE contribute significantly to the total EELS spectral weight, matching perfectly the predictions of Eqs. (9.26) and (9.12), respectively. For larger q , the spectral weight of the LFE vanishes, while in the HFE case it stays roughly constant, well described by Eq. (9.12), with a slight enhancement for momenta $q \geq 3k_F$, which should be attributed to the electron-hole continuum s_{e-h} . Thus, the plasmon and the phonon character of the LFE and the HFE, respectively, are unquestionable in the antiadiabatic regime. This is further confirmed by Fig. 9.3(d), with almost all the phonon spectral weight being associated with the HFE.

Contrary, for the highest density case shown in Fig. 9.3(c), the HFE's spectral weight is almost purely plasmon-like. As predicted by Eq. (9.11), it accounts for almost all of the total spectral weight at small momenta. For higher momenta, the spectral weight in the frequency window $\omega > \omega_+$ should rather be attributed to the electron-hole continuum. On the other hand, the LFE spectral weight may be completely ascribed to the phonon subsystem. Indeed, the LFE contribution to the EELS spectrum appears in Fig. 9.3(c) when the LFE approaches ω_{LO} , due to the electron scattering by the LO vibrations, as described by Eq. (9.12). At the same time, the phonon spectral function in Fig. 9.3(f) is fully dominated by the LFE.

The results become slightly more difficult for interpretation in the resonant regime, Figs. 9.3(b) and 9.3(e). For small momenta, both collective excitations involve a strong mixture of the phonon and the plasmon component, signaling strongly hybridized modes. However, as seen from Fig. 9.3(e), for $q \geq 0.4k_F$, the dominant character of excitations is unambiguous. In particular, the LFE is dominated by the phonon, while the HFE with the plasmon component.

The common property of all three phonon spectra in Fig. 9.2 is the phonon production effect, manifested as a small increase of the total phonon spectral weight around $q \approx 0$. For larger q , this additional phonon spectral weight vanishes and the total spectral weight approaches the value given by Eq. (9.18). Such a weak phonon production is an indication that, concerning the lattice subsystem, the ground state of the coupled phonon-plasmon system is approximately given by the LO phonon vacuum. However, this situation changes for the stronger electron-phonon interaction.

9.3.2 Strong coupling

In contrast to III-IV semiconductors, bulk transition metal oxides may host much stronger polar couplings. As a representative material with a significant electron-phonon interaction, we take anatase TiO₂, which electrons upon doping the conduction band, characterized by the effective mass $m^* = 0.42 m$, couple to a LO E_u phonon with the energy $\hbar\omega_{LO} = 108$ meV [84]. The corresponding dielectric functions read $\epsilon_\infty = 5.82$, and $\epsilon_0 = 45.1$ [212], resulting in the much larger electron-phonon interaction constant $\alpha \approx 1.09$ than in GaAs. From the experimental point of view, TiO₂ is very appealing, since ω_{LO} and Fermi wave vectors k_F corresponding to relevant electron densities are a few times larger than in GaAs, making it more suitable for experiments with low energy and momentum resolutions.

Spectral functions

In Fig. 9.4, we show the EELS spectra, Figs. 9.4(a)-9.4(c), and the phonon spectral functions corresponding to the LO E_u phonon, Figs. 9.4(d)-9.4(f), of the bulk anatase TiO₂ for three different electron densities $n = 10^{17}$ cm⁻³ ($k_F = 1.4 \cdot 10^{-2}$ Å⁻¹), $5 \cdot 10^{18}$ cm⁻³ ($k_F = 0.2$ Å⁻¹), and $5 \cdot 10^{21}$ cm⁻³ ($k_F = 0.53$ Å⁻¹). These choices of electron densities correspond to the antiadiabatic, resonant, and adiabatic regime, respectively. The structure of spectra remained overall similar to that in the weak coupling case. However, it should be immediately emphasized that in the antiadiabatic and resonant regime the excitations get much more strongly damped within the continuum. Additionally, in the antiadiabatic regime, the HFE develops a visible kink as it enters the continuum, which may well be seen in Figs. 9.4(a) and 9.4(d).

Integrated spectra

Because of the strong damping, which completely blurs some parts of the EELS and the phonon spectra, for stronger couplings, it is particularly useful to analyze the integrated spectra shown in Fig. 9.5. From Fig. 9.5(a), corresponding to the antiadiabatic regime, it is evident that the total spectral weight of the EELS spectrum is dictated by the constant spectral weight of the HFE due to the strong electron-phonon interaction, Eq. (9.12), pointing to the phonon character of the HFE, well supported by Fig. 9.5(d).

In the resonant regime, the spectral weight of the HFE continues to dominate the EELS spectrum for small q , albeit slightly higher spectral weight is confined within it than predicted by Eq. (9.12), suggesting the appreciable plasmon component in addition to the phonon one. In the adiabatic regime, similarly to the weak coupling case, the plasmon-like spectral weight of the HFE dominates the EELS spectrum for small q , while for larger momenta the total spectral weight is contributed by the LFE at ω_{LO} , as described by Eq. (9.12), and the electron-hole continuum. The latter is also true in the resonant regime. In all the regimes, despite the change

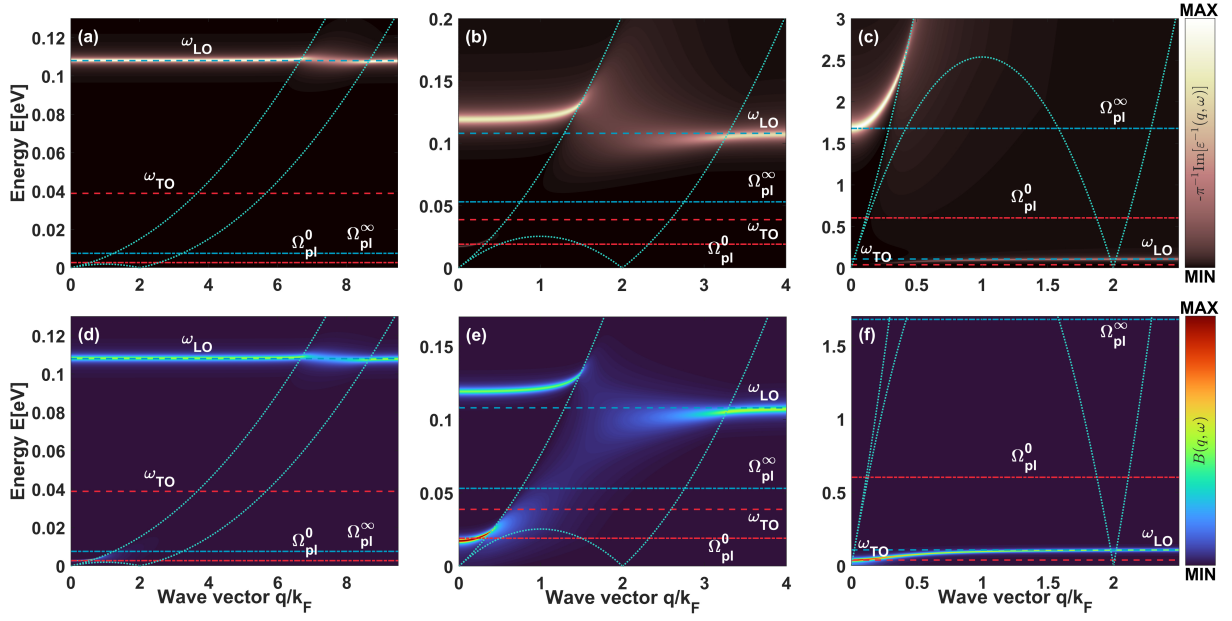


Figure 9.4: EELS spectra (upper row) and phonon spectral functions (corresponding to the LO E_u phonon) (lower row) of the bulk anatase TiO_2 for three different electron densities n . The first column corresponds to $n = 10^{17} \text{ cm}^{-3}$, the second to $n = 5 \cdot 10^{18} \text{ cm}^{-3}$, and the third to $n = 5 \cdot 10^{21} \text{ cm}^{-3}$, depicting the antiadiabatic ($\kappa \gg 1$), resonant ($\kappa \approx 1$), and adiabatic ($\kappa \ll 1$) regime, respectively. Note that MAX on the intensity scale takes a different absolute value for each of the panels.

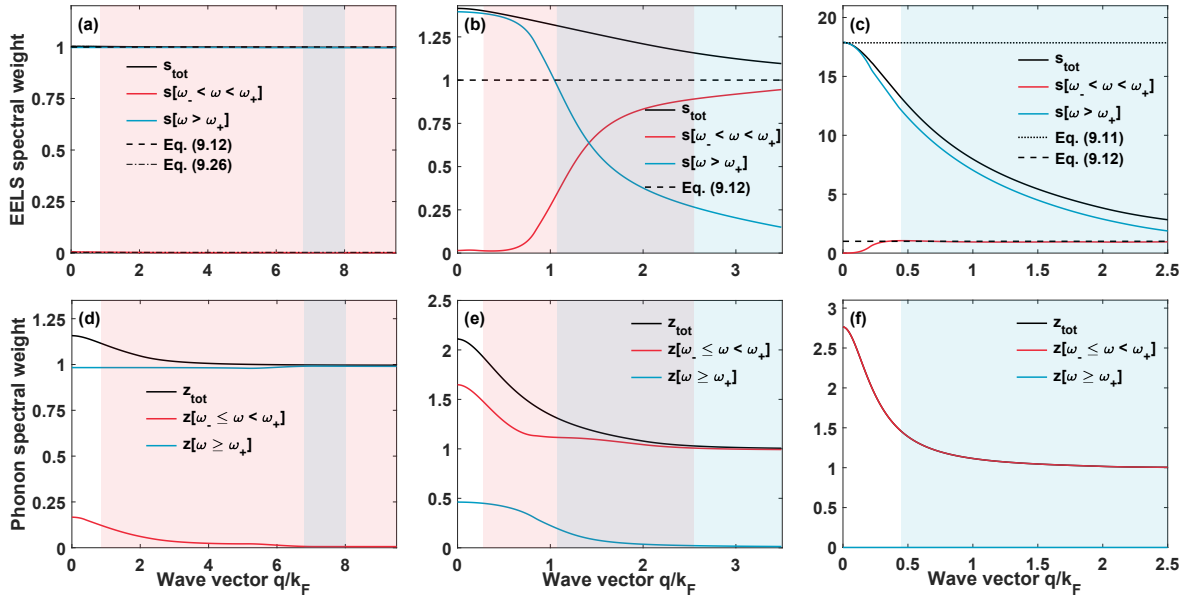


Figure 9.5: Integrated EELS spectra (upper row) and integrated phonon spectra (lower row) shown in Fig. 9.4.

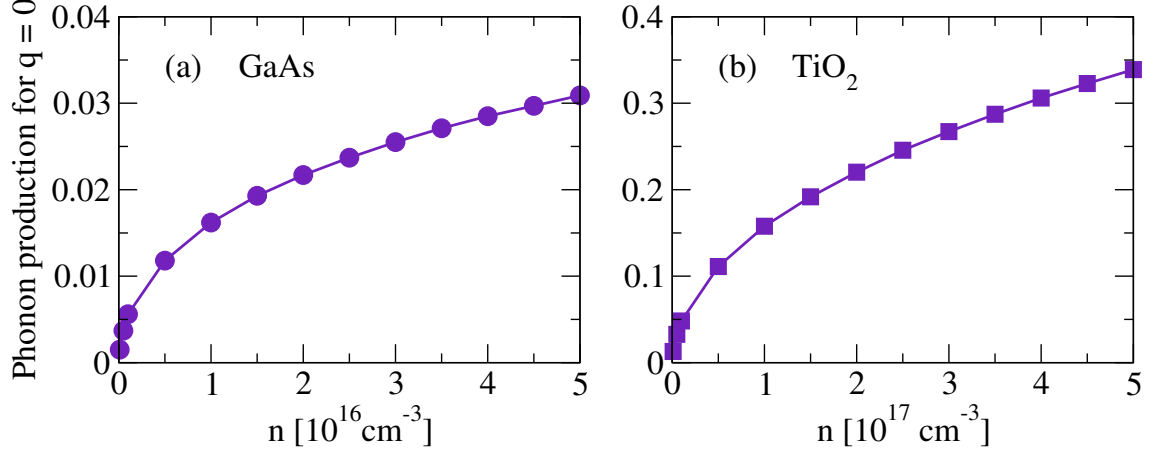


Figure 9.6: Phonon production for $q = 0$ as a function of the electron density n for (a) GaAs and (b) TiO_2 in the antiadiabatic regime.

in the character of excitations, the HFE contributes much more to the total EELS spectral weight than the LFE for small q .

Even bigger discrepancies between the weak and the strong coupling case are evident from the integrated phonon spectral functions, Figs. 9.5(d)-9.5(f). The first striking result is that the additional phonon spectral weight, associated with the phonon production, is very large for small q . This large contribution in Fig. 9.5 characterizes only the LFE for all considered electron densities. However, the physical origin of this effect seems to be quite different depending on the adiabaticity parameter. In particular, in the antiadiabatic regime, phonon production is apparently associated with plasma oscillations. Indeed, by comparing the three curves in Fig. 9.5(d), we see that all the additional phonon spectral weight due to the phonon production clearly involves only the plasmon-like LFE and not the HFE, the latter having the predominantly phonon character. This additional phonon spectral weight scales sublinearly with the electron density, as is evident from Fig. (9.6), indicating that it involves a collective effect, rather than being related to a simple polaronic dressing of individual electrons. On the other hand, in Fig. 9.5(d), one as well observes a small contribution to the phonon production belonging to the electron-hole continuum. This stems from polaronic effects, corresponding to the phonon dressing by itinerant electrons, as described in Part II.

In the adiabatic regime, the electrons are fast and dense, and for small q fully screen the LO phonon. Therefore, ω_{TO} , instead of ω_{LO} , defines the small- q LFE frequency in Fig. 9.4(f). As q increases, the LFE frequency approaches the LO phonon frequency, while the effects of the phonon production weaken. Our analysis of this additional phonon spectral weight in Fig. 9.5(f), with the details presented in Appendix D, confirms that in the adiabatic regime the LFE should be interpreted as the pure harmonic excitation of the lattice subsystem. That is, in Fig. 9.5(f), the values obtained for the phonon production scale with the LFE frequency exactly as expected for the adiabatic phonon softening effects. Namely, for softer phonons with the LFE frequency,

the uncertainty in space of lattice vibration increases, which through Eq. (9.19) explains the phonon production observed in Fig. 9.5(f).

9.4 2D case

In order to discuss the phonon-plasmon coupling in the 2D case, we choose model parameters that bear close resemblances with TMDs. In particular, for a representative value of the effective mass, we take $m^* = 0.43m$ and set the phonon energy at $\hbar\omega_{LO} = 47$ meV. Together with those two values, we make two sets of parameters S_1 and S_2 by considering the values of dielectric constants calculated in [183]. Specifically, to complete the parameter set S_1 we take $\varepsilon_\infty^1 = 15.1$ and $\varepsilon_0^1 = 15.3$ predicted for MoS₂, resulting in a weak electron-phonon interaction constant $\alpha_1 \approx 0.01$. On the other hand, the values $\varepsilon_\infty^2 = 11.2$ and $\varepsilon_0^2 = 66.7$ calculated for ZrS₂ give rise to a much stronger polar coupling with $\alpha_2 \approx 0.83$, defining the parameter set S_2 .

9.4.1 Weak coupling

In Fig. 9.7, we show the EELS spectra, Figs. 9.7(a)-9.7(b), and the phonon spectral functions corresponding to the LO phonon, Figs. 9.7(c)-9.7(d), for the parameter set S_1 and two different electron densities $n = 7 \cdot 10^{11} \text{ cm}^{-2}$ ($k_F = 2.1 \cdot 10^{-2} \text{ \AA}^{-1}$), and $5 \cdot 10^{12} \text{ cm}^{-2}$ ($k_F = 5.6 \cdot 10^{-2} \text{ \AA}^{-1}$). In the 2D case, the plasmon dispersion can be exactly calculated for all momenta [169], allowing us to track the exact dispersions Ω_{PL}^∞ and Ω_{PL}^0 in Fig. 9.7. We note that for the electron density $n = 7 \cdot 10^{11} \text{ cm}^{-2}$ the plasmon Ω_{PL}^∞ gets Landau damped before it crosses with the phonon, leading to an avoided crossing of the unperturbed modes. The corresponding EELS spectrum in Fig. 9.7(a) is clearly dominated by the plasmon-like excitation (it is hard to distinguish between Ω_{PL}^∞ and Ω_{PL}^0 due to the small difference between ε_∞^1 and ε_0^1), while the phonon spectral function in Fig. 9.7(c) shows the well-defined (throughout the whole continuum) phonon-like excitation with the constant frequency ω_{LO} , which, however, develops a faint, yet visible kink as it enters the continuum.

In the case with the higher electron density $n = 5 \cdot 10^{12} \text{ cm}^{-2}$, the unperturbed plasmon and phonon meet before entering the continuum, which is manifested in the spectra in Figs. 9.7(b) and 9.7(d) as the repulsion of two modes. In particular, the EELS spectrum shows the plasmon-like dispersion repelled at the momentum where the unperturbed phonon and plasmon modes cross. Similarly, the phonon spectral function exhibits the well-defined phonon-like excitation with the constant frequency ω_{LO} repelled at the same momentum. With the further increase of electron density, no new spectral features appear.

Integrated EELS and phonon spectra in Fig. 9.7 show identical behaviors for both electron densities considered. They are not shown here since their behaviors are trivial and confirm

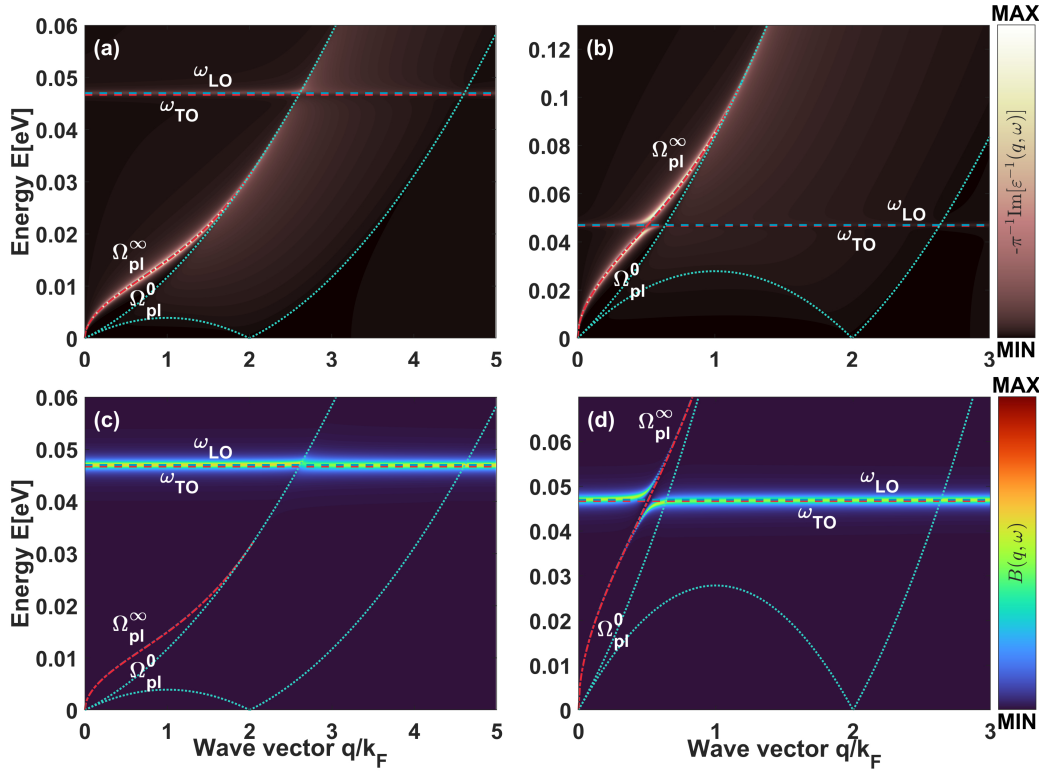


Figure 9.7: EELS spectra (upper row) and phonon spectral functions (corresponding to the LO phonon) (lower row) for the parameter set S_1 and two different electron densities n . The first column corresponds to $n = 7 \cdot 10^{11} \text{ cm}^{-2}$ and the second to $n = 5 \cdot 10^{12} \text{ cm}^{-2}$. Note that MAX on the intensity scale takes a different absolute value for each of the panels.

that the EELS spectrum is solely given by the plasmon excitation, while all the phonon spectral weight is confined at ω_{LO} . This justifies the clear distinction between the plasmon and the phonon excitation and the absence of hybridization, apart from the obvious repulsion at the crossing point. Concerning the total phonon spectral weight, it obeys the sum rule in Eq. (9.18) for all momenta, suggesting negligible phonon transfer and phonon production effects for weak couplings in 2D systems.

9.4.2 Strong coupling

Spectral functions

In Fig. 9.8, we show the EELS spectra, Figs. 9.8(a)-9.8(c), and the phonon spectral functions corresponding to the LO phonon, Figs. 9.8(d)-9.8(f), for the parameter set S_2 and three different electron densities $n = 5 \cdot 10^{11} \text{ cm}^{-2}$ ($k_F = 1.8 \cdot 10^{-2} \text{ \AA}^{-1}$), $5 \cdot 10^{12} \text{ cm}^{-2}$ ($k_F = 5.6 \cdot 10^{-2} \text{ \AA}^{-1}$), and $5 \cdot 10^{13} \text{ cm}^{-2}$ ($k_F = 1.7 \cdot 10^{-1} \text{ \AA}^{-1}$). Contrary to the 3D case where the raw spectra did not differ much in the weak and the strong coupling case, except for the damping within the continuum, the 2D spectra in Figs. 9.7 and 9.8 show drastically different behaviors. In particular, for the lowest electron density considered, $n = 5 \cdot 10^{11} \text{ cm}^{-2}$, the spectra in Figs. 9.8(a) and 9.8(d)

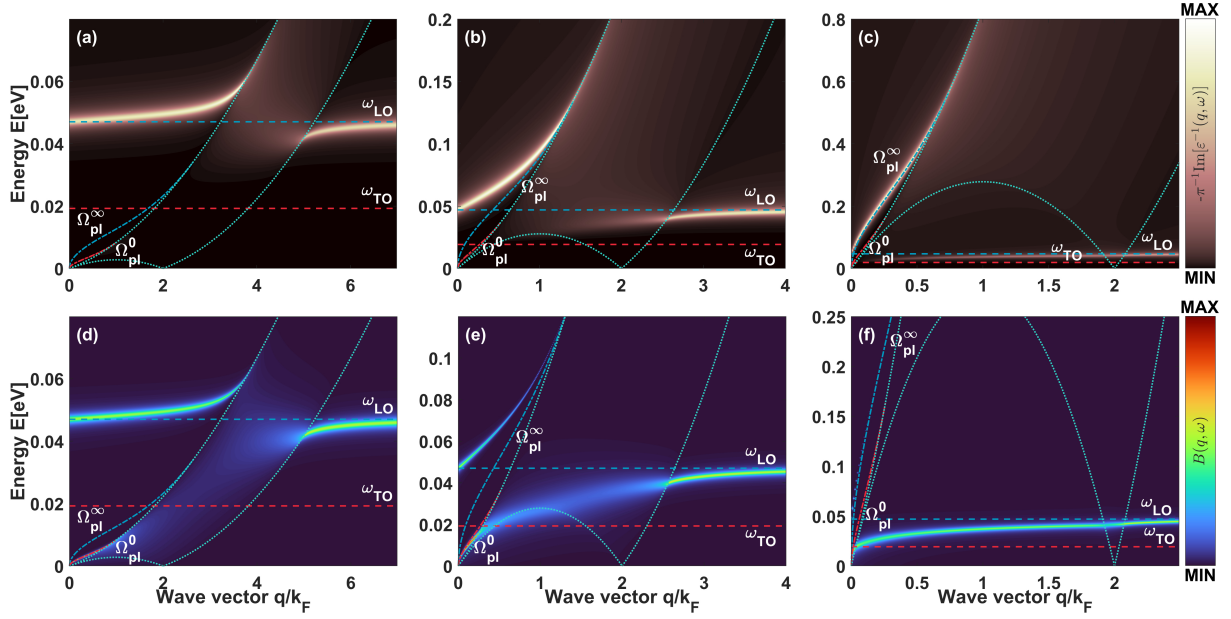


Figure 9.8: EELS spectra (upper row) and phonon spectral functions (corresponding to the LO phonon) (lower row) for the parameter set S_2 for three different electron densities. The first column corresponds to $n = 5 \cdot 10^{11} \text{ cm}^{-2}$, the second to $n = 5 \cdot 10^{12} \text{ cm}^{-2}$, and the third column to $n = 5 \cdot 10^{13} \text{ cm}^{-2}$. Note that MAX on the intensity scale takes a different absolute value for each of the panels.

show that the LFE follows the plasmon-like dispersion screened by both interband excitations and the phonon, while the HFE develops the anticipated linear dispersion and bends as it approaches the continuum. Inside the continuum, both excitations get strongly damped, while above the continuum a well-defined excitation again emerges and approaches the LO phonon frequency ω_{LO} as q increases.

With an increase of the electron density to $n = 5 \cdot 10^{12} \text{ cm}^{-2}$ two effects are readily observed. First, the linear slope of the HFE gets steeper. Second, the LFE seems to merge with the excitation above the continuum into a single LFE. For the electron density $n = 5 \cdot 10^{12} \text{ cm}^{-2}$, this single LFE is still strongly damped within the continuum and develops two kinks upon crossing the boundaries of the electron-hole continuum.

For the highest electron density $n = 5 \cdot 10^{13} \text{ cm}^{-2}$, the linear slope of the HFE gets even steeper and continues into the plasmon dispersion Ω_{pL}^∞ near the boundary of the continuum, where it gets strongly damped. The LFE becomes a well-defined excitation for all momenta, albeit weakly damped as it enters the continuum at the critical momentum defined by the crossing of the TO phonon frequency with the continuum. Both kinks in its dispersion move toward $q \approx 2k_F$. The damping of excitations for three chosen electron densities, from lower to higher, qualitatively closely follows the damping behaviors observed in the strong coupling 3D case in the antiadiabatic, resonant, and adiabatic regimes, respectively.

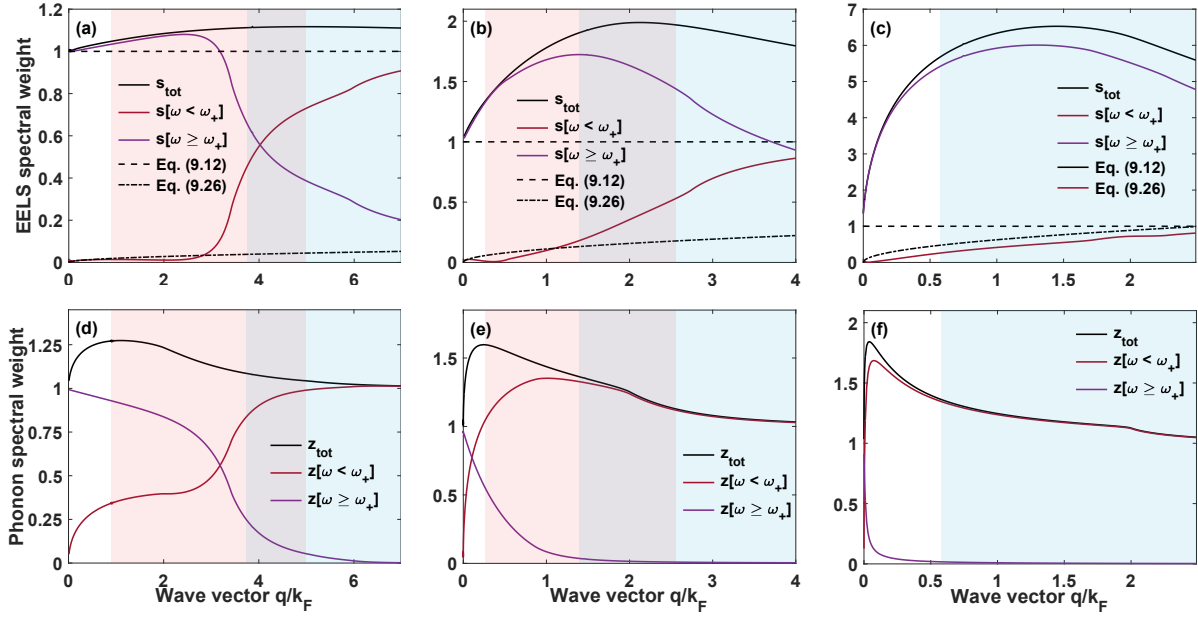


Figure 9.9: Integrated EELS spectra (upper row) and integrated phonon spectra (lower row) shown in Fig. 9.8.

Integrated spectra

Similarities between the 3D and the 2D case for strong couplings continue to show up also in the integrated spectra, presented for the 2D case in Fig. 9.9. Here, apart from the total spectral weight, we consider spectral weights in two specific frequency regions. The first corresponds to the frequency window $\omega < \omega_+$, while the second to $\omega > \omega_+$, which should provide an estimation of the spectral weights in the LFE and the HFE, respectively. In particular, for the lowest electron density $n = 5 \cdot 10^{11} \text{ cm}^{-2}$, the total EELS spectral weight around $q \approx 0$ is dictated by the spectral weight of the HFE situated around ω_{LO} . Correspondingly, the HFE can be well attributed to the phonon excitation in the long-wavelength limit, which is further supported by its dominating phonon spectral weight in Fig. 9.9(d). Regarding the LFE, although its EELS spectral weight is very small compared to that of HFE's, it well follows the behavior predicted by Eq. (9.26) for small q , and for corresponding momenta, the LFE can be associated with the Ω_{PL}^0 plasmon.

With the electron density increased to $n = 5 \cdot 10^{13} \text{ cm}^{-2}$, the phonon contribution given by Eq. (9.12) still accounts for a large amount of HFE's EELS spectral weight. However, its plasmon component also becomes appreciable, pointing to the mixed phonon-plasmon character of the HFE. Finally, for the highest electron density, the EELS spectral weight of the HFE follows the plasmon-like spectral weight given by Eq. (9.11), except around $q \approx 0$, where it approaches the value in Eq. (9.12) expected for the LO phonon. Hence, in a wide range of momenta, $0 < q \leq k_F$, we can attribute the HFE to the plasmon mode. For all electron densities, the EELS spectral weight of the LFE is negligible compared to the spectral weight confined within the HFE in the long-wavelength limit, similarly to the 3D case.

The observation that the EELS spectral weight of the HFE for $q \approx 0$ is given solely by the phonon contribution is reflected also in the phonon spectral weights in Figs. 9.9(d)-(f). Namely, for $q \approx 0$ the total phonon spectral weight is always confined within the HFE and satisfies the sum rule in Eq. (7.31). Consequently, for all electron densities around $q \approx 0$, the HFE can be attributed to the unperturbed phonon, while the LFE to the plasmon renormalized both by interband excitations and the phonon.

As q increases, the HFE (LFE) transitions from a purely phononic (plasmon Ω_{PL}^0) to a dominantly plasmonic Ω_{PL}^∞ (phonon) mode, with the transition being sharper and faster as the electron density increases. In particular, for the lowest electron density considered, the HFE (LFE) can be well attributed to the phonon (plasmon Ω_{PL}^0) mode for momenta below the continuum, with only an appreciable plasmon Ω_{PL}^∞ component of the HFE near the continuum boundary. Contrary, in the case with the highest electron density, the HFE (LFE) attains the phonon (plasmon Ω_{PL}^0) character only in a small region of the momentum space around $q \approx 0$, while for $q > 0$ it corresponds to the Ω_{PL}^∞ plasmon (phonon). For the intermediate density and finite momenta, both excitations show a strongly mixed character. Interestingly, the total phonon spectral weight in Figs. 9.9(e) and (f) exhibits a kink at the momentum $q = 2k_F$.

In accordance with the above discussion, the phonon production is absent for $q = 0$, albeit it becomes appreciable for finite, but small momenta. In the case with the lowest electron density, the phonon production can be unambiguously attributed to the plasmon-like LFE, similarly to the 3D case. On the other hand, from Fig. 9.9(f) is evident that the phonon production, again associated with the LFE, turns on and is maximal roughly around the momentum corresponding to the crossing of the LFE with the ω_{TO} phonon. This suggests that the phonon production has the same nature as in the 3D case also for very high electron densities and is related to the phonon frequency softening effects.

9.5 Static screening and static polarization approximation

We close the discussion of the phonon-plasmon coupling by commenting on the static screening approximation used frequently in *ab initio* simulations of nonadiabatic phonon spectra [180, 181, 197, 213–215]. For that purpose, with the use of the expression Eq. (9.6) for the electron dielectric function, we rewrite the RPA result for the polarization in Eq. (9.23) as

$$\Pi^{(RPA)}(\mathbf{q}, \omega) = \frac{|g(\mathbf{q})|^2}{\varepsilon^{(RPA)}(\mathbf{q}, \omega)} \chi_0(\mathbf{q}, \omega). \quad (9.32)$$

In this new form, we see that the electron dielectric function divides the squared matrix element of the electron-phonon interaction, which can be understood as if one of the electron-phonon

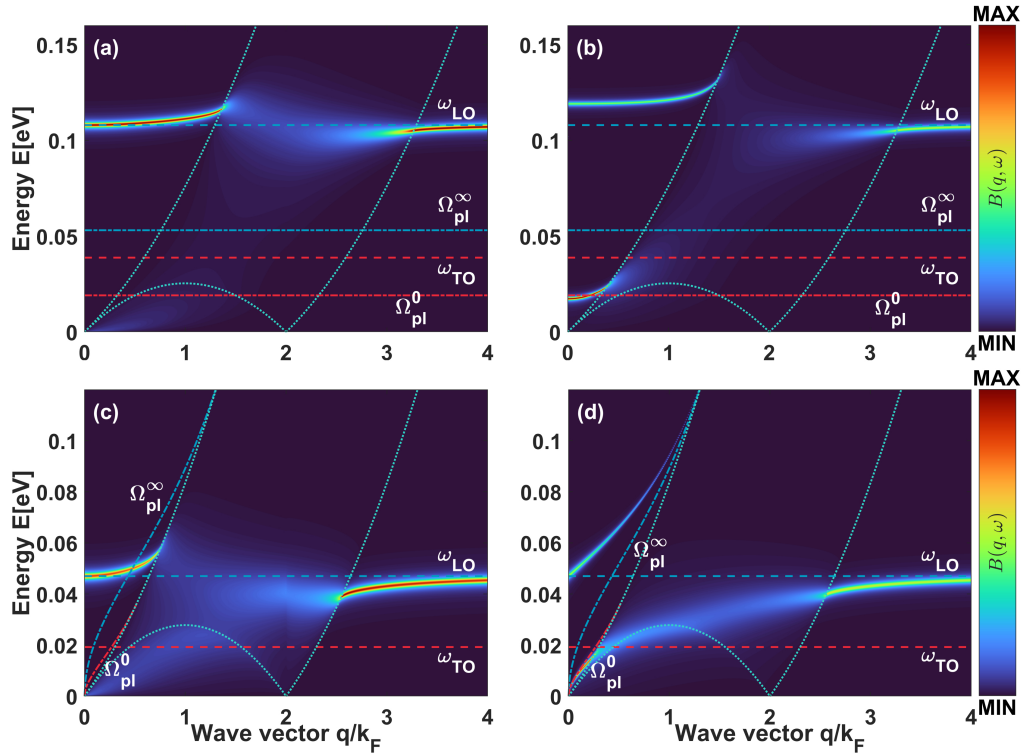


Figure 9.10: Phonon spectral functions for the bulk TiO_2 (upper row) and the 2D parameter set S_2 (lower row), and electron densities $n = 5 \cdot 10^{18} \text{ cm}^{-3}$, and $n = 5 \cdot 10^{12} \text{ cm}^{-2}$, respectively, obtained within the static screening approximation (first column) and with the full dynamic expression in the RPA for the phonon polarization (second column). Note that MAX on the intensity scale takes a different absolute value for each of the panels.

vertices is being renormalized/screened by the electron-electron interaction, see Fig. 7.1. Thus, the static screening approximation consists of approximating the electron dielectric function in the denominator of Eq. (9.32) by its static counterpart.

To compare phonon spectra obtained within the static screening approximation with spectra in the full dynamic RPA, we show in Fig. 9.10 phonon spectral functions calculated within the two approximations for the bulk TiO_2 and the 2D parameter set S_2 , and electron densities $n = 5 \cdot 10^{18} \text{ cm}^{-3}$ (corresponding to the resonant regime), and $n = 5 \cdot 10^{12} \text{ cm}^{-2}$, respectively. From Figs. 9.10(a) and 9.10(b), it is evident that the static screening approximation completely foresees the repulsion of a phonon and a plasmon in the 3D case. In particular, the phonon frequency ω_{LO} remains unperturbed in the long-wavelength limit, while the second excitation does not exist at all. The static screening approximation fails to reproduce some of the key features of the phonon spectrum in the 2D case as well. Although the HFE develops a dispersion and bends near the continuum, the expected linear dispersion of the excitation for small q is missing and the absolute values of its energies are underestimated. The well-defined LFE is also absent, analogously as in the 3D case.

The failure of the static screening approximation in describing the phonon-plasmon coupled

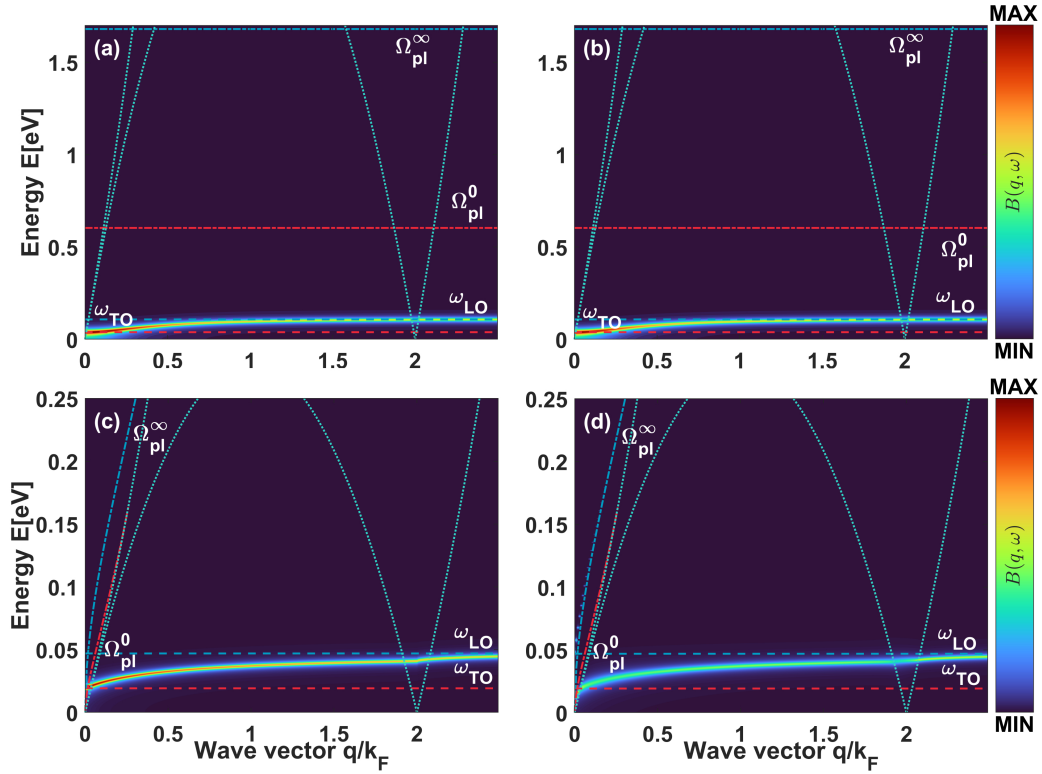


Figure 9.11: Phonon spectral functions for the bulk TiO_2 (upper row) and the 2D parameter set S_2 (lower row), and electron densities $n = 5 \cdot 10^{21} \text{ cm}^{-3}$, and $n = 5 \cdot 10^{13} \text{ cm}^{-2}$, respectively, obtained within the static polarization approximation (first column) and with the full dynamic expression in the RPA for the phonon polarization (second column). Note that MAX on the intensity scale takes a different absolute value for each of the panels.

system is, however, not surprising at all, since the static electron dielectric function cannot account for a plasmon mode. Apart from that, a more important issue lies in the lack of self-consistency of the static screening approximation which can be immediately seen from the diagrammatic expansion of the phonon propagator in Fig. 9.1. Namely, it consists of approximating some of the bubbles in the infinite chain of bubbles with their static counterpart, while for others the full dynamic dependence is kept. This suggests that instead of the static screening approximation one should rather use a self-consistent static polarization approximation, which assumes the static electron dielectric function in the denominator of Eq. (9.23), rather than in Eq. (9.32), and treats all the bubbles in the infinite chain equally with their static counterpart. We anticipate that the static polarization approximation should capture some of the key features of the full dynamic phonon spectra as long as the frequency scale of the electron subsystem is much larger than the phonon frequency scale. This should in theory hold for large electron densities when the onset of the adiabatic regime is expected.

To check the validity of the static polarization approximation, we show in Fig. 9.11 phonon spectral functions for the bulk TiO_2 (upper row) and the 2D parameter set S_2 (lower row), and electron densities $n = 5 \cdot 10^{21} \text{ cm}^{-3}$, and $n = 5 \cdot 10^{13} \text{ cm}^{-2}$, respectively, obtained within the static polarization approximation and within the fully dynamic RPA. By focusing first on the

3D case, we see that the static polarization approximation correctly describes the dispersion of the phonon-like LFE - it starts at ω_{TO} for $q = 0$ and reaches ω_{LO} at higher momenta. However, it underestimates the damping of the phonon mode within the continuum, which is just a quantitative effect, and misses the existence of the plasmon-like HFE, which phonon spectral weight is negligibly small in the full dynamic spectrum anyway. Overall, the static polarization approximation roughly satisfactorily reproduces the full RPA phonon spectrum in the adiabatic regime in the 3D case.

On the other hand, the static polarization approximation fails to reproduce the phonon spectrum in the 2D case even for the very high electron density considered. Apart from some less important discrepancies similar to the ones found in the 3D case, it predicts that the LFE saturates to ω_{TO} as the long-wavelength limit is approached and that it completely corresponds to the phonon mode. This is in sharp contrast to the result obtained by keeping the full dynamic dependence of the polarization, where the LFE follows the plasmon dispersion Ω_{PL}^0 in the long-wavelength limit and vanishes identically for $q = 0$. The reason is that the plasmon in the 2D case is gapless, and correspondingly the true adiabatic regime in the 2D case is never fulfilled. Thus, neither the static screening nor the static polarization approximation is satisfactory in the 2D case and the full dynamic dependence of the phonon polarization should be kept.

9.6 Conclusions

We systematically analyze and compare raw and integrated EELS spectra and phonon spectral functions corresponding to a LO phonon of 3D and 2D doped polar semiconductors within the full dynamic RPA. In parallel with the commonly studied influence of the adiabaticity parameter, we highlight the important role of the electron-phonon interaction strength in shaping phonon-plasmon spectral features.

By studying the raw spectra, we observe that the interaction strength strongly influences the damping of coupled excitations within the electron-hole continuum. In the 3D case for weak couplings, we note that the phonon-like excitation is well defined for all momenta, while the plasmon-like excitation gets damped as soon as it enters the continuum. Moreover, in the resonant regime, while the HFE gets strongly damped, the LFE stays well defined through almost the whole continuum. This situation changes with the increase of the interaction strength when the only well-defined excitation within the continuum is the phonon-like excitation in the adiabatic regime. In 2D cases for weak couplings, the phonon-like excitation is always well defined, while the plasmon-like excitation gets damped within the continuum. For strong couplings, the excitations' damping resembles that in the 3D strong coupling case. The excitations' dispersions in 2D cases differ significantly in the weak and the strong coupling case as well. In the weak coupling case, two excitations follow the unperturbed phonon and plasmon dispersions, with the exception of the repulsion of the renormalized dispersions where the unperturbed dispersions

meet. Contrary, for strong couplings the HFE acquires the linear dispersion in the long-wavelength limit, while the LFE's energy vanishes for $q = 0$, and gradually increases toward the LO phonon energy for very high electron densities.

Even bigger discrepancies between the weak and the strong coupling case are evident from the integrated spectra exhibiting similar behaviors in both 3D and 2D cases. In particular, while for strong couplings the HFE accounts for almost all the EELS spectral weight in the long-wavelength limit, irrespective of the adiabaticity parameter, for weak couplings the same is true only in the adiabatic limit. In the antiadiabatic and the resonant regime, the EELS spectral weight is rather approximately equally redistributed among the LFE and the HFE, which opens the possibility of estimating the electron-phonon coupling strength from (integrated) EELS spectra, even from data with very limited energy resolutions.

By projecting the excitations onto the phonon degree of freedom large phonon production contributions are revealed for strong couplings, which are of different origins than that observed in the polaron case. In the adiabatic regime, the calculated phonon production confirms that the LFE is associated with the harmonic lattice vibrations, softened by the electron screening. On contrary, in the antiadiabatic regime, the phonon production can be associated with the LFE plasmon-like mode, indicating that due to the electron-phonon interaction the cloud of virtual phonons accompanies the plasma oscillations.

Lastly, we argue that the static screening approximation generally fails to reproduce full RPA phonon spectra in the whole parametric space in both 3D and 2D cases, while the static polarization approximation works well only in the 3D adiabatic regime.

Vertex corrections and the $2k_F$ singularity

In this Chapter 10, we slightly deviate from the main theme of Part III and consider the particularly interesting subject of the role of vertex corrections on the $2k_F$ singularity stemming from the Lindhard function $\chi_0(\mathbf{q}, \omega)$. The latter is the foundation of both the Kohn anomaly and the Peierls transition in electron-phonon systems [83]. In particular, in 2D and 3D cases the Lindhard function itself is continuous and only its derivative is singular for the momentum $|\mathbf{q}| = 2k_F$. On the other hand, in the 1D case, the singularity is the most severe and the Lindhard function itself exhibits a true logarithmic singularity for the momentum $|\mathbf{q}| = 2k_F$. Following Eq. (7.5), we note that the same $2k_F$ singularity pervades the leading order polarization as well, and it is interesting to study what is its fate when high order vertex contributions in the ladder approximation to the polarization are taken into account.

10.1 Anatomy of the leading order vertex function

It proves convenient to first recall the four contributions to the leading order vertex function given by Eqs. (A.44), (A.45), (A.46), and (A.47). By taking advantage of the notation $n_{\mathbf{k}}^{\pm} = \delta_{1,\pm 1} \mp n_{\mathbf{k}}$ and by assuming the Holstein coupling, those four contributions can be rewritten as (we set again $\hbar = 1$)

$$\Gamma^{\pm\pm}(\mathbf{k}, E; \mathbf{k} + \mathbf{q}, E + \omega) = \frac{g^2}{N} \sum_{\mathbf{q}'} \frac{n_{\mathbf{k}+\mathbf{q}'}^{\pm} n_{\mathbf{k}+\mathbf{q}+\mathbf{q}'}^{\pm}}{(E \mp \omega_0 - \varepsilon_{\mathbf{k}+\mathbf{q}'} \pm i\eta)(E + \omega \mp \omega_0 - \varepsilon_{\mathbf{k}+\mathbf{q}+\mathbf{q}'} \pm i\eta)}, \quad (10.1)$$

and

$$\begin{aligned} \Gamma^{+-}(\mathbf{k}, E; \mathbf{k} + \mathbf{q}, E + \omega) &= \frac{g^2}{N} \sum_{\mathbf{q}'} \frac{n_{\mathbf{k}+\mathbf{q}'}^+ n_{\mathbf{k}+\mathbf{q}+\mathbf{q}'}^-}{\omega + \varepsilon_{\mathbf{k}+\mathbf{q}'} - \varepsilon_{\mathbf{k}+\mathbf{q}+\mathbf{q}'} - i\eta} \times \\ &\times \left\{ \frac{1}{E - \omega_0 - \varepsilon_{\mathbf{k}+\mathbf{q}'} + i\eta} - \frac{1}{E + \omega + \omega_0 - \varepsilon_{\mathbf{k}+\mathbf{q}+\mathbf{q}'} - i\eta} \right\} = \Gamma^{-+}(\mathbf{k} - \mathbf{q}, E - \omega; \mathbf{k}, E). \end{aligned} \quad (10.2)$$

Here, the newly introduced notation is handy since the superscript + can be attributed to the electron part, while the superscript - to the hole part of the fermion Green's functions

in Eq. (7.15). In particular, we can see that the contributions $\Gamma^{\pm\pm}$ contain either an electron-electron or a hole-hole process, while the contributions $\Gamma^{\pm\mp}$ contain only electron-hole processes. Evidently, the leading vertex function is contributed by different processes and the interesting question arises in which physical regimes are they relevant.

In the long-wavelength limit ($|\mathbf{q}| \rightarrow 0$), $n_{\mathbf{k}}^+ n_{\mathbf{k}+\mathbf{q}}^- \rightarrow 0$ holds, and the contributions $\Gamma^{\pm\mp}$ vanish linearly in $|\mathbf{q}|$. Consequently, only $\Gamma^{\pm\pm}$ contribute to the leading order vertex function and enter the Ward identity in Eq. (7.6). That is, Γ^{++} is related via the Ward identity to the electron self-energy Σ^+ , given by the first term in Eq. (8.3), while Γ^{--} to the hole self-energy Σ^- , that is to the second term in Eq. (8.3), yielding in total

$$\begin{aligned} \Gamma(\mathbf{k}, E; \mathbf{k}, E + \omega) &= \Gamma^{++}(\mathbf{k}, E; \mathbf{k}, E + \omega) + \Gamma^{--}(\mathbf{k}, E; \mathbf{k}, E + \omega) \\ &= \frac{\Sigma^+(\mathbf{k}, \omega) - \Sigma^+(\mathbf{k}, \omega + E)}{\omega} + \frac{\Sigma^-(\mathbf{k}, \omega) - \Sigma^-(\mathbf{k}, \omega + E)}{\omega} \\ &= \frac{\Sigma(\mathbf{k}, \omega) - \Sigma(\mathbf{k}, \omega + E)}{\omega}. \end{aligned} \quad (10.3)$$

At first glance $\Gamma^{\pm\pm}$ make a dominant contribution also in the polaron case since the contributions $\Gamma^{\pm\mp}$ are suppressed by the factor $\sum_{\mathbf{q}} n_{\mathbf{q}}^+ n_{\mathbf{k}+\mathbf{q}}^- \sim O(1/N)$. In fact, Γ^{++} corresponds to the time-ordered vertex function $\Theta^{(2)}$ introduced in Chapter 7. However, here we should be very careful since both $\Gamma^{\pm\pm}$ and $\Gamma^{\pm\mp}$ result in the polarization of the order $O(1/N)$. In particular, in the electron polaron case discussed in Chapter 7, Γ^{++} led to the time-ordered diagram in Fig. 7.5(a), while $\Gamma^{\pm\mp}$ to the time-ordered diagram in Fig. 7.5(b). It was the peculiarity of the next-to-leading order that the polarization with the vertex correction could have been written solely in terms of $\Theta^{(2)}$. This is not generally valid in higher orders, where both vertex functions with electron-electron and electron-hole processes contribute equally to the net polarization. Specifically, in the ladder approximation, all polarizations can be expressed solely in terms of Θ .

The $1/N$ suppression of the vertex functions $\Gamma^{\pm\mp}$, containing electron-hole processes, in the polaron case stems from the small phase space available for electron-hole excitations. This phase space gets larger as the electron density increases and becomes maximal for a half-filled band. In that case, we expect $\Gamma^{\pm\mp}$ to be of utter importance.

10.2 $2k_F$ singularity

10.2.1 Leading order polarization

Before inspecting the influence of vertex corrections on the $2k_F$ singularity, we briefly recall the occurrence of the $2k_F$ singularity in the leading order polarization. For that purpose, we go

back to Eq. (7.10), which in the static, $\omega = 0$, limit yields for the leading order polarization

$$\text{Re}\Pi^{(2)}(\mathbf{q}, 0) = \frac{g^2}{N} \sum_{\mathbf{k}} \frac{n_{\mathbf{k}} - n_{\mathbf{k}+\mathbf{q}}}{\varepsilon_{\mathbf{k}} - \varepsilon_{\mathbf{k}+\mathbf{q}}}. \quad (10.4)$$

We stick to the 1D case when the singularity is the strongest. In particular, in the half-filled case $k_F = \pi/2$, and the singularity is expected at $q = 2k_F = \pi$. As shown in Appendix B.3, the summation in Eq. (10.4) can be carried out analytically around $q = \pi$, giving

$$\text{Re}\Pi^{(2)}(q = \pi \pm \delta, 0) = \frac{g^2}{2\pi} \frac{2 \ln \tan \left[\frac{1}{2} \arctan \frac{\delta}{2} \right]}{t\sqrt{4 + \delta^2}} \approx \frac{g^2}{2\pi t} \ln \left[\frac{\delta}{4} \right], \quad \delta \rightarrow 0^+. \quad (10.5)$$

Here, the anticipated logarithmic singularity is clearly apparent.

10.2.2 Leading vertex contribution to polarization

In Appendix B.2.2, the leading vertex contribution to the polarization, shown diagrammatically in Fig. 7.3(d), is expressed as a sum of four contributions stemming from the four contributions of the vertex function $\Gamma^{\pm\pm}$ and $\Gamma^{\pm\mp}$. To be specific, the corresponding contributions Π^{++} , Π^{--} , Π^{+-} , and Π^{-+} that together contribute to $\Pi^{(4d)}(\mathbf{q}, \omega)$ are given by Eqs. (B.13), (B.14), (B.15), and (B.16), respectively.

For the analysis of the $|\mathbf{q}| = 2k_F$ singularity, only Π^{+-} and Π^{-+} are relevant, since for the corresponding \mathbf{q} at half-filling $n_{\mathbf{k}+\mathbf{q}}^+ = n_{\mathbf{k}}^-$ holds and contributions in Eqs. (B.13) and (B.14) vanish identically. Moreover, the identity $n_{\mathbf{k}+\mathbf{q}}^+ = n_{\mathbf{k}}^-$ also simplifies Eqs. (B.15) and (B.16), resulting in

$$\begin{aligned} \Pi^{+-}(\mathbf{q}, \omega) = \Pi^{-+}(-\mathbf{q}, -\omega) &= \frac{g^4}{N^2} \sum_{\mathbf{k}, \mathbf{k}'} \frac{(1 - n_{\mathbf{k}'})n_{\mathbf{k}'+\mathbf{q}}}{(\varepsilon_{\mathbf{k}'} - \varepsilon_{\mathbf{k}'+\mathbf{q}} + \omega - i\eta)} \times \\ &\times \left\{ \frac{n_{\mathbf{k}}(1 - n_{\mathbf{k}+\mathbf{q}})}{(\varepsilon_{\mathbf{k}+\mathbf{q}} - \varepsilon_{\mathbf{k}} - \omega - i\eta)} \left[\frac{1}{\varepsilon_{\mathbf{k}'} - \varepsilon_{\mathbf{k}} + \omega_0 - i\eta} + \frac{1}{\varepsilon_{\mathbf{k}+\mathbf{q}} - \varepsilon_{\mathbf{k}'+\mathbf{q}} + \omega_0 - i\eta} \right] \right. \\ &\left. + \frac{(1 - n_{\mathbf{k}})n_{\mathbf{k}+\mathbf{q}}}{(\varepsilon_{\mathbf{k}} - \varepsilon_{\mathbf{k}+\mathbf{q}} + \omega - i\eta)} \left[\frac{1}{\varepsilon_{\mathbf{k}'} - \varepsilon_{\mathbf{k}+\mathbf{q}} + \omega_0 + \omega - i\eta} + \frac{1}{\varepsilon_{\mathbf{k}} - \varepsilon_{\mathbf{k}'+\mathbf{q}} + \omega_0 + \omega - i\eta} \right] \right\}. \end{aligned} \quad (10.6)$$

For $\omega = 0$ in the antiadiabatic limit $\kappa = \omega_0/t \gg 1$, the expression for the real part of Eq. (10.6) reduces to

$$\text{Re}\Pi^{+-}(\mathbf{q}, 0) = \text{Re}\Pi^{-+}(-\mathbf{q}, 0) \approx \frac{2}{\omega_0} \frac{g^4}{N^2} \sum_{\mathbf{k}'} \frac{(1 - n_{\mathbf{k}'})n_{\mathbf{k}'+\mathbf{q}}}{\varepsilon_{\mathbf{k}'} - \varepsilon_{\mathbf{k}'+\mathbf{q}}} \sum_{\mathbf{k}} \frac{n_{\mathbf{k}+\mathbf{q}} - n_{\mathbf{k}}}{\varepsilon_{\mathbf{k}} - \varepsilon_{\mathbf{k}+\mathbf{q}}}, \quad (10.7)$$

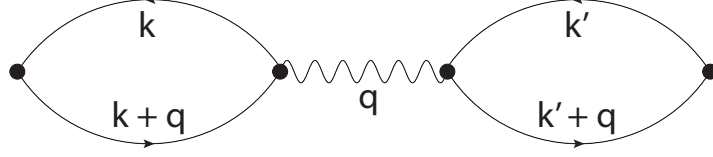


Figure 10.1: Reducible double bubble diagram in the next-to-leading order of the weak coupling perturbation theory.

giving at half-filling for the real part of $\Pi^{(4d)}(\mathbf{q}, 0)$ near $|\mathbf{q}| = 2k_F$ the same kind of summation that appears in Eq. (10.4)

$$\text{Re}\Pi^{(4d)}(\mathbf{q}, 0) \approx \text{Re}\Pi^{+-}(\mathbf{q}, 0) + \text{Re}\Pi^{-+}(-\mathbf{q}, 0) \approx \frac{2}{\omega_0} \frac{g^4}{N^2} \left[\sum_{\mathbf{k}} \frac{n_{\mathbf{k}} - n_{\mathbf{k}+\mathbf{q}}}{\varepsilon_{\mathbf{k}} - \varepsilon_{\mathbf{k}+\mathbf{q}}} \right]^2. \quad (10.8)$$

Therefore, the polarization with the leading vertex correction in the antiadiabatic limit possesses the same $2k_F$ singularity as the leading order polarization.

However, Eqs. (10.4) and (10.8) cannot be directly compared since they belong to a different order of perturbation theory. Instead, we consider the reducible double bubble diagram in the next-to-leading order, sketched diagrammatically in Fig. 10.1. By using the standard Feynman rules [40], its contribution to the polarization can be expressed as

$$\Pi^{(DB)}(\mathbf{q}, \omega) = D_0(\mathbf{q}, \omega) \left[\Pi^{(2)}(\mathbf{q}, \omega) \right]^2. \quad (10.9)$$

In the static limit, the free phonon Green's function may be written as $D_0(\mathbf{q}, 0) \approx -\frac{2}{\omega_0}$, which gives

$$\text{Re}\Pi^{(DB)}(\mathbf{q}, 0) = -\frac{2}{\omega_0} \frac{g^4}{N^2} \left[\sum_{\mathbf{k}} \frac{n_{\mathbf{k}} - n_{\mathbf{k}+\mathbf{q}}}{\varepsilon_{\mathbf{k}} - \varepsilon_{\mathbf{k}+\mathbf{q}}} \right]^2. \quad (10.10)$$

This expression is exactly equal to the one in Eq. (10.8), obtained for the polarization with the leading vertex correction in the antiadiabatic limit, albeit of the opposite sign. We are therefore left with an important result that the vertex correction in the next-to-leading order works against the $2k_F$ singularity, canceling it completely in the antiadiabatic limit. This result further opens the question of what is the overall fate of the $2k_F$ singularity in electron-phonon systems in the antiadiabatic limit. To address this issue, we consider also higher order vertex corrections, since analytical treatments of the effects of the singularity on electron and phonon properties usually rely on the RPA, which takes into account the bubble diagrams to the infinite order.

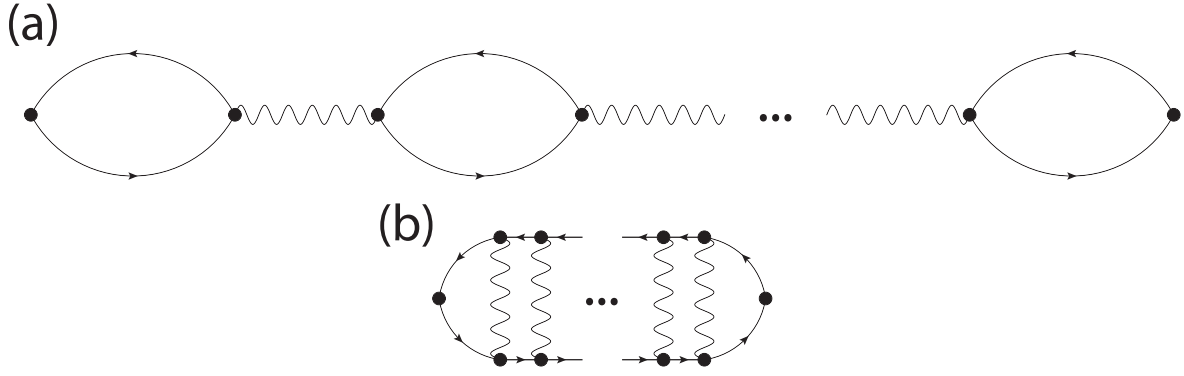


Figure 10.2: (a) Reducible n -tuple bubble and (b) n -tuple ladder polarization diagrams. The diagram in (a) contains n bubbles, while the diagram in (b) n vertical phonon lines.

10.2.3 Ladder approximation

Ladder polarization diagrams

In order to account for polarizations with vertex corrections in higher orders, we consider the ladder approximation with the n -tuple ladder polarization diagram shown in Fig. 10.2(b), coming from the $2(n+1)$ -th order of the perturbation theory. This is to be compared with the reducible n -tuple bubble diagram, shown in Fig. 10.2(a), for which the standard Feynman rules give

$$\Pi^{(nB)}(\mathbf{q}, \omega) = (-1)^n i^n \left[\frac{g}{N} \right]^{2n} [D_0(\mathbf{q}, \omega)]^{n-1} \left[\sum_{\mathbf{k}} \int_{-\infty}^{+\infty} \frac{dE}{2\pi} G_0(\mathbf{k}, E) G_0(\mathbf{k} + \mathbf{q}, E + \omega) \right]^n . \quad (10.11)$$

We note that for $n = 1$ Eq. (10.11) reduces to the expression for the leading order polarization in Eq. (7.9), which can be exploited to write for a general n

$$\Pi^{(nB)}(\mathbf{q}, \omega) = [D_0(\mathbf{q}, \omega)]^{n-1} \left[\Pi^{(2)}(\mathbf{q}, \omega) \right]^n . \quad (10.12)$$

The expression for the n -tuple ladder polarization diagram in Fig. 10.2(b) is more involving

$$\begin{aligned}
\Pi^{(nL)}(\mathbf{q}, \omega) &= (-1)^{n+1} \left[\frac{g}{N} \right]^{2(n+1)} \sum_{\mathbf{k}, \mathbf{k}_1, \dots, \mathbf{k}_n} \int_{-\infty}^{+\infty} \frac{dE}{2\pi} \int_{-\infty}^{+\infty} \frac{dE_1}{2\pi} \dots \int_{-\infty}^{+\infty} \frac{dE_n}{2\pi} \times \\
&\times G_0(\mathbf{k}, E) G_0(\mathbf{k} + \mathbf{q}, E + \omega) G_0(\mathbf{k}_1, E_1) G_0(\mathbf{k}_1 + \mathbf{q}, E_1 + \omega) \dots G_0(\mathbf{k}_n, E_n) G_0(\mathbf{k}_n + \mathbf{q}, E_n + \omega) \\
&\times D_0(\mathbf{k} - \mathbf{k}_1, E - E_1) \dots D_0(\mathbf{k}_{n-1} - \mathbf{k}_n, E_{n-1} - E_n) .
\end{aligned} \tag{10.13}$$

Here, we are interested in the antiadiabatic regime, when we may assume that the phonon propagation is instantaneous with respect to the electron propagation. This means that in time-ordered diagrams the phonon propagators have no retardation effects and may be accordingly represented by vertical lines. This as well means that the fermion propagators connecting these vertical lines in Fig. 10.2 necessarily appear in electron-hole pairs. Accordingly, all phonon propagators may be approximated by the constant static value $D_0(\mathbf{q}, 0) \approx -\frac{2}{\omega_0}$ and taken outside of the integrals, giving

$$\Pi^{(nL)}(\mathbf{q}, \omega) = (-1)^{n+1} D_0^n(\mathbf{q}, 0) \left[\frac{g}{N} \right]^{2(n+1)} \left[\sum_{\mathbf{k}} \int_{-\infty}^{+\infty} \frac{dE}{2\pi} G_0(\mathbf{k}, E) G_0(\mathbf{k} + \mathbf{q}, E + \omega) \right]^{n+1} . \tag{10.14}$$

Now, we may as well rewrite Eq. (10.14) in terms of the leading order polarization in Eq. (7.9)

$$\Pi^{(nL)}(\mathbf{q}, \omega) = (-1)^n D_0^n(\mathbf{q}, 0) \left[\Pi^{(2)}(\mathbf{q}, \omega) \right]^{n+1} . \tag{10.15}$$

As a last step in bringing Eqs. (10.12) and (10.15) into a form convenient for comparison, we note that n in Eqs. (10.12) and (10.15) does not refer to the same order of the perturbation theory. To fix that, we write both expressions in the $2(n+1)$ -th order with $n = 1, 2, 3, \dots$. In particular, by assuming the constant $D_0(\mathbf{q}, 0)$ in Eq. (10.11) we have

$$\Pi^{(2n+2B)}(\mathbf{q}, \omega) = D_0^n(\mathbf{q}, 0) \left[\Pi^{(2)}(\mathbf{q}, \omega) \right]^{n+1} , \tag{10.16}$$

and

$$\Pi^{(2n+2L)}(\mathbf{q}, \omega) = (-1)^n D_0^n(\mathbf{q}, 0) \left[\Pi^{(2)}(\mathbf{q}, \omega) \right]^{n+1} , \tag{10.17}$$

which finally gives

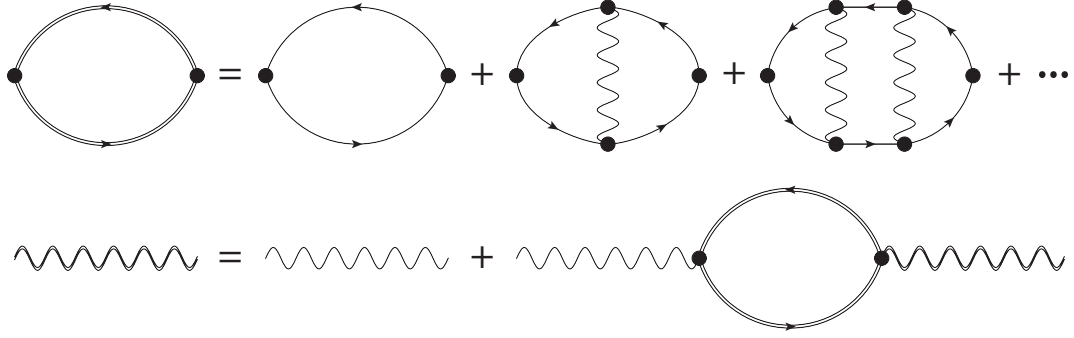


Figure 10.3: Diagrammatic content of the ladder approximation for the phonon propagator. The bubble with the double fermion lines represents the irreducible polarization which is given by the sum of the leading order and all n -tuple ladder polarizations.

$$\Pi^{(2n+2B)}(\mathbf{q}, \omega) + \Pi^{(2n+2L)}(\mathbf{q}, \omega) = \begin{cases} 0, & \text{for } n \text{ odd,} \\ 2D_0^n(\mathbf{q}, 0) [\Pi^{(2)}(\mathbf{q}, \omega)]^{n+1}, & \text{for } n \text{ even.} \end{cases} \quad (10.18)$$

The main message of Eq. (10.18) is that in the antiadiabatic regime n -tuple ladder polarizations work against the $2k_F$ singularity of bubble diagrams for n odd, while for n even they enhance it. This is a direct consequence of counting the number of closed fermion loops contained in the diagrammatic representation of the n -tuple bubble and n -tuple ladder polarization diagrams. Namely, each closed fermion loop brings the factor -1 . Since ladder polarizations diagrams have only one closed fermion loop they are always contributed with one -1 . On the other hand, n -tuple bubble diagrams are contributed either with 1 or -1 , depending on whether n is even or odd, respectively, leading either to the total subtraction or the exact addition of two contributions in the antiadiabatic regime.

Dyson series

Within the diagrammatic approach it is not consistent, however, to directly compare $\Pi^{(2n+2L)}(\mathbf{q}, \omega)$ with $\Pi^{(2n+2B)}(\mathbf{q}, \omega)$ in a given order n . The reason is that the n -tuple ladder polarizations diagrams are irreducible, while the n -tuple bubble polarization diagrams come into play through the Dyson summation of the irreducible leading order polarization. Therefore, we should sum up all irreducible polarizations diagrams first and then carry out the Dyson summation for the phonon propagator. In particular, the sum of all irreducible n -tuple ladder polarization diagrams together with the leading order polarization defines the irreducible polarization in the ladder approximation, which diagrammatic content is presented in Fig. 10.3.

In the antiadiabatic limit, $D_0(\mathbf{q}, 0) = -\frac{2}{\omega_0}$, the irreducible polarization in the ladder approximation in Fig. 10.3 reads

$$\begin{aligned}
\Pi^{(L)}(\mathbf{q}, \omega) &= \Pi^{(2)}(\mathbf{q}, \omega) + \sum_{n=1}^{\infty} \Pi^{(2n+2V)}(\mathbf{q}, \omega) \\
&= \Pi^{(2)}(\mathbf{q}, \omega) + \Pi^{(2)}(\mathbf{q}, \omega) \sum_{n=1}^{\infty} \left[\frac{2}{\omega_0} \Pi^{(2)}(\mathbf{q}, \omega) \right]^n \\
&= \Pi^{(2)}(\mathbf{q}, \omega) + \Pi^{(2)}(\mathbf{q}, \omega) \sum_{n=0}^{\infty} \left[\frac{2}{\omega_0} \Pi^{(2)}(\mathbf{q}, \omega) \right]^n - \Pi^{(2)}(\mathbf{q}, \omega) \\
&= \frac{\Pi^{(2)}(\mathbf{q}, \omega)}{1 - \frac{2}{\omega_0} \Pi^{(2)}(\mathbf{q}, \omega)} = \frac{\Pi^{(2)}(\mathbf{q}, \omega)}{1 + \Pi^{(2)}(\mathbf{q}, \omega) D_0(\mathbf{q}, 0)}.
\end{aligned} \tag{10.19}$$

With the irreducible polarization $\Pi^{(L)}(\mathbf{q}, \omega)$, the Dyson summation given by Eq. (9.20) yields for the phonon propagator

$$\begin{aligned}
D(\mathbf{q}, \omega) &= \frac{D_0(\mathbf{q}, \omega)}{1 - D_0(\mathbf{q}, \omega) \Pi^{(L)}(\mathbf{q}, \omega)} \\
&= \frac{D_0(\mathbf{q}, \omega)}{1 - D_0(\mathbf{q}, \omega) \frac{\Pi^{(2)}(\mathbf{q}, \omega)}{1 + \Pi^{(2)}(\mathbf{q}, \omega) D_0(\mathbf{q}, 0)}} \approx \frac{D_0(\mathbf{q}, \omega)}{1 - D_0(\mathbf{q}, \omega) \frac{\Pi^{(2)}(\mathbf{q}, \omega)}{1 + \Pi^{(2)}(\mathbf{q}, \omega) D_0(\mathbf{q}, \omega)}} \\
&= D_0(\mathbf{q}, \omega) + D_0(\mathbf{q}, \omega) \Pi^{(2)}(\mathbf{q}, \omega) D_0(\mathbf{q}, \omega),
\end{aligned} \tag{10.20}$$

where we have recovered the full expression for the free phonon propagator. Interestingly, the infinite order Dyson summation ended with the leading order result. Consequently, although the singular $\text{Re}\Pi^{(2)}(\mathbf{q}, \omega)$ is still present in Eq. (10.20), it does not change the phonon dispersion, however, it introduces some of the phonon spectral weight within the electron continuum, similarly like in the polaron problem, see Eq. (7.37). This finding is actually well in line with the numerical findings [216–218] suggesting the absence of softening of the phonon frequency in the antiadiabatic regime and the appearance of electronic excitations' signatures in phonon spectra. On the other hand, in the adiabatic regime, a physically very different scenario is observed involving gradual softening of the phonon frequency as the momentum $2k_F$ is approached. This second scenario goes hand in hand with the RPA treatment of the phonon propagator [83], imposing an interesting question of how vertex corrections [219–221] become growingly important as the system is varied from the adiabatic to the antiadiabatic regime, which serves as a motivation for the possible continuation of the results obtained here.

10.3 Conclusions

We divide the leading vertex function into parts containing either only electron, only hole, or only electron-hole processes. We argue that the former two enter the Ward identity and account

for the total vertex function in the polaron problem in the leading order. The latter, on the other hand, becomes growingly important as the doping starts increasing and is the most important part of the leading vertex function in the case of a half-filled band.

We show that the polarization with the leading vertex correction in the 1D case with the half-filled band exhibits the $2k_F$ singularity, which is exactly equal, but of the opposite sign, to the $2k_F$ singularity of the double bubble diagram contribution in the antiadiabatic regime. Motivated by that finding, we argue that in the antiadiabatic limit the n -tuple ladder contribution to the polarization works in favor or against the $2k_F$ singularity of the n -tuple bubble contribution, depending on whether n is odd or even. By exploiting this result in the ladder approximation, we show that the Dyson summation reduces to the leading order result for the phonon propagator. Consequently, we do not get softening of phonon frequency in the antiadiabatic regime, which is opposite to the scenario with the softening of phonon frequency at $|\mathbf{q}| = 2k_F$ expected in the adiabatic regime.

Part IV

Competition between interactions and disorder: many-body localization

From Anderson to many-body localization

In the last Part IV of the thesis, we abandon the electron-phonon interaction and consider the interplay of electron-electron interactions and disorder. In particular, we are dealing with a hot topic of the MBL phenomenon. Since this is a very interesting and fundamental problem, gaining a lot of interest in the last fifteen years, we devote the introductory Chapter 11 to a brief overview of the subject.

11.1 Anderson localization

In the late 1950s, P. W. Anderson published one of his most influential works [222] on the role of a disorder and impurities on the transport properties of crystals. His main motivation was to rationalize anomalously long spin relaxation times in phosphorus-doped silicon [223–225]. The results of Anderson’s work were, however, much conceptually deeper and opened a new perspective on the role of disorder in condensed matter systems. Namely, he showed that in certain random lattices, where the randomness is introduced by requiring the orbital on-site energy to vary randomly from site to site, electron wave functions become localized in real space, in contrast to delocalized Bloch waves in clean translationally invariant crystals - the phenomenon dubbed Anderson localization. Such lattices are characterized by the absence of diffusion, so the onset of the Anderson localization eventually leads to the metal-insulator transition. Thus, in addition to the simple band structure arguments [70] or the Mott metal-insulator transition dictated by strong electronic correlations [226], it was shown that an insulating behavior may also be driven by the disorder.

The simple toy Hamiltonian which captures the main essences of the Anderson localization is given by

$$\hat{H}_A = -t \sum_{\langle i,j \rangle} (c_i^\dagger c_j + c_j^\dagger c_i) + \sum_i h_i c_i^\dagger c_i . \quad (11.1)$$

Here, the notation $\langle i, j \rangle$ implies the hopping t only between nearest neighbours, while the diagonal (in the real space) disorder h_i is randomly distributed from the interval $-W < h_i < W$, where $W > 0$ denotes the disorder strength. In the simple limit when the hopping vanishes, $t = 0$, each electron sits at a distinct site i with the random energy h_i . Accordingly, the system is trivially localized.

The question is then what happens as the hopping t becomes finite? Surely, the states i hybridize and we would expect that electrons start to propagate through the system. However, Anderson's perturbative results showed that the probability of finding an electron at the initial site i stays finite for arbitrarily large times, while the probability for the electron occupying neighboring lattice sites exponentially falls with the distance from the site i . In other words, steady state electron wave functions are exponentially localized in real space

$$|\psi_i(r)|^2 \sim e^{-\frac{|r-r_i|}{\xi_i}}, \quad (11.2)$$

where ξ_i denotes the corresponding localization length. Here, r_i is the position of the site i in the crystal.

This perturbative Anderson's result can be easily checked numerically by the exact diagonalization of the Anderson Hamiltonian in Eq. (11.1). For that purpose, we considered a 1D lattice with $L = 16$ sites and the hopping $t = 1$ set as the unit of energy, and we calculated probability densities of typical Anderson wave functions for various disorder strengths W . The end results are shown in Fig. 11.1, together with the exponential fits in Eq. (11.2). We see that the Anderson wave functions are indeed exponentially localized in real space. Importantly, the localization is apparent for all disorder strengths, where the localization length decreases as the disorder strength increases.

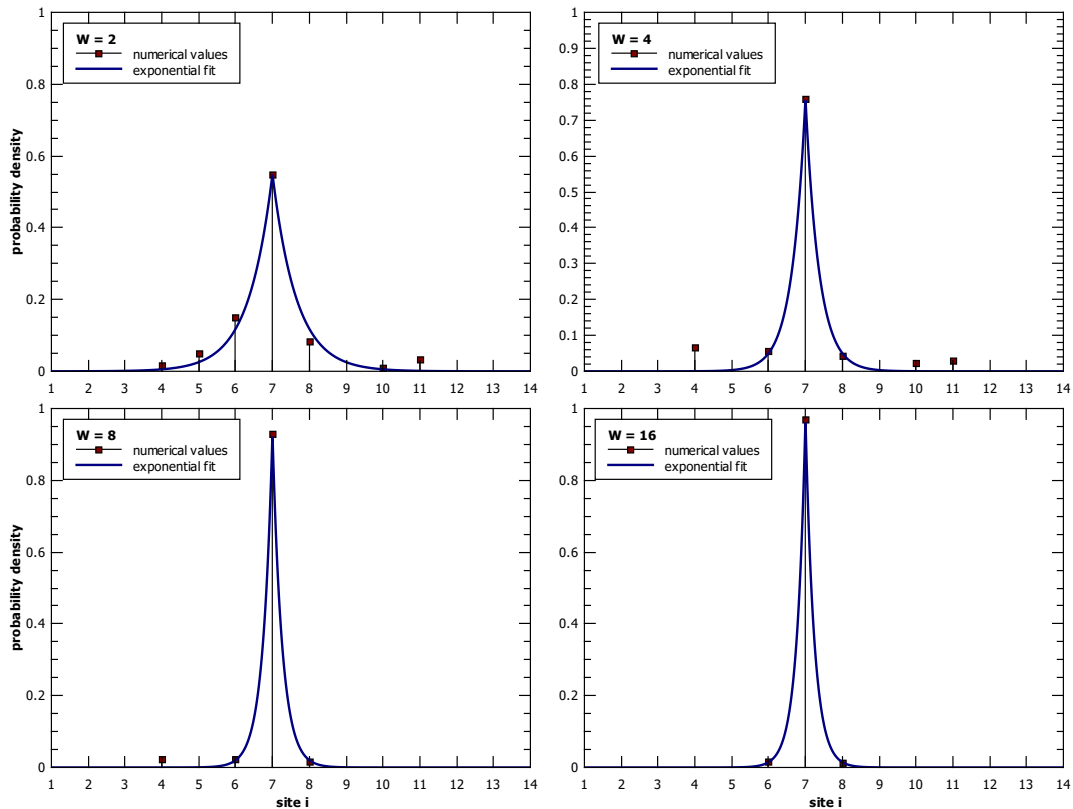


Figure 11.1: Probability densities of typical Anderson wave functions together with exponential fits in Eq. (11.2) for several disorder strengths W .

The observation that the Anderson localization occurs in the 1D case for an arbitrary disorder strength is actually well rationalized by the scaling theory of localization. In particular, in [227] it was shown that the Anderson localization arises in 1D and 2D systems for an arbitrary weak disorder strength. This is in contrast with 3D systems, for which the disorder strength W has to be strong enough for the Anderson localization to appear. Actually, in the 3D case, the situation is slightly more complicated due to the appearance of the mobility edge E_C [228]. Namely, the mobility edge separates the localized states near the lower and the upper part of an energy spectrum from the delocalized states in the middle of the spectrum. The position of the mobility edge in the spectrum is determined by the disorder strength and profoundly affects the low-temperature transport properties of the system. In particular, for $E_C > \mu$, where μ is the Fermi energy, the DC transport is absent in the low-temperature $T \rightarrow 0$ limit, while for elevated temperatures the transport is thermally activated in accordance with the Arrhenius law [229].

11.2 Many-body localization

Despite the great effort put to explore the richness of the Anderson localization phenomenon [230], the question about the stability of the Anderson localized phase concerning the interactions started to be thoroughly discussed only at the beginning of the 21st century. In the pioneering works [229, 231], it was argued that the localized phase is perturbatively stable (to very high orders) in weak interactions. Specifically, for a sufficiently strong disorder $W > W_c$, it was suggested that the DC conductivity vanishes in the presence of weak interactions up to some critical temperature. Similar conclusions have also been drawn by carrying out numerical simulations [232–234], involving averages over all many-body states ($T \rightarrow \infty$) and different disorder configurations, on several model Hamiltonians containing both the disorder and strong interactions between relevant degrees of freedom, leading to the proposal of a new stable localized phase, popularly dubbed many-body localized phase. In particular, two prototype models which are believed to exhibit the MBL phenomenon [235, 236], when the disorder strength exceeds some critical value, are the 1/2 Heisenberg spin chain in a random magnetic field and the spinless disordered chain of fermions with nearest neighbor interactions. The two models are related through the Jordan-Wigner transformation [144], while the latter model is a simple extension of the Anderson model in Eq. (11.1) with the inclusion of nearest neighbor interactions

$$\hat{H}_{MBL} = -t \sum_{\langle i,j \rangle} (c_i^\dagger c_j + c_j^\dagger c_i) + \sum_i h_i c_i^\dagger c_i + V \sum_i \hat{n}_i \hat{n}_{i+1}, \quad (11.3)$$

where \hat{n}_i is the electron density at the site i and V denotes the interaction strength.

We were careful not to state firmly that the stable many-body localized phase exists, emphasizing the fact that the occurrence of a true MBL phenomenon is still under debate. Namely, the

Hamiltonian in Eq. (11.3) is not analytically solvable, meaning that one may study its properties either by some approximate treatment or by the numerical exact diagonalization. However, the three energy scales in Eq. (11.3), namely, the kinetic energy t , the disorder strength W , and the interaction strength V , may all be comparable and is usually very hard to disentangle effects coming from the interaction and the disorder. Therefore, finding a correct approximate treatment of the MBL Hamiltonian in Eq. (11.3) is generally a very difficult task. In most of the studies, the numerical exact diagonalization is thus used, which on the other hand suffers from the exponentially large Hilbert space in system size. In particular, for a lattice with L sites and a binary degree of freedom per site, the Hilbert space dimension reads $D_{\mathcal{H}} = 2^L$, which, however, can be effectively somewhat reduced in numerical calculations by explicitly exploiting appropriate conservation laws. Accordingly, cases with $L > 16$ are out of reach for numerical simulations due to the current computational limitations. Therefore, almost all conclusions about the MBL phenomenon are obtained on 1D lattices with $L \leq 16$ sites, leaving open questions about the scaling of results to the thermodynamic limit. This problem is particularly pronounced in systems with the MBL behaviors, since potentially very slow dynamics may lead to long relaxation times over long spatial scales, not captured by the current finite-size numerical calculations.

The problem of finite-size effects was tried to be reconciled by the reduced basis approximation [237, 238]. The rough idea behind the approximation was to find only a fraction of the total Hilbert space relevant for the dynamics of some quenched initial state, which would correspondingly reduce the computational cost of the exact diagonalization and open the possibility of studying larger systems with $L > 16$ lattice sites. Specifically, the approximation made it possible to study systems with $L_{\max} \approx 30$ lattice sites, however, those L were still not large enough for a trustworthy extrapolation of the results to the thermodynamic limit. Moreover, the approximation was efficient in substantially reducing the Hilbert space only for very large disorder strengths.

Here, we put focus on the properties of the MBL phenomenon given that it exists, while in future works it would be interesting to exploit our approaches and results to study whether the true MBL phenomenon persists in thermodynamically large systems. To put our results, presented in Chapters 12 and 13, in the perspective of the current knowledge of the MBL phenomenon, in what follows, we list some of its properties as obtained from the exact numerical simulations on small 1D systems with $L \leq 16$ lattice sites.

11.2.1 Properties of many-body localized systems

Spectral properties [232, 234, 239]

As the first property of many-body localized systems, we single out the characteristic structure of their local energy spectra. In particular, the MBL is characterized by the avoided repulsion

of energy levels. This can be easily shown by considering the computational quantifier, namely, the average value of the ratio of consecutive level spacings $r_n = \min(\delta_n, \delta_{n+1})/\max(\delta_n, \delta_{n+1})$, where $\delta_n = E_{n+1} - E_n$ is the difference between two consecutive eigenenergies. Many-body localized systems show $\langle r \rangle \rightarrow 0.386$, which indicates the Poisson distribution of level spacings. This is in sharp contrast with generic interacting quantum systems showing the Wigner-Dyson distribution of level spacings.

Transport properties [240, 241]

As already stated, the DC conductivity vanishes in the many-body localized phase. Hence, the MBL is characterized by the absence of transport of globally conserved quantities. Currently, the interesting question is what are the features of transport when the disorder is moderate, albeit not strong enough for the onset of the MBL. We will provide some answers to that problem in Chapter 13.

Entanglement properties [233, 239, 242, 243]

To present the next important feature of the MBL phenomenon, we first briefly introduce the notion of entanglement entropy. For that purpose, we assume that some pure state $|n\rangle$ is given and that we have divided the full system $A \cup B$ into two subsystems A and B . Now, the entanglement entropy of the state $|n\rangle$ is defined as the trace $S(|n\rangle) = -\text{Tr}_A(\hat{\rho}_A \ln \hat{\rho}_A)$, where the reduced density matrix $\hat{\rho}_A = \text{Tr}_B |n\rangle \langle n|$ is obtained by tracing over the degrees of freedom of the subsystem B .

Such defined entanglement entropy scales with the subsystem size qualitatively quite differently in generic interacting quantum systems and many-body localized systems. In particular, in a generic quantum system, that is for a generic state corresponding to that system, the entanglement entropy shows the volume-law scaling with the size of the subsystem A . On the other hand, states of the many-body localized system exhibit the area-law scaling with the subsystem size.

The differences persist also when the dynamics of the entanglement entropy are considered. It has been shown that the entanglement entropy in many-body localized systems increases logarithmically in time, which is much slower than in generic interacting quantum systems. Specifically, it is expected that in the thermodynamic limit it increases indefinitely, while for finite systems, feasible for numerical simulations, it saturates to some finite value which is extensive, albeit lower than the value expected for a generic interacting quantum system.

11.2.2 Local integrals of motion

An important step forward in understanding the properties of the MBL phenomenon was provided by its phenomenological description in terms of quasi-local degrees of freedom called local integrals of motion (LIOMs) [244, 245]. The key assumption underlying this phenomenological approach is that there exists a quasi-local unitary transformation that diagonalizes the MBL Hamiltonian

$$\hat{H}_{MBL} = - \sum_i h_i \tau_i^z + \sum_{i,j} J_{i,j} \tau_i^z \tau_j^z + \sum_{i,j,k} J_{i,j,k} \tau_i^z \tau_j^z \tau_k^z + \dots, \quad (11.4)$$

where τ_i^z are quasi-local operators obeying the Pauli algebra, which commute mutually and with the whole Hamiltonian. They are popularly called l-bits (localized bits) and serve as a starting point for the construction of LIOMs. In particular, any product of operators τ_i^z may be seen as a valid LIOM.

The crucial feature of the phenomenological Hamiltonian in Eq. (11.4) is that τ_i^z are quasi-local. Namely, they are formally constructed from original spin (or electron density) operators $\tau_i^z = \sigma_i^z + \sum_{j,k} \sum_{\alpha,\beta=x,y,z} c_{i,j,k}^{\alpha,\beta} \sigma_j^\alpha \sigma_k^\beta + \dots$, where $c_{i,j,k}^{\alpha,\beta}$ decay exponentially with the distance between the site i and sites j, k . τ_i^z are also binary operators with eigenvalues ± 1 , so the exact many-body eigenstates of the Hamiltonian in Eq. (11.4) may be simply obtained by the set of eigenvalues for each τ_i^z . From these simple properties of l-bits, one may show that the phenomenological Hamiltonian in Eq. (11.4) exhibits many hallmarks of the MBL phenomenon, from the Poisson statistics of level spacings to the absence of transport, and peculiar properties of the entanglement entropy.

Although the notion of l-bits *de facto* resolves the MBL phenomenon in some scenarios to a great extent, it is very challenging to explicitly construct them in practice starting from some prototype MBL Hamiltonian, since as we have argued, MBL Hamiltonians cannot be analytically diagonalized. We can mention several numerical algorithms [244, 246–249] for the construction of LIOMs for small system sizes on the one hand, and a few papers devoted to the rigorous analytical [250–252], specifically perturbative, approaches to their construction on the other hand. However, none of them provide a simple and tractable set of LIOMs for some concrete model Hamiltonian exhibiting the MBL phenomenon.

Distinction between Anderson localization and MBL

The l-bits can be trivially constructed, though, in the case of the Anderson Hamiltonian in Eq. (11.1). In particular, the l-bits, in that case, correspond to the densities \hat{n}_l of electrons in a single-particle Anderson state l . Since the Anderson Hamiltonian is diagonal in the l basis, we can write

$$\hat{H}_A = \sum_l \varepsilon_l \hat{n}_l, \quad (11.5)$$

and by comparing this Hamiltonian with Eq. (11.4), we immediately notice that in the Anderson case all $J_{i,j,\dots}$ vanish, meaning that there are no interactions between l-bits. This is the crucial difference between the Anderson localization and the MBL, which heavily influences the dynamics and provides experimental means for distinguishing the two localization phenomena. In particular, interactions in Eq. (11.4) introduce a mechanism for dephasing, in addition to the simple precession due to the first term in Eq. (11.4), which entangles degrees of freedom at arbitrary distances. In systems exhibiting the MBL, the interactions $J_{i,j,\dots}$ exponentially decrease with the distance, explaining the logarithmically slow, albeit indefinite increase of the entanglement entropy in time. On the other, in an Anderson insulator, the dephasing is completely absent and the entanglement entropy saturates to some finite value even in the thermodynamic limit.

11.2.3 Thermal-MBL transition

The existence of LIOMs evidently signals the appearance of some emergent local integrabilities. Accordingly, the information about local initial conditions of the system exhibiting LIOMs may stay encoded in local observables up to very long times [244,253]. This suggests the non-ergodic behavior and the absence of thermalization in many-body localized systems. In that regard, the study of MBL has profound implications on the fundamental question of quantum chaos and quantum thermalization, providing the example of an (isolated) interacting quantum system that avoids thermalization.

As already emphasized at the beginning of Section 11.2, the MBL phenomenon sets in for sufficiently strong disorders $W > W_c$. When the disorder is low $W < W_c$, the MBL Hamiltonian in Eq. (11.3) rather shows drastically different behaviors. In particular, it has been shown [254] that for low disorders eigenstates of the Hamiltonian in Eq. (11.3) satisfy the eigenstate thermalization hypothesis (ETH) [255, 256]. Without going into too much detail, the main proposal of ETH is that each eigenstate behaves similarly to a statistical ensemble. Specifically, the ETH proposes that the reduced density matrix corresponding to an energy eigenstate takes the thermal form, which would simultaneously reconcile the quantum thermalization and the unitary quantum evolution. Accordingly, the model in Eq. (11.3) thermalizes for low disorders, which is in sharp contrast with the non-ergodic MBL behavior for strong disorders. Obviously, the transition (crossover) from the thermal to the many-body localized phase sets in as the disorder strength increases above the critical value W_c .

The thermal-MBL transition is very subtle and intriguing, and its complete understanding is currently lacking. One of the reasons for that is that it separates a thermal and a non-ergodic phase, and hence the knowledge of equilibrium statistical physics is not quite helpful. In

particular, well-established mean-field theories, like Landau's theory, are not appropriate for its description. Moreover, at the current time there exist no other simpler phenomenological theories or toy models which would help to capture the transition's essence. In the absence of its full understanding, however, it is popularly dubbed eigenstate phase transition since eigenstates in the thermal and the many-body localized phase behave radically differently, or the dynamical phase transition due to the fact that only dynamical probes may distinguish the two phases. Anyhow, the thermal-MBL transition is currently an open problem to which we devote the whole Chapter 12.

11.2.4 Experimental observations of the MBL phenomenon

The development of the field of MBL was mostly driven by theoretical curiosity, raising the question of whether the phenomenon can be observed at all in real-life experiments. This question is particularly delicate since in experiments it is quite challenging to isolate a system from the environment and to have full control of the system's parameters, such as the disorder strength and the interaction. However, while the plausible signatures of the many-body localized phase were reported in some condensed matter systems [257,258], it was for the first time shown in ultra-cold atoms and trapped ions setups [259–261] that the MBL phenomenon may truly arise in a real experiment.

In particular, cold atom setups are reasonably well isolated from an environment (baths), at least for sufficiently long times, while the disorder may be simulated with laser beams forming a quasi-periodic potential and the interaction tuned with Feshbach resonances. These ideas were implemented in [259], where, within such a setup, the study of the time evolution of the state initially prepared as the charge density wave was carried out. It was shown that for weak disorders and sufficiently long times the density homogeneously spreads through the system leaving no evidence of the initial charge density wave. Contrary, for strong disorders the traces of the initial charge density wave remained apparent for the longest accessible experimental times, providing strong evidence of the thermal-MBL transition and the MBL phenomenon.

To conclude this introductory Chapter 11, we can say that MBL experiments today play a vital role in understanding the phenomenon, going hand-by-hand with theoretical considerations. It is strongly anticipated that experiments will provide means to investigate the MBL phenomenon in higher dimensional ($D > 1$) systems and be exploited to study the thermal-MBL phase transition, both of these goals being very challenging from the theoretical point of view.

MBL as a percolation phenomenon

Parts of Chapter 12 have been published in [262]. The work discussed here was performed in collaboration with P. Prelovšek and M. Mierzejewski.

In this Chapter 12, we show that the thermal-MBL transition is accompanied by the drastic change in clustering of many-body states. Accordingly, we provide evidence that the transition may be thought of as a percolation transition, albeit in the Fock space. Our results are in line with the absence of thermalization in systems with the Hilbert space fragmentation [263–265], showing that in non-ergodic many-body localized systems the Hilbert space fragmentation is driven by the disorder. Namely, it is by now well established that the non-ergodic MBL-like behaviors are present in lattice gauge theories [263, 266], fracton systems [264], and, in general, systems with many conservation laws [265]. In all those systems the disorder is not present, but they are all characterized by the emergent set of conserved quantities and the Hilbert space fragmentation. This suggests that those two ingredients, unlike disorder, are essential for the MBL phenomenon. While the emergent set of conserved quantities in the many-body localized phase corresponds to l-bits, as discussed in Subsection 11.2.2, here we further show that the model in Eq. (11.3) exhibits the disorder-driven Hilbert space fragmentation. We note that similar ideas about the percolative nature of the thermal-MBL transition were discussed in [267–269]. However, there the connectivity of many-body states was studied by the means of hopping t , while here we consider the connectivity of many-body Anderson states through the interaction V .

12.1 MBL model in the Anderson many-body basis

In order to separately track effects of the disorder and interactions, it is convenient to divide the full MBL Hamiltonian in Eq. (11.3) into the non-interacting part, which corresponds to the Anderson Hamiltonian in Eq. (11.1), and the interacting part $\hat{H}_I = V \sum_i \hat{n}_i \hat{n}_{i+1}$. The non-interacting Anderson Hamiltonian can be easily diagonalized

$$\hat{H}_A = \sum_l \varepsilon_l \hat{\varphi}_l^\dagger \hat{\varphi}_l, \quad \varphi_l^\dagger = \sum_i \phi_{l,i} c_i^\dagger, \quad (12.1)$$

where the operator $\hat{\varphi}_l^\dagger$ ($\hat{\varphi}_l$) creates (annihilates) an electron in the single-particle Anderson localized state l , and $\phi_{l,i}$ relate the Anderson and the real space basis. Those single-particle Anderson localized states may be utilized to construct the Anderson many-body basis

$$|n\rangle = \prod_l \left(\varphi_l^\dagger\right)^{n_l} |0\rangle, \quad E_n^0 = \sum_l \epsilon_l n_l, \quad (12.2)$$

with $n_l = 0, 1$ since we consider electrons as spinless fermions.

With the inclusion of interactions, the eigenstates $|n\rangle$ start to mix. In order to track this mixing, it is convenient to rewrite the interacting Hamiltonian $\hat{H}_I = V \sum_i \hat{n}_i \hat{n}_{i+1}$ in the Anderson basis l . Since \hat{H}_I contains a two-particle interaction, it can generally be written as

$$\hat{H}_I = V \sum_{jklm} \chi_{jk}^{lm} \varphi_l^\dagger \varphi_m^\dagger \varphi_k \varphi_j, \quad (12.3)$$

where matrix elements χ_{jk}^{lm} read

$$\chi_{jk}^{lm} = \sum_i \phi_{l,i}^* \phi_{m,i+1}^* \phi_{k,i+1} \phi_{j,i}. \quad (12.4)$$

As thoroughly discussed in [238], the interacting Hamiltonian in Eq. (12.3) can be divided into three parts, depending on the number of equal indices j, k, l, m . In particular, the part with only two different indices reads

$$\hat{H}_{HF} = 2V \sum_{k>j} \left(\chi_{jk}^{jk} - \chi_{jk}^{kj}\right) \hat{n}_k \hat{n}_j. \quad (12.5)$$

It corresponds to the Hartree-Fock correction, diagonal in the many-body Anderson basis, which can be added to the Anderson Hamiltonian to redefine the unperturbed Hamiltonian $\hat{H}_0 = \hat{H}_A + \hat{H}_{HF}$. Accordingly, the new unperturbed eigenenergies read

$$\tilde{E}_n^{(0)} = E_n^{(0)} + \langle n | \hat{H}_{HF} | n \rangle = \sum_l \epsilon_l n_l + 2V \sum_{k>j} \left(\chi_{jk}^{jk} - \chi_{jk}^{kj}\right) n_k n_j. \quad (12.6)$$

The mixing of many-body Anderson states comes from the parts of the interacting Hamiltonian in Eq. (12.3) when three or all four indices j, k, l, m are different

$$\hat{H}_I^3 = V \sum_{j \neq k \neq m} \left(\chi_{jk}^{jm} + \chi_{kj}^{mj} - \chi_{jk}^{mj} - \chi_{kj}^{jm}\right) \varphi_m^\dagger \varphi_k \hat{n}_j, \quad (12.7)$$

and

$$\hat{H}_I^4 = V \sum_{\substack{j \neq k \neq l \neq m \\ l > m, k > j}} \left(\chi_{jk}^{lm} + \chi_{kj}^{ml} - \chi_{jk}^{ml} - \chi_{kj}^{lm}\right) \varphi_l^\dagger \varphi_m^\dagger \varphi_k \varphi_j, \quad (12.8)$$

describing single and double electron-hole pair excitations, respectively. We redefine the interacting part of the MBL Hamiltonian so that it contains only those two terms $\hat{H}'_I = \hat{H}_I^3 + \hat{H}_I^4$.

When discussing the clustering of many-body states, we are mostly interested in the connectivity of many-body Anderson states through the Hamiltonian \hat{H}'_I . In that regard, we primarily consider connections satisfying the resonant condition

$$|\langle n' | \hat{H}'_I | n \rangle| > R (\tilde{E}_{n'}^{(0)} - \tilde{E}_n^{(0)}) , \quad (12.9)$$

in accordance with the second-order perturbation theory. For the value of the resonant parameter R we take $R \approx 0.3$, which correctly reproduces the thermal-MBL transition expected at $W_c \sim 6-8$ [237, 239, 270] for our chosen parameter set. In all our calculations, we use $t = 1$ as the unit of energy, set $V = 2t$, and consider the half-filled case with $N = L/2$ fermions, where L is the number of lattice sites.

12.2 Many-body clustering

In order to reveal the clusterization of many-body states, it is sufficient to show that the matrix $M_{n,\mathcal{N}} = \langle n | \mathcal{N} \rangle$ has the block diagonal structure. Here, $|n\rangle$ represents a many-body Anderson state, while $|\mathcal{N}\rangle$ is an exact eigenstate, so perfect clustering implies that the many-body Anderson basis may be split into disconnected sets (clusters) such that each exact eigenstate has a projection on a single cluster only. However, to numerically reveal the block diagonal structure of $M_{n,\mathcal{N}}$, first we have to properly sort eigenstates $|n\rangle$ and $|\mathcal{N}\rangle$ since the labelling of states $|n\rangle$ is arbitrary, while states $|\mathcal{N}\rangle$ are commonly sorted according to their energies. To achieve that, we use the following scheme. We consider some arbitrary exact eigenstate and we put it at the first position $|\mathcal{N} = 1\rangle$. Then, we calculate

$$O(\mathcal{N}, \mathcal{N}') = \sum_n |\langle n | \mathcal{N} \rangle| |\langle n | \mathcal{N}' \rangle| , \quad (12.10)$$

with $|\mathcal{N} = 1\rangle$ and determine which $|\mathcal{N}'\rangle$ yields $\max_{\mathcal{N}' > \mathcal{N}} O(\mathcal{N}, \mathcal{N}') > 0$, which is then considered as the consecutive eigenstate $|\mathcal{N} = 2\rangle$. The procedure proceeds for each newly added eigenstate, grouping together all eigenstates $|\mathcal{N}\rangle$ related to the same cluster. Now that the exact eigenstates are all sorted depending on clusters they are related to, we only need to suitably sort many-body Anderson states $|n\rangle$. To do this, for each $|\mathcal{N}\rangle$, starting with $|\mathcal{N} = 1\rangle$, we simply find $|n\rangle$ which gives $\max_{n \geq \mathcal{N}} \langle n | \mathcal{N} \rangle$, defining in this way the place of $|n\rangle$ on the list, $n = \mathcal{N}$.

Following this algorithm, in Fig. 12.1(a) we show the matrix $M_{n,\mathcal{N}} = \langle n | \mathcal{N} \rangle$ obtained by the exact diagonalization of the MBL Hamiltonian in Eq. (11.3) for the disorder strength $W = 10$ and the lattice with $L = 12$ sites, with the non-resonant matrix elements excluded. From Fig. 12.1(a), the clusterization of many-body states is clearly visible. In particular, the Hilbert space is drastically fragmented, shattered into a macroscopically large number of small clusters containing no more than a few eigenstates.

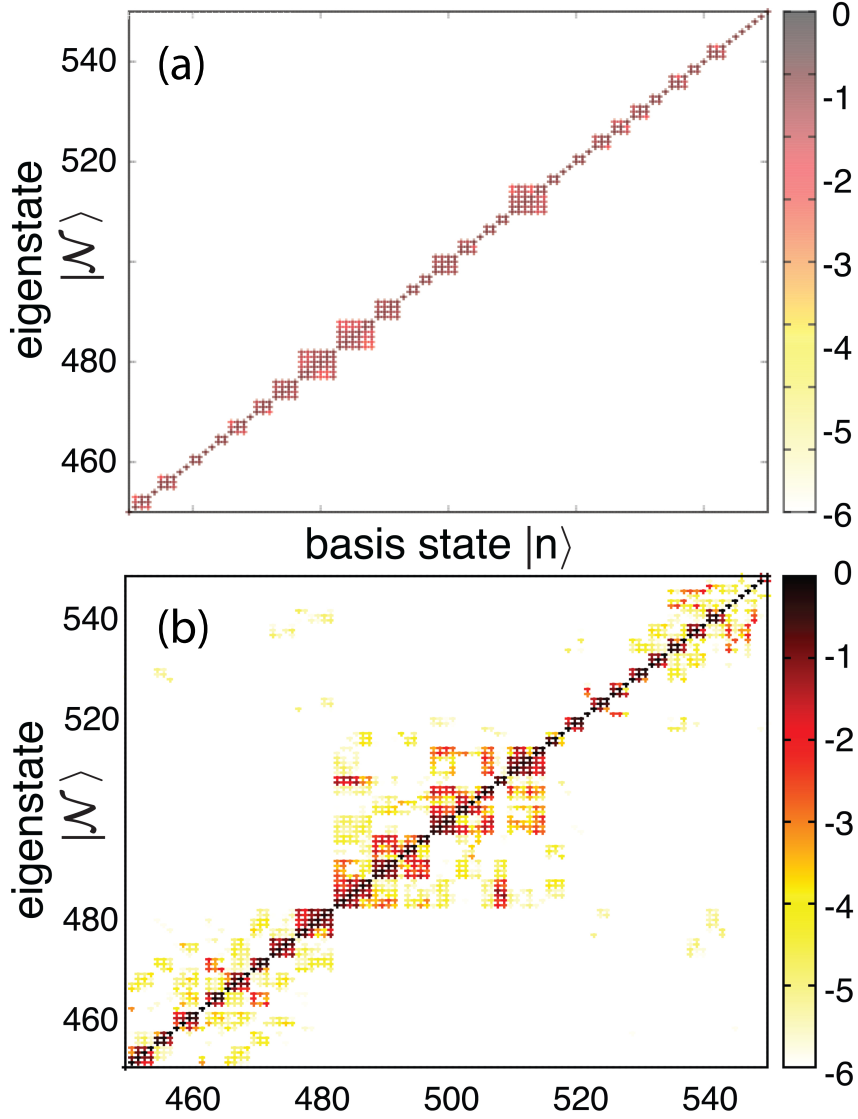


Figure 12.1: Clusterization of many-body states (a) without and (b) with resonant matrix elements in Eq. (12.9) included, for the disorder strength $W = 10$ and the lattice with $L = 12$ sites. Colorbars represent numerical values of $\log_{10} |M_{n,N}|^2$.

In order to show that this clusterization is not an artifact of neglecting non-resonant matrix elements, we repeat the same process, albeit with the full Hamiltonian, that is, with non-resonant matrix elements included. For that purpose, we keep the ordering of many-body Anderson states $|n\rangle$ as obtained for the truncated Hamiltonian, while exact eigenstates $|\mathcal{N}\rangle$ we order according to their maximal projections on states $|n\rangle$, $\mathcal{N} = n$. The resulting matrix $M_{n,N}$ for the full Hamiltonian, and the same $W = 10$ and $L = 12$ as for the truncated Hamiltonian, is shown in Fig. 12.1(b). Despite the fact that non-vanishing overlaps exist between different clusters, the block-like diagonal structure of $M_{n,N}$ is still clearly apparent. That is, the majority of overlaps is vanishingly small, such that the full Hilbert space is effectively fragmented into many small clusters even when the resonant condition is lifted. This suggests that the MBL scenario in model Eq. (11.3) is accompanied by the Hilbert space fragmentation, similarly to other, clean

translationally invariant models. We note that the further analysis of Fig. 12.1(b) may reveal an additional structure of the Hilbert space, for example multifractal properties [267, 271, 272].

12.3 Percolation in the Fock space

Now that we have established that for strong disorders $W > W_c$ the Hilbert space gets fragmented into many small clusters, it is particularly interesting to study the distribution of cluster sizes, especially as the disorder strength is varied across W_c . In accordance with the thermal-MBL transition, we expect that for $W < W_c$ one macroscopically large cluster emerges, which would signal the breakdown of the Hilbert space fragmentation and the many-body localized phase. In other words, this scenario suggests that the thermal-MBL transition can be thought of as a percolation transition, albeit in the Fock space. In order to emphasize these ideas, in our following considerations, we study the statistics of cluster sizes, where we explicitly exploit the resonant condition in Eq. (12.9). The reason for that is twofold. First, it ensures the perfect block diagonal structure of the matrix $M_{n,N}$. Second, it explicitly supports the scenario in which is the thermal-MBL transition driven by the resonant, rather than by the non-resonant transitions.

12.3.1 Statistics of cluster sizes

In order to analyse the cluster statistics, we introduce the parameter $s = N_C/N_{MB}$, as the ratio of the number of states in a cluster N_C and the total number of states $N_{MB} = \binom{L}{L/2}$. In particular, we start the analysis by considering the W dependence of the relative number of states in a maximal cluster, s_{max} . Since the number of states in the maximal cluster varies from one disorder realization to another, we evaluate typical averages $s_{max}^{typ} = \exp \langle \ln s_{max} \rangle_{dis}$, where $\langle \dots \rangle_{dis}$ represents the average over N_{dis} different disorder configurations.

In Fig. 12.2(a), we show results for s_{max}^{typ} sampled over $N_{dis} \sim 300$ disorder configurations as a function of W for four different lattice sizes $L = 12 - 24$. Although s_{max}^{typ} exhibits a moderate L dependence, it is evident that for weak disorders $W \sim 2$ practically all states belong to the maximal and thus macroscopically large cluster since $s_{max}^{typ} \rightarrow 1$. On the other hand, for significantly stronger disorders, $W \sim 10$, s_{max}^{typ} becomes vanishingly small, pointing to the degradation of the macroscopic cluster into many smaller clusters. This is well in accordance with the percolation scenario of the thermal-MBL transition and the Hilbert space fragmentation in the many-body localized phase. Note also that as the L increases, the drop of s_{max}^{typ} becomes sharper near $W \sim 8$, where the transition point is expected for the chosen parameter set.

To further support those findings, we also consider the probability distribution of cluster sizes $\mathcal{P}(s)$, which near the percolation transition exhibits the universal power-law behavior with the critical exponent τ , $\mathcal{P}(s) \sim s^{-\tau}$, in the thermodynamic limit [273]. In particular, in

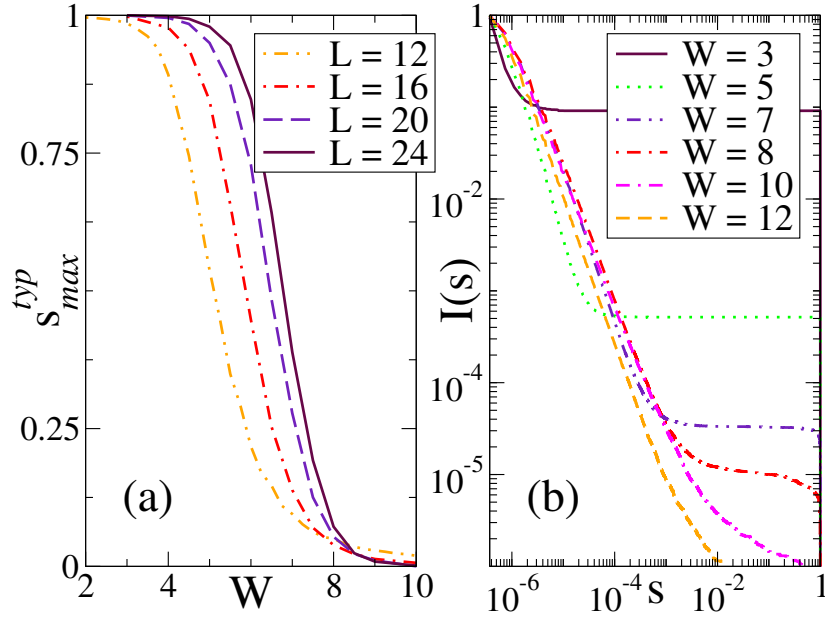


Figure 12.2: (a) Typical relative number of states in the maximal cluster averaged over $N_{dis} \sim 300$ disorder configurations in dependence on the disorder strength W for four different lattice sizes $L = 12 - 24$. (b) Integrated distribution $I(s)$ of cluster sizes s for several disorder strengths $W = 3 - 12$ evaluated for $L = 24$.

Fig. 12.2(b) we show our results in terms of the integrated distribution $I(s) = \int_s^1 \mathcal{P}(s') ds'$ for the lattice with $L = 24$ sites, obtained by averaging over $N_{dis} \sim 50$ configurations of disorder. The normalization $I(s \rightarrow 0) = 1$ is used. As is clearly evident, for $W < W_c$ the integrated distribution $I(s)$ exhibits long plateaus with the value $I(s \approx 1)$ in a broad range of s , $0 \neq s_p < s \leq 1$. This behavior is consistent with the existence of one macroscopically large cluster and several smaller clusters with the relative number of eigenstates $s < s_p$. As the disorder strength increases, the distributions near $s \approx 1$ start to bend, indicating the degradation of the macroscopically large cluster into smaller clusters. However, due to finite size effects, $I(s \approx 1)$ remains finite, albeit very low, even for $W > W_c$, signaling the finite, but very small probability of finding the macroscopic cluster even in the many-body localized phase. Lastly, let us add that the simple power-law fit of $\mathcal{P}(s)$ at $W = 8$ gives $\tau = 2.47$. Interestingly, this is very close to the value of $5/2$ predicted for the percolation models in high dimensions ($D > 6$) [274, 275], captured by the mean-field theory of the Potts model [276].

12.4 Conclusions

We show that the prototype MBL model Hamiltonian, involving a disordered chain of interacting spinless fermions, exhibits a drastic change in the clustering of many-body states as the disorder strength is varied across a critical value. In particular, for strong disorders, the Anderson many-

body basis is split into many small clusters involving no more than a few states. By inspecting the relative number of states in the largest cluster and the distribution of cluster sizes, we notice that in the opposite limit of weak disorders one macroscopically large cluster emerges. These two results point to the percolative nature of the thermal-MBL transition, albeit in the Fock space. Near the transition, the distribution of cluster sizes shows the universal power-law behavior with the exponent very close to the one predicted for percolation models in high dimensions. The shattering of the Fock space into many small clusters for strong disorders is in line with the Hilbert space fragmentation observed in disorder-free models exhibiting MBL-like behaviors.

Anomalous transport properties

Parts of Chapter 13 have been published in [262]. The work discussed here was performed in collaboration with P. Prelovšek and M. Mierzejewski.

In this last Chapter 13 of the thesis, we discuss the delicate topic of transport properties of the MBL model in Eq. (11.3) for moderate disorder strengths. In the many-body localized phase, the transport is absent and the DC conductivity vanishes. On the other hand, in the complete absence of the disorder, interactions and particle collisions lead to diffusive transport, while without interactions the model is integrable. The important question therefore arises, what is the nature of transport as soon the disorder is turned on when it is not strong enough for the MBL phenomenon to set in?

In several works [270, 277–279], an anomalously slow transport was reported in the thermal portion of the MBL phase diagram for moderate disorder strengths, ascribed to the subdiffusive-like transport regime settled in prior to the thermal-MBL transition. These results were, however, contradicted by other numerical studies [241, 280] showing non-vanishing values of the DC conductivity in the whole thermal phase, while in [281] it was argued that the observed subdiffusive regime is actually transient. The latter scenario is also favored by the numerical study [282] on large spin chains, with a conclusion that for weak disorders the purely diffusive behavior prevails. The intricate nature of the transport in the thermal portion of the MBL phase diagram below the localized phase, $W < W_c$, was further supported by several experiments [283, 284] as well. In particular, it was observed that the decay of imbalance after a quench is slow, following a power-law behavior with non-universal exponents.

Despite the great theoretical and experimental effort put to investigate anomalous transport properties in the whole thermal phase, a definite consensus about this important topic is still not provided. Hence, it is paramount to investigate in more detail this anomalous transport and its dependence on the disorder strength, as well as to understand its origins. Here, we contribute to this rich and intricate topic by investigating electron density relaxations in the context of the percolation scenario discussed in Chapter 12. In particular, following the results of the precedent Chapter 12, we investigate the relaxation of the electron density toward the equilibrium as a cascade of transitions between different many-body Anderson states in the macroscopic cluster by means of rate equations.

13.1 Density relaxations

As a probe for studying transport properties in the thermal phase, we analyze the time dependence of the density correlation function $C_q(t) = \langle \hat{\rho}_q(t) \hat{\rho}_{-q}^0 \rangle$, where $\hat{\rho}_q$ is the q component of the electron density operator and $\langle \dots \rangle$ denotes averaging over relevant many-body states. To be more specific, we are actually interested in the time-dependent diffusion function

$$D(t) = -\frac{1}{q^2} \frac{\dot{C}_q(t)}{C_q(t)}, \quad (13.1)$$

which long-time behavior may be taken as the definition of the diffusion parameter $\lim_{t \rightarrow \infty} D(t) \equiv D_0$.

Before the analysis of the behavior of $D(t)$ in the thermal part of the MBL phase diagram, it is instructive to briefly consider the behavior of the diffusion parameter D_0 in several special cases. In particular, in the many-body localized phase, the density correlation function stays finite for arbitrarily long times, $C_q(t \rightarrow \infty) = C_q^0 \neq 0$. In that case, it is easy to see from Eq. (13.1) that $D_0 = 0$, in accordance with the absence of transport. On the other hand, from the Fick's law of diffusion [285] follows $C_q(t) \propto \exp(-Dq^2t)$, and the diffusion parameter D_0 corresponds to the parameter D . The most interesting is, however, the subdiffusive case for which the decay of $C_q(t)$ is not exponential but power-law, $C_q(t) \sim t^{-\zeta}$, in which case we get

$$D(t) \sim \zeta/t, \quad D(t \rightarrow \infty) = D_0 \rightarrow 0. \quad (13.2)$$

13.1.1 Rate equations

In the presence of interactions, many-body Anderson states $|n\rangle$ are not eigenstates of the system. Nevertheless, these states may be used as quenched initial states from which the relaxation toward the equilibrium may be studied. In particular, we start from some non-equilibrium many-body state determined by the probabilities p_n , satisfying the sum rule $\sum_n p_n = 1$, of finding the state in the many-body Anderson state $|n\rangle$. Due to the interaction V , a state $|n\rangle$ may transit to a state $|n'\rangle$ and vice versa, eventually relaxing the initial charge density profile toward the equilibrium. In order to describe this relaxation, here we neglect the quantum coherence of transitions between many-body Anderson states $|n\rangle$ and regard the relaxation toward the equilibrium as a cascade of (irreversible) transitions which can be described by the rate equations for the probabilities p_n

$$\frac{d}{dt} p_n = \sum_{n' \neq n} [\Gamma_{nn'} p_{n'} - \Gamma_{n'n} p_n]. \quad (13.3)$$

For the transition rates $\Gamma_{nn'} = \Gamma_{n'n} > 0$, we take the Fermi's golden rule-like form, $\Gamma_{nn'} = \zeta |\langle n' | \hat{H}_I | n \rangle|^2 \mathcal{N}_{nn'}$, with $\zeta = 1/(\pi R)$. The resonant condition in Eq. (12.9) for transitions

between states $|n\rangle$ and $|n'\rangle$ is explicitly taken into account through the many-body density of states $\mathcal{N}_{nn'}$

$$\mathcal{N}_{nn'} \sim \frac{R}{2|\langle n' | \hat{H}'_I | n \rangle|} \Theta \left(\frac{|\langle n' | \hat{H}'_I | n \rangle|}{R} - \left(\tilde{E}_n^{(0)} - \tilde{E}_{n'}^{(0)} \right) \right), \quad (13.4)$$

so the final expression for the transition rates reads

$$\Gamma_{nn'} = \frac{|\langle n' | \hat{H}'_I | n \rangle|}{2\pi} \Theta \left(\frac{|\langle n' | \hat{H}'_I | n \rangle|}{R} - \left(\tilde{E}_n^{(0)} - \tilde{E}_{n'}^{(0)} \right) \right). \quad (13.5)$$

Following our percolation picture of the thermal-MBL transition, it is natural to assume that these transition rates between different many-body Anderson states $|n\rangle$ may be interpreted as bonds in the standard bond percolation theory.

The system in Eq. (13.3) is a linear system of N_{MB} coupled differential equations which may be easily solved numerically. Namely, its eigenvalues λ_α and eigenfunctions $w_{\alpha n}$ may be straightforwardly numerically computed. Since the rate equations are diagonal in eigenfunctions $w_{\alpha n}$, they obey a simple time evolution, $w_{\alpha n}(t) = w_{\alpha n} e^{-\lambda_\alpha t}$, which can be exploited to obtain the time evolution of probabilities $p_n(t)$ as their linear combination

$$p_n(t) = \sum_{\alpha} c_{\alpha} w_{\alpha n} e^{-\lambda_{\alpha} t}. \quad (13.6)$$

In particular, for the linear system in Eq. (13.3) the eigenfunctions $w_{\alpha n}$ may always be normalized $\sum_{\alpha} w_{\alpha n}^2 = 1$, so in the case that the initial state corresponds to a single many-body Anderson state $|n_0\rangle$, we have $p_n(0) = \delta_{nn_0}$ and

$$1 = \sum_{\alpha} c_{\alpha} w_{\alpha n_0} \quad \rightarrow \quad c_{\alpha} = w_{\alpha n_0}. \quad (13.7)$$

Density correlation function

Now we have all the ingredients to study the time evolution of the density correlation function $C_q(t) = \langle \hat{\rho}_q(t) \hat{\rho}_{-q}^0 \rangle$ within the rate equation approach. In particular, the q component of the density ρ_q may be obtained as

$$\rho_q = \sum_n n_q[n] p_n, \quad (13.8)$$

where $n_q[n]$ describes the q component of the density profile of the many-body Anderson state $|n\rangle$. $n_q[n]$ can be easily obtained in terms of the occupation of a single-particle Anderson state $n_l[n]$

$$n_q[n] = \frac{1}{\sqrt{L}} \sum_j e^{iqj} n_j[n] = \frac{1}{\sqrt{L}} \sum_{j,l} e^{iqj} |\phi_{j,l}|^2 n_l[n], \quad (13.9)$$

where $n_l[n] = 0, 1$, depending whether the single-particle Anderson state l is occupied or not in the many-body Anderson state $|n\rangle$.

By combining the above Eqs. (13.6) and (13.8) with the expression for the density correlation function, we get

$$\begin{aligned} C_q(t) &= \left\langle \sum_n n_q[n] p_n(t) \sum_{n'} n_{-q}[n'] p_{n'}(0) \right\rangle \\ &= \left\langle \sum_n n_q[n] \sum_{\alpha} c_{\alpha} w_{\alpha n} e^{-\lambda_{\alpha} t} \sum_{n'} n_{-q}[n'] \sum_{\alpha'} c_{\alpha'} w_{\alpha' n'} \right\rangle. \end{aligned} \quad (13.10)$$

By further introducing $W_{\alpha} = \sum_n n_q[n] w_{\alpha n}$ ($W_{\alpha}^* = \sum_n n_{-q}[n] w_{\alpha n}$), the expression for $C_q(t)$ takes a compact form

$$C_q(t) = \left\langle \sum_{\alpha, \alpha'} c_{\alpha} c_{\alpha'} W_{\alpha} W_{\alpha'}^* e^{-\lambda_{\alpha} t} \right\rangle, \quad (13.11)$$

which by averaging over all many-body Anderson states as the initial non-equilibrium states $|n_0\rangle$, and the use of Eq. (13.7) finally yields

$$\begin{aligned} C_q(t) &= \sum_{\alpha, \alpha'} W_{\alpha} W_{\alpha'}^* e^{-\lambda_{\alpha} t} \frac{1}{N_{MB}} \sum_{n_0} w_{\alpha n_0} w_{\alpha' n_0} \\ &= \delta_{\alpha, \alpha'} \frac{1}{N_{MB}} \sum_{\alpha, \alpha'} W_{\alpha} W_{\alpha'}^* e^{-\lambda_{\alpha} t} = \frac{1}{N_{MB}} \sum_{\alpha} |W_{\alpha}|^2 e^{-\lambda_{\alpha} t}. \end{aligned} \quad (13.12)$$

Here, all α with $\lambda_{\alpha} = 0$ should be omitted from the sum since they represent the equilibrium solutions. In particular, we consider the smallest $q = \pi/L$ in order to probe the relaxation over large spatial scales.

13.1.2 Full diagonalization of rate equations

For the moment, we deviate from our main goal of calculating the time-dependent diffusion parameter in order to briefly discuss general quantitative aspects of the rate equations solutions. In particular, we study the two-dimensional parameter space spanned by the eigenvalues λ_{α} and the inverse participation ratio for each of the solutions, $\text{IPR}_{\alpha} = \sum_n w_{\alpha n}^4$. IPR_{α} measures a level of localization of the solution in the basis of many-body Anderson states, with the values close

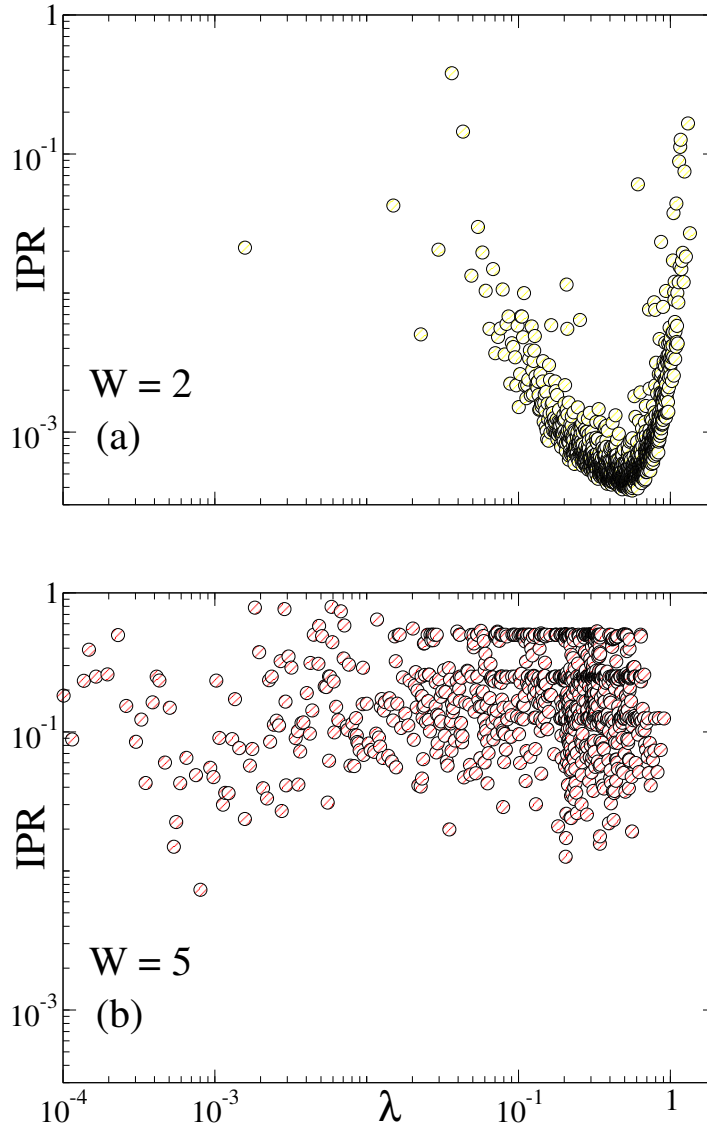


Figure 13.1: λ -IPR points obtained by the exact solution of rate equations for one configuration of disorder with the strength (a) $W = 2$ and (b) $W = 5$ on a lattice with $L = 16$ sites. In order not to overexaggerate the plot, every tenth point is shown.

to $\text{IPR}_\alpha \sim 1/N_{MB}$, and $\text{IPR}_\alpha \sim 1$, in the thermal and the MBL phase, respectively. On the other hand, large and small λ_α values correspond to fast and slow relaxation processes, respectively.

In Fig. 13.1, we plot λ -IPR points obtained by exactly solving the rate equations for one configuration of disorder and two distinct disorder strengths $W = 2$ and $W = 5$ on a lattice with $L = 16$ sites. We see that for the weaker disorder $W = 2$ almost all λ , with the exception of a few, are large with small values of the corresponding IPR. This suggests a strong delocalization in the many-body space of states and fast relaxation processes, pointing to the evidence for normal diffusive transport. On the other hand, for $W = 5$ a completely different distribution of λ -IPR points is apparent, clearly indicating a fundamentally different transport regime from the diffusive one observed for the weaker disorder. In particular, we observe a large spread of λ

values, suggesting that in addition to many fast processes, now exist also very slow relaxation processes which may be important for the active system dynamics even at very long times. This is accompanied by much higher values of IPR values, which interestingly, tend to group along the horizontal lines at values $\text{IPR} \approx 1/2, 1/4, \dots$, which is apparently related to the formation of very small clusters in the Fock space.

Time-dependent diffusion parameter

The full diagonalization of rate equations has both its advantages and downsides. On the one hand, since the Hilbert space is exponentially large in the system size L , it is restricted to systems with $L \leq 16$ lattice sites. On the other hand, it allows for the evaluation of dynamical properties over long times t , which is important when the dynamics are potentially very slow. Therefore, with the intention of exploiting the best of both worlds, in Fig. 13.2 we present results for the time-dependent diffusion parameter obtained by the full diagonalization of rate equations on a lattice with $L = 16$ sites over very long times. In particular, the cases with four different moderate disorder strengths are shown, all belonging to the thermal part of the MBL phase diagram for which anomalous transport properties are expected. For each disorder strength, the average $D(t)$ is shown, where the averaging was made over $N_{dis} \sim 200$ disorder configurations.

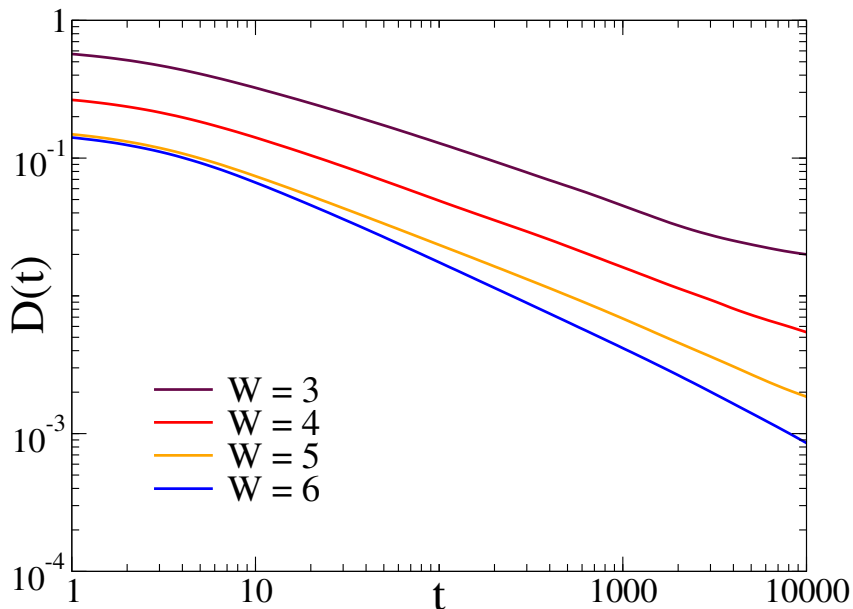


Figure 13.2: Average time-dependent diffusion parameter $D(t)$ obtained by the full diagonalization of rate equations on a lattice with $L = 16$ sites and various disorder strengths $W = 3 - 6$.

As seen from Fig. 13.2, for all disorder strengths the time-dependent diffusion parameter monotonically decreases even for the largest times shown, which may be attributed to a large

spread of eigenvalues λ , as seen from Fig. 13.1(b). Namely, as the fast relaxation processes with the large values of λ die out, the system dynamics remain active due to a large number of small λ values, leading to very slow relaxation processes. In any case, for all disorder strengths the anomalous transport, with no clear evidence of the subdiffusive character, is evident, at least for the very long times taken into account.

13.1.3 Direct time integration of rate equations

In order to probe the transport properties of systems with a somewhat larger number of lattice sites, $L \sim 24$, we soften the undoable full diagonalization approach by introducing several modifications to the calculation of the density correlation function. First, we employ the direct time integration of rate equations in Eq. (13.3), which, however, limits us to consider the system dynamics up to times that are a few orders of magnitudes shorter than the longest times obtainable by the exact diagonalization. Second, we take into account the many-body Anderson states contained only within the macroscopic cluster since it is natural to expect that the transport properties of the whole system are dominantly determined by the transport in the macroscopic cluster. Finally, to go around the infeasible sampling over all initial many-body Anderson states $|n\rangle$ within the cluster, we assume a convenient initial inhomogeneous distribution $p_n(t=0) = \frac{1}{Z} \exp[-n_q[n]/T]$, with $Z = \sum_n \exp[-n_q[n]/T]$, corresponding to a potential imposing an initial density modulation ($T = 0.5$). In particular, within such simplified scheme, we consider the time dependence of the modified density correlation function, $\tilde{C}_q(t) = \langle \hat{\rho}_q(t) \rangle / \langle \hat{\rho}_q^0 \rangle$, where $\langle \hat{\rho}_q(t) \rangle = \sum_n n_q[n] p_n \frac{\exp[-n_q[n]/T]}{Z}$.

Modified density correlation function

By taking advantage of the direct time integration of the rate equations, in Fig. 13.3 we show the modified density correlation function calculated on the lattice with $L = 24$ sites for several disorder strengths. To be specific, the average modified density correlation function is shown, with $N_{dis} \sim 50$ different disorder realizations considered. Evidently, and particularly apparent for disorder strengths $W > 2$, the modified density correlation function has neither the exponential nor the power-law form. Actually, it seems that the decays of $\tilde{C}_q(t)$ in Fig. 13.3 may be much better represented by the stretched-exponential form

$$\tilde{C}_q(t) = \exp \left[-D_0 q^2 t A(t) \right] , \quad (13.13)$$

where D_0 is an effective diffusion parameter, while $A(t) = \frac{1}{\beta} (t_0/t)^{1-\beta}$ introduces corrections due to the non-diffusive dynamics, with $\beta < 1$. Both parameters D_0 and β may be easily estimated by fitting Eq. (13.13) to our numerical results in Fig. 13.3, allowing us to study peculiarities of decay in Eq. (13.13) as the disorder strength is varied from weak to moderate values.

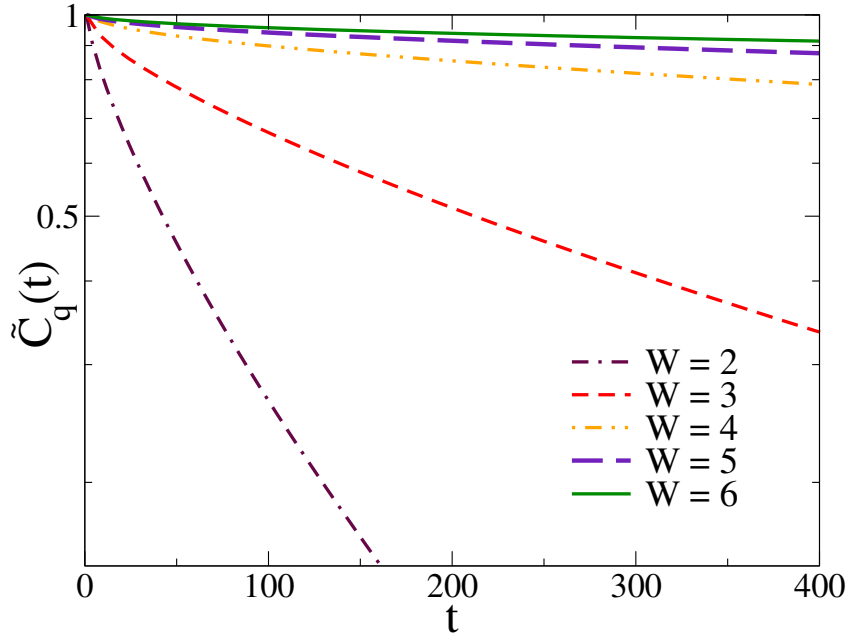


Figure 13.3: Average modified density correlation function $\tilde{C}_q(t)$ obtained by the direct time integration of rate equations on a lattice with $L = 24$ sites for several disorder strengths $W = 2-6$.

Distribution of the diffusion parameter

We should be careful, however, when estimating the diffusion parameter D_0 and the exponent β based solely on average quantities like $\tilde{C}_q(t)$ in Fig. 13.3. The reason for that lies in the generally very broad nature of distributions of physical observables in MBL models, exhibiting strong sample-to-sample fluctuations. There is no reason that the same does not hold true for the (modified) density correlation function, so the estimates based solely on the average values of $\tilde{C}_q(t)$ might be obscured.

That the nature of distributions in MBL models is generally very broad, is indeed supported by our analysis of the distribution of the time-dependent diffusion parameter $D(t)$. In particular, we have calculated the time-dependent diffusion parameter in Eq. (13.1) for each disorder configuration separately and studied how the integrated distribution $I(D)$ of $D(t)$ evolves in time. The results are presented in Fig. 13.4, where we show the integrated distribution $I(D)$ for several disorder strengths $W = 2 - 6$, evaluated at different times $t = 2^n t_0$, for the lattice with $L = 24$ sites and by employing $N_{dis} = 300$ different disorder configurations. From the technical point of view, in order to get $A(t)$ of the order of unity in the studied time window, $t \sim 10^2$, we set $t_0 = 50$. As anticipated, $I(D)$ reveals a broad distribution of D . In particular, the results appear to follow roughly a log-normal distribution which is symmetric on the $\ln D$ scale around the median D_m , defined by $I(D_m) = 1/2$.

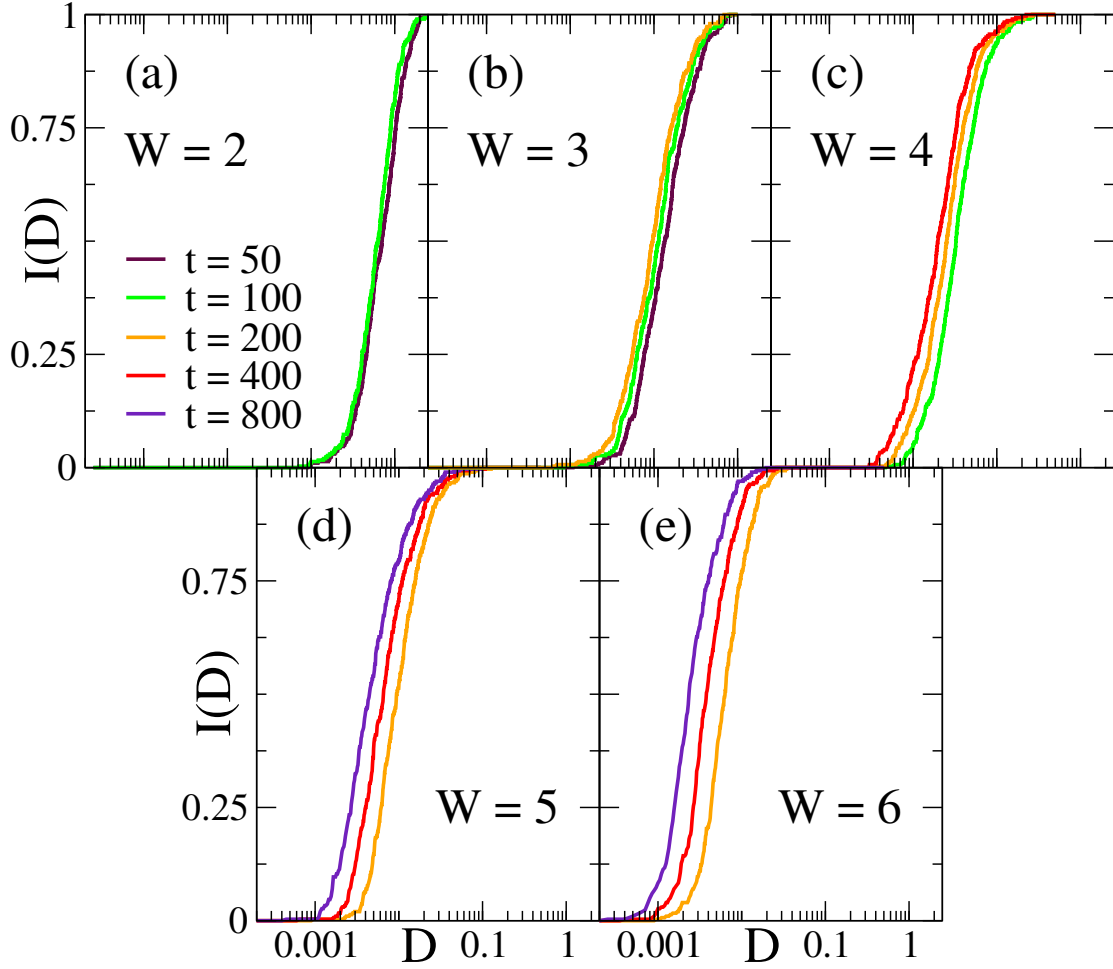


Figure 13.4: Integrated distributions $I(D)$ of the time-dependent diffusion parameter $D(t)$ evaluated by the direct time integration of the rate equations for the lattice with $L = 24$ sites at different times t , for several disorder strengths $W = 2 - 6$.

13.1.4 Characteristics of anomalous transport

A quite uniform shifting of $I(D)$ in time in Fig. 13.4 further supports the stretched-exponential form for the decay of the modified density correlation function, since by means of Eq. (13.1), Eq. (13.13) gives for the time-dependent diffusion parameter

$$D(t) = D_0 (t_0/t)^{1-\beta} . \quad (13.14)$$

In particular, while the shift of the distribution $I(D)$ for $W = 2$ is barely visible, it is quite pronounced for disorder strengths $W \geq 3$. This suggests the values $\beta \rightarrow 1$ and $\beta < 1$, that is the diffusive and the anomalous transport for $W = 2$ and $W \geq 3$, respectively, with the coefficient β getting smaller as the disorder strength W increases.

However, in order to make the most of all our results to quantify the effective diffusion parameter D_0 and the exponent β in dependence on the disorder strength as best as possible,

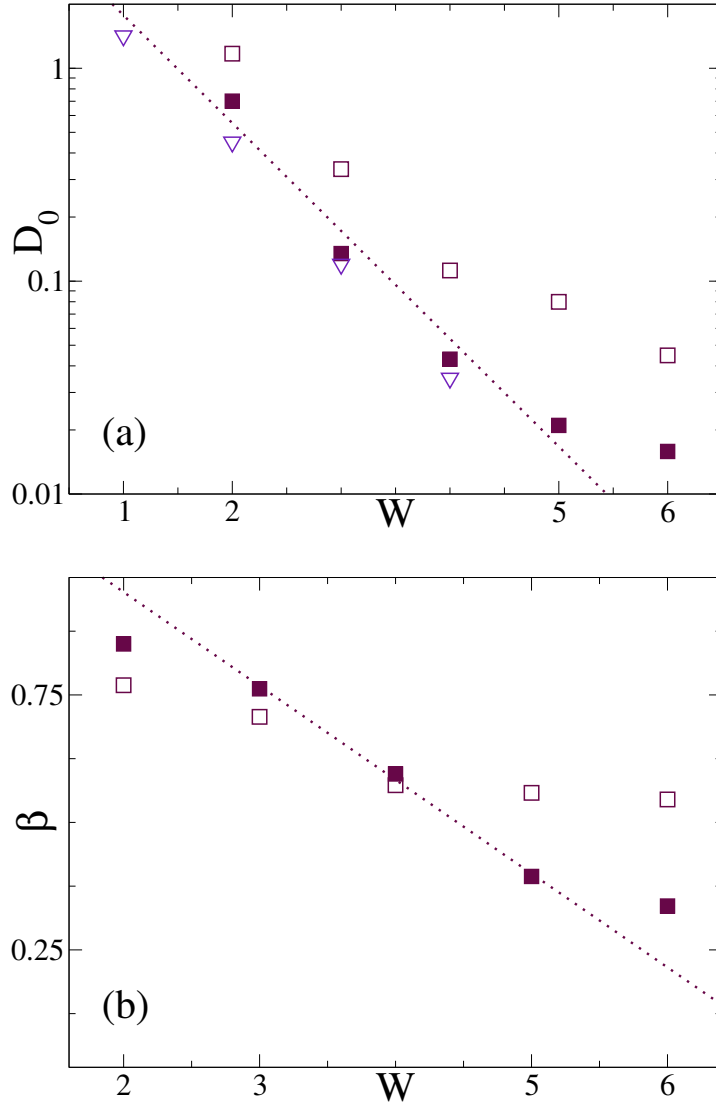


Figure 13.5: (a) Effective diffusion parameter D_0 and (b) the exponent β . Open squares show results extracted from average $\tilde{C}_q(t)$ in Fig. 13.3, while solid squares show results extracted from distributions $I(D)$ in Fig. 13.4. In (a) we also plot D_0 (open triangles) from the full quantum calculations [262]. Fits of the results obtained from the distributions $I(D)$ are denoted with the dotted lines.

we estimate $D_0(W)$ and $\beta(W)$ in three different ways. We obtain the first set of data by simply fitting the stretched-exponential form in Eq. (13.13) to the numerical results in Fig. 13.3. The second set of data is much more delicate to get and is relying on the extraction of results from the distributions $I(D)$ in Fig. 13.4. In particular, we can read off the medians $D_m(t)$ for each of the distributions, and use them together with Eq. (13.14) to estimate $D_0(W)$ and $\beta(W)$. Namely, with the use of Eq. (13.14) we can write for two different times t_1 and t_2

$$\beta = 1 - \frac{\ln(D_1/D_2)}{\ln(t_2/t_1)}. \quad (13.15)$$

Now, for the value of β we take the value obtained by substituting in Eq. (13.15) the results for two smallest consecutive times t_1 and t_2 . For example, following the results in Fig. 13.4(a), we have $\beta(W = 2) = 1 - \frac{\ln[D_m(t=50)/D_m(t=100)]}{\ln(100/50)} \approx 0.85$. With the values of β in Eq. (13.14) known, we can now also calculate the corresponding effective diffusion parameter D_0 . This completes the second set of data, obtained by considering the distributions $I(D)$. As the third and last set of data, we take the results obtained by the full quantum calculations [262], in order to test our rate equations approach both quantitatively and qualitatively.

All our results for $D_0(W)$ and $\beta(W)$ obtained from the fits of the stretched-exponential form in Eq. (13.13) to the results in Fig. 13.3 and extracted from distributions $I(D)$ in Fig. 13.4, together with the full quantum results for a comparison, are summarized in Fig. 13.5. Apparently, the effective diffusion parameter D_0 decreases roughly exponentially with the disorder strength, $D_0 \propto \exp(-bW)$, with the estimated $b \sim 1.2$, which is accompanied by the approximately linear decrease of β with W . It is interesting to note that this result is in accordance with the findings of the previous studies [286, 287], where D_0 was related to the DC conductivity, $\sigma_0 = D_0/4$, which was shown to exhibit the exponential dependence on W as well, with essentially the very same coefficient, $b \approx 1.1$. By comparing our two approximate sets of data with the full quantum calculations, we see that much more reliable results are obtained from the distributions $I(D)$, rather than from the decay of the average density correlation function, as anticipated.

13.2 Conclusions

We study the density relaxation in the thermal phase below the MBL transition in the context of rate equations by keeping only resonant transitions between many-body states. Tendencies toward the normal diffusive behavior for very weak disorders are observed, while the diffusion happens to be anomalous in a wide range of disorders $2 < W < W_c$, characterized by the dynamical exponent $\beta < 1$. The exponential decrease of the effective diffusion parameter as the disorder strength increases is apparent as well. Both very good quantitative and qualitative agreements of our rate equations approach with the full quantum results provide a strong justification of the rate equations approximation and the overall physical picture of the percolative nature of the thermal-MBL transition. In particular, the observed anomalous diffusion indicates a weakly coupled many-body substructure within the degrading macroscopic cluster, but with no evident relations to the weak-link scenario in real space.

Summary

We present novel results related to a plethora of problems involving electron-phonon correlations, interelectronic interactions, and/or the disorder. We address these problems theoretically either with the methods of the diagrammatic perturbation theory or by the exact numerical diagonalization. The former allows us to gain deeper insights into physical processes underlying the system's behaviors of interest, for which the drawing of Feynman diagrams in the time domain turns out to be particularly useful. We relate our findings to experimental results, so the results of this thesis are not only relevant for fundamental theoretical physics but are applicable in real-life experiments as well.

The exact analytical solution to the polaronic impurity problem for an arbitrary lattice model is given, including the exact treatment of all inelastic processes corresponding to the emission and absorption of real phonons. We exploit this solution to exactly solve for the electron tunneling across molecular junctions in systems with reduced dimensionality and to calculate charge mobility in the presence of dilute concentrations of polaronic impurities in semiconducting bulk systems. We find that the scattering on polaronic impurities imposes the possible explanation for unconventional power-law exponents in the temperature dependence of the charge mobility observed experimentally in various organic crystals. Our exact solution may also be readily extended to various systems of current interest, including atomically thin crystalline films, where the effects of impurities with internal degrees of freedom can be experimentally accessed through energy-loss spectroscopy, atom-probe tomography, and scanning tunneling microscopy.

We provide analytical expressions for the fermion self-energy and the phonon polarization to the next-to-leading order of the weak electron-phonon coupling translationally invariant diagrammatic perturbation theory, where special attention is devoted to vertex corrections. By focusing on the polaron limit, we perturbatively recover the known result which states that the non-local part of the electron self-energy with vertex corrections becomes irrelevant in the antiadiabatic regime. We introduce the two-vertices renormalization scheme for the treatment of phonon polarization, involving the vertex function with fermion propagators all pointing in the same direction of time. The former may rationalize the replacement of the bare electron-phonon matrix element with the screened one in cases with dilute concentrations of electrons, used frequently in *ab initio* simulations of phonon properties. We observe an additional, enhanced phonon spectral weight which we call a phonon production, and we attribute it to the virtual cloud of phonons accompanying the electron in the polaron ground state.

We provide convenient ways to directly estimate the electron-phonon interaction range and the electron-phonon coupling strength from measured ARPES and EELS spectra of strongly

doped polar materials, regardless of the limited experimental resolution. The \mathbf{k} and E structures of phonon sidebands appearing in ARPES spectra are analyzed as the function of the range of the electron-phonon interaction, which is argued that may be estimated from the confinement of the intensity of the imaginary part of the hole self-energy in the corresponding energy windows. This methodology is not restricted to electron-phonon systems only, since the electron coupling to bosonic excitations of other nature (plasmons, magnons, ...) may be analyzed in a similar manner. We show that the electron-phonon coupling strength plays a prominent role in distributing spectral weights among phonon-plasmon coupled excitations in EELS spectra, providing an experimentally convenient way to estimate it from integrated spectra. In particular, for weak couplings in the antiadiabatic and the resonant regime the EELS spectral weight is equally redistributed among coupled excitations, while in all the other parametric space the EELS spectral weight is dominantly located within the higher frequency excitation. By projecting the excitations onto the phonon degree of freedom, we also report for strong couplings large phonon production contributions, which are of very different origins depending on the adiabaticity parameter and generally different from that in the polaron limit. We show that the static screening approximation generally fails to reproduce phonon spectral functions. We argue that the vertex corrections in the ladder approximation tend to remove the $2k_F$ singularity of the Lindhard function, opening the interesting question about the Kohn anomaly and Peierls instability in the antiadiabatic regime.

Fundamental aspects of relaxation processes in strongly correlated and disordered systems are also addressed in this thesis in the context of the MBL phenomenon. By studying the MBL problem in the Fock space, we show that the system dynamics is confined up to very long times to many disconnected small many-body clusters in the Fock space. By keeping only resonant transitions between many-body states, neglecting thus perturbatively small contributions, we locate the thermal-MBL transition via the emergence of the macroscopic cluster in analogy with the percolation phase transition. On the thermal side, we use a simplified rate equations approach to study relaxation processes within the macroscopic cluster, which agrees quantitatively and qualitatively with the full quantum calculations. For very low disorder strengths the diffusive transport prevails, while for stronger disorders we find that the large portion of the thermal side is characterized by the anomalously slow relaxation toward the equilibrium.

Derivations related to fermion self-energy

In this Appendix A, we show details of calculations related to the results for the fermion self-energy used in Parts II and III. In particular, we calculate exactly the fermion self-energy in the leading order of the perturbation theory in electron-phonon interaction in the 1D case with the Holstein coupling and provide the derivations of all the fermion self-energy contributions in the next-to-leading order, with the special emphasis on the polaron limit. We consider the electron coupling to an optical phonon with a constant energy $\omega_{\mathbf{q}} \approx \omega_0$ ($\hbar = 1$).

A.1 Leading order fermion self-energy

A.1.1 Finite electron densities

The leading order fermion self-energy in electron-phonon interaction has been fully derived in Section 8.1 and reads, see Eq. (8.3)

$$\Sigma^{(2)}(\mathbf{k}, E) = \sum_{\mathbf{q}} |g(\mathbf{q})|^2 \left[\frac{1 - n_{\mathbf{k}+\mathbf{q}}}{E - \omega_0 - \xi_{\mathbf{k}+\mathbf{q}} + i\eta} + \frac{n_{\mathbf{k}+\mathbf{q}}}{E + \omega_0 - \xi_{\mathbf{k}+\mathbf{q}} - i\eta} \right]. \quad (\text{A.1})$$

In the 1D case with the Holstein coupling $g(q) = g$, the summation/integration over q can be carried out analytically for both the real and the imaginary part of local $\Sigma^{(2)}(E)$. If we assume the dispersion, $\varepsilon_k = 2t(1 - \cos k)$, such that the bottom of a band is at $\varepsilon_{k=0} = 0$, for the real part of $\Sigma^{(2)}(E)$ we have

$$\begin{aligned} \text{Re}\Sigma^{(2)}(E) &= \frac{g^2 N}{N 2\pi} \int_{-\pi}^{\pi} dq \left[\frac{1 - n_q}{E - \omega_0 + \mu - 2t(1 - \cos q)} + \frac{n_q}{E + \omega_0 + \mu - 2t(1 - \cos q)} \right] \\ &= \frac{g^2}{2\pi} \left\{ \left[\int_{-\pi}^{-k_F} + \int_{k_F}^{\pi} \right] \frac{dq}{E - \omega_0 + \mu - 2t + 2t \cos q} + \int_{-k_F}^{k_F} \frac{dq}{E + \omega_0 + \mu - 2t + 2t \cos q} \right\}, \end{aligned} \quad (\text{A.2})$$

while the imaginary part of $\Sigma^{(2)}(E)$ reads

$$\begin{aligned}
\text{Im}\Sigma^{(2)}(E) &= \frac{g^2}{N} \frac{N}{2\pi} \pi \int_{-\pi}^{\pi} dq \left[-(1-n_q)\delta(E-\omega_0+\mu-\varepsilon_q) + n_q\delta(E+\omega_0+\mu-\varepsilon_q) \right] \\
&= \frac{g^2}{2} \left\{ - \left[\int_{-\pi}^{-k_F} + \int_{k_F}^{\pi} \right] dq \delta(E-\omega_0+\mu-\varepsilon_q) + \int_{-k_F}^{k_F} dq \delta(E+\omega_0+\mu-\varepsilon_q) \right\} .
\end{aligned} \tag{A.3}$$

Due to the delta functions, the imaginary part can be trivially evaluated

$$\text{Im}\Sigma^{(2)}(E) = g^2 \left\{ - \frac{\Theta(E-\omega_0)\Theta(4t+\omega_0-\mu-E)}{\sqrt{(E-\omega_0+\mu)(4t+\omega_0-\mu-E)}} + \frac{\Theta(E+\omega_0+\mu)\Theta(-\omega_0-E)}{\sqrt{(E+\omega_0+\mu)(4t-\omega_0-\mu-E)}} \right\} . \tag{A.4}$$

For the evaluation of the real part of $\Sigma^{(2)}(E)$, we consult the integral table [59] providing

$$\int \frac{dx}{a+b\cos x} = \begin{cases} \frac{2}{\sqrt{a^2-b^2}} \arctan \left[\frac{(a-b)\tan \frac{x}{2}}{\sqrt{a^2-b^2}} \right] , & a^2 > b^2 , \\ \frac{1}{\sqrt{b^2-a^2}} \ln \left| \frac{(b-a)\tan \frac{x}{2} + \sqrt{b^2-a^2}}{(b-a)\tan \frac{x}{2} - \sqrt{b^2-a^2}} \right| , & b^2 > a^2 . \end{cases} \tag{A.5}$$

In the first term of Eq. (A.2), $a = E - \omega_0 + \mu - 2t$ and $b = 2t$, so

$$a^2 > b^2 \rightarrow (E - \omega_0 + \mu - 2t)^2 > 4t^2 \rightarrow \begin{cases} E - \omega_0 + \mu - 2t > 2t \rightarrow E > \omega_0 + 4t - \mu , \\ E - \omega_0 + \mu - 2t < -2t \rightarrow E < \omega_0 - \mu , \end{cases} \tag{A.6}$$

$$\begin{aligned}
a^2 < b^2 &\rightarrow (E - \omega_0 + \mu - 2t)^2 < 4t^2 \\
&\rightarrow -2t < E - \omega_0 + \mu - 2t < 2t \rightarrow \omega_0 - \mu < E < \omega_0 + 4t - \mu ,
\end{aligned} \tag{A.7}$$

and

$$\begin{aligned}
a^2 - b^2 &= (E - \omega_0 + \mu - 2t)^2 - 4t^2 = (E - \omega_0 + \mu)^2 - 4t(E - \omega_0 + \mu) + 4t^2 - 4t^2 \\
&= (E - \omega_0 + \mu)(E - \omega_0 + \mu - 4t) .
\end{aligned} \tag{A.8}$$

Moreover, for $a^2 > b^2$

$$\begin{aligned}
& \left[\int_{-\pi}^{-k_F} + \int_{k_F}^{\pi} \right] \frac{dx}{a + b \cos x} = \frac{2}{\sqrt{a^2 - b^2}} \left\{ \arctan \left[\frac{(a - b) \tan \frac{-k_F}{2}}{\sqrt{a^2 - b^2}} \right] - \right. \\
& \left. - \arctan \left[\frac{(a - b) \tan \frac{-\pi}{2}}{\sqrt{a^2 - b^2}} \right] + \arctan \left[\frac{(a - b) \tan \frac{\pi}{2}}{\sqrt{a^2 - b^2}} \right] - \arctan \left[\frac{(a - b) \tan \frac{k_F}{2}}{\sqrt{a^2 - b^2}} \right] \right\} \quad (\text{A.9}) \\
& = \frac{2}{\sqrt{a^2 - b^2}} \left\{ \text{sign}(a - b)\pi - 2 \arctan \left[\frac{(a - b) \tan \frac{k_F}{2}}{\sqrt{a^2 - b^2}} \right] \right\},
\end{aligned}$$

while for $a^2 < b^2$

$$\begin{aligned}
& \left[\int_{-\pi}^{-k_F} + \int_{k_F}^{\pi} \right] \frac{dx}{a + b \cos x} = \frac{1}{\sqrt{b^2 - a^2}} \left\{ \ln \left| \frac{(b - a) \tan \frac{-k_F}{2} + \sqrt{b^2 - a^2}}{(b - a) \tan \frac{-k_F}{2} - \sqrt{b^2 - a^2}} \right| - \right. \\
& \quad - \ln \left| \frac{(b - a) \tan \frac{-\pi}{2} + \sqrt{b^2 - a^2}}{(b - a) \tan \frac{-\pi}{2} - \sqrt{b^2 - a^2}} \right| + \ln \left| \frac{(b - a) \tan \frac{\pi}{2} + \sqrt{b^2 - a^2}}{(b - a) \tan \frac{\pi}{2} - \sqrt{b^2 - a^2}} \right| - \\
& \quad \left. - \ln \left| \frac{(b - a) \tan \frac{k_F}{2} + \sqrt{b^2 - a^2}}{(b - a) \tan \frac{k_F}{2} - \sqrt{b^2 - a^2}} \right| \right\} \quad (\text{A.10}) \\
& = \frac{1}{\sqrt{b^2 - a^2}} \left\{ 2 \ln \left| \frac{(b - a) \tan \frac{k_F}{2} - \sqrt{b^2 - a^2}}{(b - a) \tan \frac{k_F}{2} + \sqrt{b^2 - a^2}} \right| \right\}.
\end{aligned}$$

We have similarly for the second term in Eq. (A.2), where $a = E + \omega_0 + \mu - 2t$ and $b = 2t$

$$a^2 > b^2 \rightarrow (E + \omega_0 + \mu - 2t)^2 > 4t^2 \rightarrow \begin{cases} E + \omega_0 + \mu - 2t > 2t \rightarrow E > -\omega_0 - \mu + 4t, \\ E + \omega_0 + \mu - 2t < -2t \rightarrow E < -\omega_0 - \mu, \end{cases} \quad (\text{A.11})$$

$$\begin{aligned}
a^2 < b^2 & \rightarrow (E + \omega_0 + \mu - 2t)^2 < 4t^2 \rightarrow -2t < E + \omega_0 + \mu - 2t < 2t \\
& \rightarrow -\omega_0 - \mu < E < -\omega_0 - \mu + 4t, \quad (\text{A.12})
\end{aligned}$$

and

$$\begin{aligned}
a^2 - b^2 & = (E + \omega_0 + \mu - 2t)^2 - 4t^2 = (E + \omega_0 + \mu)^2 - 4t(E + \omega_0 + \mu) + 4t^2 - 4t^2 \\
& = (E + \omega_0 + \mu)(E + \omega_0 + \mu - 4t). \quad (\text{A.13})
\end{aligned}$$

Now, for $a^2 > b^2$ we get

$$\begin{aligned} \int_{-k_F}^{k_F} \frac{dx}{a + b \cos x} &= \frac{2}{\sqrt{a^2 - b^2}} \left\{ \arctan \left[\frac{(a - b) \tan \frac{k_F}{2}}{\sqrt{a^2 - b^2}} \right] - \arctan \left[\frac{(a - b) \tan \frac{-k_F}{2}}{\sqrt{a^2 - b^2}} \right] \right\} \\ &= \frac{2}{\sqrt{a^2 - b^2}} \left\{ 2 \arctan \left[\frac{(a - b) \tan \frac{k_F}{2}}{\sqrt{a^2 - b^2}} \right] \right\}, \end{aligned} \quad (\text{A.14})$$

while for $a^2 < b^2$

$$\begin{aligned} \int_{-k_F}^{k_F} \frac{dx}{a + b \cos x} &= \frac{1}{\sqrt{b^2 - a^2}} \left\{ \ln \left| \frac{(b - a) \tan \frac{k_F}{2} + \sqrt{b^2 - a^2}}{(b - a) \tan \frac{k_F}{2} - \sqrt{b^2 - a^2}} \right| - \right. \\ &\left. - \ln \left| \frac{(b - a) \tan \frac{-k_F}{2} + \sqrt{b^2 - a^2}}{(b - a) \tan \frac{-k_F}{2} - \sqrt{b^2 - a^2}} \right| \right\} = \frac{1}{\sqrt{b^2 - a^2}} \left\{ 2 \ln \left| \frac{(b - a) \tan \frac{k_F}{2} + \sqrt{b^2 - a^2}}{(b - a) \tan \frac{k_F}{2} - \sqrt{b^2 - a^2}} \right| \right\}. \end{aligned} \quad (\text{A.15})$$

By combining all the above results, we finally get

$$\text{Re}\Sigma^{(2)}(E) = \begin{cases} -\frac{g^2}{\sqrt{(E+\omega_0+\mu)(E+\omega_0+\mu-4t)}} \left\{ \frac{2}{\pi} \arctan \left[\frac{\sqrt{\frac{E+\omega_0+\mu-4t}{E+\omega_0+\mu}} \sqrt{\frac{\mu}{4t-\mu}}}{\sqrt{\frac{E+\omega_0+\mu-4t}{E+\omega_0+\mu}} \sqrt{\frac{\mu}{4t-\mu}}} \right] \right\}, & E < -\omega_0 - \mu, \\ \frac{g^2}{\sqrt{(E+\omega_0+\mu)(E+\omega_0+\mu-4t)}} \left\{ \frac{2}{\pi} \arctan \left[\frac{\sqrt{\frac{E+\omega_0+\mu-4t}{E+\omega_0+\mu}} \sqrt{\frac{\mu}{4t-\mu}}}{\sqrt{\frac{E+\omega_0+\mu-4t}{E+\omega_0+\mu}} \sqrt{\frac{\mu}{4t-\mu}}} \right] \right\}, & E > -\omega_0 - \mu + 4t \\ \frac{g^2}{\sqrt{(E+\omega_0+\mu)(4t-\omega_0-\mu-E)}} \left\{ \frac{1}{\pi} \ln \left| \frac{\sqrt{4t-\omega_0-\mu-E} \sqrt{\frac{\mu}{4t-\mu}} + \sqrt{E+\omega_0+\mu}}{\sqrt{4t-\omega_0-\mu-E} \sqrt{\frac{\mu}{4t-\mu}} - \sqrt{E+\omega_0+\mu}} \right| \right\}, & -\omega_0 - \mu < E < -\omega_0 - \mu + 4t, \\ -\frac{g^2}{\sqrt{(E-\omega_0+\mu)(E-\omega_0+\mu-4t)}} \left\{ 1 - \frac{2}{\pi} \arctan \left[\frac{\sqrt{\frac{E-\omega_0+\mu-4t}{E-\omega_0+\mu}} \sqrt{\frac{\mu}{4t-\mu}}}{\sqrt{\frac{E-\omega_0+\mu-4t}{E-\omega_0+\mu}} \sqrt{\frac{\mu}{4t-\mu}}} \right] \right\}, & E < \omega_0 - \mu, \\ \frac{g^2}{\sqrt{(E-\omega_0+\mu)(E-\omega_0+\mu-4t)}} \left\{ 1 - \frac{2}{\pi} \arctan \left[\frac{\sqrt{\frac{E-\omega_0+\mu-4t}{E-\omega_0+\mu}} \sqrt{\frac{\mu}{4t-\mu}}}{\sqrt{\frac{E-\omega_0+\mu-4t}{E-\omega_0+\mu}} \sqrt{\frac{\mu}{4t-\mu}}} \right] \right\}, & E > \omega_0 + 4t - \mu, \\ -\frac{g^2}{\sqrt{(E-\omega_0+\mu)(4t+\omega_0-\mu-E)}} \left\{ \frac{1}{\pi} \ln \left| \frac{\sqrt{4t+\omega_0-\mu-E} \sqrt{\frac{\mu}{4t-\mu}} + \sqrt{E-\omega_0+\mu}}{\sqrt{4t+\omega_0-\mu-E} \sqrt{\frac{\mu}{4t-\mu}} - \sqrt{E-\omega_0+\mu}} \right| \right\}, & \omega_0 - \mu < E < \omega_0 + 4t - \mu, \\ 0, & \text{elsewhere,} \end{cases} \quad (\text{A.16})$$

where we have exploited

$$\tan \frac{k_F}{2} = \frac{1 - \cos k_F}{\sin k_F} = \frac{\frac{\mu}{2t}}{\sqrt{1 - \left(\frac{2t-\mu}{2t}\right)^2}} = \sqrt{\frac{\mu}{4t - \mu}}, \quad (\text{A.17})$$

since by definition $\mu = 2t(1 - \cos k_F)$. In particular, in the polaron limit holds $\mu = 0$, which substituted in Eqs. (A.4) and (A.16) yields

$$\text{Im}\Sigma^{(2)}(E) = -\frac{g^2}{\sqrt{(E-\omega_0)(\omega_0+4t-E)}}\Theta(E-\omega_0)\Theta(\omega_0+4t-E), \quad (\text{A.18})$$

and

$$\text{Re}\Sigma^{(2)}(E) = \begin{cases} -\frac{g^2}{\sqrt{(E-\omega_0)(E-\omega_0-4t)}}, & E < \omega_0, \\ \frac{g^2}{\sqrt{(E-\omega_0)(E-\omega_0-4t)}}, & E > \omega_0 + 4t, \\ 0, & \text{elsewhere.} \end{cases} \quad (\text{A.19})$$

In 2D and 3D cases, such closed expressions for the full $\Sigma^{(2)}(\mathbf{k}, E)$ generally cannot be obtained. However, when the doping is low, such that the electron dispersion may be assumed quadratic $\varepsilon_{\mathbf{k}} = tk^2$, $\text{Im}\Sigma^{(2)}(\mathbf{k}, E)$ may be evaluated analytically in cases with the long-range Fröhlich coupling due to the appearance of the delta functions $\delta(E \pm \omega_0 - \xi_{\mathbf{q}})$. In particular, with the matrix element of the electron-phonon interaction given by $|g(\mathbf{q})|^2 = \sqrt{2}\pi\alpha/|\mathbf{q}|$, the summation/integration in Eq. (A.1) for the imaginary part of $\Sigma^{(2)}(\mathbf{k}, E)$ can be evaluated in polar coordinates in the 2D case

$$\text{Im}\Sigma^{(2)}(\mathbf{k}, E) = \frac{\sqrt{2}\pi^2\alpha}{(2\pi)^2} \int dq q \Theta(-\xi_{\mathbf{q}})\delta(E - \xi_{\mathbf{q}} + \omega_0) \int_0^{2\pi} \frac{d\phi}{\sqrt{k^2 + q^2 - 2kq \cos \phi}}. \quad (\text{A.20})$$

Integration over the polar angle ϕ yields [59]

$$\int_0^{2\pi} \frac{d\phi}{\sqrt{k^2 + q^2 - 2kq \cos \phi}} = 2 \int_0^{\pi} \frac{d\phi}{\sqrt{k^2 + q^2 - 2kq \cos \phi}} = \frac{4}{|k+q|} K\left(\frac{\sqrt{4kq}}{|k+q|}\right), \quad (\text{A.21})$$

where $K(x)$ is the complete elliptic integral of the first kind. The remaining integration over q is particularly simple due to the delta function $\delta(E - \xi_{\mathbf{q}} + \omega_0)$, giving

$$\begin{aligned} \text{Im}\Sigma^{(2)}(\mathbf{k}, E) &= \frac{\alpha}{\sqrt{2t}(\sqrt{\varepsilon_{\mathbf{k}}} + \sqrt{E + \omega_0 + \mu})} K\left(\frac{2[\varepsilon_{\mathbf{k}}(E + \omega_0 + \mu)]^{\frac{1}{4}}}{\sqrt{\varepsilon_{\mathbf{k}}} + \sqrt{E + \omega_0 + \mu}}\right) \times \\ &\times \Theta(-E - \omega_0)\Theta(E + \mu + \omega_0). \end{aligned} \quad (\text{A.22})$$

In the 3D case, the summation/integration in Eq. (A.1) for the imaginary part of $\Sigma^{(2)}(\mathbf{k}, E)$ can be carried out analytically even for an arbitrary screening of the Fröhlich interaction, $|g(\mathbf{q})|^2 = 2\sqrt{2}\pi\alpha/(|\mathbf{q}|^2 + q_{TF}^2)$, yielding [40]

$$\text{Im}\Sigma^{(2)}(\mathbf{k}, E) = \frac{\alpha}{2\sqrt{2t\varepsilon_{\mathbf{k}}}} \ln \left| \frac{\varepsilon_{TF} + (\sqrt{\varepsilon_{\mathbf{k}}} - \sqrt{E + \omega_0 + \mu})^2}{\varepsilon_{TF} + (\sqrt{\varepsilon_{\mathbf{k}}} + \sqrt{E + \omega_0 + \mu})^2} \right| \Theta(-E - \omega_0) \Theta(E + \mu + \omega_0) . \quad (\text{A.23})$$

The limit with the unscreened Fröhlich interaction is simply obtained by setting $\varepsilon_{TF} \rightarrow 0$.

A.2 Next-to-leading order fermion self-energy

In the next-to-leading order of the perturbation theory in electron-phonon interaction, there are three irreducible contributions to the fermion self-energy represented diagrammatically in Figs. 8.3 and 8.4. The two diagrams in Figs. 8.3(a) and (b) are dubbed the non-crossing and the crossing diagram, respectively, while the contribution shown in Fig. 8.4 may be viewed as the renormalization of the phonon. In what follows, we evaluate all three contributions within the zero temperature diagrammatic perturbation theory [40].

A.2.1 Non-crossing diagram

By using the standard Feynman rules [40], we can write for the fermion self-energy stemming from the non-crossing diagram in Fig. 8.3(a)

$$\begin{aligned} \Sigma^{(NC)}(\mathbf{k}, E) = & i^2 \sum_{\mathbf{q}, \mathbf{q}'} |g(\mathbf{q})|^2 |g(\mathbf{q}')|^2 \int_{-\infty}^{\infty} \frac{d\omega}{2\pi} \int_{-\infty}^{\infty} \frac{d\omega'}{2\pi} \\ & \times D_0(\mathbf{q}, \omega) D_0(\mathbf{q}', \omega') [G_0(\mathbf{k} + \mathbf{q}, E + \omega)]^2 G_0(\mathbf{k} + \mathbf{q} + \mathbf{q}', E + \omega + \omega') , \end{aligned} \quad (\text{A.24})$$

with the unperturbed fermion and the unperturbed phonon propagator reading

$$G_0(\mathbf{k}, E) = \frac{1 - n_{\mathbf{k}}}{E - \xi_{\mathbf{k}} + i\eta} + \frac{n_{\mathbf{k}}}{E - \xi_{\mathbf{k}} - i\eta} , \quad (\text{A.25})$$

and

$$D_0(\mathbf{q}, \omega) = \frac{1}{\omega - \omega_0 + i\eta} - \frac{1}{\omega + \omega_0 - i\eta} , \quad (\text{A.26})$$

respectively.

In Eq. (A.24), we recognize the expression in Eq. (8.2), appearing in the leading order self-energy contribution given by Eq. (8.1)

$$\begin{aligned}
\Sigma^{(2)}(\mathbf{k} + \mathbf{q}, E + \omega) &= i \sum_{\mathbf{q}'} |g(\mathbf{q}')|^2 \int \frac{d\omega'}{2\pi} D_0(\mathbf{q}', \omega') G_0(\mathbf{k} + \mathbf{q} + \mathbf{q}', E + \omega + \omega') \\
&= \sum_{\mathbf{q}'} |g(\mathbf{q}')|^2 \left[\frac{n_{\mathbf{k}+\mathbf{q}+\mathbf{q}'}}{E + \omega - \xi_{\mathbf{k}+\mathbf{q}+\mathbf{q}'} + \omega_0 - i\eta} + \frac{1 - n_{\mathbf{k}+\mathbf{q}+\mathbf{q}'}}{E + \omega - \xi_{\mathbf{k}+\mathbf{q}+\mathbf{q}'} - \omega_0 + i\eta} \right].
\end{aligned} \tag{A.27}$$

In terms of $\Sigma^{(2)}(\mathbf{k} + \mathbf{q}, E + \omega)$, the contribution of the non-crossing diagram may be written as

$$\Sigma^{(NC)}(\mathbf{k}, E) = i \sum_{\mathbf{q}} |g(\mathbf{q})|^2 \int_{-\infty}^{\infty} \frac{d\omega}{2\pi} D_0(\mathbf{q}, \omega) [G_0(\mathbf{k} + \mathbf{q}, E + \omega)]^2 \Sigma^{(2)}(\mathbf{k} + \mathbf{q}, E + \omega), \tag{A.28}$$

where

$$[G_0(\mathbf{k} + \mathbf{q}, E + \omega)]^2 = \frac{(1 - n_{\mathbf{k}+\mathbf{q}})^2}{(E + \omega - \xi_{\mathbf{k}+\mathbf{q}} + i\eta)^2} + \frac{(n_{\mathbf{k}+\mathbf{q}})^2}{(E + \omega - \xi_{\mathbf{k}+\mathbf{q}} - i\eta)^2}, \tag{A.29}$$

since $(1 - n_{\mathbf{k}+\mathbf{q}})n_{\mathbf{k}+\mathbf{q}} = 0$ holds at zero temperature.

In order to rationalize Eq. (A.28) further, we consider four terms of the product $[G_0(\mathbf{k} + \mathbf{q}, E + \omega)]^2 \Sigma^{(2)}(\mathbf{k} + \mathbf{q}, E + \omega) = \sum_{\mathbf{q}'} |g(\mathbf{q}')|^2 (w_1 + w_2 + w_3 + w_4)$, where

$$w_1 = \frac{(1 - n_{\mathbf{k}+\mathbf{q}})^2 n_{\mathbf{k}+\mathbf{q}+\mathbf{q}'}}{(E + \omega - \xi_{\mathbf{k}+\mathbf{q}} + i\eta)^2 (\omega + E + \omega_0 - \xi_{\mathbf{k}+\mathbf{q}+\mathbf{q}'} - i\eta)}, \tag{A.30}$$

$$w_2 = \frac{(1 - n_{\mathbf{k}+\mathbf{q}})^2 (1 - n_{\mathbf{k}+\mathbf{q}+\mathbf{q}'})}{(E + \omega - \xi_{\mathbf{k}+\mathbf{q}} + i\eta)^2 (\omega + E - \omega_0 - \xi_{\mathbf{k}+\mathbf{q}+\mathbf{q}'} + i\eta)}, \tag{A.31}$$

$$w_3 = \frac{(n_{\mathbf{k}+\mathbf{q}})^2 n_{\mathbf{k}+\mathbf{q}+\mathbf{q}'}}{(E + \omega - \xi_{\mathbf{k}+\mathbf{q}} - i\eta)^2 (\omega + E + \omega_0 - \xi_{\mathbf{k}+\mathbf{q}+\mathbf{q}'} - i\eta)}, \tag{A.32}$$

$$w_4 = \frac{(n_{\mathbf{k}+\mathbf{q}})^2 (1 - n_{\mathbf{k}+\mathbf{q}+\mathbf{q}'})}{(E + \omega - \xi_{\mathbf{k}+\mathbf{q}} - i\eta)^2 (\omega + E - \omega_0 - \xi_{\mathbf{k}+\mathbf{q}+\mathbf{q}'} + i\eta)}. \tag{A.33}$$

As the last step in obtaining $\Sigma^{(NC)}(\mathbf{k}, E)$, these four terms should be multiplied with the phonon propagator $D_0(\mathbf{q}, \omega)$ and the integration in the complex plane over ω carried out. While performing the integrations, it is useful to note that w_2 and w_3 involve poles only in one half of the complex plane. The final result for $\Sigma^{(NC)}(\mathbf{k}, E)$ can be expressed as a sum of six contributions

$$\Sigma^{(NC)}(\mathbf{k}, E) = \sum_{\mathbf{q}, \mathbf{q}'} |g(\mathbf{q})|^2 |g(\mathbf{q}')|^2 \sum_{i=1}^6 \sigma_i^{(NC)}, \tag{A.34}$$

where

$$\sigma_1^{(NC)} = \frac{(1 - n_{\mathbf{k}+\mathbf{q}})^2 n_{\mathbf{k}+\mathbf{q}+\mathbf{q}'}}{(E - \xi_{\mathbf{k}+\mathbf{q}+\mathbf{q}'} + 2\omega_0 - i\eta)(\xi_{\mathbf{k}+\mathbf{q}+\mathbf{q}'} - \omega_0 - \xi_{\mathbf{k}+\mathbf{q}} + i\eta)^2}, \quad (\text{A.35})$$

$$\sigma_2^{(NC)} = -\frac{(1 - n_{\mathbf{k}+\mathbf{q}})^2 n_{\mathbf{k}+\mathbf{q}+\mathbf{q}'}}{(E - \omega_0 - \xi_{\mathbf{k}+\mathbf{q}} + i\eta)(\xi_{\mathbf{k}+\mathbf{q}+\mathbf{q}'} - \omega_0 - \xi_{\mathbf{k}+\mathbf{q}} + i\eta)} \times \left[\frac{1}{E - \omega_0 - \xi_{\mathbf{k}+\mathbf{q}} + i\eta} + \frac{1}{\xi_{\mathbf{k}+\mathbf{q}+\mathbf{q}'} - \omega_0 - \xi_{\mathbf{k}+\mathbf{q}} + i\eta} \right], \quad (\text{A.36})$$

$$\sigma_3^{(NC)} = \frac{(1 - n_{\mathbf{k}+\mathbf{q}})^2 (1 - n_{\mathbf{k}+\mathbf{q}+\mathbf{q}'})}{(E - \omega_0 - \xi_{\mathbf{k}+\mathbf{q}} + i\eta)^2 (E - 2\omega_0 - \xi_{\mathbf{k}+\mathbf{q}+\mathbf{q}'} + i\eta)}, \quad (\text{A.37})$$

$$\sigma_4^{(NC)} = \frac{(n_{\mathbf{k}+\mathbf{q}})^2 n_{\mathbf{k}+\mathbf{q}+\mathbf{q}'}}{(E - \xi_{\mathbf{k}+\mathbf{q}} + \omega_0 - i\eta)^2 (E + 2\omega_0 - \xi_{\mathbf{k}+\mathbf{q}+\mathbf{q}'} - i\eta)}, \quad (\text{A.38})$$

$$\sigma_5^{(NC)} = -\frac{(n_{\mathbf{k}+\mathbf{q}})^2 (1 - n_{\mathbf{k}+\mathbf{q}+\mathbf{q}'})}{(E + \omega_0 - \xi_{\mathbf{k}+\mathbf{q}} - i\eta)(\xi_{\mathbf{k}+\mathbf{q}+\mathbf{q}'} + \omega_0 - \xi_{\mathbf{k}+\mathbf{q}} - i\eta)} \times \left[\frac{1}{E + \omega_0 - \xi_{\mathbf{k}+\mathbf{q}} - i\eta} + \frac{1}{\xi_{\mathbf{k}+\mathbf{q}+\mathbf{q}'} + \omega_0 - \xi_{\mathbf{k}+\mathbf{q}} - i\eta} \right], \quad (\text{A.39})$$

and

$$\sigma_6^{(NC)} = \frac{(n_{\mathbf{k}+\mathbf{q}})^2 (1 - n_{\mathbf{k}+\mathbf{q}+\mathbf{q}'})}{(E - 2\omega_0 - \xi_{\mathbf{k}+\mathbf{q}+\mathbf{q}'} + i\eta)(\xi_{\mathbf{k}+\mathbf{q}+\mathbf{q}'} + \omega_0 - \xi_{\mathbf{k}+\mathbf{q}} - i\eta)^2}. \quad (\text{A.40})$$

A.2.2 Crossing diagram

Following the Feynman rules [40], the expression for the fermion self-energy stemming from the crossing diagram in Fig. 8.3(b) may be casted in the form

$$\Sigma^{(C)}(\mathbf{k}, E) = i^2 \sum_{\mathbf{q}} |g(\mathbf{q})|^2 \int_{-\infty}^{\infty} \frac{d\omega}{2\pi} \Gamma^{(2)}(\mathbf{k}, E; \mathbf{k}+\mathbf{q}, E+\omega) D_0(\mathbf{q}, \omega) G_0(\mathbf{k}+\mathbf{q}, E+\omega), \quad (\text{A.41})$$

where

$$\Gamma^{(2)}(\mathbf{k}, E; \mathbf{k}+\mathbf{q}, E+\omega) = \sum_{\mathbf{q}'} |g(\mathbf{q}')|^2 \int_{-\infty}^{\infty} \frac{d\omega'}{2\pi} D_0(\mathbf{q}', \omega') G_0(\mathbf{k}+\mathbf{q}', E+\omega') \times \\ \times G_0(\mathbf{k}+\mathbf{q}+\mathbf{q}', E+\omega+\omega'), \quad (\text{A.42})$$

is the leading order contribution to the vertex function. $\Gamma^{(2)}(\mathbf{k}, E; \mathbf{k} + \mathbf{q}, E + \omega)$ can be expressed as a sum of four contributions after the straightforward integration over ω' in the complex plane

$$\Gamma^{(2)}(\mathbf{k}, E; \mathbf{k} + \mathbf{q}, E + \omega) = \sum_{i=1}^4 \Gamma_i^{(2)}(\mathbf{k}, E; \mathbf{k} + \mathbf{q}, E + \omega) = \sum_{\mathbf{q}'} |g(\mathbf{q}')|^2 \sum_{i=1}^4 \gamma_i, \quad (\text{A.43})$$

where

$$\gamma_1 = \frac{(1 - n_{\mathbf{k}+\mathbf{q}+\mathbf{q}'})(1 - n_{\mathbf{k}+\mathbf{q}'})}{(E + \omega - \xi_{\mathbf{k}+\mathbf{q}+\mathbf{q}'} - \omega_0 + i\eta)(E - \xi_{\mathbf{k}+\mathbf{q}'} - \omega_0 + i\eta)}, \quad (\text{A.44})$$

$$\gamma_2 = -\frac{(1 - n_{\mathbf{k}+\mathbf{q}+\mathbf{q}'})n_{\mathbf{k}+\mathbf{q}'}}{\omega + \xi_{\mathbf{k}+\mathbf{q}'} - \xi_{\mathbf{k}+\mathbf{q}+\mathbf{q}'} + i\eta} \left[\frac{1}{E + \omega - \xi_{\mathbf{k}+\mathbf{q}+\mathbf{q}'} - \omega_0 + i\eta} - \frac{1}{E - \xi_{\mathbf{k}+\mathbf{q}'} + \omega_0 - i\eta} \right], \quad (\text{A.45})$$

$$\gamma_3 = -\frac{(1 - n_{\mathbf{k}+\mathbf{q}'})n_{\mathbf{k}+\mathbf{q}+\mathbf{q}'}}{\omega + \xi_{\mathbf{k}+\mathbf{q}'} - \xi_{\mathbf{k}+\mathbf{q}+\mathbf{q}'} - i\eta} \left[\frac{1}{E + \omega - \xi_{\mathbf{k}+\mathbf{q}+\mathbf{q}'} + \omega_0 - i\eta} - \frac{1}{E - \xi_{\mathbf{k}+\mathbf{q}'} - \omega_0 + i\eta} \right], \quad (\text{A.46})$$

and

$$\gamma_4 = \frac{n_{\mathbf{k}+\mathbf{q}+\mathbf{q}'}n_{\mathbf{k}+\mathbf{q}'}}{(E + \omega - \xi_{\mathbf{k}+\mathbf{q}+\mathbf{q}'} + \omega_0 - i\eta)(E - \xi_{\mathbf{k}+\mathbf{q}'} + \omega_0 - i\eta)}. \quad (\text{A.47})$$

In order to get the final result for $\Sigma^{(C)}(\mathbf{k}, E)$, these four contributions should be multiplied by the two remaining ω -dependent propagators

$$D_0(\mathbf{q}, \omega)G_0(\mathbf{k} + \mathbf{q}, E + \omega) = \frac{(1 - n_{\mathbf{k}+\mathbf{q}})}{(\omega - \omega_0 + i\eta)(E + \omega - \xi_{\mathbf{k}+\mathbf{q}} + i\eta)} - \frac{n_{\mathbf{k}+\mathbf{q}}}{(\omega + \omega_0 - i\eta)(E + \omega - \xi_{\mathbf{k}+\mathbf{q}} - i\eta)} - \frac{(1 - n_{\mathbf{k}+\mathbf{q}})}{(\omega + \omega_0 - i\eta)(E + \omega - \xi_{\mathbf{k}+\mathbf{q}} + i\eta)} + \frac{n_{\mathbf{k}+\mathbf{q}}}{(\omega - \omega_0 + i\eta)(E + \omega - \xi_{\mathbf{k}+\mathbf{q}} - i\eta)}, \quad (\text{A.48})$$

and the integration over ω in the complex plane carried out, resulting in a total of eighteen contributions to the fermion self-energy coming from the crossing diagram

$$\Sigma^{(C)}(\mathbf{k}, E) = \sum_{\mathbf{q}, \mathbf{q}'} |g(\mathbf{q})|^2 |g(\mathbf{q}')|^2 \sum_{i=1}^{18} \sigma_i^{(C)}, \quad (\text{A.49})$$

with

$$\sigma_1^{(C)} = -\frac{n_{\mathbf{k}+\mathbf{q}}(1-n_{\mathbf{k}+\mathbf{q}+q'})(1-n_{\mathbf{k}+\mathbf{q}'})}{(\xi_{\mathbf{k}+\mathbf{q}}-\omega_0-\xi_{\mathbf{k}+\mathbf{q}+q'}+i\eta)(E-2\omega_0-\xi_{\mathbf{k}+\mathbf{q}+q'}+i\eta)(E-\omega_0-\xi_{\mathbf{k}+\mathbf{q}'}+i\eta)}, \quad (\text{A.50})$$

$$\sigma_2^{(C)} = \frac{(1-n_{\mathbf{k}+\mathbf{q}})(1-n_{\mathbf{k}+\mathbf{q}+q'})(1-n_{\mathbf{k}+\mathbf{q}'})}{(E-2\omega_0-\xi_{\mathbf{k}+\mathbf{q}+q'}+i\eta)(E-\omega_0-\xi_{\mathbf{k}+\mathbf{q}}+i\eta)(E-\omega_0-\xi_{\mathbf{k}+\mathbf{q}'}+i\eta)}, \quad (\text{A.51})$$

$$\sigma_3^{(C)} = \frac{n_{\mathbf{k}+\mathbf{q}}(1-n_{\mathbf{k}+\mathbf{q}+q'})(1-n_{\mathbf{k}+\mathbf{q}'})}{(\xi_{\mathbf{k}+\mathbf{q}}-\omega_0-\xi_{\mathbf{k}+\mathbf{q}+q'}+i\eta)(E-\omega_0-\xi_{\mathbf{k}+\mathbf{q}'}+i\eta)(E+\omega_0-\xi_{\mathbf{k}+\mathbf{q}}-i\eta)}, \quad (\text{A.52})$$

$$\sigma_4^{(C)} = -\frac{n_{\mathbf{k}+\mathbf{q}}(1-n_{\mathbf{k}+\mathbf{q}+q'})n_{\mathbf{k}+\mathbf{q}'}}{(\xi_{\mathbf{k}+\mathbf{q}'}-\omega_0-\xi_{\mathbf{k}+\mathbf{q}+q'}+i\eta)(E-2\omega_0-\xi_{\mathbf{k}+\mathbf{q}+q'}+i\eta)(E-\omega_0-\xi_{\mathbf{k}+\mathbf{q}})} - \frac{n_{\mathbf{k}+\mathbf{q}}(1-n_{\mathbf{k}+\mathbf{q}+q'})n_{\mathbf{k}+\mathbf{q}'}}{(\xi_{\mathbf{k}+\mathbf{q}}-\omega_0-\xi_{\mathbf{k}+\mathbf{q}+q'}+i\eta)(E-\xi_{\mathbf{k}+\mathbf{q}}-\xi_{\mathbf{k}+\mathbf{q}'}+\xi_{\mathbf{k}+\mathbf{q}+q'}-i\eta)(E-\omega_0-\xi_{\mathbf{k}+\mathbf{q}})}, \quad (\text{A.53})$$

$$\sigma_5^{(C)} = -\frac{(1-n_{\mathbf{k}+\mathbf{q}})(1-n_{\mathbf{k}+\mathbf{q}+q'})n_{\mathbf{k}+\mathbf{q}'}}{(\xi_{\mathbf{k}+\mathbf{q}'}-\omega_0-\xi_{\mathbf{k}+\mathbf{q}+q'}+i\eta)(E-2\omega_0-\xi_{\mathbf{k}+\mathbf{q}+q'}+i\eta)(E-\omega_0-\xi_{\mathbf{k}+\mathbf{q}}+i\eta)}, \quad (\text{A.54})$$

$$\sigma_6^{(C)} = \frac{n_{\mathbf{k}+\mathbf{q}}(1-n_{\mathbf{k}+\mathbf{q}+q'})n_{\mathbf{k}+\mathbf{q}'}}{(\xi_{\mathbf{k}+\mathbf{q}}-\omega_0-\xi_{\mathbf{k}+\mathbf{q}+q'}+i\eta)(E-\xi_{\mathbf{k}+\mathbf{q}}-\xi_{\mathbf{k}+\mathbf{q}'}+\xi_{\mathbf{k}+\mathbf{q}+q'}-i\eta)(E+\omega_0-\xi_{\mathbf{k}+\mathbf{q}}-i\eta)}, \quad (\text{A.55})$$

$$\sigma_7^{(C)} = \frac{n_{\mathbf{k}+\mathbf{q}}(1-n_{\mathbf{k}+\mathbf{q}+q'})n_{\mathbf{k}+\mathbf{q}'}}{(\xi_{\mathbf{k}+\mathbf{q}'}-\omega_0-\xi_{\mathbf{k}+\mathbf{q}+q'}+i\eta)(E-\xi_{\mathbf{k}+\mathbf{q}}-\xi_{\mathbf{k}+\mathbf{q}'}+\xi_{\mathbf{k}+\mathbf{q}+q'}-i\eta)(E+\omega_0-\xi_{\mathbf{k}+\mathbf{q}'}-i\eta)}, \quad (\text{A.56})$$

$$\sigma_8^{(C)} = \frac{(1-n_{\mathbf{k}+\mathbf{q}})(1-n_{\mathbf{k}+\mathbf{q}+q'})n_{\mathbf{k}+\mathbf{q}'}}{(\xi_{\mathbf{k}+\mathbf{q}'}-\omega_0-\xi_{\mathbf{k}+\mathbf{q}+q'}+i\eta)(E-\omega_0-\xi_{\mathbf{k}+\mathbf{q}}+i\eta)(E+\omega_0-\xi_{\mathbf{k}+\mathbf{q}'}-i\eta)}, \quad (\text{A.57})$$

$$\sigma_9^{(C)} = -\frac{n_{\mathbf{k}+\mathbf{q}}(1-n_{\mathbf{k}+\mathbf{q}+q'})n_{\mathbf{k}+\mathbf{q}'}}{(E-\xi_{\mathbf{k}+\mathbf{q}}-\xi_{\mathbf{k}+\mathbf{q}'}+\xi_{\mathbf{k}+\mathbf{q}+q'}-i\eta)(E+\omega_0-\xi_{\mathbf{k}+\mathbf{q}}-i\eta)(E+\omega_0-\xi_{\mathbf{k}+\mathbf{q}'}-i\eta)}, \quad (\text{A.58})$$

$$\sigma_{10}^{(C)} = -\frac{(1-n_{\mathbf{k}+\mathbf{q}})n_{\mathbf{k}+\mathbf{q}+\mathbf{q}'}(1-n_{\mathbf{k}+\mathbf{q}'})}{(\xi_{\mathbf{k}+\mathbf{q}'}+\omega_0-\xi_{\mathbf{k}+\mathbf{q}+\mathbf{q}'}-i\eta)(E+2\omega_0-\xi_{\mathbf{k}+\mathbf{q}+\mathbf{q}'}-i\eta)(E+\omega_0-\xi_{\mathbf{k}+\mathbf{q}})} - \frac{(1-n_{\mathbf{k}+\mathbf{q}})n_{\mathbf{k}+\mathbf{q}+\mathbf{q}'}(1-n_{\mathbf{k}+\mathbf{q}'})}{(\xi_{\mathbf{k}+\mathbf{q}}+\omega_0-\xi_{\mathbf{k}+\mathbf{q}+\mathbf{q}'}-i\eta)(E-\xi_{\mathbf{k}+\mathbf{q}}-\xi_{\mathbf{k}+\mathbf{q}'}+\xi_{\mathbf{k}+\mathbf{q}+\mathbf{q}'}+i\eta)(E+\omega_0-\xi_{\mathbf{k}+\mathbf{q}})}, \quad (\text{A.59})$$

$$\sigma_{11}^{(C)} = \frac{(1-n_{\mathbf{k}+\mathbf{q}})n_{\mathbf{k}+\mathbf{q}+\mathbf{q}'}(1-n_{\mathbf{k}+\mathbf{q}'})}{(\xi_{\mathbf{k}+\mathbf{q}}+\omega_0-\xi_{\mathbf{k}+\mathbf{q}+\mathbf{q}'}-i\eta)(E-\xi_{\mathbf{k}+\mathbf{q}}-\xi_{\mathbf{k}+\mathbf{q}'}+\xi_{\mathbf{k}+\mathbf{q}+\mathbf{q}'}+i\eta)(E-\omega_0-\xi_{\mathbf{k}+\mathbf{q}}+i\eta)}, \quad (\text{A.60})$$

$$\sigma_{12}^{(C)} = -\frac{n_{\mathbf{k}+\mathbf{q}}n_{\mathbf{k}+\mathbf{q}+\mathbf{q}'}(1-n_{\mathbf{k}+\mathbf{q}'})}{(\xi_{\mathbf{k}+\mathbf{q}'}+\omega_0-\xi_{\mathbf{k}+\mathbf{q}+\mathbf{q}'}-i\eta)(E+2\omega_0-\xi_{\mathbf{k}+\mathbf{q}+\mathbf{q}'}-i\eta)(E+\omega_0-\xi_{\mathbf{k}+\mathbf{q}}-i\eta)}, \quad (\text{A.61})$$

$$\sigma_{13}^{(C)} = \frac{(1-n_{\mathbf{k}+\mathbf{q}})n_{\mathbf{k}+\mathbf{q}+\mathbf{q}'}(1-n_{\mathbf{k}+\mathbf{q}'})}{(\xi_{\mathbf{k}+\mathbf{q}'}+\omega_0-\xi_{\mathbf{k}+\mathbf{q}+\mathbf{q}'}-i\eta)(E-\xi_{\mathbf{k}+\mathbf{q}}-\xi_{\mathbf{k}+\mathbf{q}'}+\xi_{\mathbf{k}+\mathbf{q}+\mathbf{q}'}+i\eta)(E-\omega_0-\xi_{\mathbf{k}+\mathbf{q}'}+i\eta)}, \quad (\text{A.62})$$

$$\sigma_{14}^{(C)} = -\frac{(1-n_{\mathbf{k}+\mathbf{q}})n_{\mathbf{k}+\mathbf{q}+\mathbf{q}'}(1-n_{\mathbf{k}+\mathbf{q}'})}{(E-\xi_{\mathbf{k}+\mathbf{q}}-\xi_{\mathbf{k}+\mathbf{q}'}+\xi_{\mathbf{k}+\mathbf{q}+\mathbf{q}'}+i\eta)(E-\omega_0-\xi_{\mathbf{k}+\mathbf{q}}+i\eta)(E-\omega_0-\xi_{\mathbf{k}+\mathbf{q}'}+i\eta)}, \quad (\text{A.63})$$

$$\sigma_{15}^{(C)} = \frac{n_{\mathbf{k}+\mathbf{q}}n_{\mathbf{k}+\mathbf{q}+\mathbf{q}'}(1-n_{\mathbf{k}+\mathbf{q}'})}{(\xi_{\mathbf{k}+\mathbf{q}'}+\omega_0-\xi_{\mathbf{k}+\mathbf{q}+\mathbf{q}'}-i\eta)(E-\omega_0-\xi_{\mathbf{k}+\mathbf{q}'}+i\eta)(E+\omega_0-\xi_{\mathbf{k}+\mathbf{q}}-i\eta)}, \quad (\text{A.64})$$

$$\sigma_{16}^{(C)} = -\frac{(1-n_{\mathbf{k}+\mathbf{q}})n_{\mathbf{k}+\mathbf{q}+\mathbf{q}'}n_{\mathbf{k}+\mathbf{q}'}}{(\xi_{\mathbf{k}+\mathbf{q}}+\omega_0-\xi_{\mathbf{k}+\mathbf{q}+\mathbf{q}'}-i\eta)(E+2\omega_0-\xi_{\mathbf{k}+\mathbf{q}+\mathbf{q}'}-i\eta)(E+\omega_0-\xi_{\mathbf{k}+\mathbf{q}'}-i\eta)}, \quad (\text{A.65})$$

$$\sigma_{17}^{(C)} = \frac{(1-n_{\mathbf{k}+\mathbf{q}})n_{\mathbf{k}+\mathbf{q}+\mathbf{q}'}n_{\mathbf{k}+\mathbf{q}'}}{(\xi_{\mathbf{k}+\mathbf{q}}+\omega_0-\xi_{\mathbf{k}+\mathbf{q}+\mathbf{q}'}-i\eta)(E-\omega_0-\xi_{\mathbf{k}+\mathbf{q}}+i\eta)(E+\omega_0-\xi_{\mathbf{k}+\mathbf{q}'}-i\eta)}, \quad (\text{A.66})$$

and

$$\sigma_{18}^{(C)} = \frac{n_{\mathbf{k}+\mathbf{q}} n_{\mathbf{k}+\mathbf{q}+\mathbf{q}'} n_{\mathbf{k}+\mathbf{q}'}}{(E + 2\omega_0 - \xi_{\mathbf{k}+\mathbf{q}+\mathbf{q}'} - i\eta)(E + \omega_0 - \xi_{\mathbf{k}+\mathbf{q}'} - i\eta)(E + \omega_0 - \xi_{\mathbf{k}+\mathbf{q}} - i\eta)}. \quad (\text{A.67})$$

A.2.3 Bubble diagram

Lastly, for the fermion self-energy stemming from the diagram in Fig. 8.4 involving the renormalization of the phonon, we can write

$$\begin{aligned} \Sigma^{(B)}(\mathbf{k}, E) &= -i^2 \sum_{\mathbf{q}, \mathbf{q}'} |g(\mathbf{q})|^4 \int_{-\infty}^{\infty} \frac{d\omega}{2\pi} [D_0(\mathbf{q}, \omega)]^2 G_0(\mathbf{k} + \mathbf{q}, E + \omega) \times \\ &\quad \times \int_{-\infty}^{\infty} \frac{d\omega'}{2\pi} G_0(\mathbf{q}', \omega') G_0(\mathbf{q} + \mathbf{q}', \omega + \omega') \\ &= -i^2 \sum_{\mathbf{q}} |g(\mathbf{q})|^4 \int_{-\infty}^{\infty} \frac{d\omega}{2\pi} [D_0(\mathbf{q}, \omega)]^2 G_0(\mathbf{k} + \mathbf{q}, E + \omega) \chi_0(\mathbf{q}, \omega), \end{aligned} \quad (\text{A.68})$$

where we have exploited the expression for the Lindhard function

$$\begin{aligned} \chi_0(\mathbf{q}, \omega) &= \sum_{\mathbf{q}'} \int_{-\infty}^{\infty} \frac{d\omega'}{2\pi} G^{(0)}(\mathbf{q}', \omega') G^{(0)}(\mathbf{q} + \mathbf{q}', \omega + \omega') \\ &= \sum_{\mathbf{q}'} i \left[\frac{n_{\mathbf{q}'}(1 - n_{\mathbf{q}+\mathbf{q}'})}{\omega + \xi_{\mathbf{q}'} - \xi_{\mathbf{q}+\mathbf{q}'} + i\eta} - \frac{(1 - n_{\mathbf{q}'})n_{\mathbf{q}+\mathbf{q}'}}{\omega + \xi_{\mathbf{q}'} - \xi_{\mathbf{q}+\mathbf{q}'} - i\eta} \right]. \end{aligned} \quad (\text{A.69})$$

The product of $\chi_0(\mathbf{q}, \omega)$ with the rest of ω -dependent propagators reads

$$\begin{aligned} [D_0(\mathbf{q}, \omega)]^2 G_0(\mathbf{k} + \mathbf{q}, E + \omega) \chi_0(\mathbf{q}, \omega) &= \sum_{\mathbf{q}'} i \left[\frac{1}{\omega - \omega_0 + i\eta} \frac{1}{\omega - \omega_0 + i\eta} - \right. \\ &\quad \left. - \frac{1}{\omega + \omega_0 - i\eta} \frac{1}{\omega - \omega_0 + i\eta} - \frac{1}{\omega + \omega_0 - i\eta} \frac{1}{\omega - \omega_0 + i\eta} + \frac{1}{\omega + \omega_0 - i\eta} \frac{1}{\omega + \omega_0 - i\eta} \right] \times \\ &\quad \times \left[\frac{(1 - n_{\mathbf{k}+\mathbf{q}})}{E + \omega - \xi_{\mathbf{k}+\mathbf{q}} + i\eta} \frac{n_{\mathbf{q}'}(1 - n_{\mathbf{q}+\mathbf{q}'})}{\omega + \xi_{\mathbf{q}'} - \xi_{\mathbf{q}+\mathbf{q}'} + i\eta} + \frac{n_{\mathbf{k}+\mathbf{q}}}{E + \omega - \xi_{\mathbf{k}+\mathbf{q}} - i\eta} \frac{n_{\mathbf{q}'}(1 - n_{\mathbf{q}+\mathbf{q}'})}{\omega + \xi_{\mathbf{q}'} - \xi_{\mathbf{q}+\mathbf{q}'} + i\eta} - \right. \\ &\quad \left. - \frac{(1 - n_{\mathbf{q}'})n_{\mathbf{q}+\mathbf{q}'}}{\omega + \xi_{\mathbf{q}'} - \xi_{\mathbf{q}+\mathbf{q}'} - i\eta} \frac{(1 - n_{\mathbf{k}+\mathbf{q}})}{E + \omega - \xi_{\mathbf{k}+\mathbf{q}} + i\eta} - \frac{(1 - n_{\mathbf{q}'})n_{\mathbf{q}+\mathbf{q}'}}{\omega + \xi_{\mathbf{q}'} - \xi_{\mathbf{q}+\mathbf{q}'} - i\eta} \frac{n_{\mathbf{k}+\mathbf{q}}}{E + \omega - \xi_{\mathbf{k}+\mathbf{q}} - i\eta} \right], \end{aligned} \quad (\text{A.70})$$

which after the integration over ω in the complex plane yields fourteen contributions to $\Sigma^{(B)}(\mathbf{k}, E)$

$$\Sigma^{(B)}(\mathbf{k}, E) = \sum_{\mathbf{q}, \mathbf{q}'} |g(\mathbf{q})|^4 \sum_{i=1}^{14} \sigma_i^{(B)}, \quad (\text{A.71})$$

with

$$\sigma_1^{(B)} = \frac{n_{\mathbf{k}+\mathbf{q}}(1-n_{\mathbf{q}+\mathbf{q}'}n_{\mathbf{q}'})}{(E-\xi_{\mathbf{k}+\mathbf{q}}+\omega_0-i\eta)^2(E-\xi_{\mathbf{k}+\mathbf{q}}-\xi_{\mathbf{q}'}+\xi_{\mathbf{q}+\mathbf{q}'}-i\eta)}, \quad (\text{A.72})$$

$$\sigma_2^{(B)} = \frac{(1-n_{\mathbf{k}+\mathbf{q}})n_{\mathbf{q}+\mathbf{q}'}(1-n_{\mathbf{q}'})}{(\xi_{\mathbf{q}+\mathbf{q}'}-\xi_{\mathbf{q}'}-\omega_0+i\eta)^2(E-\xi_{\mathbf{k}+\mathbf{q}}-\xi_{\mathbf{q}'}+\xi_{\mathbf{q}+\mathbf{q}'}+i\eta)}, \quad (\text{A.73})$$

$$\sigma_3^{(B)} = \frac{n_{\mathbf{k}+\mathbf{q}}n_{\mathbf{q}+\mathbf{q}'}(1-n_{\mathbf{q}'})}{(\xi_{\mathbf{q}+\mathbf{q}'}-\xi_{\mathbf{q}'}-\omega_0+i\eta)^2(E-\xi_{\mathbf{k}+\mathbf{q}}-\xi_{\mathbf{q}'}+\xi_{\mathbf{q}+\mathbf{q}'}-)} - \frac{n_{\mathbf{k}+\mathbf{q}}n_{\mathbf{q}+\mathbf{q}'}(1-n_{\mathbf{q}'})}{(E-\xi_{\mathbf{k}+\mathbf{q}}+\omega_0-i\eta)^2(E-\xi_{\mathbf{k}+\mathbf{q}}-\xi_{\mathbf{q}'}+\xi_{\mathbf{q}+\mathbf{q}'}-)}, \quad (\text{A.74})$$

$$\sigma_4^{(B)} = -\frac{(1-n_{\mathbf{k}+\mathbf{q}})(1-n_{\mathbf{q}+\mathbf{q}'}n_{\mathbf{q}'})}{(2\omega_0-i\eta)(E-\xi_{\mathbf{k}+\mathbf{q}}-\omega_0+i\eta)(\xi_{\mathbf{q}'}-\xi_{\mathbf{q}+\mathbf{q}'}-\omega_0+i\eta)}, \quad (\text{A.75})$$

$$\sigma_5^{(B)} = -\frac{n_{\mathbf{k}+\mathbf{q}}(1-n_{\mathbf{q}+\mathbf{q}'}n_{\mathbf{q}'})}{(2\omega_0-i\eta)(E-\xi_{\mathbf{k}+\mathbf{q}}-\omega_0)(\xi_{\mathbf{q}'}-\xi_{\mathbf{q}+\mathbf{q}'}-\omega_0+i\eta)} - \frac{n_{\mathbf{k}+\mathbf{q}}(1-n_{\mathbf{q}+\mathbf{q}'}n_{\mathbf{q}'})}{(E-\xi_{\mathbf{k}+\mathbf{q}}-\omega_0)(E-\xi_{\mathbf{k}+\mathbf{q}}+\omega_0-i\eta)(E-\xi_{\mathbf{k}+\mathbf{q}}-\xi_{\mathbf{q}'}+\xi_{\mathbf{q}+\mathbf{q}'}-i\eta)}, \quad (\text{A.76})$$

$$\sigma_6^{(B)} = \frac{(1-n_{\mathbf{k}+\mathbf{q}})n_{\mathbf{q}+\mathbf{q}'}(1-n_{\mathbf{q}'})}{(2\omega_0-i\eta)(E-\xi_{\mathbf{k}+\mathbf{q}}-\omega_0+i\eta)(\xi_{\mathbf{q}'}-\xi_{\mathbf{q}+\mathbf{q}'}-\omega_0)} - \frac{(1-n_{\mathbf{k}+\mathbf{q}})n_{\mathbf{q}+\mathbf{q}'}(1-n_{\mathbf{q}'})}{(\xi_{\mathbf{q}+\mathbf{q}'}-\xi_{\mathbf{q}'}+\omega_0)(\xi_{\mathbf{q}+\mathbf{q}'}-\xi_{\mathbf{q}'}-\omega_0+i\eta)(E-\xi_{\mathbf{k}+\mathbf{q}}-\xi_{\mathbf{q}'}+\xi_{\mathbf{q}+\mathbf{q}'}+i\eta)}, \quad (\text{A.77})$$

$$\sigma_7^{(B)} = \frac{n_{\mathbf{k}+\mathbf{q}}n_{\mathbf{q}+\mathbf{q}'}(1-n_{\mathbf{q}'})}{(2\omega_0-i\eta)(E-\xi_{\mathbf{k}+\mathbf{q}}+\omega_0-i\eta)(\xi_{\mathbf{q}'}-\xi_{\mathbf{q}+\mathbf{q}'}+\omega_0-i\eta)}, \quad (\text{A.78})$$

$$\sigma_8^{(B)} = -\frac{(1 - n_{\mathbf{k}+\mathbf{q}})(1 - n_{\mathbf{q}+\mathbf{q}'})n_{\mathbf{q}'}}{(2\omega_0 - i\eta)(E - \xi_{\mathbf{k}+\mathbf{q}} - \omega_0 + i\eta)(\xi_{\mathbf{q}'} - \xi_{\mathbf{q}+\mathbf{q}'} - \omega_0 + i\eta)}, \quad (\text{A.79})$$

$$\begin{aligned} \sigma_9^{(B)} = & -\frac{n_{\mathbf{k}+\mathbf{q}}(1 - n_{\mathbf{q}+\mathbf{q}'})n_{\mathbf{q}'}}{(2\omega_0 - i\eta)(E - \xi_{\mathbf{k}+\mathbf{q}} - \omega_0)(\xi_{\mathbf{q}'} - \xi_{\mathbf{q}+\mathbf{q}'} - \omega_0 + i\eta)} - \\ & -\frac{n_{\mathbf{k}+\mathbf{q}}(1 - n_{\mathbf{q}+\mathbf{q}'})n_{\mathbf{q}'}}{(E - \xi_{\mathbf{k}+\mathbf{q}} - \omega_0)(E - \xi_{\mathbf{k}+\mathbf{q}} + \omega_0 - i\eta)(E - \xi_{\mathbf{k}+\mathbf{q}} - \xi_{\mathbf{q}'} + \xi_{\mathbf{q}+\mathbf{q}'} - i\eta)}, \end{aligned} \quad (\text{A.80})$$

$$\begin{aligned} \sigma_{10}^{(B)} = & \frac{(1 - n_{\mathbf{k}+\mathbf{q}})n_{\mathbf{q}+\mathbf{q}'}(1 - n_{\mathbf{q}'})}{(2\omega_0 - i\eta)(E - \xi_{\mathbf{k}+\mathbf{q}} - \omega_0 + i\eta)(\xi_{\mathbf{q}'} - \xi_{\mathbf{q}+\mathbf{q}'} - \omega_0)} - \\ & -\frac{(1 - n_{\mathbf{k}+\mathbf{q}})n_{\mathbf{q}+\mathbf{q}'}(1 - n_{\mathbf{q}'})}{(\xi_{\mathbf{q}+\mathbf{q}'} - \xi_{\mathbf{q}'} + \omega_0)(\xi_{\mathbf{q}+\mathbf{q}'} - \xi_{\mathbf{q}'} - \omega_0 + i\eta)(E - \xi_{\mathbf{k}+\mathbf{q}} - \xi_{\mathbf{q}'} + \xi_{\mathbf{q}+\mathbf{q}'} + i\eta)}, \end{aligned} \quad (\text{A.81})$$

$$\sigma_{11}^{(B)} = \frac{n_{\mathbf{k}+\mathbf{q}}n_{\mathbf{q}+\mathbf{q}'}(1 - n_{\mathbf{q}'})}{(2\omega_0 - i\eta)(E - \xi_{\mathbf{k}+\mathbf{q}} + \omega_0 - i\eta)(\xi_{\mathbf{q}'} - \xi_{\mathbf{q}+\mathbf{q}'} + \omega_0 - i\eta)}, \quad (\text{A.82})$$

$$\begin{aligned} \sigma_{12}^{(B)} = & -\frac{(1 - n_{\mathbf{k}+\mathbf{q}})(1 - n_{\mathbf{q}+\mathbf{q}'})n_{\mathbf{q}'}}{(E - \xi_{\mathbf{k}+\mathbf{q}} - \omega_0 + i\eta)^2(E - \xi_{\mathbf{k}+\mathbf{q}} - \xi_{\mathbf{q}'} + \xi_{\mathbf{q}+\mathbf{q}'})} + \\ & +\frac{(1 - n_{\mathbf{k}+\mathbf{q}})(1 - n_{\mathbf{q}+\mathbf{q}'})n_{\mathbf{q}'}}{(\xi_{\mathbf{q}+\mathbf{q}'} - \xi_{\mathbf{q}'} + \omega_0 - i\eta)^2(E - \xi_{\mathbf{k}+\mathbf{q}} - \xi_{\mathbf{q}'} + \xi_{\mathbf{q}+\mathbf{q}'})}, \end{aligned} \quad (\text{A.83})$$

$$\sigma_{13}^{(B)} = \frac{n_{\mathbf{k}+\mathbf{q}}(1 - n_{\mathbf{q}+\mathbf{q}'})n_{\mathbf{q}'}}{(\xi_{\mathbf{q}+\mathbf{q}'} - \xi_{\mathbf{q}'} + \omega_0 - i\eta)^2(E - \xi_{\mathbf{k}+\mathbf{q}} - \xi_{\mathbf{q}'} + \xi_{\mathbf{q}+\mathbf{q}'} - i\eta)}, \quad (\text{A.84})$$

and

$$\sigma_{14}^{(B)} = \frac{(1 - n_{\mathbf{k}+\mathbf{q}})n_{\mathbf{q}+\mathbf{q}'}(1 - n_{\mathbf{q}'})}{(E - \xi_{\mathbf{k}+\mathbf{q}} - \omega_0 + i\eta)^2(E - \xi_{\mathbf{k}+\mathbf{q}} - \xi_{\mathbf{q}'} + \xi_{\mathbf{q}+\mathbf{q}'} + i\eta)}. \quad (\text{A.85})$$

By taking a closer look at Eqs. (A.72), (A.76), (A.80), and (A.84), we note that $\text{Im}\Sigma^{(B)}(\mathbf{k}, E)$ attains non-vanishing values around the Fermi level for $E < 0$. In particular, in the corresponding energy window, we have

$$\begin{aligned}
\text{Im}\Sigma^{(B)}(\mathbf{k}, E) &= \pi \sum_{\mathbf{q}, \mathbf{q}'} |g(\mathbf{q})|^4 \left[\frac{1}{(\xi_{\mathbf{q}'} - \xi_{\mathbf{q}+\mathbf{q}'} + \omega_0)^2} - \frac{2}{(\xi_{\mathbf{q}'} - \xi_{\mathbf{q}+\mathbf{q}'} - \omega_0)(\xi_{\mathbf{q}'} - \xi_{\mathbf{q}+\mathbf{q}'} + \omega_0)} + \right. \\
&\quad \left. + \frac{1}{(\xi_{\mathbf{q}'} - \xi_{\mathbf{q}+\mathbf{q}'} - \omega_0)^2} \right] n_{\mathbf{k}+\mathbf{q}}(1 - n_{\mathbf{q}+\mathbf{q}'}) n_{\mathbf{q}'} \delta(E - \xi_{\mathbf{k}+\mathbf{q}} - \xi_{\mathbf{q}'} + \xi_{\mathbf{q}+\mathbf{q}'}) \\
&= \pi \sum_{\mathbf{q}, \mathbf{q}'} |g(\mathbf{q})|^4 \left[\frac{(\xi_{\mathbf{q}'} - \xi_{\mathbf{q}+\mathbf{q}'} - \omega_0)^2 - 2(\xi_{\mathbf{q}'} - \xi_{\mathbf{q}+\mathbf{q}'} - \omega_0)(\xi_{\mathbf{q}'} - \xi_{\mathbf{q}+\mathbf{q}'} + \omega_0) + (\xi_{\mathbf{q}'} - \xi_{\mathbf{q}+\mathbf{q}'} + \omega_0)^2}{(\xi_{\mathbf{q}'} - \xi_{\mathbf{q}+\mathbf{q}'} - \omega_0)^2 (\xi_{\mathbf{q}'} - \xi_{\mathbf{q}+\mathbf{q}'} + \omega_0)^2} \right] \times \\
&\quad \times n_{\mathbf{k}+\mathbf{q}}(1 - n_{\mathbf{q}+\mathbf{q}'}) n_{\mathbf{q}'} \delta(E - \xi_{\mathbf{k}+\mathbf{q}} - \xi_{\mathbf{q}'} + \xi_{\mathbf{q}+\mathbf{q}'}) \\
&= \pi \sum_{\mathbf{q}, \mathbf{q}'} |g(\mathbf{q})|^4 \frac{4\omega_0^2}{\left[(\xi_{\mathbf{q}'} - \xi_{\mathbf{q}+\mathbf{q}'} - \omega_0)^2 - \omega_0^2 \right]^2} n_{\mathbf{k}+\mathbf{q}}(1 - n_{\mathbf{q}+\mathbf{q}'}) n_{\mathbf{q}'} \delta(E - \xi_{\mathbf{k}+\mathbf{q}} - \xi_{\mathbf{q}'} + \xi_{\mathbf{q}+\mathbf{q}'}) \\
&= \pi \sum_{\mathbf{q}, \mathbf{q}'} |g(\mathbf{q})|^4 \frac{4\omega_0^2}{\left[(\xi_{\mathbf{k}+\mathbf{q}'} - \xi_{\mathbf{k}+\mathbf{q}+\mathbf{q}'} - \omega_0)^2 - \omega_0^2 \right]^2} n_{\mathbf{k}+\mathbf{q}}(1 - n_{\mathbf{k}+\mathbf{q}+\mathbf{q}'}) n_{\mathbf{k}+\mathbf{q}'} \delta(E - \xi_{\mathbf{k}+\mathbf{q}} - \xi_{\mathbf{k}+\mathbf{q}'} + \xi_{\mathbf{k}+\mathbf{q}+\mathbf{q}'}).
\end{aligned} \tag{A.86}$$

A.2.4 Polaron limit

The results for the next-to-leading electron self-energy contributions in the polaron limit may be obtained by simply setting $n_{\mathbf{k}} = 0$ in Eqs. (A.34) and (A.49). However, for the purposes of Part II, we need only the next-to-leading electron self-energy contributions in the 1D case with the Holstein coupling in the energy window below the phonon energy, which were already calculated in [102]. Therefore, we exploit the results from [102] and bring them into a convenient form suitable for our purposes.

Non-crossing diagram

Following [102], the contribution to the electron self-energy coming from the non-crossing diagram in the polaron limit in the 1D case with the Holstein coupling below the phonon energy reads

$$\Sigma^{(NC)}(E < \omega_0) = \frac{g^4}{(2t)^3} I'(\varepsilon) I(\varepsilon + \alpha). \tag{A.87}$$

Here, $\varepsilon = \frac{\omega_0 - E}{2t}$, $\alpha = \frac{\omega_0}{2t}$, and $I(\varepsilon) = \frac{1}{2t\sqrt{\varepsilon(\varepsilon+2t)}}$, yielding simply

$$\Sigma^{(NC)}(E < \omega_0) = -g^4 \frac{1}{(E - \omega_0)^{\frac{3}{2}} (E - \omega_0 - 4t)^{\frac{3}{2}} (E - 2\omega_0)^{\frac{1}{2}} (E - 2\omega_0 - 4t)^{\frac{1}{2}}}. \tag{A.88}$$

Crossing diagram

On the other hand, adapting the required expression for the electron self-energy due to the crossing diagram requires more work, since from [102] we have

$$\Sigma^{(C)}(k, E < \omega_0) = -\frac{g^4}{t^3} \frac{x_+^2 y_+ - x_-^2 y_-}{(x_+ - x_-)^2 (y_+ - y_-)} \frac{1}{x_+^2 y_+ + x_-^2 y_- - 2 \cos k}, \quad (\text{A.89})$$

where

$$x_{\pm} = \gamma_1 \pm \sqrt{\gamma_1^2 - 1}, \quad y_{\pm} = \gamma_2 \pm \sqrt{\gamma_2^2 - 1}, \quad \gamma_n = 1 + n\alpha - E/2t > 1, \quad x_+ x_- = y_+ y_- = 1. \quad (\text{A.90})$$

We evaluate

$$x_+^2 = \gamma_1^2 + 2\gamma_1 \sqrt{\gamma_1^2 - 1} + \gamma_1^2 - 1 = 2\gamma_1 \left(\gamma_1 + \sqrt{\gamma_1^2 - 1} \right) - 1 = 2\gamma_1 x_+ - 1, \quad (\text{A.91})$$

$$x_-^2 = \gamma_1^2 - 2\gamma_1 \sqrt{\gamma_1^2 - 1} + \gamma_1^2 - 1 = 2\gamma_1 \left(\gamma_1 - \sqrt{\gamma_1^2 - 1} \right) - 1 = 2\gamma_1 x_- - 1, \quad (\text{A.92})$$

yielding

$$x_+^2 y_+ \pm x_-^2 y_- = 2\gamma_1 x_+ y_+ - y_+ \pm 2\gamma_1 x_- y_- \mp y_- = 2\gamma_1 (x_+ y_+ \pm x_- y_-) - (y_+ \pm y_-). \quad (\text{A.93})$$

Moreover

$$x_+ - x_- = 2\sqrt{\gamma_1^2 - 1}, \quad y_+ + y_- = 2\gamma_2, \quad y_+ - y_- = 2\sqrt{\gamma_2^2 - 1}, \quad (\text{A.94})$$

$$\begin{aligned} x_+ y_+ + x_- y_- &= \left(\gamma_1 + \sqrt{\gamma_1^2 - 1} \right) \left(\gamma_2 + \sqrt{\gamma_2^2 - 1} \right) + \left(\gamma_1 - \sqrt{\gamma_1^2 - 1} \right) \left(\gamma_2 - \sqrt{\gamma_2^2 - 1} \right) \\ &= \gamma_1 \gamma_2 + \gamma_1 \sqrt{\gamma_2^2 - 1} + \gamma_2 \sqrt{\gamma_1^2 - 1} + \sqrt{\gamma_1^2 - 1} \sqrt{\gamma_2^2 - 1} \\ &\quad + \gamma_1 \gamma_2 - \gamma_1 \sqrt{\gamma_2^2 - 1} - \gamma_2 \sqrt{\gamma_1^2 - 1} + \sqrt{\gamma_1^2 - 1} \sqrt{\gamma_2^2 - 1} \\ &= 2 \left(\gamma_1 \gamma_2 + \sqrt{\gamma_1^2 - 1} \sqrt{\gamma_2^2 - 1} \right), \end{aligned} \quad (\text{A.95})$$

$$\begin{aligned}
x_+y_+ - x_-y_- &= \left(\gamma_1 + \sqrt{\gamma_1^2 - 1} \right) \left(\gamma_2 + \sqrt{\gamma_2^2 - 1} \right) - \left(\gamma_1 - \sqrt{\gamma_1^2 - 1} \right) \left(\gamma_2 - \sqrt{\gamma_2^2 - 1} \right) \\
&= \gamma_1\gamma_2 + \gamma_1\sqrt{\gamma_2^2 - 1} + \gamma_2\sqrt{\gamma_1^2 - 1} + \sqrt{\gamma_1^2 - 1}\sqrt{\gamma_2^2 - 1} \\
&\quad - \gamma_1\gamma_2 + \gamma_1\sqrt{\gamma_2^2 - 1} + \gamma_2\sqrt{\gamma_1^2 - 1} - \sqrt{\gamma_1^2 - 1}\sqrt{\gamma_2^2 - 1} \\
&= 2 \left(\gamma_1\sqrt{\gamma_2^2 - 1} + \gamma_2\sqrt{\gamma_1^2 - 1} \right),
\end{aligned} \tag{A.96}$$

and

$$\begin{aligned}
x_+^2y_+ - x_-^2y_- &= 2\gamma_1(x_+y_+ - x_-y_-) - (y_+ - y_-) \\
&= 4\gamma_1 \left(\gamma_1\sqrt{\gamma_2^2 - 1} + \gamma_2\sqrt{\gamma_1^2 - 1} \right) - 2\sqrt{\gamma_2^2 - 1} \\
&= 2 \left[(2\gamma_1^2 - 1) \sqrt{\gamma_2^2 - 1} + 2\gamma_1\gamma_2\sqrt{\gamma_1^2 - 1} \right].
\end{aligned} \tag{A.97}$$

By combining all the above results, we get

$$\begin{aligned}
x_+^2y_+ + x_-^2y_- &= 2\gamma_1(x_+y_+ + x_-y_-) - (y_+ + y_-) = 4 \left(\gamma_1^2\gamma_2 + \gamma_1\sqrt{\gamma_1^2 - 1}\sqrt{\gamma_2^2 - 1} \right) - 2\gamma_2 \\
&= 2 \left[\gamma_2 (2\gamma_1^2 - 1) + 2\gamma_1\sqrt{\gamma_1^2 - 1}\sqrt{\gamma_2^2 - 1} \right] \\
&= 2(1 + \omega_0/t - E/2t) \left[2(1 + \omega_0/2t - E/2t)^2 - 1 \right] + \\
&\quad + 4(1 + \omega_0/2t - E/2t) \sqrt{(2 + \omega_0/2t - E/2t)(\omega_0/2t - E/2t)(2 + \omega_0/t - E/2t)(\omega_0/t - E/2t)} \\
&= \frac{1}{2t^3} (2t + 2\omega_0 - E) \left[(2t + \omega_0 - E)^2 - 2t^2 \right] + \\
&\quad + \frac{1}{2t^3} (2t + \omega_0 - E) \sqrt{(4t + \omega_0 - E)(\omega_0 - E)(4t + 2\omega_0 - E)(2\omega_0 - E)},
\end{aligned} \tag{A.98}$$

and

$$\begin{aligned}
\frac{x_+^2 y_+ - x_-^2 y_-}{(x_+ - x_-)^2 (y_+ - y_-)} &= \frac{2 \left[(2\gamma_1^2 - 1) \sqrt{\gamma_2^2 - 1} + 2\gamma_1 \gamma_2 \sqrt{\gamma_1^2 - 1} \right]}{8 (\gamma_1^2 - 1) \sqrt{\gamma_2^2 - 1}} \\
&= \frac{1}{4} \left[\frac{2\gamma_1^2 - 1}{\gamma_1^2 - 1} + \frac{2\gamma_1 \gamma_2}{\sqrt{\gamma_1^2 - 1} \sqrt{\gamma_2^2 - 1}} \right] = \frac{1}{4} \left[\frac{2(1 + \omega_0/2t - E/2t)^2 - 1}{(\omega_0/2t - E/2t)(2 + \omega_0/2t - E/2t)} + \right. \\
&\quad \left. + \frac{2(1 + \omega_0/2t - E/2t)(1 + \omega_0/t - E/2t)}{\sqrt{(2 + \omega_0/2t - E/2t)(\omega_0/2t - E/2t)(2 + \omega_0/t - E/2t)(\omega_0/t - E/2t)}} \right] \\
&= \frac{1}{2} \left[\frac{(2t + \omega_0 - E)^2 - 2t^2}{(\omega_0 - E)(4t + \omega_0 - E)} + \frac{(2t + \omega_0 - E)(2t + 2\omega_0 - E)}{\sqrt{(4t + \omega_0 - E)(\omega_0 - E)(4t + 2\omega_0 - E)(2\omega_0 - E)}} \right], \tag{A.99}
\end{aligned}$$

which in total yields

$$\begin{aligned}
\Sigma^{(C)}(k, E < \omega_0) &= -g^4 \left[\frac{(2t + \omega_0 - E)^2 - 2t^2}{(\omega_0 - E)(4t + \omega_0 - E)} + \frac{(2t + \omega_0 - E)(2t + 2\omega_0 - E)}{\sqrt{(4t + \omega_0 - E)(\omega_0 - E)(4t + 2\omega_0 - E)(2\omega_0 - E)}} \right] \times \\
&\quad \times \frac{1}{(2t + 2\omega_0 - E) \left[(2t + \omega_0 - E)^2 - 2t^2 \right] + (2t + \omega_0 - E) \sqrt{(4t + \omega_0 - E)(\omega_0 - E)(4t + 2\omega_0 - E)(2\omega_0 - E)} - 4t^3 \cos k}. \tag{A.100}
\end{aligned}$$

Vertex function

When we consider the electron self-energy in the polaron limit, we may set $n_{\mathbf{k}} = 0$ in the expression for the leading order vertex function given by Eq. (A.42), emphasizing the fact that it may only contain electron processes. It is evident then that only the term given by Eq. (A.44) survives, giving

$$\Gamma^{(2)}(0, 0; \mathbf{q}, \omega) \equiv \Theta^{(2)}(\mathbf{q}, \omega) = - \sum_{\mathbf{q}'} |g(\mathbf{q}')|^2 \frac{1}{(\omega - \xi_{\mathbf{q}+\mathbf{q}'} - \omega_0 + i\eta)(\xi_{\mathbf{q}'} + \omega_0)}. \tag{A.101}$$

In the 1D case with the Holstein coupling for energies below the phonon energy, the summation/integration over q' in Eq. (A.101) has been also carried out analytically in [102], with the result

$$\Theta^{(2)}(q, \omega) = - \frac{g^2}{t^2} \frac{x_+ y_+ - x_- y_-}{(x_+ - x_-)(y_+ - y_-)} \frac{z_q}{(1 - \delta_+ z_q)(1 - \delta_- z_q)}, \tag{A.102}$$

where $\delta_{\pm} = y_{\pm}/x_{\mp}$ ($\delta_+ \delta_- = 1$), and $z_q = e^{iq}$. By exploiting the results in Eqs. (A.94) and (A.96),

we have

$$\frac{x_+y_+ - x_-y_-}{(x_+ - x_-)(y_+ - y_-)} = \frac{\gamma_1\sqrt{\gamma_2^2 - 1} + \gamma_2\sqrt{\gamma_1^2 - 1}}{2\sqrt{\gamma_1^2 - 1}\sqrt{\gamma_2^2 - 1}} = \frac{1}{2} \left[\frac{\gamma_1}{\sqrt{\gamma_1^2 - 1}} + \frac{\gamma_2}{\sqrt{\gamma_2^2 - 1}} \right], \quad (\text{A.103})$$

and

$$\begin{aligned} \frac{1}{(1 - \delta_+z_q)(1 - \delta_-z_q)} &= \frac{1}{1 - (\delta_+ + \delta_-)z_q + z_q^2} = \frac{1}{1 - (x_+y_+ + x_-y_-)z_q + z_q^2} \\ &= \frac{1}{z_q} \frac{1}{z_q + z_q^{-1} - 2 \left(\gamma_1\gamma_2 + \sqrt{\gamma_1^2 - 1}\sqrt{\gamma_2^2 - 1} \right)} \\ &= \frac{1}{z_q} \frac{1}{2 \cos q - 2 \left(\gamma_1\gamma_2 + \sqrt{\gamma_1^2 - 1}\sqrt{\gamma_2^2 - 1} \right)}, \end{aligned} \quad (\text{A.104})$$

yielding

$$\Theta^{(2)}(q, \omega) = \frac{g^2}{t^2} \left[\frac{\frac{\gamma_1}{\sqrt{\gamma_1^2 - 1}} + \frac{\gamma_2}{\sqrt{\gamma_2^2 - 1}}}{\gamma_1\gamma_2 + \sqrt{\gamma_1^2 - 1}\sqrt{\gamma_2^2 - 1} - \cos q} \right]. \quad (\text{A.105})$$

By exploiting Eq. (A.90), we finally get

$$\Theta^{(2)}(q, \omega) = g^2 \left\{ \frac{\frac{(\omega_0 + 2t)}{\sqrt{\omega_0(\omega_0 + 4t)}} + \frac{(\omega_0 - \omega + 2t)}{\sqrt{(\omega_0 - \omega)(\omega_0 - \omega + 4t)}}}{(\omega_0 + 2t)(\omega_0 - \omega + 2t) + \sqrt{\omega_0(\omega_0 + 4t)(\omega_0 - \omega)(\omega_0 - \omega + 4t)} - 4t^2 \cos q} \right\}. \quad (\text{A.106})$$

Derivations related to phonon polarization

In this Appendix B, we show details of calculations related to the results for the phonon polarization used in Parts II and III. In particular, we find the exact solution for the phonon propagator for the homogeneous $q = 0$ mode and calculate the phonon polarization in the next-to-leading order of the perturbation theory in electron-phonon interaction for arbitrary \mathbf{q} , with the special emphasis on the polaron limit. In addition, we recall the occurrence of the $2k_F$ logarithmic singularity in the Lindhard function in the 1D case. We explicitly assume the constant phonon energy $\omega_{\mathbf{q}} \approx \omega_0$ ($\hbar = 1$) and the Holstein coupling in all calculations.

B.1 The homogeneous $|\mathbf{q}| = 0$ mode

There is a special case for which the Holstein model is exactly solvable [118]. In particular, for $|\mathbf{q}| = 0$ the Holstein model describes the phonon interacting with the total electron density and effectively reduces to the model of the harmonic oscillator in a constant external field. This problem is exactly solvable and describes the oscillations of phonons around the new equilibrium position, with the phonon eigenstates being the coherent states [40]. Consequently, we can find the exact solution for the phonon propagator $D(0, \omega)$ as follows.

We exploit the fact that the exact phonon eigenstates are coherent states and write the phonon propagator in the Lehmann representation [16]

$$D(0, \omega) = \sum_n \left[\frac{|\langle \alpha | (a + a^\dagger) | \alpha_n \rangle|^2}{\omega - (E_n - E_0) + i\eta} - \frac{|\langle \alpha | (a + a^\dagger) | \alpha_n \rangle|^2}{\omega + (E_n - E_0) - i\eta} \right], \quad (\text{B.1})$$

with the ground state $|\alpha\rangle = D(\alpha) |0\rangle$, where $D(\alpha) = e^{\alpha a^\dagger - \alpha^* a}$ is the displacement operator and $|0\rangle$ the vacuum of a phonons, and the ground state energy $E_0 = \frac{\omega_0}{2} - \alpha^2 \omega_0$. Energies of excited states $|\alpha_n\rangle = D(\alpha) |n\rangle = \frac{(a^\dagger - \alpha)^n}{\sqrt{n!}} |\alpha\rangle$ read $E_n = \omega_0(n + \frac{1}{2}) - \alpha^2 \omega_0$. Here, $\alpha = \frac{N_{el}g}{\sqrt{N}\omega_0}$, with N_{el} the number of electrons on a lattice with N sites. Since $|\alpha\rangle$ is the coherent state, $a|\alpha\rangle = \alpha|\alpha\rangle$, we have

$$\begin{aligned}
\langle \alpha | (a + a^\dagger) | \alpha_n \rangle &= \langle \alpha | (a + a^\dagger) \frac{(a^\dagger - \alpha)^n}{\sqrt{n!}} | \alpha \rangle \\
&= \langle \alpha | (a + a^\dagger) \frac{1}{\sqrt{n!}} \sum_{m=0}^n (-1)^m \binom{n}{m} (a^\dagger)^{n-m} \alpha^m | \alpha \rangle \\
&= \frac{1}{\sqrt{n!}} \sum_{m=0}^n (-1)^m \binom{n}{m} \alpha^m [\langle \alpha | a (a^\dagger)^{n-m} | \alpha \rangle + \langle \alpha | a^\dagger (a^\dagger)^{n-m} | \alpha \rangle] \\
&= \frac{1}{\sqrt{n!}} \sum_{m=0}^n (-1)^m \binom{n}{m} \alpha^m \langle \alpha | [(n-m)(a^\dagger)^{n-m-1} + (a^\dagger)^{n-m} a + a^\dagger (a^\dagger)^{n-m}] | \alpha \rangle \\
&= \frac{1}{\sqrt{n!}} \sum_{m=0}^n (-1)^m \binom{n}{m} [(n-m)\alpha^{n-1} + \alpha^{n+1} + \alpha^{n+1}] \\
&= \frac{\alpha^n}{\sqrt{n!}} \sum_{m=0}^n (-1)^m \binom{n}{m} [(n-m)\alpha^{-1} + 2\alpha] .
\end{aligned} \tag{B.2}$$

Next, we use

$$\sum_{m=0}^n (-1)^m \binom{n}{m} = \delta_{n,0} , \quad \text{and} , \quad \sum_{m=0}^n (-1)^m \binom{n}{m} (n-m) = \delta_{n,1} , \tag{B.3}$$

to finally obtain

$$D(0, \omega) = D_0(0, \omega) + 4\alpha^2 \left[\frac{1}{\omega + i\eta} - \frac{1}{\omega - i\eta} \right] . \tag{B.4}$$

B.2 Next-to-leading order phonon polarization

There are three contributions to the phonon polarization in the next-to-leading order of the perturbation theory in electron-phonon interaction represented diagrammatically in Figs. 7.3(b), (c), and (d). Two diagrams in Figs. 7.3(b) and (c) clearly involve the renormalization of fermion lines and are correspondingly called self-energy contributions. On the other hand, the diagram in Fig. 7.3(d) represents the leading vertex contribution to polarization.

B.2.1 Self-energy contributions

By using the Feynmann rules [40], we can write for the two self-energy polarization contributions in Figs. 7.3(b) and (c)

$$\begin{aligned} \Pi^{(4b)}(\mathbf{q}, \omega) = & -i^2 \frac{g^4}{N^2} \sum_{\mathbf{k}, \mathbf{q}'} \int_{-\infty}^{+\infty} \frac{dE}{2\pi} G_0(\mathbf{k}, E) [G_0(\mathbf{k} + \mathbf{q}, E + \omega)]^2 \times \\ & \times \int_{-\infty}^{+\infty} \frac{d\omega'}{2\pi} G_0(\mathbf{k} + \mathbf{q} + \mathbf{q}', E + \omega + \omega') D_0(\mathbf{q}', \omega') , \end{aligned} \quad (\text{B.5})$$

and

$$\begin{aligned} \Pi^{(4c)}(\mathbf{q}, \omega) = & -i^2 \frac{g^4}{N^2} \sum_{\mathbf{k}, \mathbf{q}'} \int_{-\infty}^{+\infty} \frac{dE}{2\pi} [G_0(\mathbf{k}, E)]^2 G_0(\mathbf{k} + \mathbf{q}, E + \omega) \times \\ & \times \int_{-\infty}^{+\infty} \frac{d\omega'}{2\pi} G_0(\mathbf{k} + \mathbf{q}', E + \omega') D_0(\mathbf{q}', \omega') . \end{aligned} \quad (\text{B.6})$$

It is immediately evident that those two contributions are not independent, since the set of transformations $\mathbf{k} \rightarrow \mathbf{k} - \mathbf{q}$, $\mathbf{q} \rightarrow -\mathbf{q}$, $E \rightarrow E - \omega$, $\omega \rightarrow -\omega$, relate the two polarizations

$$\Pi^{(4c)}(\mathbf{q}, \omega) = \Pi^{(4b)}(-\mathbf{q}, -\omega) . \quad (\text{B.7})$$

Therefore, we evaluate only $\Pi^{(4b)}(\mathbf{q}, \omega)$.

Similarly like in the expression for the non-crossing diagram given by Eq. (A.24), in Eq. (B.5) we again recognize the expression for the leading order fermion self-energy given by Eq. (A.27)

$$\Pi^{(4b)}(\mathbf{q}, \omega) = -i \frac{g^2}{N} \sum_{\mathbf{k}} \int_{-\infty}^{+\infty} \frac{dE}{2\pi} G_0(\mathbf{k}, E) [G_0(\mathbf{k} + \mathbf{q}, E + \omega)]^2 \Sigma^{(2)}(\mathbf{k} + \mathbf{q}, E + \omega) , \quad (\text{B.8})$$

which now multiplies

$$\begin{aligned} & G_0(\mathbf{k}, E) [G_0(\mathbf{k} + \mathbf{q}, E + \omega)]^2 = \\ & = \left[\frac{1 - n_{\mathbf{k}}}{E - \xi_{\mathbf{k}} + i\eta} + \frac{n_{\mathbf{k}}}{E - \xi_{\mathbf{k}} - i\eta} \right] \left[\left(\frac{1 - n_{\mathbf{k}+\mathbf{q}}}{E + \omega - \xi_{\mathbf{k}+\mathbf{q}} + i\eta} \right)^2 + \left(\frac{n_{\mathbf{k}+\mathbf{q}}}{E + \omega - \xi_{\mathbf{k}+\mathbf{q}} - i\eta} \right)^2 \right] . \end{aligned} \quad (\text{B.9})$$

The product $G_0(\mathbf{k}, E) [G_0(\mathbf{k} + \mathbf{q}, E + \omega)]^2 \Sigma^{(2)}(\mathbf{k} + \mathbf{q}, E + \omega)$ has eight contributions in total, which after the straightforward integrations over ω in the complex plane yield

$$\begin{aligned}
\Pi^{(4b)}(\mathbf{q}, \omega) &= \frac{g^4}{N^2} \sum_{\mathbf{k}, \mathbf{q}'} \times \\
&\times \left\{ (1 - n_{\mathbf{k}+\mathbf{q}+\mathbf{q}'}) \left[-\frac{n_{\mathbf{k}} n_{\mathbf{k}+\mathbf{q}}^2}{(\xi_{\mathbf{k}+\mathbf{q}+\mathbf{q}'} - \xi_{\mathbf{k}+\mathbf{q}} + \omega_0 - i\eta)^2 (\xi_{\mathbf{k}+\mathbf{q}+\mathbf{q}'} - \xi_{\mathbf{k}} + \omega_0 - \omega - i\eta)} + \right. \right. \\
&+ \frac{(1 - n_{\mathbf{k}}) n_{\mathbf{k}+\mathbf{q}}^2}{\xi_{\mathbf{k}} - \xi_{\mathbf{k}+\mathbf{q}+\mathbf{q}'} - \omega_0 + \omega} \left(\frac{1}{(\xi_{\mathbf{k}+\mathbf{q}+\mathbf{q}'} - \xi_{\mathbf{k}+\mathbf{q}} + \omega_0 - i\eta)^2} - \frac{1}{(\xi_{\mathbf{k}} - \xi_{\mathbf{k}+\mathbf{q}} + \omega - i\eta)^2} \right) - \\
&\left. - \frac{n_{\mathbf{k}} (1 - n_{\mathbf{k}+\mathbf{q}})^2}{(\xi_{\mathbf{k}+\mathbf{q}} - \xi_{\mathbf{k}} - \omega - i\eta)^2 (\xi_{\mathbf{k}+\mathbf{q}+\mathbf{q}'} - \xi_{\mathbf{k}} + \omega_0 - \omega - i\eta)} \right] + \\
&+ n_{\mathbf{k}+\mathbf{q}+\mathbf{q}'} \left[-\frac{(1 - n_{\mathbf{k}}) n_{\mathbf{k}+\mathbf{q}}^2}{(\xi_{\mathbf{k}+\mathbf{q}} - \xi_{\mathbf{k}} - \omega + i\eta)^2 (\xi_{\mathbf{k}} - \xi_{\mathbf{k}+\mathbf{q}+\mathbf{q}'} + \omega_0 + \omega - i\eta)} + \right. \\
&+ \frac{n_{\mathbf{k}} (1 - n_{\mathbf{k}+\mathbf{q}})^2}{\xi_{\mathbf{k}} - \xi_{\mathbf{k}+\mathbf{q}+\mathbf{q}'} + \omega_0 + \omega} \left(\frac{1}{(\xi_{\mathbf{k}} - \xi_{\mathbf{k}+\mathbf{q}} + \omega + i\eta)^2} - \frac{1}{(\xi_{\mathbf{k}+\mathbf{q}+\mathbf{q}'} - \xi_{\mathbf{k}+\mathbf{q}} - \omega_0 + i\eta)^2} \right) - \\
&\left. \left. - \frac{(1 - n_{\mathbf{k}}) (1 - n_{\mathbf{k}+\mathbf{q}})^2}{(\xi_{\mathbf{k}} - \xi_{\mathbf{k}+\mathbf{q}+\mathbf{q}'} + \omega_0 + \omega - i\eta) (\xi_{\mathbf{k}+\mathbf{q}+\mathbf{q}'} - \xi_{\mathbf{k}+\mathbf{q}} - \omega_0 + i\eta)^2} \right] \right\}. \tag{B.10}
\end{aligned}$$

B.2.2 Vertex contribution

The expression for the polarization involving the leading vertex correction, represented diagrammatically in Fig. 7.3, may be written in terms of the leading order vertex function $\Gamma^{(2)}(\mathbf{k}, E; \mathbf{k} + \mathbf{q}, E + \omega)$

$$\Pi^{(4d)}(\mathbf{q}, \omega) = -\frac{g^2}{N} \sum_{\mathbf{k}} \int_{-\infty}^{+\infty} \frac{dE}{2\pi} G_0(\mathbf{k}, E) G_0(\mathbf{k} + \mathbf{q}, E + \omega) \Gamma^{(2)}(\mathbf{k}, E; \mathbf{k} + \mathbf{q}, E + \omega). \tag{B.11}$$

$\Gamma^{(2)}(\mathbf{k}, E; \mathbf{k} + \mathbf{q}, E + \omega)$ was already calculated in Appendix A.2.2, where it was decomposed into four contributions $\Gamma_i^{(2)}$. In order to get $\Pi^{(4d)}(\mathbf{q}, \omega)$, those four contributions should be multiplied with

$$\begin{aligned}
G_0(\mathbf{k}, E) G_0(\mathbf{k} + \mathbf{q}, E + \omega) &= \frac{1 - n_{\mathbf{k}}}{E - \xi_{\mathbf{k}} + i\eta} \frac{1 - n_{\mathbf{k}+\mathbf{q}}}{E + \omega - \xi_{\mathbf{k}+\mathbf{q}} + i\eta} + \frac{1 - n_{\mathbf{k}}}{E - \xi_{\mathbf{k}} + i\eta} \frac{n_{\mathbf{k}+\mathbf{q}}}{E + \omega - \xi_{\mathbf{k}+\mathbf{q}} - i\eta} + \\
&+ \frac{n_{\mathbf{k}}}{E - \xi_{\mathbf{k}} - i\eta} \frac{1 - n_{\mathbf{k}+\mathbf{q}}}{E + \omega - \xi_{\mathbf{k}+\mathbf{q}} + i\eta} + \frac{n_{\mathbf{k}}}{E - \xi_{\mathbf{k}} - i\eta} \frac{n_{\mathbf{k}+\mathbf{q}}}{E + \omega - \xi_{\mathbf{k}+\mathbf{q}} - i\eta}, \tag{B.12}
\end{aligned}$$

and the integration over E in the complex plane carried out. The integrations are tedious, albeit straightforward to evaluate, and yield

$$\begin{aligned}
\Pi_1^{(4d)}(\mathbf{q}, \omega) &= -i \frac{g^2}{N} \sum_{\mathbf{k}} \int \frac{dE}{2\pi} G_0(\mathbf{k}, E) G_0(\mathbf{k} + \mathbf{q}, E + \omega) \Gamma_1^{(2)}(\mathbf{k}, E; \mathbf{k} + \mathbf{q}, E + \omega) \\
&= -\frac{g^4}{N^2} \sum_{\mathbf{k}, \mathbf{k}'} (1 - n_{\mathbf{k}'}) (1 - n_{\mathbf{k}'+\mathbf{q}}) \times \\
&\quad \times \left\{ \frac{n_{\mathbf{k}} (1 - n_{\mathbf{k}+\mathbf{q}})}{(\xi_{\mathbf{k}+\mathbf{q}} - \xi_{\mathbf{k}} - \omega - i\eta)(\xi_{\mathbf{k}'} - \xi_{\mathbf{k}} + \omega_0 - i\eta)(\xi_{\mathbf{k}'+\mathbf{q}} - \xi_{\mathbf{k}} + \omega_0 - \omega - i\eta)} + \right. \\
&\quad + \frac{(1 - n_{\mathbf{k}}) n_{\mathbf{k}+\mathbf{q}}}{(\xi_{\mathbf{k}} - \xi_{\mathbf{k}+\mathbf{q}} + \omega - i\eta)(\xi_{\mathbf{k}'} - \xi_{\mathbf{k}+\mathbf{q}} + \omega_0 + \omega - i\eta)(\xi_{\mathbf{k}'+\mathbf{q}} - \xi_{\mathbf{k}+\mathbf{q}} + \omega_0 - i\eta)} + \\
&\quad + \frac{n_{\mathbf{k}} n_{\mathbf{k}+\mathbf{q}}}{(\xi_{\mathbf{k}+\mathbf{q}} - \xi_{\mathbf{k}} - \omega)} \left[\frac{1}{(\xi_{\mathbf{k}'} - \xi_{\mathbf{k}} + \omega_0 - i\eta)(\xi_{\mathbf{k}'+\mathbf{q}} - \xi_{\mathbf{k}} + \omega_0 - \omega - i\eta)} - \right. \\
&\quad \left. \left. - \frac{1}{(\xi_{\mathbf{k}'} - \xi_{\mathbf{k}+\mathbf{q}} + \omega_0 + \omega - i\eta)(\xi_{\mathbf{k}'+\mathbf{q}} - \xi_{\mathbf{k}+\mathbf{q}} + \omega_0 - i\eta)} \right] \right\}, \tag{B.13}
\end{aligned}$$

$$\begin{aligned}
\Pi_2^{(4d)}(\mathbf{q}, \omega) &= -i \frac{g^2}{N} \sum_{\mathbf{k}} \int \frac{dE}{2\pi} G_0(\mathbf{k}, E) G_0(\mathbf{k} + \mathbf{q}, E + \omega) \Gamma_2^{(2)}(\mathbf{k}, E; \mathbf{k} + \mathbf{q}, E + \omega) \\
&= -\frac{g^4}{N^2} \sum_{\mathbf{k}, \mathbf{k}'} n_{\mathbf{k}'} n_{\mathbf{k}'+\mathbf{q}} \times \\
&\quad \times \left\{ \frac{n_{\mathbf{k}} (1 - n_{\mathbf{k}+\mathbf{q}})}{(\xi_{\mathbf{k}+\mathbf{q}} - \xi_{\mathbf{k}} - \omega - i\eta)(\xi_{\mathbf{k}+\mathbf{q}} - \xi_{\mathbf{k}'} + \omega_0 - \omega - i\eta)(\xi_{\mathbf{k}+\mathbf{q}} - \xi_{\mathbf{k}'+\mathbf{q}} + \omega_0 - i\eta)} + \right. \\
&\quad + \frac{(1 - n_{\mathbf{k}}) n_{\mathbf{k}+\mathbf{q}}}{(\xi_{\mathbf{k}} - \xi_{\mathbf{k}+\mathbf{q}} + \omega - i\eta)(\xi_{\mathbf{k}} - \xi_{\mathbf{k}'} + \omega_0 - i\eta)(\xi_{\mathbf{k}} - \xi_{\mathbf{k}'+\mathbf{q}} + \omega_0 + \omega - i\eta)} + \\
&\quad + \frac{(1 - n_{\mathbf{k}})(1 - n_{\mathbf{k}+\mathbf{q}})}{(\xi_{\mathbf{k}'+\mathbf{q}} - \xi_{\mathbf{k}'} - \omega)} \left[\frac{1}{(\xi_{\mathbf{k}} - \xi_{\mathbf{k}'} + \omega_0 - i\eta)(\xi_{\mathbf{k}+\mathbf{q}} - \xi_{\mathbf{k}'} + \omega_0 - \omega - i\eta)} - \right. \\
&\quad \left. \left. - \frac{1}{(\xi_{\mathbf{k}} - \xi_{\mathbf{k}'+\mathbf{q}} + \omega_0 + \omega - i\eta)(\xi_{\mathbf{k}+\mathbf{q}} - \xi_{\mathbf{k}'+\mathbf{q}} + \omega_0 - i\eta)} \right] \right\}, \tag{B.14}
\end{aligned}$$

$$\begin{aligned}
\Pi_3^{(4d)}(\mathbf{q}, \omega) &= -i \frac{g^2}{N} \sum_{\mathbf{k}} \int \frac{dE}{2\pi} G_0(\mathbf{k}, E) G_0(\mathbf{k} + \mathbf{q}, E + \omega) \Gamma_3^{(2)}(\mathbf{k}, E; \mathbf{k} + \mathbf{q}, E + \omega) \\
&= \frac{g^4}{N^2} \sum_{\mathbf{k}, \mathbf{k}'} \frac{(1 - n_{\mathbf{k}'}) n_{\mathbf{k}'+\mathbf{q}}}{(\xi_{\mathbf{k}'} - \xi_{\mathbf{k}'+\mathbf{q}} + \omega - i\eta)} \left[-\frac{n_{\mathbf{k}} n_{\mathbf{k}+\mathbf{q}}}{(\xi_{\mathbf{k}'} - \xi_{\mathbf{k}} + \omega_0 - i\eta)(\xi_{\mathbf{k}'} - \xi_{\mathbf{k}+\mathbf{q}} + \omega_0 + \omega - i\eta)} + \right. \\
&\quad + \frac{n_{\mathbf{k}} (1 - n_{\mathbf{k}+\mathbf{q}})}{(\xi_{\mathbf{k}+\mathbf{q}} - \xi_{\mathbf{k}} - \omega - i\eta)} \left\{ \frac{1}{\xi_{\mathbf{k}'} - \xi_{\mathbf{k}} + \omega_0 - i\eta} + \frac{1}{\xi_{\mathbf{k}+\mathbf{q}} - \xi_{\mathbf{k}'+\mathbf{q}} + \omega_0 - i\eta} \right\} + \\
&\quad + \frac{(1 - n_{\mathbf{k}}) n_{\mathbf{k}+\mathbf{q}}}{(\xi_{\mathbf{k}} - \xi_{\mathbf{k}+\mathbf{q}} + \omega - i\eta)} \left\{ \frac{1}{\xi_{\mathbf{k}'} - \xi_{\mathbf{k}+\mathbf{q}} + \omega_0 + \omega - i\eta} + \frac{1}{\xi_{\mathbf{k}} - \xi_{\mathbf{k}'+\mathbf{q}} + \omega_0 + \omega - i\eta} \right\} - \\
&\quad \left. - \frac{(1 - n_{\mathbf{k}})(1 - n_{\mathbf{k}+\mathbf{q}})}{(\xi_{\mathbf{k}} - \xi_{\mathbf{k}'+\mathbf{q}} + \omega_0 + \omega - i\eta)(\xi_{\mathbf{k}+\mathbf{q}} - \xi_{\mathbf{k}'+\mathbf{q}} + \omega_0 - i\eta)} \right], \tag{B.15}
\end{aligned}$$

and

$$\begin{aligned}
\Pi_4^{(4d)}(\mathbf{q}, \omega) &= -i \frac{g^2}{N} \sum_{\mathbf{k}} \int \frac{dE}{2\pi} G_0(\mathbf{k}, E) G_0(\mathbf{k} + \mathbf{q}, E + \omega) \Gamma^{(2d)}(\mathbf{k}, E; \mathbf{k} + \mathbf{q}, E + \omega) \\
&= -i \frac{g^2}{N} \sum_{\mathbf{k}} \int \frac{dE}{2\pi} G_0(\mathbf{k}, E) G_0(\mathbf{k} + \mathbf{q}, E + \omega) \Gamma^{(2c)}(\mathbf{k} + \mathbf{q}, E + \omega; \mathbf{k}, E) \\
&= -i \frac{g^2}{N} \sum_{\mathbf{p}} \int \frac{dE}{2\pi} G_0(\mathbf{p} - \mathbf{q}, E - \omega) G_0(\mathbf{p}, E) \Gamma^{(2c)}(\mathbf{p}, E; \mathbf{p} - \mathbf{q}, E - \omega) \\
&= \Pi_3^{(4d)}(-\mathbf{q}, -\omega) .
\end{aligned} \tag{B.16}$$

B.2.3 Ward identity

For the momentum $|\mathbf{q}| = 0$, a lot of contributions to $\Pi^{(4)}(0, \omega)$ vanish identically. This is due to the Fermi-Dirac distributions, satisfying $n_{\mathbf{k}}^2 = n_{\mathbf{k}}$, $(1 - n_{\mathbf{k}})^2 = 1 - n_{\mathbf{k}}$, and $n_{\mathbf{k}}(1 - n_{\mathbf{k}}) = 0$ for an arbitrary momentum \mathbf{k} at zero temperature. In particular, the polarization $\Pi^{(4b)}(\mathbf{q}, \omega)$ containing the self-energy contribution for $|\mathbf{q}| = 0$ reduces to

$$\begin{aligned}
\Pi^{(4b)}(0, \omega) &= -\frac{g^4}{N^2} \sum_{\mathbf{k}, \mathbf{k}'} \left[\frac{n_{\mathbf{k}}(1 - n_{\mathbf{k}'})}{(\xi_{\mathbf{k}'} - \xi_{\mathbf{k}} + \omega_0 - i\eta)^2 (\xi_{\mathbf{k}'} - \xi_{\mathbf{k}} + \omega_0 + \omega - i\eta)} + \right. \\
&\quad \left. + \frac{(1 - n_{\mathbf{k}})n_{\mathbf{k}'}}{(\xi_{\mathbf{k}} - \xi_{\mathbf{k}'} + \omega_0 - i\eta)^2 (\xi_{\mathbf{k}} - \xi_{\mathbf{k}'} + \omega_0 - \omega - i\eta)} \right] = -\frac{g^4}{N^2} \sum_{\mathbf{k}, \mathbf{k}'} \frac{n_{\mathbf{k}}(1 - n_{\mathbf{k}'})}{(\xi_{\mathbf{k}'} - \xi_{\mathbf{k}} + \omega_0 - i\eta)^2} \times \\
&\quad \times \left[\frac{1}{\xi_{\mathbf{k}'} - \xi_{\mathbf{k}} + \omega_0 + \omega - i\eta} + \frac{1}{\xi_{\mathbf{k}'} - \xi_{\mathbf{k}} + \omega_0 - \omega - i\eta} \right] \\
&= -\frac{g^4}{N^2} \sum_{\mathbf{k}, \mathbf{k}'} \frac{2n_{\mathbf{k}}(1 - n_{\mathbf{k}'})}{(\xi_{\mathbf{k}'} - \xi_{\mathbf{k}} + \omega_0 - i\eta) \{(\xi_{\mathbf{k}'} - \xi_{\mathbf{k}} + \omega_0 - i\eta)^2 - \omega^2\}} .
\end{aligned} \tag{B.17}$$

Since $\Pi^{(4b)}(0, \omega)$ is symmetric in ω , we immediately get $\Pi^{(4c)}(0, \omega) = \Pi^{(4b)}(0, -\omega) = \Pi^{(4b)}(0, \omega)$, so the net contribution to the next-to-leading order polarization from the self-energy contributions read $2\Pi^{(4b)}(0, \omega)$.

Next, by considering the polarization with the vertex correction $\Pi^{(4d)}(0, \omega)$, we note that $\Pi_3^{(4d)}(0, \omega) = \Pi_4^{(4d)}(0, \omega) = 0$ vanish identically owing to the common factor $n_{\mathbf{k}}(1 - n_{\mathbf{k}}) = 0$. The remaining two contributions $\Pi_1^{(4d)}(0, \omega)$ and $\Pi_2^{(4d)}(0, \omega)$ can be expressed as follows

$$\Pi_1^{(4d)}(0, \omega) = \Pi_2^{(4d)}(0, \omega) = \frac{g^4}{N^2} \sum_{\mathbf{k}, \mathbf{k}'} \frac{2(1 - n_{\mathbf{k}})n_{\mathbf{k}'}}{(\xi_{\mathbf{k}} - \xi_{\mathbf{k}'} + \omega_0 - i\eta) \{(\xi_{\mathbf{k}} - \xi_{\mathbf{k}'} + \omega_0 - i\eta)^2 - \omega^2\}} , \tag{B.18}$$

so the net contribution of $\Pi^{(4d)}(0, \omega)$ reads $2\Pi_1^{(4d)}(0, \omega)$.

We note that expressions in Eqs. (B.17) and (B.18) are identical up to the $-$ sign, so the net contribution $\Pi^{(4)}(0, \omega) = 2\Pi^{(4b)}(0, \omega) + 2\Pi_1^{(4d)}(0, \omega) = 0$ vanishes, which explicitly proves the Ward identity in the next-to-leading order.

B.2.4 Polaron limit

Phonon polarization

When we consider phonon properties in the polaron limit, dominant contributions to the polarization are of the order $\mathcal{O}(1/N)$, with N being the number of lattice sites, and might be obtained by simply putting $n_{\mathbf{q}} = \delta_{\mathbf{q},0}$ in expressions for the polarization obtained for finite electron densities. In particular, in the next-to-leading order, the polarization involving self-energy contributions given by Eq. (B.10) simplifies drastically

$$\begin{aligned}
\Pi^{(4b)}(\mathbf{q}, \omega) &\approx \frac{g^4}{N^2} \sum_{\mathbf{k}, \mathbf{q}'} \left\{ -\frac{n_{\mathbf{k}}}{(\xi_{\mathbf{k}+\mathbf{q}} - \xi_{\mathbf{k}} - \omega - i\eta)^2 (\xi_{\mathbf{k}+\mathbf{q}+\mathbf{q}'} - \xi_{\mathbf{k}} + \omega_0 - \omega - i\eta)} + \right. \\
&+ \frac{n_{\mathbf{k}+\mathbf{q}}}{\xi_{\mathbf{k}} - \xi_{\mathbf{k}+\mathbf{q}+\mathbf{q}'} - \omega_0 + \omega} \left[\frac{1}{(\xi_{\mathbf{k}+\mathbf{q}+\mathbf{q}'} - \xi_{\mathbf{k}+\mathbf{q}} + \omega_0 - i\eta)^2} - \frac{1}{(\xi_{\mathbf{k}} - \xi_{\mathbf{k}+\mathbf{q}} + \omega - i\eta)^2} \right] + \\
&+ n_{\mathbf{k}+\mathbf{q}+\mathbf{q}'} \left[-\frac{1}{(\xi_{\mathbf{k}} - \xi_{\mathbf{k}+\mathbf{q}+\mathbf{q}'} + \omega_0 + \omega - i\eta) (\xi_{\mathbf{k}+\mathbf{q}+\mathbf{q}'} - \xi_{\mathbf{k}+\mathbf{q}} - \omega_0 + i\eta)^2} \right] \left. \right\} \\
&\approx \frac{g^4}{N^2} \sum_{\mathbf{k}} \left\{ -\frac{1}{(\xi_{\mathbf{q}} - \omega - i\eta)^2 (\xi_{\mathbf{k}+\mathbf{q}} + \omega_0 - \omega - i\eta)} + \right. \\
&+ \frac{1}{\xi_{\mathbf{q}} - \xi_{\mathbf{k}} - \omega_0 + \omega} \left[\frac{1}{(\xi_{\mathbf{k}} + \omega_0 - i\eta)^2} - \frac{1}{(\xi_{\mathbf{q}} + \omega - i\eta)^2} \right] - \\
&- \frac{1}{(\xi_{\mathbf{k}} + \omega_0 + \omega - i\eta) (-\xi_{\mathbf{k}+\mathbf{q}} - \omega_0 + i\eta)^2} \left. \right\} \\
&= \frac{g^4}{N^2} \sum_{\mathbf{k}} \left\{ -\frac{1}{(\xi_{\mathbf{q}} - \omega - i\eta)^2 (\xi_{\mathbf{k}+\mathbf{q}} + \omega_{\mathbf{k}} - \omega - i\eta)} + \right. \\
&+ \frac{1}{(\xi_{\mathbf{q}} + \omega - i\eta)} \frac{1}{(-\xi_{\mathbf{k}} - \omega_0 + i\eta)^2} + \frac{1}{(\xi_{\mathbf{k}} + \omega_0 - i\eta)} \frac{1}{(-\xi_{\mathbf{q}} - \omega + i\eta)^2} - \\
&- \frac{1}{(\xi_{\mathbf{k}} + \omega_0 + \omega - i\eta) (-\xi_{\mathbf{k}+\mathbf{q}} - \omega_0 + i\eta)^2} \left. \right\}, \tag{B.19}
\end{aligned}$$

where in obtaining the last equality we have used the identity $\frac{1}{A+B} \left[\frac{1}{A^2} - \frac{1}{B^2} \right] = \frac{1}{A^2B} - \frac{1}{AB^2}$. The contribution $\Pi^{(4c)}(\mathbf{q}, \omega)$ can now be also easily obtained via the relation

$$\begin{aligned} \Pi^{(4c)}(\mathbf{q}, \omega) = \Pi^{(4b)}(-\mathbf{q}, -\omega) = \frac{g^4}{N^2} \sum_{\mathbf{k}} \left\{ -\frac{1}{(\xi_{\mathbf{q}} + \omega - i\eta)^2 (\xi_{\mathbf{k}} + \omega_0 + \omega - i\eta)} + \right. \\ \left. + \frac{1}{(\xi_{\mathbf{q}} - \omega - i\eta)} \frac{1}{(-\xi_{\mathbf{k}+\mathbf{q}} - \omega_0 + i\eta)^2} + \frac{1}{(\xi_{\mathbf{k}+\mathbf{q}} + \omega_0 - i\eta)} \frac{1}{(-\xi_{\mathbf{q}} + \omega + i\eta)^2} - \right. \\ \left. - \frac{1}{(\xi_{\mathbf{k}+\mathbf{q}} + \omega_0 - \omega - i\eta) (-\xi_{\mathbf{k}} - \omega_0 + i\eta)^2} \right\}. \end{aligned} \quad (\text{B.20})$$

Similarly, $1/N$ contributions of the polarization with the leading vertex correction come only from $\Pi_1^{(4d)}(\mathbf{q}, \omega)$, $\Pi_3^{(4d)}(\mathbf{q}, \omega)$, and $\Pi_4^{(4d)}(\mathbf{q}, \omega)$, given by Eqs. (B.13), (B.15), and (B.16), respectively (note that $\Pi_2^{(4d)}(\mathbf{q}, \omega)$ does not contribute in the polaron limit), and read

$$\begin{aligned} \Pi_1^{(4d)}(\mathbf{q}, \omega) \approx -\frac{g^4}{N^2} \sum_{\mathbf{k}, \mathbf{k}'} \left[\frac{n_{\mathbf{k}}}{(\xi_{\mathbf{k}+\mathbf{q}} - \xi_{\mathbf{k}} - \omega - i\eta)(\xi_{\mathbf{k}'} - \xi_{\mathbf{k}} + \omega_0 - i\eta)(\xi_{\mathbf{k}'+\mathbf{q}} - \xi_{\mathbf{k}} + \omega_0 - \omega - i\eta)} + \right. \\ \left. + \frac{n_{\mathbf{k}+\mathbf{q}}}{(\xi_{\mathbf{k}} - \xi_{\mathbf{k}+\mathbf{q}} + \omega - i\eta)(\xi_{\mathbf{k}'} - \xi_{\mathbf{k}+\mathbf{q}} + \omega_0 + \omega - i\eta)(\xi_{\mathbf{k}'+\mathbf{q}} - \xi_{\mathbf{k}+\mathbf{q}} + \omega_0 - i\eta)} \right] \\ \approx -\frac{g^4}{N^2} \sum_{\mathbf{k}} \left[\frac{1}{(\xi_{\mathbf{q}} - \omega - i\eta)(\xi_{\mathbf{k}} + \omega_0 - i\eta)(\xi_{\mathbf{k}+\mathbf{q}} + \omega_0 - \omega - i\eta)} + \right. \\ \left. + \frac{1}{(\xi_{\mathbf{q}} + \omega - i\eta)(\xi_{\mathbf{k}} + \omega_0 + \omega - i\eta)(\xi_{\mathbf{k}+\mathbf{q}} + \omega_0 - i\eta)} \right], \end{aligned}$$

$$\begin{aligned} \Pi_3^{(4d)}(\mathbf{q}, \omega) \approx -\frac{g^4}{N^2} \sum_{\mathbf{k}, \mathbf{k}'} \frac{n_{\mathbf{k}'+\mathbf{q}}}{(\xi_{\mathbf{k}'} - \xi_{\mathbf{k}'+\mathbf{q}} + \omega - i\eta)(\xi_{\mathbf{k}} - \xi_{\mathbf{k}'+\mathbf{q}} + \omega_0 + \omega - i\eta)(\xi_{\mathbf{k}+\mathbf{q}} - \xi_{\mathbf{k}'+\mathbf{q}} + \omega_0 - i\eta)} \\ \approx -\frac{g^4}{N^2} \sum_{\mathbf{k}} \frac{1}{(\xi_{\mathbf{q}} + \omega - i\eta)(\xi_{\mathbf{k}} + \omega_0 + \omega - i\eta)(\xi_{\mathbf{k}+\mathbf{q}} + \omega_0 - i\eta)}, \end{aligned} \quad (\text{B.21})$$

and

$$\Pi_4^{(4d)}(\mathbf{q}, \omega) = \Pi_3^{(4d)}(-\mathbf{q}, -\omega) = -\frac{g^4}{N^2} \sum_{\mathbf{k}} \frac{1}{(\xi_{\mathbf{q}} - \omega - i\eta)(\xi_{\mathbf{k}+\mathbf{q}} + \omega_0 - \omega - i\eta)(\xi_{\mathbf{k}} + \omega_0 - i\eta)}, \quad (\text{B.22})$$

giving in total

$$\begin{aligned} \Pi^{(4d)}(\mathbf{q}, \omega) \approx & -2 \frac{g^4}{N^2} \sum_{\mathbf{k}} \left[\frac{1}{(\xi_{\mathbf{q}} - \omega - i\eta)(\xi_{\mathbf{k}} + \omega_0 - i\eta)(\xi_{\mathbf{k}+\mathbf{q}} + \omega_0 - \omega - i\eta)} + \right. \\ & \left. + \frac{1}{(\xi_{\mathbf{q}} + \omega - i\eta)(\xi_{\mathbf{k}} + \omega_0 + \omega - i\eta)(\xi_{\mathbf{k}+\mathbf{q}} + \omega_0 - i\eta)} \right], \end{aligned} \quad (\text{B.23})$$

in the polaron limit.

Phonon spectral weight

With $\Pi^{(4b)}(\mathbf{q}, \omega)$, $\Pi^{(4c)}(\mathbf{q}, \omega)$, and $\Pi^{(4d)}(\mathbf{q}, \omega)$ known in the polaron limit, we can calculate their imaginary parts. In particular, we are interested in $\text{Im}\Pi^{(4)}(\mathbf{q}, \omega < \omega_0)$ in the energy region below the phonon energy, which should correspond to the phonon spectral weight in the polaron band, as described in Section 7.3.

From Eq. (B.19), we have for $0 < \omega < \omega_0$ and $\xi_{\mathbf{q}} < \omega_0$

$$\text{Im}\Pi^{(4b)}(\mathbf{q}, \omega < \omega_0) = \pi \frac{g^4}{N^2} \sum_{\mathbf{k}} \frac{1}{(\xi_{\mathbf{k}+\mathbf{q}} + \omega_0 - \omega)^2} \delta(\omega - \xi_{\mathbf{q}}), \quad (\text{B.24})$$

where we have used the identity $\frac{1}{(\omega \pm i\eta)^2} = \frac{1}{\omega^2} \mp i\pi\delta(0)\frac{d}{d\omega}$ [124]. Similarly, from Eq. (B.20) we have

$$\text{Im}\Pi^{(4c)}(\mathbf{q}, \omega < \omega_0) = \pi \frac{g^4}{N^2} \sum_{\mathbf{k}} \frac{1}{(\xi_{\mathbf{k}} + \omega_0)^2} \delta(\omega - \xi_{\mathbf{q}}). \quad (\text{B.25})$$

Lastly, Eq. (B.23) gives in the energy region below the phonon energy

$$\text{Im}\Pi^{(4d)}(\mathbf{q}, \omega < \omega_0) = -\pi 2 \frac{g^4}{N^2} \sum_{\mathbf{k}'} \frac{1}{(\xi_{\mathbf{k}'} + \omega_0)(\xi_{\mathbf{k}'+\mathbf{q}} + \omega_0 - \omega)} \delta(\omega - \xi_{\mathbf{q}}), \quad (\text{B.26})$$

yielding in total

$$\begin{aligned} \text{Im}\Pi^{(4)}(\mathbf{q}, \omega < \omega_0) &= \pi \frac{g^4}{N^2} \sum_{\mathbf{k}} \left[\frac{1}{\xi_{\mathbf{k}+\mathbf{q}} + \omega_0 - \omega} - \frac{1}{\xi_{\mathbf{k}} + \omega_0} \right]^2 \delta(\omega - \xi_{\mathbf{q}}) \\ &\equiv \pi \frac{g^2}{N} F_{\mathbf{q}} \delta(\omega - \xi_{\mathbf{q}}). \end{aligned} \quad (\text{B.27})$$

It is interesting to note that the spectral weight in the polaron band due to the polarization with the vertex correction is actually proportional to the vertex function $\Theta^{(2)}(\mathbf{q}, \varepsilon_{\mathbf{q}})$, see Eq. (A.101), motivating us to distinguish different contributions of $F_{\mathbf{q}} = Z_0 + Z_{\mathbf{q}} + 2\Theta^{(2)}(\mathbf{q}, \varepsilon_{\mathbf{q}})$. Here, Z_0 and $Z_{\mathbf{q}}$ come from the self-energy contributions and read

$$Z_{\mathbf{q}} = \frac{g^2}{N} \sum_{\mathbf{k}} \frac{1}{(\xi_{\mathbf{k}+\mathbf{q}} + \omega_0 - \xi_{\mathbf{q}})^2}. \quad (\text{B.28})$$

The summation/integration over k in Eq. (B.28) in the 1D case can be calculated analytically as we shall now show. We consider the summation

$$f(\omega) = \frac{g^2}{N} \sum_k \frac{1}{(\varepsilon_k + \omega_0 - \omega)^2}, \quad (\text{B.29})$$

and exploit the integration over the unit circle

$$\frac{1}{N} \sum_k = \frac{1}{2\pi} \int_{-\pi}^{\pi} dk = \frac{1}{2\pi} \int_0^{2\pi} d\phi = \oint_{|z|=1} \frac{dz}{iz2\pi}, \quad (\text{B.30})$$

where $z = e^{ik}$ and $\varepsilon_k = 2t(1 - \frac{1}{2}z - \frac{1}{2}z^{-1})$, so

$$f(\omega) = g^2 \frac{1}{2\pi} \oint_{|z|=1} \frac{dz}{iz} \frac{1}{(2t - t(z + z^{-1}) + \omega_0 - \omega)^2}. \quad (\text{B.31})$$

We are interested in the poles of the function under the integral, so we work out the denominator

$$\begin{aligned} & t^2 z^2 - 2t(2t + \omega_0 - \omega)z + (2t + \omega_0 - \omega)^2 + 2t^2 - 2t(2t + \omega_0 - \omega)z^{-1} + t^2 z^{-2} = \\ & = (z^2 + z^{-2}) - \frac{2t(2t + \omega_0 - \omega)}{t^2} (z + z^{-1}) + \left[\frac{(2t + \omega_0 - \omega)^2}{t^2} + 2 \right] = 0, \end{aligned} \quad (\text{B.32})$$

where in the second row we have divided the expression by t^2 . Next, we introduce $x \equiv z + z^{-1}$, and one can easily show that $x^2 - 2 = z^2 + z^{-2}$, so we end up with the quadratic equation

$$x^2 - \frac{2(2t + \omega_0 - \omega)}{t}x + \frac{(2t + \omega_0 - \omega)^2}{t^2} = 0 \quad (\text{B.33})$$

which solutions are

$$x_{1,2} = \frac{(2t + \omega_0 - \omega)}{t} \equiv x. \quad (\text{B.34})$$

Thus, we have two two-fold degenerate solutions given by the equation, $z^2 - xz + 1 = 0$, which solutions are

$$z_{1,2} = \frac{x \pm \sqrt{x^2 - 4}}{2}. \quad (\text{B.35})$$

By introducing $y \equiv \frac{x}{2} = \frac{2t + \omega_0 - \omega}{2t}$, we can write

$$z_{1,2} = y \pm \sqrt{y^2 - 1} \quad (\text{B.36})$$

giving finally the poles of the denominator under the integral. Correspondingly, we can write

$$f(\omega) = g^2 \frac{-i}{2\pi t^2} \oint_C dz \frac{z}{(z - z_1)^2 (z - z_2)^2}. \quad (\text{B.37})$$

We have two second order poles and to check whether they contribute to the integral we have to check whether they sit on the inside or the outside of the unit circle. Namely, $z_{1,2}$ will contribute to the integral if

$$|z_{1,2}| \leq 1. \quad (\text{B.38})$$

In particular, we are interested in energies $\omega < \omega_0$, for which $y = 1 + \frac{\omega_0 - \omega}{2t} > 1$, so only $z_2 = y - \sqrt{y^2 - 1}$ lies within the unit circle in our case. Correspondingly, we evaluate the residue z_2

$$\begin{aligned} \text{Res}[z_2] &= \lim_{z \rightarrow z_2} \frac{d}{dz} \left[(z - z_2)^2 \frac{z}{(z - z_1)^2 (z - z_2)^2} \right] \\ &= \lim_{z \rightarrow z_2} \frac{(z - z_1)^2 - 2z(z - z_1)}{(z - z_1)^4} = \frac{(z_2 - z_1)^2 - 2z_2(z_2 - z_1)}{(z_2 - z_1)^4} \\ &= \frac{4(y^2 - 1) + 4(y - \sqrt{y^2 - 1})\sqrt{y^2 - 1}}{16(y^2 - 1)^2} = \frac{y}{4(y^2 - 1)^{\frac{3}{2}}}, \end{aligned} \quad (\text{B.39})$$

providing the solution for $f(\omega)$ in the energy range $\omega < \omega_0$

$$f(\omega) = g^2 \frac{-i}{2\pi t^2} 2\pi i \text{Res}[z_2] = g^2 \frac{2t + \omega_0 - \omega}{[(\omega_0 - \omega)(4t + \omega_0 - \omega)]^{\frac{3}{2}}}. \quad (\text{B.40})$$

B.3 $2k_F$ singularity

In this last Section B.3 of Appendix B, we derive the result in Eq. (10.5), explicitly recovering the existence of the $2k_F$ logarithmic singularity in the leading order polarization in the 1D case. In particular, we consider the static leading order polarization given by Eq. (10.4) in the 1D half-filled case, with $k_F = \frac{\pi}{2}$. We then have $2k_F = \pi$ and we are interested in the behavior of Eq. (10.4) in the vicinity of that momentum

$$\text{Re}\Pi^{(2)}(q, 0) = \frac{g^2}{N} \sum_k \frac{n_k - n_{k+q}}{\varepsilon_k - \varepsilon_{k+q}}, \quad q = \pi \pm \delta, \quad |\delta| \ll 1. \quad (\text{B.41})$$

Exactly at half-filling and for $q = 2k_F = \pi$ ($\delta = 0$) the Fermi-Dirac distribution satisfies $n_{k+q} = (1 - n_k)$, while for the finite $\delta > 0$ we can decompose the sum in Eq. (B.41) into five contributions

$$\begin{aligned} \sum_k [n_k - n_{k+q}] &= \sum_{k=-\pi}^{-\frac{\pi}{2}-\delta} [n_k - (1 - n_k)] + \sum_{k=-\frac{\pi}{2}-\delta}^{-\frac{\pi}{2}} [n_k - n_k] + \sum_{k=-\frac{\pi}{2}}^{\frac{\pi}{2}-\delta} [n_k - (1 - n_k)] + \\ &+ \sum_{k=\frac{\pi}{2}-\delta}^{\frac{\pi}{2}} [n_k - n_k] + \sum_{k=\frac{\pi}{2}}^{\pi} [n_k - (1 - n_k)] \\ &= \left[\sum_{k=-\pi}^{-\frac{\pi}{2}-\delta} + \sum_{k=-\frac{\pi}{2}}^{\frac{\pi}{2}-\delta} + \sum_{k=\frac{\pi}{2}}^{\pi} \right] [2n_k - 1] = \sum_{k=-\pi}^{-\frac{\pi}{2}-\delta} [-1] + \sum_{k=-\frac{\pi}{2}}^{\frac{\pi}{2}-\delta} [+1] + \sum_{k=\frac{\pi}{2}}^{\pi} [-1], \end{aligned} \quad (\text{B.42})$$

which helps us get rid of the Fermi-Dirac distribution. What is left is to evaluate $\sum_k \frac{1}{\varepsilon_k - \varepsilon_{k+q}}$ for three momentum regions in Eq. (B.42) and take care of the proper sign for each of the contribution.

While evaluating the integrals, we use

$$\begin{aligned} \varepsilon_{k+q} &= -2t \cos(k + \pi + \delta) \approx -2t [\cos(k + \pi) - \delta \sin(k + \pi)] = -2t [-\cos k + \delta \sin k] \\ &= -\varepsilon_k - 2t\delta \sin k, \end{aligned} \quad (\text{B.43})$$

valid for small δ and consult the integral table [59]. We have

$$\begin{aligned}
-\sum_{k=-\pi}^{-\frac{\pi}{2}-\delta} \left[\frac{1}{\varepsilon_k - \varepsilon_{k+q}} \right] &= -\sum_{k=-\pi}^{-\frac{\pi}{2}-\delta} \frac{1}{2\varepsilon_k + 2t\delta \sin k} = -\frac{N}{2\pi} \int_{-\pi}^{-\frac{\pi}{2}-\delta} \frac{dk}{-4t \cos k + 2t\delta \sin k} \\
&= -\frac{N}{2\pi} \int_{-\frac{\pi}{2}}^{-\delta} \frac{dk}{4t \sin k + 2t\delta \cos k} = \frac{N}{2\pi} \int_{-\delta}^{-\frac{\pi}{2}} \frac{dk}{4t \sin k + 2t\delta \cos k} \\
&= \frac{N}{2\pi} \frac{\ln \tan \left[\frac{1}{2} (\arctan \frac{\delta}{2} - \frac{\pi}{2}) \right]}{2t\sqrt{4 + \delta^2}} - \frac{N}{2\pi} \frac{\ln \tan \left[\frac{1}{2} (\arctan \frac{\delta}{2} - \delta) \right]}{2t\sqrt{4 + \delta^2}} \\
&\approx -\frac{N}{2\pi} \frac{\ln \tan \left[\frac{1}{2} \arctan \frac{\delta}{2} \right]}{2t\sqrt{4 + \delta^2}},
\end{aligned} \tag{B.44}$$

since $\tan \left[\frac{1}{2} (\frac{\pi}{2} - \arctan \frac{\delta}{2}) \right] \rightarrow 1$. Similarly

$$\sum_{k=-\frac{\pi}{2}}^{\frac{\pi}{2}-\delta} \left[\frac{1}{\varepsilon_k - \varepsilon_{k+q}} \right] \approx -2 \frac{N}{2\pi} \frac{\ln \tan \left[\frac{1}{2} \arctan \frac{\delta}{2} \right]}{2t\sqrt{4 + \delta^2}}, \tag{B.45}$$

and

$$-\sum_{k=\frac{\pi}{2}}^{\pi} \left[\frac{1}{\varepsilon_k - \varepsilon_{k+q}} \right] \approx -\frac{N}{2\pi} \frac{\ln \tan \left[\frac{1}{2} \arctan \frac{\delta}{2} \right]}{2t\sqrt{4 + \delta^2}}, \tag{B.46}$$

so in total we get

$$\Pi^{(0)}(q = \pi \pm \delta, 0) = -\frac{g^2}{2\pi} \left[2 \frac{\ln \tan \left[\frac{1}{2} \arctan \frac{\delta}{2} \right]}{t\sqrt{4 + \delta^2}} \right] \approx -\frac{g^2}{2\pi t} \ln \left[\frac{\delta}{4} \right]. \tag{B.47}$$

Comment on the expansion of the Green's function

Generally, the exact Green's function can be written as

$$G = \frac{(1 + C^{(2)} + C^{(4)} + \dots)(1 + D^{(2)} + D^{(4)} + \dots)}{(1 + D^{(2)} + D^{(4)} + \dots)}, \quad (\text{C.1})$$

where $1 + C^{(2)} + C^{(4)} + \dots$ represents the sum of contributions of all connected diagrams, while $1 + D^{(2)} + D^{(4)} + \dots$ represents the sum of contributions of all disconnected diagrams, order by order in some perturbation parameter. The usual approach is to consider only connected diagrams in Green's function expansion, due to the evident cancellation of the contributions of disconnected diagrams in the denominator and the numerator. In that case, to the leading order, we have

$$G^{(2)} = 1 + C^{(2)}. \quad (\text{C.2})$$

However, we can first work out the product in the numerator and only then consider the disconnected diagrams in the denominator. Following that approach, we get to the leading order

$$\begin{aligned} G^{(2)} &= \frac{(1 + C^{(2)})(1 + D^{(2)})}{1 + D^{(2)}} = \frac{1 + C^{(2)} + D^{(2)} + C^{(2)}D^{(2)}}{1 + D^{(2)}} \approx \frac{1 + C^{(2)} - C^{(2)}}{1 + D^{(2)}} = \frac{1}{1 + D^{(2)}} \\ &\approx 1 - D^{(2)} = 1 + C^{(2)}, \end{aligned} \quad (\text{C.3})$$

where we have assumed $C^{(2)} = -D^{(2)}$. In both cases, the same result for G is obtained.

To show an example of how this works in praxis, we consider the time-ordered leading order Green's functions in a weak electron-phonon coupling perturbation theory with a self-energy contribution and a vacuum fluctuation represented by the connected and the disconnected diagrams in Figs. C.1(a) and (b), respectively. By using the Feynman rules in the time-domain [16], for the connected diagram in Fig. C.1(a) we can write

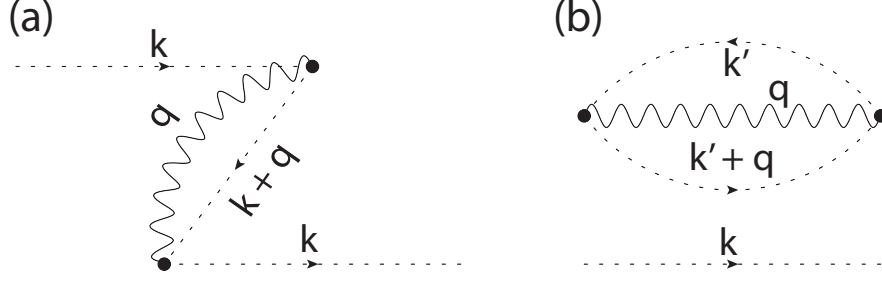


Figure C.1: Diagrammatic representation of the time-ordered leading order Green's functions in a weak electron-phonon coupling perturbation theory involving (a) a self-energy contribution and (b) a vacuum fluctuation.

$$\begin{aligned}
G_C^+(\mathbf{k}, t - t') &= i^2 \sum_{\mathbf{q}} |g(\mathbf{q})|^2 \int dt_1 \int dt_2 G_0^-(\mathbf{k} + \mathbf{q}, t_2 - t_1) D_0(\mathbf{q}, t_1 - t_2) \times \\
&\quad \times G_0^+(\mathbf{k}, t_1 - t') G_0^+(\mathbf{k}, t - t_2) \\
&= - \sum_{\mathbf{q}} |g(\mathbf{q})|^2 \int dt_1 \int dt_2 G_0^-(\mathbf{k} + \mathbf{q}, t_2 - t_1) D_0(\mathbf{q}, t_1 - t_2) \times \\
&\quad \times [iG_0^+(\mathbf{k}, t_1 - t_2) G_0^+(\mathbf{k}, t_2 - t')] [iG_0^+(\mathbf{k}, t - t_1) G_0^+(\mathbf{k}, t_1 - t_2)] \\
&= -G_0^+(\mathbf{k}, t - t') \times \\
&\quad \times \sum_{\mathbf{q}} |g(\mathbf{q})|^2 \int dt_1 \int dt_2 G_0^+(\mathbf{k}, t_1 - t_2) G_0^-(\mathbf{k} + \mathbf{q}, t_2 - t_1) D_0(\mathbf{q}, t_1 - t_2) .
\end{aligned} \tag{C.4}$$

where we have used properties of unperturbed time-ordered fermion Green's functions

$$\begin{aligned}
G_0^+(\mathbf{k}, t - t_1) G_0^+(\mathbf{k}, t_1 - t') &= \left[-i\Theta(t - t_1) n_{\mathbf{k}} e^{-i\xi_{\mathbf{k}}(t-t_1)} \right] \left[-i\Theta(t_1 - t') n_{\mathbf{k}} e^{-i\xi_{\mathbf{k}}(t_1-t')} \right] \\
&= -\Theta(t - t') n_{\mathbf{k}} e^{-i\xi_{\mathbf{k}}(t-t')} = -iG_0^+(\mathbf{k}, t - t') ,
\end{aligned} \tag{C.5}$$

and

$$\begin{aligned}
G_0^+(\mathbf{k}, t_4 - t_3) G_0^+(\mathbf{k}, t_3 - t_2) G_0^+(\mathbf{k}, t_2 - t_1) &= -iG_0^+(\mathbf{k}, t_4 - t_2) G_0^+(\mathbf{k}, t_2 - t_1) \\
&= -G_0^+(\mathbf{k}, t_4 - t_1) .
\end{aligned} \tag{C.6}$$

Similarly, we have for the disconnected diagram in Fig. C.1(b)

$$\begin{aligned}
G_D^+(\mathbf{k}, t - t') &= -i^2 G_0^+(\mathbf{k}, t - t') \\
&\times \sum_{\mathbf{q}, \mathbf{k}'} |g(\mathbf{q})|^2 \int dt_1 \int dt_2 G_0^+(\mathbf{k}', t_1 - t_2) G_0^-(\mathbf{k}' + \mathbf{q}, t_2 - t_1) D_0(\mathbf{q}, t_1 - t_2) ,
\end{aligned}
\tag{C.7}$$

where an additional $-$ sign appears due to the closed fermion loop. Evidently, $\mathbf{k}' = \mathbf{k}$ component of $G_D^+(\mathbf{k}, t - t')$ exactly cancels $G_C^+(\mathbf{k}, t - t')$.

Following the standard Green's function expansion, we can disregard all disconnected diagrams and consider in the expansion only connected diagrams, including the non-physical diagram in Fig. C.1(a) which violates the Pauli exclusion principle. Alternatively, according to Eq. (C.3), we can get rid of non-physical diagrams in the expansion by explicitly keeping also disconnected diagrams, like the one in Fig. C.1(b).

Phonon production for squeezed states

The Lehmann representation of the longitudinal optical (LO) phonon Green's function is given by [16]

$$D(\mathbf{q}, \omega) = \sum_n \left[\frac{|\langle \Omega | (a_{\mathbf{q}} + a_{-\mathbf{q}}^\dagger) | \Omega_n \rangle|^2}{\omega - (E_n - E_0) + i\eta} - \frac{|\langle \Omega | (a_{\mathbf{q}} + a_{-\mathbf{q}}^\dagger) | \Omega_n \rangle|^2}{\omega + (E_n - E_0) - i\eta} \right], \quad (\text{D.1})$$

where $|\Omega\rangle$ and $|\Omega_n\rangle$ are the exact ground and the excited states of the (interacting) system, respectively. From Eq. (D.1), it is easy to check that the integrated LO phonon spectral weight satisfies Eq. (9.19)

$$\frac{-1}{2\pi} \int_{-\infty}^{\infty} \text{Im} D(\mathbf{q}, \omega) d\omega = \sum_n |\langle \Omega | (a_{\mathbf{q}} + a_{-\mathbf{q}}^\dagger) | \Omega_n \rangle|^2 = \langle \Omega | (1 + 2a_{\mathbf{q}}^\dagger a_{\mathbf{q}} + a_{\mathbf{q}} a_{-\mathbf{q}} + a_{\mathbf{q}}^\dagger a_{-\mathbf{q}}^\dagger) | \Omega \rangle. \quad (\text{D.2})$$

By assuming that the ground state of the lattice subsystem is given by squeezed states of harmonic oscillators

$$|\Omega\rangle = \prod_{\mathbf{q}} \exp \left[\frac{1}{2} \left(\gamma_{\mathbf{q}}^* a_{\mathbf{q}}^2 - \gamma_{\mathbf{q}} a_{\mathbf{q}}^{\dagger 2} \right) \right] |\Omega_0\rangle, \quad (\text{D.3})$$

with $\gamma_{\mathbf{q}} = |\gamma_{\mathbf{q}}| e^{i\Theta}$ and $|\Omega_0\rangle$ the LO phonon vacuum, from Eq. (D.1) we obtain

$$\langle \Omega | \hat{x}_{\mathbf{q}} \hat{x}_{-\mathbf{q}} | \Omega \rangle = \frac{\hbar}{2M\omega_{LO}} \left(\cosh^2 |\gamma_{\mathbf{q}}| + \sinh^2 |\gamma_{\mathbf{q}}| + 2 \cos \Theta \cosh |\gamma_{\mathbf{q}}| \sinh |\gamma_{\mathbf{q}}| \right). \quad (\text{D.4})$$

For $\Theta = \pi$, the squeezed state is elongated along the real-space coordinate $x_{\mathbf{q}}$. Thus, assuming that the LO phonon is fully screened and that the zero-point motion is characterized by the TO frequency, we get

$$\langle \Omega | \hat{x}_{\mathbf{q}} \hat{x}_{-\mathbf{q}} | \Omega \rangle = \frac{\hbar}{2M\omega_{LO}} e^{2|\gamma|} = \frac{\hbar}{2M\omega_{TO}}. \quad (\text{D.5})$$

For GaAs and TiO₂, $e^{2|\gamma|} = \omega_{LO}/\omega_{TO} = \sqrt{\varepsilon_0/\varepsilon_\infty}$ approximately equals $e^{2|\gamma|} \approx 1.08$ and $e^{2|\gamma|} \approx 2.78$, respectively. Those are almost the same values of the total phonon spectral weights

obtained in Figs. 9.3(f) and 9.5(f) for the soft $q \approx 0$ phonon, which frequency is very close to ω_{TO} .

References

- [1] M. Thomson, *Modern Particle Physics*. Cambridge University Press, Cambridge, UK, 2013.
- [2] P. W. Anderson, “More Is Different”, *Science* **177**, 393 (1972).
- [3] F. A. J. Haas, *Aristotle: On generation and corruption, book I: Symposium Aristotelicum*. Clarendon Press, Oxford, UK, 2004.
- [4] N. W. Ashcroft and N. D. Mermin, *Solid State Physics*. Harcourt College Publishers, Orlando, FL, 1976.
- [5] L. D. Landau, “The theory of a Fermi liquid”, *J. Exp. Theor. Phys.* **3**, 920 (1957).
- [6] D. Bohm and D. Pines, “A Collective Description of Electron Interactions. I. Magnetic Interactions”, *Phys. Rev.* **82**, 625–634 (1951).
- [7] D. Pines and D. Bohm, “A Collective Description of Electron Interactions: II. Collective vs Individual Particle Aspects of the Interactions”, *Phys. Rev.* **85**, 338–353 (1952).
- [8] D. Bohm and D. Pines, “A Collective Description of Electron Interactions: III. Coulomb Interactions in a Degenerate Electron Gas”, *Phys. Rev.* **92**, 609–625 (1953).
- [9] J. Bardeen, L. N. Cooper, and J. R. Schrieffer, “Theory of Superconductivity”, *Phys. Rev.* **108**, 1175–1204 (1957).
- [10] H. Kamerlingh Onnes *Commun. Phys. Lab. Univ. Leiden. Suppl.* **29** (1911).
- [11] C. Proust and L. Taillefer, “The Remarkable Underlying Ground States of Cuprate Superconductors”, *Annu. Rev. Condens. Matter Phys.* **10**, 409 (2019).
- [12] C. N. R. Rao, “Transition Metal Oxides”, *Annu. Rev. Phys. Chem.* **40**, 291 (1989).
- [13] M. N. Gastiasoro, J. Ruhman, and R. M. Fernandes, “Superconductivity in dilute SrTiO₃: A review”, *Ann. Phys. (N. Y.)* **417**, 168107 (2020).
- [14] K. Kanoda and R. Kato, “Mott Physics in Organic Conductors with Triangular Lattices”, *Annu. Rev. Condens. Matter Phys.* **2**, 167 (2011).
- [15] P. Hohenberg and W. Kohn, “Inhomogeneous Electron Gas”, *Phys. Rev.* **136**, B864 (1964).

- [16] A. Fetter and J. D. Walecka, *Quantum Theory of Many-Particle Systems*. The McGraw-Hill Book Company, USA, 1971.
- [17] J. Krsnik, I. Batistić, A. Marunović, E. Tutiš, and O. S. Barišić, “Exact solution of electronic transport in semiconductors dominated by scattering on polaronic impurities”, *Phys. Rev. B* **102**, 241111 (2020).
- [18] J. Bonča and S. A. Trugman, “Effect of Inelastic Processes on Tunneling”, *Phys. Rev. Lett.* **75**, 2566–2569 (1995).
- [19] J. Bonča and S. A. Trugman, “Inelastic Quantum Transport”, *Phys. Rev. Lett.* **79**, 4874–4877 (1997).
- [20] K. Haule and J. Bonča, “Inelastic tunneling through mesoscopic structures”, *Phys. Rev. B* **59**, 13087–13093 (1999).
- [21] M. A. Reed, “Inelastic electron tunneling spectroscopy”, *Mater. Today* **11**, 46–50 (2008).
- [22] R. C. Jaklevic and J. Lambe, “Molecular Vibration Spectra by Electron Tunneling”, *Phys. Rev. Lett.* **17**, 1139–1140 (1966).
- [23] J. Lambe and R. C. Jaklevic, “Molecular Vibration Spectra by Inelastic Electron Tunneling”, *Phys. Rev.* **165**, 821–832 (1968).
- [24] V. J. Goldman, D. C. Tsui, and J. E. Cunningham, “Evidence for LO-phonon-emission-assisted tunneling in double-barrier heterostructures”, *Phys. Rev. B* **36**, 7635–7637 (1987).
- [25] J. R. Hahn and W. Ho, “Oxidation of a Single Carbon Monoxide Molecule Manipulated and Induced with a Scanning Tunneling Microscope”, *Phys. Rev. Lett.* **87**, 166102 (2001).
- [26] J. R. Hahn and W. Ho, “Single Molecule Imaging and Vibrational Spectroscopy with a Chemically Modified Tip of a Scanning Tunneling Microscope”, *Phys. Rev. Lett.* **87**, 196102 (2001).
- [27] L. H. Yu, Z. K. Keane, J. W. Ciszek, L. Cheng, M. P. Stewart, J. M. Tour, and D. Natelson, “Inelastic Electron Tunneling via Molecular Vibrations in Single-Molecule Transistors”, *Phys. Rev. Lett.* **93**, 266802 (2004).
- [28] W. H. A. Thijssen, D. Djukic, A. F. Otte, R. H. Bremmer, and J. M. van Ruitenbeek, “Vibrationally Induced Two-Level Systems in Single-Molecule Junctions”, *Phys. Rev. Lett.* **97**, 226806 (2006).
- [29] X. Mettan, J. Jaćimović, O. S. Barišić, A. Pisoni, I. Batistić, E. Horváth, S. Brown, L. Rossi, P. Szirmai, B. Farkas, H. Berger, and L. Forró, “Tailoring thermal conduction in anatase TiO₂”, *Commun. Phys.* **2**, 123 (2019).

- [30] N. Karl, “Charge carrier transport in organic semiconductors”, *Synth. Met.* **133**, 649–657 (2003).
- [31] Y. Krupskaya, M. Gibertini, N. Marzari, and A. F. Morpurgo, “Band-Like Electron Transport with Record-High Mobility in the TCNQ Family”, *Adv. Mater.* **27**, 2453–2458 (2015).
- [32] V. Podzorov, E. Menard, A. Borissov, V. Kiryukhin, J. A. Rogers, and M. E. Gershenson, “Intrinsic Charge Transport on the Surface of Organic Semiconductors”, *Phys. Rev. Lett.* **93**, 086602 (2004).
- [33] V. M. Kenkre, J. D. Andersen, D. H. Dunlap, and C. B. Duke, “Unified theory of the mobilities of photoinjected electrons in naphthalene”, *Phys. Rev. Lett.* **62**, 1165–1168 (1989).
- [34] L. Giuggioli, J. D. Andersen, and V. M. Kenkre, “Mobility theory of intermediate-bandwidth carriers in organic crystals: Scattering by acoustic and optical phonons”, *Phys. Rev. B* **67**, 045110 (2003).
- [35] A. Troisi, “Prediction of the Absolute Charge Mobility of Molecular Semiconductors: the Case of Rubrene”, *Adv. Mater.* **19**, 2000–2004 (2007).
- [36] S. Fratini and S. Ciuchi, “Bandlike motion and mobility saturation in organic molecular semiconductors”, *Phys. Rev. Lett.* **103**, 266601 (2009).
- [37] G. Nan, X. Yang, L. Wang, Z. Shuai, and Y. Zhao, “Nuclear tunneling effects of charge transport in rubrene, tetracene, and pentacene”, *Phys. Rev. B* **79**, 115203 (2009).
- [38] S. Ciuchi, S. Fratini, and D. Mayou, “Transient localization in crystalline organic semiconductors”, *Phys. Rev. B* **83**, 081202 (2011).
- [39] X. Wang and A. Dodabalapur, “Going beyond polaronic theories in describing charge transport in rubrene single crystals”, *Appl. Phys. Lett.* **116**, 093301 (2020).
- [40] G. D. Mahan, *Many-Particle Physics, 3rd edition*. Kluwer Academic/Plenum Publishers, New York, 2000.
- [41] E. N. Economou, *Green’s Functions in Quantum Physics*. Springer, Berlin Heidelberg, 2006.
- [42] M. Cini and A. D’Andrea, “Resonant broadening of quasi-atomic Auger spectra by elementary excitations”, *J. Phys. C: Solid State Phys.* **16**, 4469–4478 (1983).
- [43] B. Y. Gelfand, S. Schmitt-Rink, and A. F. J. Levi, “Tunneling in the presence of phonons: A solvable model”, *Phys. Rev. Lett.* **62**, 1683–1686 (1989).

- [44] J. Loos, T. Koch, A. Alvermann, A. R. Bishop, and H. Fehske, “Phonon affected transport through molecular quantum dots”, *J. Condens. Matter Phys.* **21**, 395601 (2009).
- [45] R. Härtle and M. Thoss, “Vibrational instabilities in resonant electron transport through single-molecule junctions”, *Phys. Rev. B* **83**, 125419 (2011).
- [46] J. Lu, R. Wang, J. Ren, M. Kulkarni, and J.-H. Jiang, “Quantum-dot circuit-QED thermoelectric diodes and transistors”, *Phys. Rev. B* **99**, 035129 (2019).
- [47] X. Zotos, F. Naef, and P. Prelovsek, “Transport and conservation laws”, *Phys. Rev. B* **55**, 11029–11032 (1997).
- [48] L. I. Schiff, *Quantum Mechanics*. McGraw-Hill, USA, 1968.
- [49] T. Horiguchi and T. Morita, “Note on the lattice Green's function for the simple cubic lattice”, *J. Phys. C Solid State Phys.* **8**, L232–L235 (1975).
- [50] T. Morita and T. Horiguchi, “Lattice Green's Functions for the Cubic Lattices in Terms of the Complete Elliptic Integral”, *J. Math. Phys.* **12**, 981–986 (1971).
- [51] S. Katsura and S. Inawashiro, “Asymptotic Form of the Lattice Green's Function of the Simple Cubic Lattice”, *Prog. Theor. Phys.* **50**, 82–94 (1973).
- [52] J. Callaway, “Theory of Scattering in Solids”, *J. Math. Phys.* **5**, 783–798 (1964).
- [53] O. L. Krivanek, M. F. Chisholm, V. Nicolosi, T. J. Pennycook, G. J. Corbin, N. Dellby, M. F. Murfitt, C. S. Own, Z. S. Szilagyí, M. P. Oxley, P. S. T., and S. J. Pennycook, “Atom-by-atom structural and chemical analysis by annular dark-field electron microscopy”, *Nature* **464**, 571–574 (2010).
- [54] M. Berthe, A. Urbieto, L. Perdigão, B. Grandidier, D. Deresmes, C. Delerue, D. Stiévenard, R. Rurali, N. Lorente, L. Magaud, and P. Ordejón, “Electron Transport via Local Polarons at Interface Atoms”, *Phys. Rev. Lett.* **97**, 206801 (2006).
- [55] M. Rashidi, J. A. J. Burgess, M. Taucer, R. Achal, J. L. Pitters, S. Loth, and R. A. Wolkow, “Time-resolved single dopant charge dynamics in silicon”, *Nat. Commun.* **7**, 13258 (2016).
- [56] I. Delač Marion, D. Čapeta, B. Pielić, F. Faraguna, A. Gallardo, P. Pou, B. Biel, N. Vujičić, and M. Kralj, “Atomic-scale defects and electronic properties of a transferred synthesized MoS₂ monolayer”, *Nanotechnology* **29**, 305703 (2018).
- [57] H. Ebrahimnejad and M. Berciu, “Trapping of three-dimensional Holstein polarons by various impurities”, *Phys. Rev. B* **85**, 165117 (2012).

- [58] J. M. Ziman, *Principles of the Theory of Solids*. Cambridge University Press, Cambridge, UK, 1972.
- [59] I. S. Gradshteyn and I. M. Ryzhik, *Table of Integrals, Series, and Products*. Elsevier, USA, 2007.
- [60] L. D. Landau, “The roots of polaron theory”, *Phys. Z. Sowjetunion* **3**, 664 (1933).
- [61] S. A. Jackson and P. M. Platzman, “Polaronic aspects of two-dimensional electrons on films of liquid He”, *Phys. Rev. B* **24**, 499(R) (1981).
- [62] O. Hipolito, G. A. Farias, and N. Studart, “Localization energy and effective mass of an electron on the surface of liquid helium”, *Surf. Sci.* **113**, 394 (1982).
- [63] G. E. Marques and N. Studart, “Polaronic state of electrons on the surface of liquid-helium films: A self-consistent treatment”, *Phys. Rev. B* **39**, 4133 (1989).
- [64] R. Schmidt and M. Lemeshko, “Rotation of Quantum Impurities in the Presence of a Many-Body Environment”, *Phys. Rev. Lett.* **114**, 203001 (2015).
- [65] X. Li, G. Bighin, E. Yakaboylu, and M. Lemeshko, “Variational approaches to quantum impurities: from the Fröhlich polaron to the angulon”, *Mol. Phys.* **117**, 1981 (2019).
- [66] F. M. Cucchiatti and E. Timmermans, “Strong-Coupling Polarons in Dilute Gas Bose-Einstein Condensates”, *Phys. Rev. Lett.* **96**, 210401 (2006).
- [67] J. Tempere, W. Casteels, M. K. Oberthaler, S. Knoop, E. Timmermans, and J. T. Devreese, “Feynman path-integral treatment of the BEC-impurity polaron”, *Phys. Rev. B* **80**, 184504 (2009).
- [68] M.-G. Hu, M. J. Van de Graaff, D. Kedar, J. P. Corson, E. A. Cornell, and D. S. Jin, “Bose Polarons in the Strongly Interacting Regime”, *Phys. Rev. Lett.* **117**, 055301 (2016).
- [69] N. B. Jørgensen, L. Wacker, K. T. Skalmstang, M. M. Parish, J. Levinsen, R. S. Christensen, G. M. Bruun, and J. J. Arlt, “Observation of Attractive and Repulsive Polarons in a Bose-Einstein Condensate”, *Phys. Rev. Lett.* **117**, 055302 (2016).
- [70] C. Kittel, *Introduction to Solid State Physics*, 8th edition. John Wiley & Sons, Inc, Hoboken, NJ, 2005.
- [71] A. J. Millis, P. B. Littlewood, and B. I. Shraiman, “Double Exchange Alone Does Not Explain the Resistivity of $\text{La}_{1-x}\text{Sr}_2\text{MnO}_3$ ”, *Phys. Rev. Lett.* **74**, 5144 (1995).
- [72] A. J. Millis, B. I. Shraiman, and R. Mueller, “Dynamic Jahn-Teller Effect and Colossal Magnetoresistance in $\text{La}_{1-x}\text{Sr}_2\text{MnO}_3$ ”, *Phys. Rev. Lett.* **77**, 175 (1996).

- [73] A. S. Alexandrov and A. M. Bratkovsky, “Carrier Density Collapse and Colossal Magnetoresistance in Doped Manganites”, *Phys. Rev. Lett.* **82**, 141 (1999).
- [74] D. M. Edwards, “Ferromagnetism and electron-phonon coupling in the manganites”, *Adv. Phys.* **51**, 1259 (2002).
- [75] C. Hartinger, F. Mayr, A. Loidl, and T. Kopp, “Polaronic excitations in colossal magnetoresistance manganite films”, *Phys. Rev. B* **73**, 024408 (2006).
- [76] A. J. Heeger, S. Kivelson, J. R. Schrieffer, and W. P. Su, “Solitons in conducting polymers”, *Rev. Mod. Phys.* **60**, 781–850 (1988).
- [77] J. Takeda, M. Okada, S. Kurita, K. Tanaka, and T. Suemoto, “Resonance Raman enhancement for photoinduced polaronic states of a quasi-one-dimensional mixed-valence platinum complex”, *Phys. Rev. B* **52**, 14441–14444 (1995).
- [78] G. S. Kanner, G. F. Strouse, B. I. Swanson, M. Sinclair, J. P. Jiang, and N. Peyghambarian, “Subpicosecond dynamics of excitons and photoexcited intrinsic polarons in the quasi-one-dimensional solid PtCl”, *Phys. Rev. B* **56**, 2501–2509 (1997).
- [79] H. Okamoto, Y. Kaga, Y. Shimada, Y. Oka, Y. Iwasa, T. Mitani, and M. Yamashita, “Conversion of Excitons to Spin-Soliton Pairs in Quasi-One-Dimensional Halogen-Bridged Metal Complexes”, *Phys. Rev. Lett.* **80**, 861–864 (1998).
- [80] B. I. Swanson, J. A. Brozik, S. P. Love, G. F. Strouse, A. P. Shreve, A. R. Bishop, W.-Z. Wang, and M. I. Salkola, “Observation of Intrinsically Localized Modes in a Discrete Low-Dimensional Material”, *Phys. Rev. Lett.* **82**, 3288–3291 (1999).
- [81] S. Tretiak, A. Piryatinski, A. Saxena, R. L. Martin, and A. R. Bishop, “On the existence of photoexcited breathers in conducting polymers”, *Phys. Rev. B* **70**, 233203 (2004).
- [82] H. C. F. Martens and H. B. Brom, “A quantitative evaluation of metallic conduction in conjugated polymers”, *Phys. Rev. B* **70**, 241201 (2004).
- [83] J. Sólyom, *Fundamentals of the Physics of Solids, Volume III: Normal, Broken-Symmetry, and Correlated Systems*. Springer, Berlin Heidelberg, 2010.
- [84] S. Moser, L. Moreschini, J. Jaćimović, O. S. Barišić, H. Berger, A. Magrez, Y. J. Chang, K. S. Kim, A. Bostwick, E. Rotenberg, L. Forró, and M. Grioni, “Tunable Polaronic Conduction in Anatase TiO₂”, *Phys. Rev. Lett.* **110**, 196403 (2013).
- [85] C. Chen, J. Avila, E. Frantteskakis, A. Levy, and M. C. Asensio, “Observation of a two-dimensional liquid of Fröhlich polarons at the bare SrTiO₃ surface”, *Nat. Commun.* **6**, 8585 (2015).

- [86] R. Yukawa, K. Ozawa, S. Yamamoto, H. Iwasawa, K. Shimada, E. F. Schwier, K. Yoshimatsu, H. Kumigashira, H. Namatame, M. Taniguchi, and I. Matsuda, “Phonon-dressed two-dimensional carriers on the ZnO surface”, *Phys. Rev. B* **94**, 165313 (2016).
- [87] C. Cancellieri, A. S. Mishchenko, U. Achauer, A. Filippetti, C. Faber, O. S. Barišić, V. A. Rogalev, T. Schmitt, N. Nagaosa, and V. N. Strocov, “Polaronic metal state at the LaAlO₃/SrTiO₃ interface”, *Nat. Commun.* **7**, 10386 (2016).
- [88] N. Plakida, *High-Temperature Cuprate Superconductors: Experiment, Theory and Applications*. Springer, Berlin Heidelberg, 2010.
- [89] A. Damascelli, Z. Hussain, and Z.-X. Shen, “Angle-resolved photoemission studies of the cuprate superconductors”, *Rev. Mod. Phys.* **75**, 473 (2003).
- [90] A. R. Bishop, D. Mihailovic, and J. Mustre de Leone, “Signatures of mesoscopic Jahn-Teller polaron inhomogeneities in high-temperature superconductors”, *J. Phys.: Condens. Matter* **15**, L169 (2003).
- [91] L. Cappelluti and L. Pietronero, “Nonadiabatic electron–phonon effects in low carrier density superconductors”, *Phys. Stat. Sol. (B)* **242**, 133 (2004).
- [92] J. C. Zhang, E. M. Levenson-Falk, B. J. Ramshaw, D. A. Bonn, R. Liang, W. N. Hardy, S. Hartnoll, and A. Kapitulnik, “Anomalous Thermal Diffusivity in Underdoped YBa₂Cu₃O_{6+x}”, *Proc. Natl. Acad. Sci. U.S.A.* **114**, 5378 (2017).
- [93] J. Zhang, E. D. Kountz, E. M. Levenson-Falk, D. Song, R. L. Greene, and A. Kapitulnik, “Thermal diffusivity above the Mott-Ioffe-Regel limit”, *Phys. Rev. B* **100**, 241114 (2019).
- [94] C. H. Mousatov and S. A. Hartnoll, “Phonons, electrons and thermal transport in Planckian high T_c materials”, *npj Quantum Mater.* **6**, 81 (2021).
- [95] A. S. Alexandrov and N. Mott, *Polarons and Bipolarons*. World Scientific Publishing Co. Pte. Ltd., Singapore, 1995.
- [96] O. S. Barišić and B. S., “Phase diagram of the Holstein polaron in one dimension”, *Eur. Phys. J. B* **64**, 1–18 (2008).
- [97] A. H. Romero, D. W. Brown, and K. Lindenberg, “Polaron effective mass, band distortion, and self-trapping in the Holstein molecular-crystal model”, *Phys. Rev. B* **59**, 13728–13740 (1999).
- [98] B. Gerlach and H. Löwen, “Proof of the nonexistence of (formal) phase transitions in polaron systems. I”, *Phys. Rev. B* **35**, 4291–4296 (1987).

- [99] H. Löwen, “Absence of phase transitions in Holstein systems”, *Phys. Rev. B* **37**, 8661–8667 (1988).
- [100] R. P. Feynman, “Slow Electrons in a Polar Crystal”, *Phys. Rev.* **97**, 660–665 (1955).
- [101] J. Bonča, S. A. Trugman, and I. Batistčić, “Holstein polaron”, *Phys. Rev. B* **60**, 1633 (1999).
- [102] O. S. Barišić, “Holstein light quantum polarons on the one-dimensional lattice”, *Phys. Rev. B* **73**, 214304 (2006).
- [103] E. Jeckelmann and S. R. White, “Density-matrix renormalization-group study of the polaron problem in the Holstein model”, *Phys. Rev. B* **57**, 6376 (1998).
- [104] N. V. Prokof’ev and B. V. Svistunov, “Polaron Problem by Diagrammatic Quantum Monte Carlo”, *Phys. Rev. Lett.* **81**, 2514 (1998).
- [105] A. S. Mishchenko, N. V. Prokof’ev, A. Sakamoto, and B. V. Svistunov, “Diagrammatic quantum Monte Carlo study of the Fröhlich polaron”, *Phys. Rev. B* **62**, 6317 (2000).
- [106] E. Y. Loh, J. E. Gubernatis, R. T. Scalettar, S. R. White, D. J. Scalapino, and R. L. Sugar, “Sign problem in the numerical simulation of many-electron systems”, *Phys. Rev. B* **41**, 9301 (1990).
- [107] A. S. Mishchenko, N. Nagaosa, N. V. Prokof’ev, A. Sakamoto, and B. V. Svistunov, “Optical Conductivity of the Fröhlich Polaron”, *Phys. Rev. Lett.* **91**, 236401 (2003).
- [108] A. S. Mishchenko, L. Pollet, N. V. Prokof’ev, A. Kumar, D. L. Maslov, and N. Nagaosa, “Polaron Mobility in the “Beyond Quasiparticles” Regime”, *Phys. Rev. Lett.* **123**, 076601 (2019).
- [109] S. Ciuchi, F. de Pasquale, S. Fratini, and D. Feinberg, “Dynamical mean-field theory of the small polaron”, *Phys. Rev. B* **56**, 4494 (1997).
- [110] O. S. Barišić, “Diagrammatic content of the dynamical mean-field theory for the Holstein polaron problem in finite dimensions”, *Phys. Rev. B* **76**, 193106 (2007).
- [111] O. S. Barišić, “Comment on “Green’s Function of a Dressed Particle””, *Phys. Rev. Lett.* **98**, 209701 (2007).
- [112] M. Berciu, “Green’s Function of a Dressed Particle”, *Phys. Rev. Lett.* **97**, 036402 (2006).
- [113] G. L. Goodvin, M. Berciu, and G. A. Sawatzky, “Green’s function of the Holstein polaron”, *Phys. Rev. B* **74**, 245104 (2006).
- [114] M. Jarrell, “Hubbard model in infinite dimensions: A quantum Monte Carlo study”, *Phys. Rev. Lett.* **69**, 168–171 (1992).

- [115] O. S. Barišić and S. Barišić, “Quantum adiabatic polarons by translationally invariant perturbation theory”, *Eur. Phys. J. B* **54**, 1–9 (2006).
- [116] M. V. Tkach, J. O. Seti, O. M. Voitsekhivska, and O. Y. Pytiuk, “Renormalized energy of ground and first excited state of Fröhlich polaron in the range of weak coupling”, *Condens. Matter Phys.* **18**, 33707 (2015).
- [117] V. V. Kabanov, “Adiabatic theory of the polaron spectral function.” arXiv:2011.08638, 2020.
- [118] O. S. Barišić, *Holsteinovi polaroni i bipolaroni*. Doktorska disertacija, Prirodoslovno-matematički fakultet, Sveučilište u Zagrebu, 2005.
- [119] A. B. Migdal, “Interaction Between Electrons and Lattice Vibrations in a Normal Metal”, *J. Exptl. Theoret. Phys. (U.S.S.R.)* **34**, 1438–1446 (1958).
- [120] I. G. Lang and Y. A. Firsov *Zh. Eksp. Teor. Fiz.* **43**, 1843 (1962).
- [121] A. S. Alexandrov and J. Ranninger, “Polaronic effects in the photoemission spectra of strongly coupled electron-phonon systems”, *Phys. Rev. B* **45**, 13109–13112 (1992).
- [122] J. Loos, M. Hohenadler, A. Alvermann, and H. Fehske, “Phonon spectral function of the Holstein polaron”, *J. Condens. Matter Phys.* **18**, 7299–7312 (2006).
- [123] J. C. Ward, “An Identity in Quantum Electrodynamics”, *Phys. Rev.* **78**, 182–182 (1950).
- [124] Z. H. Levine and E. Cockayne, “The Pole Term in Linear Response Theory: An Example From the Transverse Response of the Electron Gas”, *J. Res. Natl. Inst. Stand. Technol.* **113**, 229 (2008).
- [125] J. Krsnik, V. N. Strocov, N. Nagaosa, O. S. Barišić, Z. Rukelj, S. M. Yakubanya, and A. S. Mishchenko, “Manifestations of the electron-phonon interaction range in angle-resolved photoemission spectra”, *Phys. Rev. B* **102**, 121108 (2020).
- [126] J. Schrieffer, *Theory Of Superconductivity*. Westview Press, USA, 1983.
- [127] X. Zhu, Y. Cao, J. Zhang, E. W. Plummer, and J. Guo, “Classification of charge density waves based on their nature”, *Proc. Natl. Acas. Sci. U.S.A.* **112**, 2367–2371 (2015).
- [128] J.-P. Pouget, “The Peierls instability and charge density wave in one-dimensional electronic conductors”, *C. R. Physique* **17**, 332–356 (2016).
- [129] M. Hohenadler and H. Fehske, “Density waves in strongly correlated quantum chains”, *Eur. Phys. J. B* **91**, 204 (2018).

- [130] C. Verdi, F. Caruso, and F. Giustino, “Origin of the crossover from polarons to Fermi liquids in transition metal oxides”, *Nat. Commun.* **8**, 15769 (2017).
- [131] F. Caruso, C. Verdi, S. Poncé, and F. Giustino, “Electron-plasmon and electron-phonon satellites in the angle-resolved photoelectron spectra of *n*-doped anatase TiO₂”, *Phys. Rev. B* **97**, 165113 (2018).
- [132] A. Mooradian and G. B. Wright, “Observation of the Interaction of Plasmons with Longitudinal Optical Phonons in GaAs”, *Phys. Rev. Lett.* **16**, 999–1001 (1966).
- [133] G. Abstreiter, R. Trommer, M. Cardona, and A. Pinczuk, “Coupled plasmon-LO phonon modes and Lindhard-Mermin dielectric function of *n*-GaAs”, *Solid State Commun.* **30**, 703–707 (1979).
- [134] B. Tell and R. J. Martin, “Raman Scattering by Coupled Optical-Phonon-Plasmon Modes in GaAs”, *Phys. Rev.* **167**, 381–386 (1968).
- [135] K. Murase, S. Katayama, Y. Ando, and H. Kawamura, “Observation of a Coupled Phonon-Damped-Plasmon Mode in *n*-GaAs by Raman Scattering”, *Phys. Rev. Lett.* **33**, 1481–1484 (1974).
- [136] K. M. Romanek, H. Nather, and E. O. Göbel, “Light scattering from optically excited electron-hole plasmas in GaAs”, *Solid State Commun.* **39**, 23–26 (1981).
- [137] R. Fukasawa and S. Perkowitz, “Raman-scattering spectra of coupled LO-phonon–hole-plasmon modes in p-type GaAs”, *Phys. Rev. B* **50**, 14119–14124 (1994).
- [138] C. G. Olson and D. W. Lynch, “Longitudinal-Optical-Phonon-Plasmon Coupling in GaAs”, *Phys. Rev.* **177**, 1231–1234 (1969).
- [139] A. A. Kukharskii, “Plasmon-phonon coupling in GaAs”, *Solid State Commun.* **13**, no. 11, 1761–1765 (1973).
- [140] H. R. Chandrasekhar and A. K. Ramdas, “Nonparabolicity of the conduction band and the coupled plasmon-phonon modes in *n*-GaAs”, *Phys. Rev. B* **21**, 1511–1515 (1980).
- [141] F. Gervais, J.-L. Servoin, A. Baratoff, J. G. Bednorz, and G. Binnig, “Temperature dependence of plasmons in Nb-doped SrTiO₃”, *Phys. Rev. B* **47**, 8187–8194 (1993).
- [142] C. Z. Bi, J. Y. Ma, J. Yan, X. Fang, B. R. Zhao, D. Z. Yao, and X. G. Qiu, “Electron–phonon coupling in Nb-doped SrTiO₃ single crystal”, *J. Condens. Matter Phys.* **18**, 2553–2561 (2006).
- [143] M. Radović, Z. Dohčević-Mitrović, N. Paunović, S. Bošković, N. Tomić, N. Tadić, and I. Belča, “Infrared study of plasmon-phonon coupling in pure and Nd-doped CeO_{2-y} nanocrystals”, *J. Phys. D: Appl. Phys* **48**, 065301 (2015).

- [144] P. Coleman, *Introduction to Many-Body Physics*. Cambridge University Press, Cambridge, UK, 2015.
- [145] R. D. Mattuck, *A Guide to Feynman Diagrams in the Many-body Problem*. The McGraw-Hill Book Company, USA, 1967.
- [146] A. S. Alexandrov, *Theory of Superconductivity: From Weak to Strong Coupling*. CRC Press, Boca Raton, FL, 2003.
- [147] Z. Wang, S. McKeown Walker, A. Tamai, Y. Wang, Z. Ristic, F. Y. Bruno, A. de la Torre, S. Riccò, N. C. Plumb, M. Shi, P. Hlawenka, J. Sánchez-Barriga, V. A., T. K. Kim, M. Hoesch, P. D. C. King, W. Meevasana, U. Diebold, J. Mesot, B. Moritz, T. P. Devereaux, and F. Radovic, M. abd Baumberger, “Tailoring the nature and strength of electron–phonon interactions in the SrTiO₃(001) 2D electron liquid”, *Nat. Mater.* **15**, 935 (2016).
- [148] C. Zhang, Z. Liu, Z. Chen, Y. Xie, R. He, S. Tang, J. He, W. Li, T. Jia, S. N. Rebec, E. Y. Ma, Y. H., M. Hashimoto, D. Lu, S.-K. Mo, Y. Hikita, R. G. Moore, H. Y. Hwang, D. Lee, and Z. Shen, “Ubiquitous strong electron–phonon coupling at the interface of FeSe/SrTiO₃”, *Nat. Commun.* **8**, 14468 (2017).
- [149] J. M. Riley, F. Caruso, C. Verdi, L. B. Duffy, M. D. Watson, L. Bawden, K. Volckaert, G. van der Lann, T. Hesjedal, M. Hoesch, F. Giustino, and P. D. C. King, “Crossover from lattice to plasmonic polarons of a spin-polarised electron gas in ferromagnetic EuO”, *Nat. Commun.* **9**, 2305 (2018).
- [150] M.-A. Husanu, L. Vistoli, C. Verdi, A. Sander, V. Garcia, J. Rault, F. Bisti, L. L. Lev, T. Schmitt, F. Giustino, A. S. Mishchenko, M. Bibes, and V. N. Strocov, “Electron-polaron dichotomy of charge carriers in perovskite oxides”, *Commun. Phys.* **3**, 62 (2020).
- [151] F. Giustino, “Electron-phonon interactions from first principles”, *Rev. Mod. Phys.* **89**, 015003 (2017).
- [152] G. Antonius, S. Poncé, E. Lantagne-Hurtubise, G. Auclair, X. Gonze, and M. Côté, “Dynamical and anharmonic effects on the electron-phonon coupling and the zero-point renormalization of the electronic structure”, *Phys. Rev. B* **92**, 085137 (2015).
- [153] S. Poncé, E. Margine, C. Verdi, and F. Giustino, “EPW: Electron–phonon coupling, transport and superconducting properties using maximally localized Wannier functions”, *Comput. Phys. Commun.* **209**, 116–133 (2016).
- [154] S. M. Story, J. J. Kas, F. D. Vila, M. J. Verstraete, and J. J. Rehr, “Cumulant expansion for phonon contributions to the electron spectral function”, *Phys. Rev. B* **90**, 195135 (2014).

- [155] B. Gumhalter, V. Kovač, F. Caruso, H. Lambert, and F. Giustino, “On the combined use of GW approximation and cumulant expansion in the calculations of quasiparticle spectra: The paradigm of Si valence bands”, *Phys. Rev. B* **94**, 035103 (2016).
- [156] J. T. Devreese and A. S. Alexandrov, “Fröhlich polaron and bipolaron: recent developments”, *Rep. Prog. Phys.* **72**, 066501 (2009).
- [157] F. M. Peeters, W. Xiaoguang, and J. T. Devreese, “Ground-state energy of a polaron in n dimensions”, *Phys. Rev. B* **33**, 3926–3934 (1986).
- [158] A. Chikina, F. Lechermann, M.-A. Husanu, M. Caputo, C. Cancellieri, X. Wang, T. Schmitt, M. Radovic, and V. N. Strocov, “Orbital Ordering of the Mobile and Localized Electrons at Oxygen-Deficient $\text{LaAlO}_3/\text{SrTiO}_3$ Interfaces”, *ACS Nano* **12**, 7927 (2018).
- [159] J. Krsnik and O. S. Barišić, “Importance of coupling strength in shaping electron energy loss and phonon spectra of phonon-plasmon systems”, *Phys. Rev. B* **106**, 075207 (2022).
- [160] I. Yokota, “On the Coupling between Optical Lattice Vibrations and Carrier Plasma Oscillations in Polar Semiconductors”, *J. Phys. Soc. Japan* **16**, 2075–2075 (1961).
- [161] B. B. Varga, “Coupling of Plasmons to Polar Phonons in Degenerate Semiconductors”, *Phys. Rev.* **137**, A1896–A1902 (1965).
- [162] K. S. Singwi and M. P. Tosi, “Interaction of Plasmons and Optical Phonons in Degenerate Semiconductors”, *Phys. Rev.* **147**, 658–662 (1966).
- [163] W. Cochran, R. A. Cowley, G. Dolling, and M. M. Elcombe, “The crystal dynamics of lead telluride”, *Proc. R. Soc. A: Math. Phys. Eng. Sci.* **293**, 433–451 (1966).
- [164] T. Inaoka, “Structure of coupled plasmon-phonon modes in degenerate polar semiconductors”, *J. Phys.: Condens. Matter* **3**, 4825–4840 (1991).
- [165] K. Ishioka, A. K. Basak, and H. Petek, “Allowed and forbidden Raman scattering mechanisms for detection of coherent LO phonon and plasmon-coupled modes in GaAs”, *Phys. Rev. B* **84**, 235202 (2011).
- [166] Basak, A. K. and Petek, H. and Ishioka, K. and Thatcher, E. M. and Stanton, C. J., “Ultrafast coupling of coherent phonons with a nonequilibrium electron-hole plasma in GaAs”, *Phys. Rev. B* **91**, 125201 (2015).
- [167] K. Ishioka, K. Brixius, U. Höfer, A. Rustagi, E. M. Thatcher, C. J. Stanton, and H. Petek, “Dynamically coupled plasmon-phonon modes in GaP: An indirect-gap polar semiconductor”, *Phys. Rev. B* **92**, 205203 (2015).

- [168] J. Hu, H. Zhang, Y. Sun, O. V. Misochko, and K. G. Nakamura, “Temperature effect on the coupling between coherent longitudinal phonons and plasmons in n -type and p -type GaAs”, *Phys. Rev. B* **97**, 165307 (2018).
- [169] A. Czachor, A. Holas, S. R. Sharma, and K. S. Singwi, “Dynamical correlations in a two-dimensional electron gas: First-order perturbation theory”, *Phys. Rev. B* **25**, 2144–2159 (1982).
- [170] Y. Liu and R. F. Willis, “Plasmon-phonon strongly coupled mode in epitaxial graphene”, *Phys. Rev. B* **81**, 081406 (2010).
- [171] R. J. Koch, T. Seyller, and J. A. Schaefer, “Strong phonon-plasmon coupled modes in the graphene/silicon carbide heterosystem”, *Phys. Rev. B* **82**, 201413 (2010).
- [172] Z. Fei, G. O. Andreev, W. Bao, L. M. Zhang, A. S. McLeod, C. Wang, M. K. Stewart, Z. Zhao, G. Dominguez, M. Thiemens, M. M. Fogler, M. J. Tauber, A. H. Castro-Neto, C. N. Lau, F. Keilmann, and D. N. Basov, “Infrared Nanoscopy of Dirac Plasmons at the Graphene–SiO₂ Interface”, *Nano Lett.* **11**, 4701–4705 (2011).
- [173] H. Yan, T. Low, W. Zhu, Y. Wu, M. Freitag, X. Li, F. Guinea, P. Avouris, and F. Xia, “Damping pathways of mid-infrared plasmons in graphene nanostructures”, *Nat. Photonics* **7**, 394–399 (2013).
- [174] X. Zhu, W. Wang, W. Yan, M. B. Larsen, P. Bøggild, T. Garm Pederson, S. Xiao, J. Zi, and N. A. Mortensen, “Plasmon–Phonon Coupling in Large-Area Graphene Dot and Antidot Arrays Fabricated by Nanosphere Lithography”, *Nano Lett.* **14**, 2907–2913 (2014).
- [175] I. D. Barcelos, A. R. Cadore, A. B. Alencar, F. C. B. Maia, E. Mania, R. F. Oliveira, C. C. B. Bufon, A. Malachias, E. O. Freitas, R. L. Moreira, and H. Chacham, “Infrared Fingerprints of Natural 2D Talc and Plasmon–Phonon Coupling in Graphene–Talc Heterostructures”, *ACS Photonics* **5**, 1912–1918 (2018).
- [176] F. J. Bezares, A. De Sanctis, J. R. M. Saavedra, A. Woessner, P. Alonso-González, I. Amenabar, J. Chen, T. H. Bointon, S. Dai, M. M. Fogler, D. N. Basov, R. Hillenbrand, M. F. Craciun, F. García de Abajo, S. Russo, and F. H. L. Koppens, “Intrinsic Plasmon–Phonon Interactions in Highly Doped Graphene: A Near-Field Imaging Study”, *Nano Lett.* **17**, 5908–5913 (2017).
- [177] K. Kaasbjerg, K. S. Thygesen, and K. W. Jacobsen, “Phonon-limited mobility in n -type single-layer MoS₂ from first principles”, *Phys. Rev. B* **85**, 115317 (2012).
- [178] K. Kaasbjerg, K. S. Thygesen, and A.-P. Jauho, “Acoustic phonon limited mobility in two-dimensional semiconductors: Deformation potential and piezoelectric scattering in monolayer MoS₂ from first principles”, *Phys. Rev. B* **87**, 235312 (2013).

- [179] M. Kang, S. Won Jung, W. J. Shin, Y. Sohn, S. H. Ryu, T. K. Kim, M. Hoesh, and K. S. Kim, “Holstein polaron in a valley-degenerate two-dimensional semiconductor”, *Nature Mater.* **17**, 676–680 (2018).
- [180] P. Garcia-Goiricelaya, J. Lafuente-Bartolome, I. G. Gurtubay, and A. Eiguren, “Emergence of large nonadiabatic effects induced by the electron-phonon interaction on the complex vibrational quasiparticle spectrum of doped monolayer MoS₂”, *Phys. Rev. B* **101**, 054304 (2020).
- [181] D. Novko, “Broken adiabaticity induced by Lifshitz transition in MoS₂ and WS₂ single layers”, *Commun. Phys.* **3**, 30 (2020).
- [182] P. Patoka, G. Ulrich, A. E. Nguyen, L. Bartels, P. A. Dowben, V. Turkowski, T. S. Rahman, P. Hermann, B. Kästner, A. Hoehl, G. Ulm, and E. Rühl, “Nanoscale plasmonic phenomena in CVD-grown MoS₂ monolayer revealed by ultra-broadband synchrotron radiation based nano-FTIR spectroscopy and near-field microscopy”, *Opt. Express* **24**, 4600–4600 (2016).
- [183] A. Laturia, M. L. Van de Put, and W. G. Vandenberghe, “Dielectric properties of hexagonal boron nitride and transition metal dichalcogenides: from monolayer to bulk”, *npj 2D Mater. Appl.* **6**, 6 (2018).
- [184] N. Glebko, I. Aleksandrova, G. C. Tewari, T. S. Tripathi, M. Karppinen, and A. J. Karttunen, “Electronic and Vibrational Properties of TiS₂, ZrS₂, and HfS₂: Periodic Trends Studied by Dispersion-Corrected Hybrid Density Functional Methods”, *J. Phys. Chem C* **122**, 26835–26844 (2018).
- [185] S. M. Oliver, J. J. Fox, A. Hashemi, A. Singh, R. L. Cavalero, S. Yee, D. W. Snyder, R. Jaramillo, H.-P. Komsa, and P. M. Vora, “Phonons and excitons in ZrSe₂–ZrS₂ alloys”, *J. Mater. Chem. C* **8**, 5732–5743 (2020).
- [186] L. F. Lemmens and J. T. Devreese, “Collective excitations of the polaron-gas”, *Solid State Commun.* **14**, 1339–1341 (1974).
- [187] L. F. Lemmens, F. Brosens, and J. T. Devreese, “The energy loss function of the polaron gas”, *Solid State Commun.* **17**, 337–339 (1975).
- [188] W. Xiaoguang, F. M. Peeters, and J. T. Devreese, “Plasmon-phonon coupling in a two-dimensional electron gas”, *Phys. Rev. B* **32**, 6982–6985 (1985).
- [189] F. M. Peeters, W. Xiaoguang, and J. T. Devreese, “Coupled plasmon–LO-phonon modes in Ga_xIn_{1-x}As heterostructures”, *Phys. Rev. B* **36**, 7518–7522 (1987).
- [190] L. Wendler, “Landau damped collective excitations of the quasi-two-dimensional polaron gas in double heterostructures”, *Solid State Commun.* **65**, 1197–1201 (1988).

- [191] L. Wendler, R. Haupt, and V. G. Grigoryan, “Electron-phonon interaction, dynamical screening and collective excitations in heterostructures: III. Coupled intra- and intersub-band plasmon-phonons”, *Phys. B: Condens. Matter* **167**, 113–123 (1990).
- [192] E. H. Hwang, R. Sensarma, and S. Das Sarma, “Plasmon-phonon coupling in graphene”, *Phys. Rev. B* **82**, 195406 (2010).
- [193] H. M. Dong, Z. H. Tao, Y. F. Duan, F. Huang, and C. X. Zhao, “Coupled plasmon–phonon modes in monolayer MoS₂”, *J. Condens. Matter Phys.* **32**, 125703 (2019).
- [194] M. E. Kim, A. Das, and S. D. Senturia, “Electron scattering interaction with coupled plasmon-polar-phonon modes in degenerate semiconductors”, *Phys. Rev. B* **18**, 6890–6899 (1978).
- [195] H. Sato and Y. Hori, “Theoretical analysis of plasmon, polar phonon, and hot-electron energy relaxation in nondegenerate semiconductors”, *Phys. Rev. B* **36**, 6033–6039 (1987).
- [196] K.-S. Yi and H.-J. Kim, “Spectral analysis on a phonon spectral function of a solid-state plasma in a doped semiconductor”, *Curr. Appl. Phys.* **15**, 335–341 (2015).
- [197] D. Novko, “Nonadiabatic coupling effects in MgB₂ reexamined”, *Phys. Rev. B* **98**, 041112 (2018).
- [198] C. J. Powell and J. B. Swan, “Origin of the Characteristic Electron Energy Losses in Aluminum”, *Phys. Rev.* **115**, 869–875 (1959).
- [199] C. J. Powell and J. B. Swan, “Origin of the Characteristic Electron Energy Losses in Magnesium”, *Phys. Rev.* **116**, 81–83 (1959).
- [200] T. Nagao, S. Yaginuma, C. Liu, T. Inaoka, V. U. Nazarov, T. Nakayama, and M. Aono, “Plasmon confinement in atomically thin and flat metallic films”, in *Plasmonics: Metallic Nanostructures and Their Optical Properties V* (M. I. Stockman, ed.), **6641**, 113 – 121, International Society for Optics and Photonics, SPIE, (2007).
- [201] C. S. Granerød, S. R. Bilden, T. Aarholt, Y.-F. Yao, C. C. Yang, D. C. Look, L. Vines, K. M. Johansen, and O. Prytz, “Direct observation of conduction band plasmons and the related Burstein-Moss shift in highly doped semiconductors: A STEM-EELS study of Ga-doped ZnO”, *Phys. Rev. B* **98**, 115301 (2018).
- [202] H. Yang, E. L. Garfunkel, and P. E. Batson, “Probing free carrier plasmons in doped semiconductors using spatially resolved electron energy loss spectroscopy”, *Phys. Rev. B* **102**, 205427 (2020).

- [203] O. L. Krivanek, T. C. Lovejoy, N. Dellby, T. Aoki, R. W. Carpenter, P. Rez, E. Soignard, J. Zhu, P. E. Batson, M. J. Lagos, R. F. Egerton, and P. A. Crozier, “Vibrational spectroscopy in the electron microscope”, *Nature* **514**, 209–212 (2014).
- [204] V. N. Smolyaninova, J. W. Lynn, N. P. Butch, H. Chen-Mayer, J. C. Prestigiacomo, M. S. Osofsky, and I. I. Smolyaninov, “Observation of plasmon-phonons in a metamaterial superconductor using inelastic neutron scattering”, *Phys. Rev. B* **100**, 024515 (2019).
- [205] B. N. Brockhouse and A. T. Stewart, “Scattering of Neutrons by Phonons in an Aluminum Single Crystal”, *Phys. Rev.* **100**, 756–757 (1955).
- [206] D. Strauch and B. Dorner, “Phonon dispersion in GaAs”, *J. Condens. Matter Phys.* **2**, 1457–1474 (1990).
- [207] J. T. Devreese, “Fröhlich Polarons. Lecture course including detailed theoretical derivations.” arXiv:1012.4576, 2015.
- [208] F. Caruso, D. Novko, and C. Draxl, “Phonon-assisted damping of plasmons in three- and two-dimensional metals”, *Phys. Rev. B* **97**, 205118 (2018).
- [209] I. S. Tupitsyn, A. S. Mishchenko, N. Nagaosa, and N. Prokof’ev, “Coulomb and electron-phonon interactions in metals”, *Phys. Rev. B* **94**, 155145 (2016).
- [210] M. Bogdan, “Lindhard function of a d-dimensional fermi gas.” arXiv:1111.5337, 2011.
- [211] J. Tempere and J. T. Devreese, “Optical absorption of an interacting many-polaron gas”, *Phys. Rev. B* **64**, 104504 (2001).
- [212] R. J. Gonzalez, R. Zallen, and H. Berger, “Infrared reflectivity and lattice fundamentals in anatase TiO_2 ”, *Phys. Rev. B* **55**, 7014–7017 (1997).
- [213] M. Lazzeri and F. Mauri, “Nonadiabatic Kohn Anomaly in a Doped Graphene Monolayer”, *Phys. Rev. Lett.* **97**, 266407 (2006).
- [214] A. M. Saitta, M. Lazzeri, M. Calandra, and F. Mauri, “Giant Nonadiabatic Effects in Layer Metals: Raman Spectra of Intercalated Graphite Explained”, *Phys. Rev. Lett.* **100**, 226401 (2008).
- [215] F. Caruso, M. Hoesch, P. Achatz, J. Serrano, M. Krisch, E. Bustarret, and F. Giustino, “Nonadiabatic Kohn Anomaly in Heavily Boron-Doped Diamond”, *Phys. Rev. Lett.* **119**, 017001 (2017).
- [216] M. Hohenadler, G. Wellein, A. R. Bishop, A. Alvermann, and H. Fehske, “Spectral signatures of the Luttinger liquid to the charge-density-wave transition”, *Phys. Rev. B* **73**, 245120 (2006).

- [217] S. Sykora, A. Hübsch, and K. W. Becker, “Dominant particle-hole contributions to the phonon dynamics in the spinless one-dimensional Holstein model”, *EPL* **76**, 644–650 (2006).
- [218] M. Weber, F. F. Assaad, and M. Hohenadler, “Phonon spectral function of the one-dimensional Holstein-Hubbard model”, *Phys. Rev. B* **91**, 235150 (2015).
- [219] I. Kupčić, Z. Rukelj, and S. Barišić, “CDW fluctuations and the pseudogap in the single-particle conductivity of quasi-1D Peierls CDW systems: II”, *J. Condens. Matter Phys.* **26**, 195601 (2014).
- [220] I. Kupčić, “Damping effects in doped graphene: The relaxation-time approximation”, *Phys. Rev. B* **90**, 205426 (2014).
- [221] I. Kupčić, “General theory of intraband relaxation processes in heavily doped graphene”, *Phys. Rev. B* **91**, 205428 (2015).
- [222] P. W. Anderson, “Absence of Diffusion in Certain Random Lattices”, *Phys. Rev.* **109**, 1492–1505 (1958).
- [223] G. Feher, R. C. Fletcher, and E. A. Gere, “Exchange Effects in Spin Resonance of Impurity Atoms in Silicon”, *Phys. Rev.* **100**, 1784–1786 (1955).
- [224] G. Feher, “Electron Spin Resonance Experiments on Donors in Silicon. I. Electronic Structure of Donors by the Electron Nuclear Double Resonance Technique”, *Phys. Rev.* **114**, 1219–1244 (1959).
- [225] G. Feher and E. A. Gere, “Electron Spin Resonance Experiments on Donors in Silicon. II. Electron Spin Relaxation Effects”, *Phys. Rev.* **114**, 1245–1256 (1959).
- [226] N. F. Mott, “The Basis of the Electron Theory of Metals, with Special Reference to the Transition Metals”, *Proc. Phys. Soc. A* **62**, 416–422 (1949).
- [227] E. Abrahams, P. W. Anderson, D. C. Licciardello, and T. V. Ramakrishnan, “Scaling Theory of Localization: Absence of Quantum Diffusion in Two Dimensions”, *Phys. Rev. Lett.* **42**, 673–676 (1979).
- [228] N. Mott, “The mobility edge since 1967”, *J. Phys. C Solid State Phys.* **20**, 3075–3102 (1987).
- [229] D. M. Basko, I. L. Aleiner, and B. L. Altshuler, “Metal–insulator transition in a weakly interacting many-electron system with localized single-particle states”, *Ann. Phys. (N. Y.)* **321**, 1126–1205 (2006).

- [230] B. Kramer and A. MacKinnon, “Localization: theory and experiment”, *Rep. Prog. Phys.* **56**, 1469–1564 (1993).
- [231] I. V. Gornyi, A. D. Mirlin, and D. G. Polyakov, “Interacting Electrons in Disordered Wires: Anderson Localization and Low- T Transport”, *Phys. Rev. Lett.* **95**, 206603 (2005).
- [232] V. Oganesyan and D. A. Huse, “Localization of interacting fermions at high temperature”, *Phys. Rev. B* **75**, 155111 (2007).
- [233] M. Žnidarič, T. Prosen, and P. Prelovšek, “Many-body localization in the Heisenberg XXZ magnet in a random field”, *Phys. Rev. B* **77**, 064426 (2008).
- [234] A. Pal and D. A. Huse, “Many-body localization phase transition”, *Phys. Rev. B* **82**, 174411 (2010).
- [235] R. Nandkishore and D. A. Huse, “Many-Body Localization and Thermalization in Quantum Statistical Mechanics”, *Annu. Rev. Condens. Matter Phys.* **6**, 15–38 (2015).
- [236] A. Fabien and N. Laflorencie, “Many-body localization: An introduction and selected topics”, *C. R. Phys.* **19**, 498–525 (2018).
- [237] P. Prelovšek, O. S. Barišić, and M. Mierzejewski, “Reduced-basis approach to many-body localization”, *Phys. Rev. B* **97**, 035104 (2018).
- [238] J. Krsnik, *Mnogočestična lokalizacija: dugovremenske koreacije gustoće naboja*. Diplomski rad, Prirodoslovno-matematički fakultet, Sveučilište u Zagrebu, 2018.
- [239] D. J. Luitz, N. Laflorencie, and F. Alet, “Many-body localization edge in the random-field Heisenberg chain”, *Phys. Rev. B* **91**, 081103 (2015).
- [240] T. C. Berkelbach and D. R. Reichman, “Conductivity of disordered quantum lattice models at infinite temperature: Many-body localization”, *Phys. Rev. B* **81**, 224429 (2010).
- [241] O. S. Barišić, J. Kokalj, I. Balog, and P. Prelovšek, “Dynamical conductivity and its fluctuations along the crossover to many-body localization”, *Phys. Rev. B* **94**, 045126 (2016).
- [242] B. Bauer and C. Nayak, “Area laws in a many-body localized state and its implications for topological order”, *J. Stat. Mech. Theory Exp.* **2013**, P09005 (2013).
- [243] J. H. Bardarson, F. Pollmann, and J. E. Moore, “Unbounded Growth of Entanglement in Models of Many-Body Localization”, *Phys. Rev. Lett.* **109**, 017202 (2012).
- [244] M. Serbyn, Z. Papić, and D. A. Abanin, “Local Conservation Laws and the Structure of the Many-Body Localized States”, *Phys. Rev. Lett.* **111**, 127201 (2013).

- [245] D. A. Huse, R. Nandkishore, and V. Oganesyan, “Phenomenology of fully many-body-localized systems”, *Phys. Rev. B* **90**, 174202 (2014).
- [246] A. Chandran, I. H. Kim, G. Vidal, and D. A. Abanin, “Constructing local integrals of motion in the many-body localized phase”, *Phys. Rev. B* **91**, 085425 (2015).
- [247] T. E. O’Brien, D. A. Abanin, G. Vidal, and Z. Papić, “Explicit construction of local conserved operators in disordered many-body systems”, *Phys. Rev. B* **94**, 144208 (2016).
- [248] L. Rademaker and M. Ortuño, “Explicit Local Integrals of Motion for the Many-Body Localized State”, *Phys. Rev. Lett.* **116**, 010404 (2016).
- [249] M. Mierzejewski, M. Kozarzewski, and P. Prelovšek, “Counting local integrals of motion in disordered spinless-fermion and Hubbard chains”, *Phys. Rev. B* **97**, 064204 (2018).
- [250] J. Z. Imbrie, “On Many-Body Localization for Quantum Spin Chains”, *J. Stat. Phys.* **163**, 998–1048 (2016).
- [251] J. Z. Imbrie, “Diagonalization and Many-Body Localization for a Disordered Quantum Spin Chain”, *Phys. Rev. Lett.* **117**, 027201 (2016).
- [252] J. Z. Imbrie, V. Ros, and A. Scardicchio, “Local integrals of motion in many-body localized systems”, *Ann. Phys. (Berl.)* **529**, 1600278 (2017).
- [253] M. Mierzejewski, J. Herbrych, and P. Prelovšek, “Universal dynamics of density correlations at the transition to the many-body localized state”, *Phys. Rev. B* **94**, 224207 (2016).
- [254] D. J. Luitz, “Long tail distributions near the many-body localization transition”, *Phys. Rev. B* **93**, 134201 (2016).
- [255] J. M. Deutsch, “Quantum statistical mechanics in a closed system”, *Phys. Rev. A* **43**, 2046–2049 (1991).
- [256] M. Srednicki, “Chaos and quantum thermalization”, *Phys. Rev. E* **50**, 888–901 (1994).
- [257] M. Ovadia, D. Kalok, I. Tamir, S. Mitra, B. Sacépé, and D. Shahar, “Evidence for a Finite-Temperature Insulator”, *Sci. Rep.* **5**, 13503 (2015).
- [258] K. X. Wei, C. Ramanathan, and P. Cappellaro, “Exploring Localization in Nuclear Spin Chains”, *Phys. Rev. Lett.* **120**, 070501 (2018).
- [259] M. Schreiber, S. S. Hodgman, P. Bordia, H. P. Lüschen, M. H. Fischer, R. Vosk, E. Altman, U. Schneider, and I. Bloch, “Observation of many-body localization of interacting fermions in a quasirandom optical lattice”, *Science* **349**, 842–845 (2015).

- [260] P. Naldesi, E. Ercolessi, and T. Roscilde, “Detecting a many-body mobility edge with quantum quenches”, *SciPost Phys.* **1**, 010 (2016).
- [261] J. Smith, P. Lee, A. Richerme, B. Neyenhuis, P. W. Hess, P. Hauke, M. Heyl, D. A. Huse, and C. Monroe, “Many-body localization in a quantum simulator with programmable random disorder”, *Nat. Phys.* **12**, 907–911 (2016).
- [262] P. Prelovšek, M. Mierzejewski, J. Kršnik, and O. S. Barišić, “Many-body localization as a percolation phenomenon”, *Phys. Rev. B* **103**, 045139 (2021).
- [263] M. Brenes, M. Dalmonte, M. Heyl, and A. Scardicchio, “Many-Body Localization Dynamics from Gauge Invariance”, *Phys. Rev. Lett.* **120**, 030601 (2018).
- [264] P. Sala, T. Rakovszky, R. Verresen, M. Knap, and F. Pollmann, “Ergodicity Breaking Arising from Hilbert Space Fragmentation in Dipole-Conserving Hamiltonians”, *Phys. Rev. X* **10**, 011047 (2020).
- [265] V. Khemani, M. Hermele, and R. Nandkishore, “Localization from Hilbert space shattering: From theory to physical realizations”, *Phys. Rev. B* **101**, 174204 (2020).
- [266] A. Smith, J. Knolle, D. L. Kovrizhin, and R. Moessner, “Disorder-Free Localization”, *Phys. Rev. Lett.* **118**, 266601 (2017).
- [267] S. Roy, D. E. Logan, and J. T. Chalker, “Exact solution of a percolation analog for the many-body localization transition”, *Phys. Rev. B* **99**, 220201 (2019).
- [268] D. E. Logan and S. Welsh, “Many-body localization in Fock space: A local perspective”, *Phys. Rev. B* **99**, 045131 (2019).
- [269] S. Roy, J. T. Chalker, and D. E. Logan, “Percolation in Fock space as a proxy for many-body localization”, *Phys. Rev. B* **99**, 104206 (2019).
- [270] Y. Bar Lev, G. Cohen, and D. R. Reichman, “Absence of Diffusion in an Interacting System of Spinless Fermions on a One-Dimensional Disordered Lattice”, *Phys. Rev. Lett.* **114**, 100601 (2015).
- [271] M. Serbyn, Z. Papić, and D. A. Abanin, “Thouless energy and multifractality across the many-body localization transition”, *Phys. Rev. B* **96**, 104201 (2017).
- [272] N. Macé, F. Alet, and N. Laflorencie, “Multifractal Scalings Across the Many-Body Localization Transition”, *Phys. Rev. Lett.* **123**, 180601 (2019).
- [273] J. Cardy, *Scaling and Renormalization in Statistical Physics*. Cambridge University Press, Cambridge, UK, 1966.
- [274] D. Stauffer, “Scaling theory of percolation clusters”, *Phys. Rep.* **54**, 1–74 (1979).

- [275] A. A. Saberi, “Recent advances in percolation theory and its applications”, *Phys. Rep.* **578**, 1–32 (2015).
- [276] F. Schwabl, *Statistical Mechanics*. Springer, Berlin Heidelberg, 2006.
- [277] K. Agarwal, S. Gopalakrishnan, M. Knap, M. Müller, and E. Demler, “Anomalous Diffusion and Griffiths Effects Near the Many-Body Localization Transition”, *Phys. Rev. Lett.* **114**, 160401 (2015).
- [278] D. J. Luitz, N. Laflorencie, and F. Alet, “Extended slow dynamical regime close to the many-body localization transition”, *Phys. Rev. B* **93**, 060201 (2016).
- [279] S. Gopalakrishnan, M. Müller, V. Khemani, M. Knap, E. Demler, and D. A. Huse, “Low-frequency conductivity in many-body localized systems”, *Phys. Rev. B* **92**, 104202 (2015).
- [280] R. Steinigeweg, J. Herbrych, F. Pollmann, and W. Brenig, “Typicality approach to the optical conductivity in thermal and many-body localized phases”, *Phys. Rev. B* **94**, 180401 (2016).
- [281] S. Bera, G. De Tomasi, F. Weiner, and F. Evers, “Density Propagator for Many-Body Localization: Finite-Size Effects, Transient Subdiffusion, and Exponential Decay”, *Phys. Rev. Lett.* **118**, 196801 (2017).
- [282] M. Žnidarič, A. Scardicchio, and V. K. Varma, “Diffusive and Subdiffusive Spin Transport in the Ergodic Phase of a Many-Body Localizable System”, *Phys. Rev. Lett.* **117**, 040601 (2016).
- [283] P. Bordia, H. Lüschen, S. Scherg, S. Gopalakrishnan, M. Knap, U. Schneider, and I. Bloch, “Probing Slow Relaxation and Many-Body Localization in Two-Dimensional Quasiperiodic Systems”, *Phys. Rev. X* **7**, 041047 (2017).
- [284] H. P. Lüschen, P. Bordia, S. Scherg, F. Alet, E. Altman, U. Schneider, and I. Bloch, “Observation of Slow Dynamics near the Many-Body Localization Transition in One-Dimensional Quasiperiodic Systems”, *Phys. Rev. Lett.* **119**, 260401 (2017).
- [285] A. Fick, “Über Diffusion”, *Ann. Phys. (Berl.)* **170**, 59–86 (1855).
- [286] P. Prelovšek, M. Mierzejewski, O. S. Barišić, and J. Herbrych, “Density correlations and transport in models of many-body localization”, *Ann. Phys. (Berl.)* **529**, 1600362 (2017).
- [287] O. S. Barišić and P. Prelovšek, “Conductivity in a disordered one-dimensional system of interacting fermions”, *Phys. Rev. B* **82**, 161106 (2010).

Curriculum Vitae with the List of Publications

Juraj Krsnik was born on the 28th of December 1994 in Zagreb, Croatia. After completing his secondary education at “Srednja škola Krapina”, in 2013 he enrolled in the research-oriented physics study program at the Department of Physics, Faculty of Science, University of Zagreb. In 2017 he was awarded the scholarship of excellence for research-oriented study physics students from the Institute of Physics, Zagreb. In 2018 he graduated on the subject of many-body localization under the supervision of dr. Osor Slaven Barišić. The same year he enrolled in the doctoral program in condensed matter theory at the Department of Physics, Faculty of Science, University of Zagreb working as a research assistant in the group led by dr. Osor Slaven Barišić at the Institute of Physics, Zagreb, and as an external teaching assistant at the Faculty of Science. His teaching activities include courses: Solid State Physics 1 and 2 and Selected Topics in Condensed Matter Physics. During his PhD studies, he published 5 papers, among which he is the first author of three papers.

List of Publications

5. **J. Krsnik** and O. S. Barišić, “Importance of coupling strength in shaping electron energy loss and phonon spectra of phonon-plasmon systems”, *Phys. Rev. B* **106**, 075207 (2022), [arXiv:2112.07265](#).
4. X. Mettan, E. Martino, L. Rossi, J. Jaćimović, **J. Krsnik**, O. S. Barišić, N. Babcsán, S. Beke, R. Mokso, G. Kaptay, and L. Forró, “Acoustic-Pressure-Assisted Engineering of Aluminium Foams”, *Adv. Eng. Mater* **23**, 2100306 (2021), [arXiv:2103.15225](#).
3. P. Prelovšek, M. Mierzejewski, **J. Krsnik**, and O. S. Barišić, “Many-body localization as a percolation phenomenon”, *Phys. Rev. B* **103**, 045139 (2021), [arXiv:2010.12295](#).
2. **J. Krsnik**, I. Batistić, A. Marunović, E. Tutiš, and O. S. Barišić, “Exact solution of electronic transport in semiconductors dominated by scattering on polaronic impurities”, *Phys. Rev. B* **102**, 241111(R) (2020), [arXiv:2002.12833](#).
1. **J. Krsnik**, V. N. Strocov, N. Nagaosa, O. S. Barišić, Z. Rukelj, S. M. Yakubanya, and A. S. Mishchenko, “Manifestations of the electron-phonon interaction range in angle-resolved photoemission spectra”, *Phys. Rev. B* **102**, 121108(R) (2020), [arXiv:1911.10985](#).